DEVELOPMENT OF PHYSICAL MODELS FOR MESOSCOPIC SIMULATION OF GAS-SURFACE INTERACTIONS

BY

KRISHNAN SWAMINATHAN-GOPALAN

DISSERTATION

Submitted in partial fulfillment of the requirements
for the degree of Doctor of Philosophy in Mechanical Engineering
in the Graduate College of the
University of Illinois at Urbana-Champaign, 2019

Urbana, Illinois

Doctoral Committee:

Professor Kelly A. Stephani, Chair
Professor Elif Ertekin
Professor Nick Glumac
Professor David Flaherty
Doctor Nagi Mansour

Abstract

This work is focused on the development of physically consistent models for the mesoscopic and macroscopic simulation of gas-surface interactions relevant for hypersonics and high-temperature aerothermodynamic applications. Both non-reactive and reactive interactions are considered with a special focus on desorption. The aim of the work is to employ microscopic information in the form of detailed experiments, numerical simulations, and fundamental theories, as a basis to construct general, accurate and physically realistic models for the interaction of oxygen: atomic (reactive) and molecular (non-reactive) with carbon surfaces: flat (vitreous) and complex porous microstructure (FiberForm®) at high temperatures ranging from 500 K to 2000 K. These models may be employed directly in conventional computational fluid dynamics (CFD), kinetic simulation, and material response tools for the study of non-equilibrium gas-surface interactions.

A detailed finite-rate surface chemistry model for the interaction of oxygen with vitreous carbon (VC) surface is developed from molecular beam experimental data using direct simulation Monte Carlo (DSMC). First, a generalized finite-rate surface chemistry framework incorporating a comprehensive list of reaction mechanisms is developed and implemented into the DSMC solver. The various mechanisms include adsorption, desorption, Eley-Rideal (ER), and several types of Langmuir-Hinshelwood (LH) mechanisms. Both gas-surface (e.g., adsorption, ER) and pure-surface (e.g., desorption) reaction mechanisms are incorporated, and the framework also includes catalytic or surface altering mechanisms involving the participation of the bulk-phase species (e.g., bulk carbon atoms). Expressions for the microscopic parameters of reaction probabilities (for gas-surface

reactions) and frequencies (for pure-surface reactions) that are required for DSMC are derived from the surface properties and macroscopic parameters such as rate constants, sticking coefficients, etc. This framework is used to numerically simulate the hyperthermal pulsed beam surface scattering experiments. Next, a general methodology for constructing finite rate surface chemistry models using time-of-flight (TOF) and angular distribution data obtained from pulsed hyperthermal beam experiments is presented. A detailed study is performed to analyze the TOF distributions corresponding to the various reaction mechanisms at diverse conditions using the DSMC surface chemistry framework. This information is used to identify and isolate the products formed through different reaction mechanisms from the molecular beam experimental data of oxygen on vitreous carbon. A general methodology to derive the reaction rate constants which takes into account the pulsed nature of the beam is described and used to derive the rates within the vitreous carbon oxidation model. The constructed finite rate surface chemistry model provides excellent agreement with the experimental TOF and angular distribution as well as the total product fluxes.

As a next step, the derived vitreous carbon oxidation model is extended to FiberForm®, which is used as a precursor of NASA's TPS material Phenolic Impregnated Carbon Ablator (PICA). The purpose of this study is to investigate the reactive interaction of fibrous carbon with atomic oxygen in a complex microstructure, which is the primary source of carbon removal at lower temperatures. The detailed microstructure of FiberForm® obtained from X-ray micro-tomography is used in the porous microstructure analysis (PuMA) simulations to capture the complexity of the porous and fibrous characteristic of FiberForm®. Comparison between the experimental and PuMA time-of-flight (TOF) distributions are presented for both the reactive interaction of the oxygen beam and the non-reactive interaction of the argon beam. It was also found that a significantly higher amount of CO (up to 30% of the total product flux) is generated when the beam interacted with FiberForm®, when compared with vitreous carbon. This is postulated to be primarily a result of multiple collisions of oxygen with the fibers,

resulting in an higher effective rate of CO production. Multiple collisions are also found to thermalize the O atoms, in addition to the adsorption/desorption process. The effect of microstructure is concluded to be crucial in determining the final composition and energy distributions of the products. Thus, an effective model for the oxygen interaction with FiberForm®, fully accounting for the detailed microstructure, for use in Computational Fluid Dynamics (CFD) and material response codes, is presented. In order to construct the effective surface chemistry model for FiberForm®, the VC model was applied to the detailed microstructure of FiberForm® to obtain the product fluxes at various porosities. At higher porosities, higher mole fractions of CO and lower amounts of O (up to 10% of the total product flux) were observed. This is due to the greater penetration of the incoming beam atoms into the microstructure leading to more collisions with the surface, resulting in the higher mole fraction of CO. This effect is more pronounced at higher temperatures when the probability of CO formation during a single collision is smaller. The effective model reaction mechanisms are assumed to be the same as that of the VC model, as well as the desorption rate constant values. Simulations performed using the constructed effective rates with a flat plate provided excellent agreement with the experimental TOF and angular distributions, and with the analyzed experimental fluxes. This effective model also provides excellent agreement with the PuMA data for the entire porosity range of interest.

In order to study the non-reactive (inelastic) scattering process, Molecular dynamics /Quasi-classical trajectory (MD-QCT) simulations and molecule-surface scattering (MSS) theory are used. The system of interest in this work is the gas-surface interactions of O_2 molecules striking a carbon surface. MD-QCT technique uses quasi-classical methods to represent the internal energies of the systems within MD and thus can be used to model accurate post-reaction and post-collision molecular internal energy distributions. The MSS theory employs a theoretical framework which accounts for several mechanisms of energy transfer between the substrate and gas particles including multi-phonon excitations,

and translational, rotational and vibrational energy transfer. This framework is quasi-classical and employs classical treatment of translational and rotational modes while the vibrational mode is considered quantum-mechanically. A range of initial translational energies of the molecule and the surface temperature is considered to elucidate the dependence of the scattered molecule properties on these parameters. The quantities of interest in this work are the final energy (translational, rotational and vibrational) and polar angular distributions. The values of the fitted MSS model parameters are presented along with their variation with the initial molecule translational energy and the surface temperature, along with the physical significance of their variation.

Finally, the desorption of O/CO from graphitic carbon surfaces is investigated using a one-dimensional model describing the adsorbate interactions with the surface phonon bath. The kinetics of desorption are described through the solution of a master equation for the time-dependent population of the adsorbate in an oscillator state, which is modified through thermal fluctuations at the surface. The interaction of the adsorbate with the surface phonons is explicitly captured by using the computed phonon density of states (PDOS) of the surface. The coupling of the adsorbate with the phonon bath results in the transition of the adsorbate up and down a vibrational ladder. The adsorbate-surface interaction is represented in the model using a Morse potential, which allows for the desorption process to be directly modeled as a transition from bound to free (continuum) state. The PDOS is an important input within the phonon-induced desorption (PID) model, which is a property of the material and the lattice and is highly sensitive to the presence of defects. The effect of random surface defects, etch pits, and adsorbates on the PDOS is considered in the present work. The presence of defects causes a redshift and broadening of the PDOS, which in turn changes the phonon frequency modes available for adsorbate coupling at the surface. This PDOS including defects is used within the PID model to predict the desorption rate constant. Using the realistic PDOS distributions, the PID model was used to compute the transition and desorption rates for both pristine and defective

systems. Mathissen's rule is used to compute the phonon relaxation time for pristine and defective systems based on the phonon scattering times for each of the different scattering processes. First, the desorption rates of the pristine system is fitted against the experimental values to obtain the Morse potential parameters for each of the observed adatoms. These Morse potential parameters are used along with the defective PDOS and phonon relaxation time to compute the desorption rates for the defective system. The defective system rates (both transition and desorption) were consistently lower in comparison with the pristine system. The difference between the transition rates is more significant at lower initial states due to higher energy spacing between the levels. In the case of the desorption rates, the difference between the defective and pristine system is more significant at higher temperatures. The desorption rates for each of the system shows an order of magnitude decrease with the strongly bound systems exhibiting the greatest reduction in the desorption rates.

Summava sonnanga

Veeta katti paru,

Kalyanatha panni paru,

Thesis ah ezhidhi paru...

- Tamil proverb (modified by SGK)

"If we knew what we were doing, it wouldn't be called research "

- Albert Einstein (maybe?)

To my amma, appa and akka

To my chella thatha and paati

To my advisor and all my teachers, from pre-kindergarten to post-graduate

Acknowledgments

First and foremost, I would like to thank my advisor Assistant Professor Kelly Stephani for providing me an opportunity to work in her research group, and for always being available for discussions. Her constant guidance and mentorship throughout the program were crucial in successful completion of the research projects and this thesis. I am extremely grateful to have an advisor with such patience and understanding. Right from my childhood, I have always been blessed with amazing teachers who have not only imparted knowledge, but also have been a unequivocable source of motivation and inspiration. To all those teachers, from pre-kindergarten to post-graduate, and to my advisor - *shri gurubhyo namaha*.

I benefited greatly from the collaboration with NASA-ARC. The discussions with Nagi, Francesco, Arnaud, and Joseph really expanded my horizons and gave me a great appreciation towards the final application of my research work. I would also like to thank my other collaborators from Montana State University.

I also thank my colleagues within the CKG group at UIUC, Taiyo, Sharanya, Tom, Sashank, Ben and Chaitanya; and other groups in UIUC, Revathi, Neil, Vegnesh and Saurabh. Thanks for the amazing discussions both within and outside of research.

I immensely enjoyed and learned a lot from attending various conferences throughout my graduate life. It also led to innumerable discussions with fellow graduate students and professors to mention a few: Maitreyee, Amal, Robin, Durgesh, Jeremie, Particia, Pierre; Profs Panesi, Levin, Boyd, van Duin, Rakesh Kumar, Kustova, Giovangigli, Hadjiconstaninou: Doctors Wysong, Liechty, Gallis, Plimpton, Jost.

I also like to extend my thanks to my friends here at UIUC, Ameya, Vignesh, Robin, Preethi, Rajavasanth, Mitisha, Samya, who have been with me through the ups and downs of this "Doctorate" journey. Special double mention to Sharanya and Chaitanya who were both research and chat buddies. To all my friends and relatives outside of UIUC, Abhinav, Ashwin, Prashanth, Nivedhita, Priya, thank you for being there for me from afar. And special thanks to my best friend Shashank Bharadwaj, a chat with whom, would always uplift my spirits, no matter the eight thousand miles between.

Finally, I would like to express my gratitude to my parents, Swaminathan and Nagalakshmi; my sister, Charanya; and my grandparents, Narayanan and Savithri; to whom I owe all that I am today. Thank you for showering unconditional love, and for showing unwavering belief in me.

Table of Contents

List of Tables

List of Figures

List of Abbreviations

AA	Associative Adsorption
ad	adsorption
CD	Condensation
CFD	Computational Fluid Dynamics
CI	Collision Induced
CLL	Cercignani-Lampis-Lord
$conj$	conjugate
CPU	Central processing unit
DA	Dissociative Adsorption
DI	Direct impact
DS	desorption
$DSMC$	direct simulation Monte Carlo
EB	Energy barrier
EDF	Energy distribution function
ER	Eley-Rideal reaction mechanism
eV	electron-volt
Exp	Experiment
GPU	Graphic processing unit
GS	Gas-surface
HA	Hot-atom
ID	Impact dissociation
IS	impulsive scattering
LH	Langmuir-Hinshelwood reaction mechanism

MB	Maxwell-Boltzmann
MD	Molecular Dynamics
MSS	Molecular Surface Scattering
max	maximum
min	minimum
$NASA$	National Aeronautics and Space Administration
NT	Non-thermal
$PDOS$	Phonon density of states
pen	penalty
Ph	Phonon
$PICA$	Phenolic impregnated carbon ablator
PID	Phonon-induced desorption
$prob$	Probability
$PuMA$	Porous microstructure analysis software
PS	Pure-surface
QCT	Quasi-classical trajectory
SB	Sublimation
TD	thermal desorption
TOF	time-of-flight
$tors$	torsion
TST	Transition state theory
$VACF$	Velocity auto-correlation function
val	valence
VC	Vitreous carbon
VDF	Velocity Distribution Function
vdW	van der Waals

List of Symbols

English

A, B	chemical species in the gas phase
$A(s), B(s)$	chemical species adsorbed on the surface
A_v	Avogadro's number
a, b	Annihilation operator
$a^\dagger, b^\dagger$	Creation operator
D	Diameter
E	Energy
$\tilde{e}$	polarization vector
F_N	ratio of real to simulated particles in DSMC
f	Distribution function
g	density of states
H	Height, Hamiltonian
$h, \hbar$	Planck's constant
I	moment of inertia, Angular momentum, interaction
i	imaginary number
j	rotational quantum number
K	equilibrium constant, scattering kernel, kinetic energy
k	reaction rate constant
k_b	Boltzmann's constant
l	Angular momentum, lattice
$M(b)$	bulk species on the surface
m	mass

N_A	total number of species A
n_A	surface number density of species A
n	number density, population distribution
P	Probability
p	linear momentum, particle
Q	Correlation function, atom positions
q	vibrational quantum number
R	position vector, m
Rn	Uniform random number between 0 and 1
r	Rate of reaction
S	Sticking coefficient
S_0	Sticking coefficient at zero surface coverage
S_p	Area of surface element
(s)	empty surface site
T	Temperature
t	time
u	velocity
u_0	mean velocity
V	potential
v	velocity, vibrational quantum number
v_R	Average phonon velocity
W	Debye-Waller factor, transition rate matrix

Greek

α	accommodation coefficients
β	Temperature exponent
Δ	inverse relaxation time
ε	energy
ϵ	porosity, continuum

ζ	polarization
θ	surface coverage, polar angle, angle of rotation
λ	phonons
μ	Mass ratio, reduced mass
ν	frequency of the reaction, site exponent
ρ	number density, density matrix
τ	characteristic time, scattering form factor, time constant
Φ	surface site density
ϕ	volume fraction, azimuthal angle, rad
χ	Scattering angle, rad
Ω	Sold angle
ω	frequency, angular velocity

Super-/Sub-scripts

a	adsorbate, activation
act	activation
ads	adsorption
$b, barr$	barrier
bp	bulk phase
bs	bulk species
$cond$	condensation
d	desorption
des	desorption
$diff$	diffusion
eq	equilibrium
f	final, formation
$form$	formation
g	gas-phase
i	initial, incident, incoming

$n, norm$	normal direction
$prod$	product
R, rot	Rotational
$reac$	reactant
$s, surf$	surface
sp	surface phase
ss	surface site set
sub	sublimation
T, tr	Translational
$t, tngt$	tangential direction
tot	total
V, v, vib	Vibrational
x, y, z	direction

Chapter 1

Introduction

1.1 Motivation

Developing accurate surface interaction and chemistry models is important for a number of applications such as manufacturing of chemical products, TPS (thermal protection systems) design, as well as material processing for semiconductors, and technologies for medical sciences, corrosion protection, lubrication, etc. Fundamental knowledge about the interaction mechanisms and their rates is critical in modeling and development of various heterogeneous catalytic processes and other aforementioned technologies.

Entry vehicles are exposed to aerothermodynamic heating during entry into a planetary atmosphere and require thermal protection systems (TPS) to shield the vehicle and its crew from the chemically reacting high temperature gases. Low-density carbon/phenolic ablators, built upon a rigid carbon fiber preform impregnated with phenolic resin, have proven to be a successful class of TPS materials for exploration missions. The flagship architecture within this class is the Phenolic-Impregnated Carbon Ablator (PICA). This material was successfully used on the Mars Science Laboratory (MSL) and Stardust missions. Modeling the performance and behavior of spacecraft TPS materials as they are exposed to extreme flight conditions is a challenging multi-scale problem. A schematic of a porous TPS undergoing ablation is shown in Fig. 1.1 where the key competing processes are highlighted.

Within the material, the fully charred (pyrolyzed) phenolic phase leaves a carbonized matrix (composed of carbon preform and charred phenolic) which in-

teracts with the reactive species in the boundary layer through heterogeneous reactions. The main material recession process in air is the heterogeneous oxidation of carbon. In addition, it is also the chief contributor to the exothermicity of the ablation zone, especially at the surface of the TPS, where the highly reactive matrix leaves the carbon preform exposed to incoming oxidants. Thus a detailed model for gas surface interactions and surface oxidation of carbon is of paramount importance for the accurate modeling of TPS recession. Within the hypersonic community, gas-phase chemistry has received a lot of interest [11, 12, 13, 14, 15, 16, 17, 18, 19, 20, 21, 22, 23, 24, 25, 26, 27, 28, 29, 30, 31, 32], whereas gas-surface interactions and surface chemistry has been relatively under-investigated. This work is focused on the development of physically consistent, predictive models for mesoscopic and macroscopic simulation of gas-surface interactions.

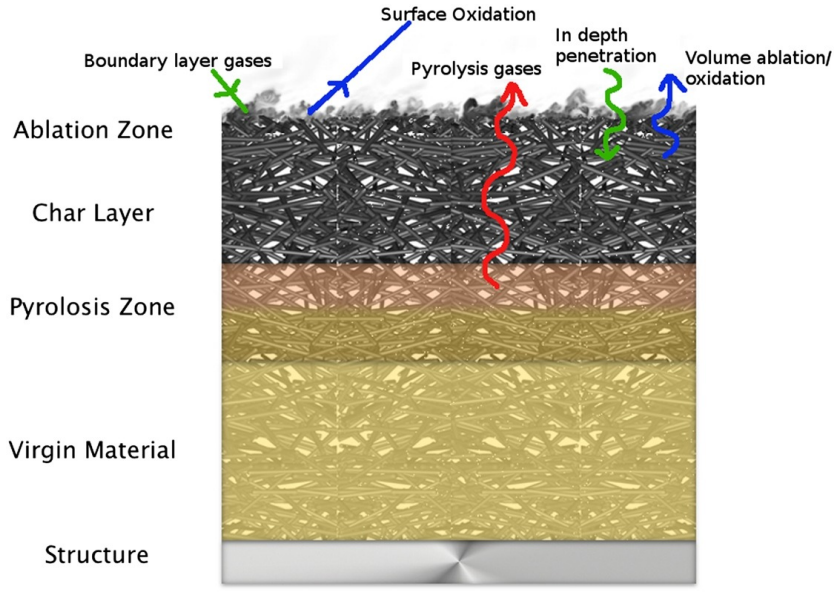

Figure 1.1: Schematic of ablation process in porous TPS [2].

Developing a predictive surface interaction model that is applicable over a wide temperature range can be complicated owing to competing mechanisms, such as adsorption, desorption, and chemical reactions. The reaction rate constant values are also usually very sensitive to the surface conditions, temperature, pressure,

etc., owing to the large disparities in the activation energies and power law dependencies [33, 34, 35]. Surface chemistry models are often developed using macroscopic experimental data such as total product fluxes, heat flux measurements, material recession, radiative signatures, etc [35, 36, 37, 38, 39, 40, 41, 42, 43, 44, 45, 46, 47, 48, 49, 50, 51, 52]. These quantities are used to infer the concentration of the various products near the surface, which are then used to obtain the corresponding reaction rates. Often one or more reaction mechanisms are simply assumed for each of the products in order to fit the rate constants to an Arrhenius form. However, these fits are derived from experimentally measured macroscopic properties that are a result of highly coupled processes on and near the surface, which are almost impossible to isolate [35, 36]. Although such an approach can be used to reproduce the observed data *a-posteriori*, the extension of such models for *a-priori* prediction at conditions different from those of the experiments remains a great challenge. Detailed mesoscopic models describing the fundamental interaction at the gas-surface interface are lacking. In the present work, microscopic gas-surface interaction details obtained from molecular beam experiments are employed to develop detailed physical models for use in mesoscopic and macroscopic scale simulations.

Continuum modeling approaches have been traditionally used to describe the processes at the macroscopic scales. However, this approximation breaks down when the length scales approach the mean free path of the system [53, 54, 55, 56]. The continuum description also fails due to the rarefaction effects induced by the presence of large gradients within the system [57, 58, 59, 60, 61, 62]. In recent years, an increasing number of applications involve conditions which render the continuum approximation invalid, for example, hypersonic re-entry flows, micro and nano-scale devices, micro-porous catalysis. In such cases, kinetic based methods like direct simulation Monte Carlo (DSMC) [53, 63, 64, 65, 66], which employ a molecular description of the gas are necessary to obtain high-fidelity solutions.

1.2 Reactive Gas-Surface Interaction

1.2.1 Carbon oxidation surface chemistry models

Processes involving the interaction of oxygen with carbon surfaces are important for a wide variety of applications, and the oxidation of carbon surfaces by molecular or atomic oxygen has been studied extensively from both experimental and theoretical perspectives [67, 68, 69, 70, 71, 72, 73, 74, 75, 76, 77, 78, 79, 80, 81, 82, 83, 84, 85, 5]. A vast number of studies involving carbon oxidation by molecular oxygen have provided a wealth of information including quantification of etch rates [78, 83, 84], activation energies associated with formation and desorption of CO and CO_2 products [75, 77, 82, 84], and finite rate models characterizing Arrhenius rate parameters for CO and CO_2 reaction pathways [75, 84, 86]. Oxidation of a carbon surface exposed to molecular oxygen (O_2) is known to initiate at active edge sites or surface defects, resulting in mass loss at the surface through CO and CO_2 desorption. Such processes occur at relatively high temperatures (>800 K) and involve activation energies greater than 1.6 eV [73, 87], while reaction of O_2 with the basal plane requires temperatures greater than 1500 K [88]. CO_2 is mainly observed at lower temperatures, while CO is present at low and high temperatures. The amount of CO is generally higher than the amount of CO_2 [89, 90, 91, 92, 93, 94, 95]. CO desorption observed in TPD experiments also produce broad bands indicating multiple pathways. These broadenings are a result of multiple functional groups and also significant dependence of each functional groups on the chemical/geomteric surroundings [93, 96, 97, 98, 99, 100]. In general, the characterization of the carbon surface oxygen groups is highly complex owing to the wide range of functional groups that are present, and the resulting interactions and transformations between them. Further, the bonding and stability of these groups are highly dependent on the presence of neighboring groups, site geometry, spin configuration, and structure [100, 101, 102, 103].

Carbon oxidation by atomic oxygen has also received considerable attention

[70, 74, 78, 79, 80], motivated by applications ranging from spacecraft thermal protection materials [85, 104, 105, 106, 107, 108], and more recently, surface chemistry of graphene and carbon nanotubes [77, 82]. Early studies involving oxidation of graphite by atomic oxygen found activation energies as low as 0.4 eV for surface temperatures up to 450 K, approaching activation energies of nearly zero at higher temperatures [73]. Wong *et al.* [70], Hahn [78], and Nicholson *et al.* [88] characterized the modes of O-atom attack and etch rates on graphite (natural) or highly oriented pyrolytic graphite (HOPG). Etching was found to initiate on the basal plane of graphite starting at temperatures of 373 K [70]. Hahn [78] investigated the oxidation of HOPG over a temperature range of 823-1223 K. Below temperatures of 1100 K, etching was found to initiate at point defects on the basal plane, while pit formation occurs at both point defects and basal plane atoms above 1100 K. Activation energies associated with lateral etching (pit growth) and vertical etching (pit initiation) on the basal planes of 1.48 eV and 2.0 eV were reported. It was suggested that CO rather than CO_2 was the primary product in the vertical etching, owing to the extraction of basal plane carbon atoms by atomic oxygen. It is noted that the oxygen source used in this study was dry air, thus any atomic oxygen incident on the surface is likely to have formed through gas-phase dissociation near the heated surface, although the ratio of O/O_2 is not reported. Nicholson *et al.* examined the oxidation of HOPG by a hyperthermal beam oxygen source (70% $O(^3P)$ atomic oxygen, 30% O_2) at a lower temperature range (298-423 K) and found an activation energy of 0.1 eV. This value was comparably lower than previously reported activation energies for atomic or molecular oxygen interaction with HOPG, and was attributed to the high energy of the incident beam particles [88].

Density functional calculations provide additional insight regarding surface groups, reaction pathways, and corresponding activation energies associated with carbon oxidation [74, 77, 80, 82, 101, 109, 110, 111, 112, 113, 114, 115, 116, 117, 118, 119, 120, 121, 122, 103, 123]. For the case of an oxygen molecule on carbon surfaces, several functional groups and their transformations and mechanisms for

subsequent desorption of O_2, CO and CO_2 have been studied. The important functional groups associated with the desorption of CO are carbonyl [100, 112, 102, 124, 113, 101, 118, 115, 114, 123] and semiquinone groups [112, 111, 113, 122, 116, 114], while some studies also suggest ether [102, 123, 80] and carboxyl groups [100, 118, 116]. Among these groups, semiquinone is shown to have the highest energy barrier, although these barriers are highly dependent on the mechanism and local site structure [111, 113, 101]. The carboxyl group is identified to be the main precursor in the desorption of CO_2[122, 100, 116]. However, at higher temperatures, the CO desorption from the carboxyl group is shown to have a lower barrier than the CO_2 desorption [122, 100]. In addition to these functional groups, oxygen can also be present as an epoxide on the surface, which is less likely to directly desorb; adsorbed oxygen, however, lowers the barrier for the desorption of CO/CO_2 from other functional groups [118, 120, 125, 126] Some mechanisms of CO/CO_2 formation were also shown to be independent of the oxidizing agent [122]. Atomic oxygen is found to adsorb onto the graphite basal plane at bridge sites, over the C-C bonds. The desorption energies associated with O adsorbed at bridge sites on graphite have been computed by Sorescu *et al.* [82] for both spin-singlet and spin-triplet epoxide structures from spin-polarized density functional calculations. The activation energy for O desorption from the spin-singlet epoxide configuration is 1.91 eV [80, 82], while O desorption from the spin-triplet configuration is considerably lower at 0.33 eV. In general, surface diffusion of O adatoms is found to be a necessary step for the formation of these products to be thermodynamically favorable [74, 80, 109], and is characterized by an activation energy of 0.5 eV.

In order to model the carbon-oxidation reactions at the macroscopic level, several attempts have been made to formulate simple finite rate models with effective mechanisms and reaction rates. Reviews regarding such models for the chemisorption of O_2 and further reactions on carbon surfaces can be found in Refs. [127, 126, 123, 119]. For atomic oxygen interaction with carbon surfaces, a number of finite-rate reaction models have been proposed with relevance to

spacecraft thermal protection systems. Under hypersonic atmospheric entry conditions, the shock-heated flow surrounding the vehicle results in gas-phase dissociation of O_2 molecules, providing a supply of atomic oxygen to the carbon surface. Two of the more commonly used high-temperature carbon oxidation models in the literature are the Park model [37], and Zhluktov and Abe (ZA) model [36]. Several modifications and improvements to these original models have also been proposed, most notably by Chen and Milos [38] (a variant of the Park model), and Alba [128] (a variant of the ZA model). An extensive numerical analysis and comparison among the existing models was presented by Candler [129, 130], and considerable differences were found among model predictions. From these studies, it was concluded that improvements to the existing models should be made through validation against detailed experimental measurements.

It is important to note that the finite-rate models mentioned above have been developed from macroscopic experimental data such as composition, heat and mass flux, and radiative signatures. These macroscopic quantities are a result of various surface and gas-phase processes which are highly coupled and often impossible to isolate. Furthermore, the relative prominence of the various reaction mechanisms may exhibit great variation resulting from the changes in rate constants and activation energies that are highly dependent on surface conditions, temperature, pressure, etc. [128, 33, 35, 34]. Important quantities, such as the mass loss rate, are known to be very sensitive to the external conditions and may vary by orders of magnitude [128]. Thus, a detailed surface chemistry model incorporating the physics at the microscopic level is of great importance.

1.2.2 Molecular Beam Experiments

Experimental data elucidating the molecular level details of the gas-surface interactions is of paramount importance in constructing a general, physically accurate surface chemistry model. Molecular beam experiments have been used extensively to study the kinetics and dynamics of gas-surface interactions [131,

132, 133, 134, 135, 136, 137, 138, 139, 140, 141, 142, 143, 144, 145, 146]. These experiments are usually performed in high vacuum environments, thus isolating the surface mechanisms from the gas-phase kinetics. The beam is directed at the surface of interest, where the incident atoms/molecules can undergo chemical reactions or simply scatter from the surface non-reactively. The scattered products are typically detected using a mass spectrometer as a function of angle and time. Analyzing the reactive and non-reactively scattered products can help to elucidate the gas-surface collisions at the atomic level. Particularly, the using a super-/hyperthermal beam provides an excellent way of distinguishing the reactive and impulsively scattered products. These beams can introduce the gas-phase reactants to the surface in a continuous manner or in terms of short bursts (pulses). Modulation of the beam into short pulses is ideal for introducing small controlled amounts of the gas onto the surface and further allows the study of the relative rates of different surface processes. The time resolved measurements, commonly known as time-of-flight (TOF) distributions, in addition to the composition of the surface scattered species, can be used to examine the time scales of the surface reactions, which may range from tenths of microseconds up to seconds [147, 148, 5, 149, 150, 151, 152, 153, 154, 155, 156, 157, 158, 159, 160, 161, 162, 163, 164, 165, 166, 167, 168, 169, 170, 171, 172, 173, 174, 175, 176, 177, 178, 179, 180, 181, 182, 183, 184]. This information provides a more detailed understanding of the possible mechanisms through which the detected products are formed.

The classical study by Olander *et al.* [185] investigated the interactions of a modulated beam of molecular oxygen (O_2) with the basal plane of pyrolytic graphite. Products scattered from the surface, including reaction products (CO and CO_2) and non-reactively scattered O_2 supplied by the beam, were detected by a mass spectrometer and collected over a range of surface temperatures. A hysteresis was found in the CO production rate, suggesting the importance of oxygen surface coverage in formation of the CO products. The reaction probability of CO was also observed to exhibit a peak at approximately 1400 K (owing to the competition of CO activation and desorption of O from the surface), and

migration of adsorbed oxygen to reactive edge sites was found to be an intermediate step in CO formation as well. The reaction probabilities characterized in this study, however, are limited to molecular oxygen interactions with carbon. Although both O and O_2 have been shown to react with basal plane atoms (in addition to defects and edge sites), O_2 must first undergo dissociative chemisorption, after which the resulting chemisorbed O atoms can react via largely the same reaction mechanisms by which an adsorbed O atom would react to form CO/CO_2 products. Thus, the reaction probabilities for CO/CO_2 formation from an O_2 source are remarkably different from that of an O atom source, owing to the additional dissociative chemisorption step. Until recently, experimental data that characterize carbon/atomic oxygen interactions at the microscopic level have not been available. Molecular beam-surface scattering experiments performed by Minton *et al.* [5] utilized a hyperthermal beam of primarily atomic oxygen with relatively low flux in high vacuum conditions. This ensures that localized interactions are limited to gas-surface processes [5]. Time-of-flight (TOF) data obtained from these experiments provide valuable information regarding reaction products and may also be used to distinguish products formed through mechanisms with different characteristic time scales.

Recent efforts by Poovathingal *et al.* [33, 34] have employed these molecular beam experimental data to construct a new finite rate surface oxidation model for carbon-based ablators in hypersonic flows. In their work, a finite rate model (herein referred to as the Poovathingal-Schwartzentruber-Murray-Minton (PSMM) model) was constructed from the molecular beam-surface scattering data [5]. Macroscopic reaction rates were obtained based on fits to the scattered product fluxes that were determined directly from the TOF data. In addition, efforts have been made to develop general methodologies for deriving detailed finite-rate surface chemistry models from molecular beam experiments [186, 107, 106, 187, 188, 6, 189, 190].

1.2.3 Mesoscopic Simulation Methodologies

Historically, ablation models used in hypersonic reentry simulations have been formulated as either surface models, one-dimensional volume averaged models [191, 192], and more recently have been formulated as two/three-dimensional volume averaged models [193, 194, 195, 196, 197, 198, 199, 200]. Such volume-averaged approaches [201] require model closures for the physical processes occurring within the porous material, which are typically derived from sparse experimental data.

Directly simulating the in-depth processes at the microscale may help resolve many of the model uncertainties and may help inform volume-averaged models. Lachaud *et al.* [202] used a random walk algorithm to simulate microscale diffusion through the material coupled with a marching cubes approach to track the moving fiber geometry due to ablation. This work by Lachaud *et al.* [202] successfully demonstrated how the in-depth penetration of oxygen atoms into the material could be simulated. However, the random walk approach is accurate only for single component diffusion and neglects convective gas transport, multicomponent diffusion, gas-phase chemistry, and non-continuum effects that arise from the fiber length scales approach the mean-free-path in the gas under many conditions of interest [203, 204, 205, 206, 207, 208, 209].

In order to address some of the aforementioned limitations, the current work employs the DSMC method to simulate the relevant gas-phase and gas-surface processes at the microscale. The DSMC method [53, 210] employs a molecular description of the gas and is capable of simulating all relevant physics including convection, multicomponent diffusion, gas-phase and gas-surface chemistry, and is accurate for flow conditions ranging from continuum to free-molecular [211, 57, 59, 212, 213, 214, 215, 216, 217, 218]. The use of DSMC to simulate flow over and within TPS microstructure was demonstrated for artificially generated microstructure [219] as well as for microstructure obtained through X-ray microtomography [220]. Finally, DSMC has also recently been used to study permeability in porous TPS materials [219, 221, 222, 223].

The current work is motivated by ongoing efforts to develop a DSMC-based simulation tool for carbon-based ablators. The simulation tool incorporates a surface recession model for a realistic porous carbon-fiber based substrate (FiberForm®) into DSMC [222, 224, 221, 225, 226, 227], enabling a fully-coupled simulation capability involving surface recession, gas-surface interactions, and gas-phase reactions for an ablation environment [219, 220, 225, 228, 229]. This work focuses on the development and validation of a DSMC gas-surface interaction model for carbon oxidation within this simulation tool.

1.3 Gas-Surface Interactions in FiberForm

1.3.1 Scattering within porous fibrous network

Most of the commonly used TPS materials are highly(>80%) porous and contain a complex network of carbon fibers of micrometer size impregnated with a phenolic resin [202, 230, 223, 222, 104, 231]. The pores within these TPS materials serve as pathways for high-temperature boundary layer gases to penetrate and interact thermally as well as chemically with the material, causing it to degrade or undergo ablation. The gases generated as a product of pyrolysis also flow through this porous network, and are eventually transported to the surface, producing a blow-out of pyrolysis gases that further helps mitigate the effective heat transfer from the incoming plasma, thus improving the efficiency of the TPS. Within the material, the fully charred (pyrolyzed) phenolic phase leaves a carbonized matrix. The carbonaceous remains, composed of carbon preform and charred phenolic, interact with the reactive species in the boundary layer through heterogeneous reactions. The main material recession processes in air are heterogeneous oxidation, phase changes, and mechanical erosion by friction and shear stress (referred to as spallation). This work focus on the heterogeneous oxidation processes, which are the chief contributors to the exothermicity of the ablation zone, especially at the surface of the TPS. For highly porous ablators, where the reacting gases can

percolate in-depth, it is important to consider the oxidation phenomenon at the scale of the fibers in order to understand the competing effects of diffusional mass transport and gas-surface reactions.

In order to obtain the microstructure of the carbon preform, Lachaud and Vignoles [232] used simplified digital models that describe the statistical, three-dimensional (3D) morphology of composite materials. This was also applied to study oxidation of carbon/phenolic ablators using artificially generated materials [202]. Using synthetic material models to mimic the microstructure of real composites has some limitations. Features of real materials, such as complex fiber morphologies, fiber clusters, actual pore-size distribution and other irregular characteristics, are very difficult to describe analytically and are not captured by ideal geometries. Synchrotron X-ray micro-tomography (micro-CT), used in the past to image C/C composites [233], was recently applied to image substrates of carbon/phenolic ablators [234, 104, 222]. The technique provides a high-fidelity digital representation of the actual material microstructure where the geometry of the fibers is captured as a 3D matrix of grayscale values. Modern micro-CT instruments can reach voxel resolutions below a micrometer, thus are able to resolve the fibrous structures of carbon preform material in detail. The gray-scale value within a voxel is proportional to the absorption of X-rays by the material, hence to the material density.

1.3.2 Effective models for FiberForm

The performance of TPS materials is typically assessed by material response (MR) codes [191, 235, 236, 237, 194] that model ablation processes and the resulting material degradation. Some of the commonly used MR codes are Charring Materials Thermal Response and Ablation (CMA) [238], Fully Implicit Ablation and Thermal response (FIAT) [191], 3dFIAT [239, 240], Two-dimensional Implicit Thermal response And ablatioN (TITAN) [241],CHarring Ablator Response (CHAR) [192, 242, 198], Modeling of Pyrolysis and Ablation Response

(MOPAR) [243, 244, 245], Kentucky Aerothermodynamics and Ablation Response System - Material Response (KATS-MR) [194, 195, 196] and Porous-material Analysis Toolbox based on OpenFOAM (PATO) [237].

Heritage MR codes take a simplified approach and use recession rates directly from experiments, while newer codes use overal reaction rates along with the microstructure to model the ablation process. Thus, these codes require bulk reaction rates of the complex, highly irregular microstructures, obtained from either experiments or computations, to accurately model the ablation of the porous networks of materials, that is not readily available.

1.4 Non-reactive scattering of molecules from surfaces

1.4.1 Molecular Dynamic Simulations

Non-reactive interaction of gases with the surfaces results in interesting and important physical processes such as the energy transfer between the gas and surface, and also between the translational and internal (rotational and vibrational) modes for the case of diatomic and polyatomic species. Scientists have studied this phenomena for decades using experiments [246, 247, 248, 249, 250, 251, 252, 253, 254, 255, 256, 146, 257, 258, 259, 260, 261, 262, 263, 264, 265, 266, 267, 268, 269, 270, 271, 272] and theory [273, 274, 275, 276, 277, 278, 279, 280, 281, 282, 283, 284]. With the development of new experimental techniques and quantum-mechanical theories, the understanding of this inelastic scattering process has increased substantially over the years. However, accurate description of the final scattered distributions of the molecules for a range of initial conditions is still lacking. In addition, these experimental data are still limited to a small number of chemical species. Furthermore, there has been little focus on the final internal energy distributions of molecules and the energy transfer mechanisms with the surface and the translational mode of the molecule.

In recent years, numerical simulations have been used to gain insight into the

gas-surface interaction process. These scattering events can be studied using simulation techniques such as molecular dynamics (MD) [285, 286, 287, 288, 289, 290, 291, 271, 292, 293, 294, 295, 296, 291, 297]. Within MD, the Newton's equations of motion are used to determine the trajectory of the atoms in the systems. The force interaction between the atoms are calculated using the inter-atomic potential, which is the most important input into the MD simulations. This technique can be used to model the interaction of the incoming gas molecules with the surface and the subsequent post collisional properties as a function of various incidence parameters and state of the system. With the ever-increasing computational power and resources along with the rapid development of fast numerical techniques, accelerated algorithms and parallel processing, MD can be used to model atomic interactions over temporal and spatial scales relevant for gas-surface scattering process. In addition, recent years have witnessed the development of physically accurate inter-atomic potentials using detailed quantum mechanical data, thus leading to accurate representation of the atomic interactions.

1.4.2 Models for non-reactive gas-surface scattering

The most common approach in modeling the gas-surface interactions has involved the use of simple models with a wide range of tunable/fitting parameters to match experimental observations. Some of the commonly used gas-surface scattering models include Maxwell [298, 299], Cercignani-Lampis-Lord (CLL) model [300, 301, 302], hard-cube model [303, 304, 305], soft-cube model [306, 307], washboard model [308, 309, 310], hard-sphere model [311], soft-sphere model [312], and multi-stage models [297, 290]. Although such an approach can be used to reproduce the observed data *a posteriori*, the extension of such models for *a priori* prediction at conditions different from those of the experiments remains a great challenge. Further, all of these models have been developed for continuum systems, while a state resolved description is necessary for accurate and high-fidelity representation of the gas-surface and subsequent gas-phase interaction processes [313, 314, 315,

316, 317, 318].

A collision with the surface can lead to a variety of different outcomes, for example inelastic scattering, physisorption, chemisorption, and direct impact reactions. In all of the cases, an important channel for the exchange of energy is phonon annihilation or creation, which in most cases is by far the dominant mechanisms for energy transfer, although excitation of electron-hole pairs or other elementary electronic excitations may play a role. Thus, a detailed theoretical approach which includes the interaction and energy exchange between the atom/molecule and the phonons at the surface is necessary for an appropriate description of the gas-surface interaction over a wide variety of conditions.

The first theoretical calculations accounting for the interaction of the gas particles with the surface phonons were performed by Jackson and Mott [319, 320]. Their calculations were the first to describe the energy transfer in surface scattering by what is known as a single-phonon distorted wave Born approximation. Later Lennard-Jones and co-workers performed calculations which underlined the importance of energy transfer to the phonons during both inelastic scattering and reactive scattering [321, 322, 323, 324, 325, 326]. Their calculations were also done using the distorted wave Born approximation, and they also investigated multiple phonon transfers.

In recent years there have been a number of general approaches to the inelastic surface scattering problem that are capable in principle of describing the complete picture of multiquantum exchanges upon collision [327, 328, 329, 330, 331, 332, 333, 334, 335, 275, 276, 336, 337, 338, 339, 340, 341, 281, 282, 342, 283], most of which involve semiclassical approximations or at least invoke some form of the trajectory approximation [343, 344, 345, 346]. In particular, detailed theories of inelastic surface scattering based on the powerful transition matrix formalism have been developed by Beeby [327, 328], Brenig [333, 336], Brako and Newns [275, 276], and Manson [281, 282, 283]. This approach is utilized and extended in the current work to describe the gas-surface interaction process.

1.5 Desorption from surfaces

1.5.1 Phonon-induced Desorption

Conversion and transfer of energy among reactants and between reactants and a catalyst is characteristic of all stages of catalytic processes. A gas particle desorbing from a surface must acquire an energy that is somewhat larger than the negative of the energy of the bound state it occupied in equilibrium. Reactant and product particles can couple to several types of excitations constituting the heat bath of the system and facilitating energy dissipation, like the vibrational (localized and delocalized phonons) and electronic degrees of freedom. Their role in dissipation processes depends largely on the strength of coupling to reactants in each reaction channel and the density of excitations that contribute to the energy transfer processes. In most cases, the coupling of the substrate to the electronic degrees of freedom are weaker in comparison to the phonon coupling. Thus, phonon-induced desorption is one of the major pathways through which desorption occurs.

Desorption of thermal products from the substrate occur through the interaction with the phonon bath on the surface. Yet, even the latest models characterize the rate of desorption only as a function of temperature. The effect on the desorption rate due to variations in the surface phonons which is a function of the surface structure and configuration need to be characterized for these systems. A mesoscale description of the surface energetics which participate in, and promote, the desorption of surface adsorbates and oxidation products is currently lacking.

Various theoretical models have been developed to describe the exchange of energy between the adsorbate and the surface phonons and the desorption process [8, 347, 348, 349, 350, 351]. Most of these models use a half collision analog of a gas particle interacting with the surface. The Hamiltonian of the system is described at the initial state with the adsorbate on the surface, and the final state with no interaction between the surface and gas particle. Goldys and

Gortel [348] proposed a one-dimensional quantum statistical model to describe physisorption processes within a semi-infinite solid. Ying and Bendow [8, 347] proposed a three dimensional model multi-phonon interaction theory which uses the time- and position-dependent displacement-displacement correlation function of the lattice to obtain the desorption rate. Recently Gumhalter [351] presented a theory focusing on the energy transfer to the surface phonons during the desorption process.

All of these models usually employ the simple harmonic oscillators (SHO) to describe the vibrational bond between adsorbate and the surface. However, within the harmonic approximation, the bond breaking is not inherently captured and has to be imposed, typically as a vibrational threshold beyond which desorption is assumed. In addition, the energy spacing between the oscillator levels are constant within the SHO approximation, which becomes a poor approximation particularly at the higher energy levels. Furthermore, the SHO allows only mono-quantum jumps, which again breaks down at higher energy levels. The Morse potential provides a much better approximation to the adsorbate surface bond with decreasing energy gaps at higher levels, finite probability of multi-quantum transitions and a clear threshold between the free and bound states.

Efrima and co-workers [349, 350] have developed a theory which utilizes the Morse potential for describing the adsorbate-surface potential. The Morse potential is more realistic for capturing the vibrational interaction between the surface and adsorbate as it allows for multi-quantum jumps, and also the energy spacing decreases with increasing energy with a clear threshold for desorption. The transition between the levels is assumed to follow a Markoffian random walk. A transition matrix is computed for the probabilities of jumping between the oscialltor levels based on the PDOS of the surface and the aforementioned Morse potential. This theory is utilized within the current work to describe the desorption of O and CO from carbon surfaces.

1.5.2 Surface Phonon Density of States

Phonons generally affect the thermal, optical, mechanical, and electrical properties of materials. While the phonon density of states (PDOS) is primarily a function of the local atomic structure, it is also sensitive to atomic-level stresses and the microstructure. The presence of adsorbates and defects on the surface are known to cause deviations to the PDOS from the corresponding bulk structure. Thus, it is natural to expect that even small concentrations of defects in graphitic carbon may lead to specific shifts, broadenings and additional characteristic singularities in the phonon densities of states and thus change the material specific heat and transport properties. Such effects in carbon used as TPS are very significant because of the continual change in the lattice of the material owing to the reactive interaction and erosion due to ablation.

Changes in the phonon density of states not only affect the material thermophysical properties, but also affects the adsorption and reaction rates and thereby the ablation and recession rates. Although the effects of point defects caused due to irradiation on graphite has been examined previously in the literature [352, 353, 354, 355, 356], the main type of defect encountered during ablation is etch pits occurring as a result of oxidation reaction due to atomic oxygen. The effect of such etch pits individually and in the presence of point defects (perhaps introduced by fabrication/processing) need to be studied. Further, the surface coverage of adsorbates on ablative carbon surface exposed to atmospheric (re)entry is expected to be high and close to saturation. Thus, effect of adsorbates on the PDOS at high surface coverages should also be examined.

1.6 Scope

This work is focused on the development of physically consistent models for mesoscopic and macroscopic simulation of gas-surface interactions. This work considers both non-reactive and reactive interactions with a special focus on desorption.

Developing a predictive surface interaction model that is applicable over a wide temperature range can be complicated owing to competing mechanisms, such as adsorption, desorption, and chemical reactions. The reaction rate constant values are also usually very sensitive to the surface conditions, temperature, pressure, etc., owing to the large disparities in the activation energies and power law dependencies. In addition, non-equilibrium phenomena is frequently encountered in the systems of interest. Thus, detailed mesoscopic models describing the fundamental interaction at the gas-surface interface is necessary for obtaining high-fidelity solutions. The aim of the work is to employ microscopic information in the form of detailed experiments, numerical simulations, and fundamental theories, as a basis to construct very general, accurate and physically realistic models. The purpose of these investigations is to develop high-fidelity models that can be directly used in cases of non-equilibrium which is frequently encountered in the systems of interest.

This work introduces a new generalized surface chemistry framework that is comprehensive and can be applied to any mesoscopic and macroscopic simulation techniques. This framework is used to devise a general approach for constructing finite rate surface chemistry models using pulsed hyperthermal beam experimental data. This general methodology along with the detailed surface chemistry framework is used to construct a surface chemistry model for the carbon and atomic oxygen system. This model, which was developed for a flat carbon surface is extended to porous FiberForm® with complex microstructure. Further, effective models that inherently account for the FiberForm® microstructure are also developed.

Next, the focus of this work is shifted to non-reactive gas-surface interaction of molecules. MD-QCT simulation technique and the MSS theoretical model is used to study the inelastic scattering between the molecular oxygen and carbon. Finally, the desorption process is analyzed within the framework of phonon-induced desorption model for pristine and defective surfaces. Realistic surface phonon density of states is used to investigate the variation in the desorption rates of

atomic oxygen and carbon monoxide from carbon surfaces. The major efforts and contributions of this dissertation are summarized below.

- Developed a generalized surface chemistry framework incorporating a comprehensive list of reaction mechanisms, including gas-surface and pure-surface reactions as well as catalytic and surface altering mechanisms.
- Implemented the detailed surface chemistry framework into DSMC solver SPARTA and Porous microstructure analysis software PuMA.
- Developed a general methodology to derive physically consistent finite rate surface chemistry models from pulsed hyperthermal beam experimental data.
- Performed detailed analysis of the molecular beam experimental data of atomic oxygen interacting with vitreous carbon surface to identify the reaction mechanisms occurring within the system.
- Constructed a detailed finite rate carbon oxidation surface chemistry model with physically consistent mechanisms and precise rate constants based on the vitreous carbon experimental data.
- Extended the vitreous carbon oxidation model to FiberForm® and studied the final reactive product fluxes as a function of microstructure properties.
- Formulated a novel approach to include the microstructure information within the finite-rate surface chemistry models, thus enabling the direct use of these models within continuum solvers.
- Constructed an effective surface oxidation model for FiberForm® where the rate constants are a function of porosity in addition to the surface temperature.
- Performed MD-QCT simulations of non-reactive gas-surface scattering of rotationally and vibrationally resolved O_2 on carbon surfaces; and analyzed the final energy and angular distributions for various initial conditions to

elucidate the effect of the initial molecule translational energy and surface temperature.

- Utilized the MSS theory to describe the inelastic gas-surface interaction of molecular oxygen with carbon surfaces; calibrated the MSS model parameters using the final energy and angular distribution from MD.

- Performed PDOS calculations using MD on carbon surfaces to analyze and understand its dependence on the commonly encountered defects during ablation.

- Utilized the phonon-induced desorption model to study the effect of defects on the transition and desorption rates.

Although the methodologies and models described in this work are applied to particular systems, many of these approaches can either be used directly or can be easily extended in a straightforward manner to study various other systems and under different conditions.

1.7 Outline

The subsequent portion of the thesis is organized as follows. Chapter 2 provides an outline of the recently developed detailed surface chemistry framework in DSMC. New model forms for the surface reaction probabilities are introduced based on the mechanisms included in this framework. This chapter also provides detailed information regarding the modeling of gas-surface (GS) reactions and pure-surface (PS) reactions, and also describes the various scattering models. This detailed surface chemistry framework is used to computationally model the molecular beam experiments, outlined in Chapter 3. This is used as a basis to develop a general approach for constructing surface chemistry models from hyperthermal beam experimental data. This chapter describes the use of DSMC to analyze the different

components of the experimental distributions that correspond to the various surface mechanisms to identify the different components of the experimental TOF distributions. This is followed by the discussion of the appropriate procedure to compute the total fluxes of each surface reaction product from the experimental distributions (both TOF and angular data). This chapter ends with the presentation of the general calibration methodology which is used to compute the rate constants. The comprehensive surface chemistry framework from Chapter 2 and general construction methodology from Chapter 3 is used to develop a detailed carbon oxidation model consisting of physically consistent reaction mechanisms and rates in Chapter 4.

Chapter 5 extends the VC model developed in Chapter 4 to FiberForm®, which is the basis for the TPS material PICA (Phenolic Impregnated Carbon Ablator), commonly used by NASA. This chapter starts by describing the micro-tomography procedure used to obtain the FiberForm® samples. In addition to the reactive scattering of oxygen from FiberForm®, this chapter also analyses the non-reactive interaction between FiberForm® and argon. This chapter concludes with a comparison of the FiberForm® molecular beam experimental results with the DSMC/PuMA results where the VC model applied to FiberForm®. From this study, porosity is identified to be one of the most important property of the microstructure which determines the final concentration of the oxidation products. Chapter 6 focuses on developing effective models, which do not require the complete microstructure, from the detailed VC model for FiberForm®. The rate constants within the effective model inherently contain the information of the microstructure and thus can be used directly and consistently in continuum solvers where the surface is treated as flat. This chapter also quantifies the effect of porosity on the final reaction products of FiberForm®, and develops effective rate constants that are a function of porosity in addition to the temperature.

In Chapter 7, the focus is shifted to non-reactive interaction of molecules with surfaces. The MD-QCT method is used to perform simulations of the inelastic interaction of O_2 molecules with carbon surfaces. The final energy (translational,

rotational, and vibrational) and angular distributions for a wide range of initial conditions are computed and analyzed to elucidate the gas-surface scattering process. In particular, the effect of varying the initial molecule translational energy and the surface temperature is studied. Chapter 8 uses a different approach to describe the same inelastic scattering event: through a rigorous theoretical model based on gas-phonon interactions at the surface. This molecule surface scattering (MSS) model considers several such mechanisms including multi-phonon processes, translational and internal mode (rotational and vibrational) excitations. A state-resolved description of the scattered particles is obtained as an output from this model through the evaluation of the detailed scattering kernels and transition matrix. The "free" parameters within the MSS theory are calibrated against the MD-QCT data from the previous chapter. In addition, this chapter also discusses the physical significance of the variation of these parameters with the initial conditions.

The final part of the thesis is aimed at studying the desorption of adsorbates from the surface as a result of thermal fluctuations. Similar to the non-reactive scattering, the surface phonons play the major role within the thermal desorption process. Thus, Chapter 9 is focused on characterizing the surface phonon modes and density of states in the presence of various factors such as etch pits, random surface roughness, and adsorbates with different configurations. Chapter 10 presents a rigorous theoretical model for describing the desorption of adsorbed atoms/molecules due to interaction with the surface phonons. The adsorbate-surface interaction (oscillator) is described using the realistic Morse potential. This oscillator is coupled with the phonon bath leading to excitations and de-excitations along the vibrational 'ladder'. This process can be described as a random walk using the Markoffian approximation and first order master equation is solved for the probability in a given state. The transition matrix describing the probability of transition between the oscillator energy levels is calculated and is used to obtain the desorption rate constants. The transition and desorption rates of both pristine and defective systems are computed using this procedure,

and are compared and analyzed. Finally, the conclusions, key contributions and recommendations for future work are presented in Chapter 11.

Part I

Vitreous Carbon Surface Oxidation Model

Chapter 2

Generalized Surface Chemistry Framework

2.1 Overview

Many state-of-the-art DSMC codes like SPARTA [357], DAC [358, 359], and MAP [360] employ relatively simple surface interaction models. Surface reaction processes include only basic reaction mechanisms such as dissociation, recombination and exchange reactions. There is no provision for the gas-phase species to adsorb on the surface and undergo reactions based on finite-rate kinetics. In order to improve the surface reaction modeling capability in DSMC, a general finite-rate surface chemistry framework incorporating several reaction mechanisms is developed and implemented into SPARTA. This enables the user to model a variety of surface reactions via user-specified reaction rates and surface properties, without the need for modifying the source code. The basic approach is to stochastically model the various competing surface reaction mechanisms occurring on a set of active sites on a Langmuirian surface. Both gas-surface (GS) and pure-surface (PS) reaction mechanisms are incorporated into this framework. This framework is introduced and outlined in preparation for simulating and analyzing the pulsed hyperthermal beam experiments and the construction of finite rate surface chemistry models presented in Chapter 3.

This chapter provides an outline of the detailed surface chemistry framework in DSMC. New model forms for the surface reaction probabilities are introduced based on the mechanisms included in this framework. Section 2.2 presents the system definitions within the proposed framework, followed by some theory and description about the various surface reaction mechanisms in Section 2.3. Detailed

information regarding the modeling of GS reactions and PS reactions are provided in Section 2.4 and Section 2.5 respectively. Section 2.6 describes the various scattering models and finally, conclusions are presented in Section 2.7.

2.2 System Definitions

Recently Marschall, Maclean and Driver presented a general finite rate surface chemistry framework for computational fluid dynamics (CFD) solver [3, 361]. The general terminology and definitions introduced in their work, namely the representation of different phases and surface sites, is adopted by the current framework. The system under consideration is a gas/solid material interface (Fig. 2.1). In addition to the gas environment, two additional environments, namely the surface interface and bulk material are included in the system model. Each environment can consist of one or more "phases", which are distinct, non-interacting regions.

The surface environment is comprised of sites, where gas-phase species can adsorb and react with species from gas, surface or bulk environments. The surface is treated as a Langmuirian surface, however all the surface sites need not be similar. Each surface environment can have multiple phases. The species adsorbed on different phases cannot interact with each other. The purpose of including multiple phases is to account for the representation of composite materials, where different regions can exhibit different types of chemical reactivity. Further, each surface phase can have multiple sets of sites. These different types of surface sites are assumed to be distributed uniformly within the surface phase. Surface reactions involving species adsorbed on different type of sites within a surface phase are possible. Such a representation of sites can be very useful for modeling different types of surfaces, for example, material containing non-homogeneous surface composition such as SiO_2, SiC, etc, or for modeling homogeneous materials containing sites of different internal bondings (electronic structure and configuration) which exhibit large differences in their reactivities [362, 363]. Each set of sites within each surface phase is distinct and can be distinguished for the purpose of

performing surface reactions. For example, a gas-phase species can be specified to adsorb only on a particular type of site and not on other types of sites within the same surface phase. The number and concentration of surface sites and surface phases can change as the material undergoes surface-altering reactions.

The bulk environment can also contain several phases, each of them occupying a specified volume fraction. The purpose is to model composite materials like porous carbon phenolic TPS. Each of the bulk phases are assumed to be distributed uniformly and the concentration of each phase is equal to its volume fraction. As surface-altering reactions occur, the total volume of the bulk phase is allowed to change.

All of the surface and bulk environments are present within each triangular surface element in DSMC as shown in Fig. 2.1 (b). The surface phases and site sets are distributed uniformly throughout the surface element. Within the current framework, the motion of the adsorbed atoms are not explicitly modeled, hence the particles are deleted when they undergo adsorption. The information of the adsorbates (like surface coverage, etc.) are stored within each surface elements. All the surface reactions are performed based on the concentrations within each surface element. Currently, the surface is treated as an infinite sink and source, *i.e.,* surface morphology does not change even when they undergo bulk phase removal or addition.

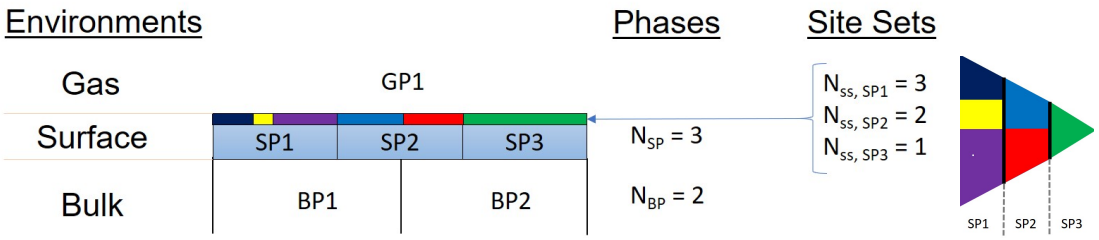

Figure 2.1: (a) Surface reaction framework system consisting of environments, surface phases and sets of active sites. Taken from Marschall and Maclean [3]. (b) The same framework shown within a triangular surface element in DSMC.

2.3 Types of reactions

One way of characterizing the surface reactions is based on the participation of the surface atoms in the reactions. If the surface atoms only act as catalysts to promote the reaction, then it is termed as catalytic reactions. On the other hand, if the surface atoms participate in the reaction to form products, they are termed as surface participation reactions.

Employing another criteria, surface reactions can be categorized in a different manner: gas-surface (GS) and pure-surface (PS) reactions. The GS reactions involve both gas-phase and adsorbed species as reactants. On the other hand, the PS reactions involve only adsorbed (physisorbed or chemisorbed) reactants and do not include any gas-phase atoms or molecules. From a DSMC implementation viewpoint, this type of characterization based on the presence of gas-phase reactants is more meaningful since GS reactions are performed when the atom/-molecules strikes the surface (as a part of the move kernel), while PS reactions are performed separately within each time step. Hence this type of characterization will be followed in this paper, where the modeling of the GS and PS reactions will be discussed individually.

Before proceeding to the implementation details regarding the different surface reactions, some theory that will be useful in the modeling of the common surface reactions are presented in this section. Appendix A contains information regarding additional surface reaction mechanisms.

2.3.1 Adsorption

Adsorption is the adhesion of atoms/molecules on a surface and is the necessary first step in all of the surface mediated reactions. Based on the nature of bonding, there are two modes of adsorption: physisorption and chemisorption. In physisorption, the atom/molecule is only weakly bound to the substrate by Van der Waals - type forces. However, in chemisorption, a strong bond is formed be-

tween the adsorbate and substrate involving significant rearrangement of electron density.

A different method of categorizing adsorption reactions is depending on whether the incoming gas-phase particle dissociates in the process. It is common for molecules to dissociate upon striking the surface and bond as smaller molecules or atoms. By definition atoms can only associatively adsorb, while molecules can either associatively or dissociatively adsorb.

$$\textit{Associative Adsorption}: \qquad O(g) + (s) \longrightarrow O(s) \quad O_2(g) + (s) \longrightarrow O_2(s) \tag{2.1a}$$

$$\textit{Dissociative Adsorption}: \quad O_2(s) + (s) \longrightarrow O(s) + O(g) \quad O_2(g) + 2(s) \longrightarrow 2O(s) \tag{2.1b}$$

In a similar manner, adsorption can also be categorized based on the motion of the adsorbate. If the atom/molecule diffuses on the surface, the process is termed as mobile adsorption. On the other hand, the diffusion barrier can be large, restricting the motion of the adsorbate, leading to immobile adsorption.

Yet another method of classifying is through the dynamic pathway through which the adsorption reaction occurs: direct and indirect adsorption. The direct adsorption process is one in which the particle collides with the surface and immediately bonds with the site at the point of impact. In the indirect mode, the particle first adsorbs as a precursor (intermediate). This precursor is weakly bound (maybe physisorbed) and can move freely over the surface. After a short time, it forms a bond with an appropriate adsorption site (chemisorption).

2.3.1.1 Direct adsorption - Langmuir Model

Langmuir first proposed this direct adsorption model [364], where the atom/-molecule adsorbs immediately on the surface site it strikes. In this case, the probability of adsorption depends on two factors. First, the particle must strike

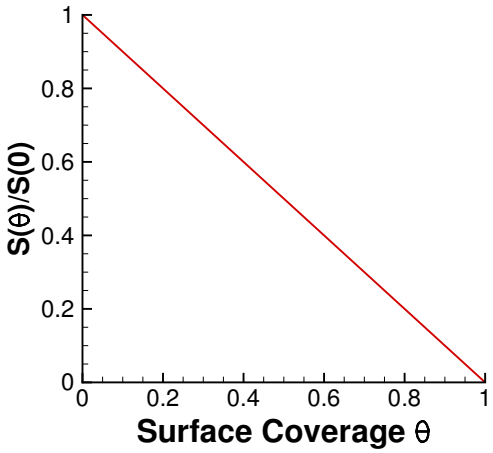

Figure 2.2: Variation of S(θ)/S(0) with surface coverage in a Langmuir (direct) adsorption model for a single adsorbate ($\alpha = 1$).

an empty site (not occupied by another adsorbed species), and second, this interaction with the empty site must result in an adsorption process. The probability of striking an empty site is determined based on the current surface coverage (θ), and the probability of adsorbing on an empty site is determined by the sticking coefficient (S_0):

$$P(ad) = S(\theta) = S_0 * (1 - \theta)^{\alpha} \tag{2.2}$$

The term α is the number of species that adsorb, which is 1 for associative adsorption and 2 or more for dissociative adsorption. The adsorption probability shows a linear dependence on the surface coverage. This is shown in Fig. 2.2 for a single adsorbate ($\alpha = 1$).

2.3.1.2 Indirect adsorption - Kisliuk Model

In the indirect adsorption model, the particle does not chemisorb directly on the site that it first strikes. Instead, the particle gets trapped and forms a loosely bound intermediate or precursor that is short lived. This intermediate can move freely on the surface like a two-dimensional gas, hence this model is also termed as mobile adsorption. If a suitable site is encountered, then chemisorption of the

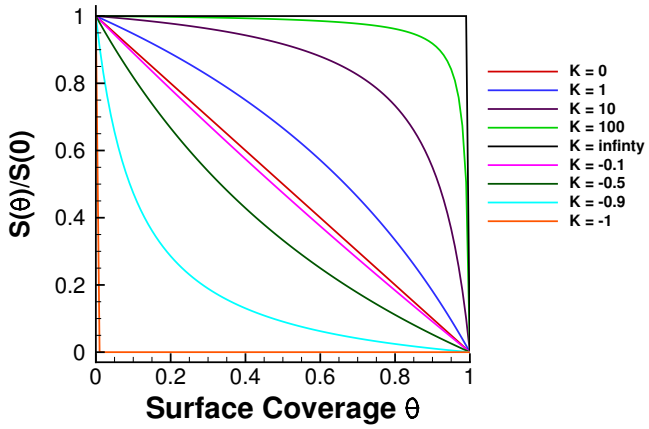

Figure 2.3: Variation of S(θ)/S(0) with surface coverage according to Kisliuk's model [4] in a indirect adsorption mechanism for a single adsorbate ($\alpha = 1$).

precursor occurs, else it desorbs from the surface. A simple model for this was presented by Kisliuk [4, 365], where the variation of the sticking coefficient as a function of θ is as follows:

$$\frac{S(\theta)}{S(0)} = \frac{(1 + K_{eq})(1 - \theta)^{\alpha}}{1 + K_{eq}(1 - \theta)^{\alpha}} \tag{2.3}$$

Here K_{eq} is the equilibrium constant of the adsorption-desorption process of the intermediate.

$$K_{eq} = \frac{k^*_{ads}}{k^*_{des}} \tag{2.4}$$

Note that the notations followed here are from Somorjai [366]. The variation of sticking coefficient with surface coverage for different value of K_{eq} are shown in Fig. 2.3. For an ideal precursor ($K_{eq} = \infty$), the sticking coefficient is equal to S(0) for all values of θ except 1. This model reduces to the Langmuir model when $K_{eq} = 0$. However, K_{eq} is expected to have a temperature dependence. Although this model is not derived from first principles, it is well grounded in physics and reproduces many experimental observations [4, 365, 367, 368, 369].

In general, the indirect or precursor-mediated adsorption is much more likely than direct adsorption. This due to the lower entropy loss encountered in the case of indirect adsorption compared to the direct adsorption [364, 366].

An adsorbed atom/molecule on the surface can exist in a wide variety of configurations. For example, an oxygen atom adsorbing on a carbon surface can be bound as different functional groups: semiquinone, lactone, ether, carbonyl etc., [80]. In addition, it can also immediately react upon adsorption through an adsorption-mediated reaction to form CO(s) that stays adsorbed on the surface. Hence within this framework, adsorption includes all the possible processes by which the incoming particle forms a bond with the surface. In order to obtain information regarding the nature of the bond or the composition of the particle after it adsorbs, the exact adsorption-mediated reaction process must be identified.

2.3.2 Desorption

The desorption process is the opposite of adsorption, where the bond between the atom/molecule and substrate is broken to give rise to gas-phase products. These gas-phase products are expected to be in full thermal accommodation to the surface temperature.

2.3.2.1 Desorption pathway

Similar to adsorption, desorption can also occur via direct and indirect modes. The direct mode is when the chemisorbed particle directly desorbs into the gas-phase. The rate of the reaction will be proportional to the coverage for the direct mode.

$$r_{des} = k_{des}\theta \tag{2.5}$$

However, this process can also occur indirectly through a short lived precursor. In this case, the rate of desorption might not be a linear function of coverage [366, 369].

$$r_{des} = \frac{k_{des}\theta}{K_{eq}(1-\theta)+1} \tag{2.6}$$

Here K_{eq} is the equilibrium constant of the adsorption of the intermediate back to the chemisorbed state and the desorption of the intermediate into gas phase.

$$K_{eq} = \frac{k^*_{ads}}{k^*_{des}} \tag{2.7}$$

2.3.2.2 Definition of the rate constant

Transition State Theory (TST) is commonly used for predicting the rate constant for desorption. Based on the particular system and the assumptions made while employing TST, several possible expressions for the rate constant can be obtained. The generic expression for the TST rate constant can be written as [364]

$$k_{TST} = \nu_{rc} \left(q_{vib}\right)_{rc} \left(K^{\ddagger}_{eq}\right)' \tag{2.8}$$

ν_{rc} and $\left(q_{vib}\right)_{rc}$ are respectively the frequency and the vibrational partition function of the reaction coordinate. $\left(K^{\ddagger}_{eq}\right)'$ is the equilibrium constant between the reactants and the transition state (TS) excluding the reaction coordinate (expressed as the ratio of partition functions). Thus, the product of $\left(q_{vib}\right)_{rc}$ and $\left(K^{\ddagger}_{eq}\right)'$ gives the complete equilibrium constant. Depending on the temperature of the system and the vibrational energy, different expressions can be obtained for the product of ν_{rc} and $\left(q_{vib}\right)_{rc}$.

Table 2.1: Values of $\left(q_{vib}\right)_{rc}$ and $\nu_{rc}\left(q_{vib}\right)_{rc}$ obtained for different cases.

Case	$\left(q_{vib}\right)_{rc}$	$\nu_{rc}\left(q_{vib}\right)_{rc}$
$h\nu_{rc} << k_bT$	$\frac{k_bT}{h\nu_{rc}}$	$\frac{k_bT}{h}$
$h\nu_{rc} >> k_bT$	1	ν_{rc}
$h\nu_{rc} \sim k_bT$	$\frac{e^{\frac{-h\nu_{rc}}{2k_bT}}}{1-e^{\frac{-h\nu_{rc}}{k_bT}}}$	$\frac{\nu_{rc}e^{\frac{-h\nu_{rc}}{2k_bT}}}{1-e^{\frac{-h\nu_{rc}}{k_bT}}}$

The equilibrium constant $\left(K^{\ddagger}_{eq}\right)'$ is defined as [364]

$$\left(K_{eq}^{\ddagger}\right)' = \frac{q'_{TST}}{q_{reac}} \tag{2.9}$$

Here q'_{TST} is the partition function of the TS excluding the reaction coordinate and q_{reac} is the partition function of the reactants.

Assuming that the TS is very similar to the reactant, but only differ in the energy of the bond with the surface, the following expression for $\left(K_{eq}^{\ddagger}\right)'$ is obtained:

$$\left(K_{eq}^{\ddagger}\right)' = e^{\frac{-E_{ads}}{k_b T}} \tag{2.10}$$

However, if the TS is assumed to be loosely bound which can move freely on the surface (2D gas) [370], while the reactant (adsorbed particle) has a vibration mode of frequency ν_1 perpendicular to the surface and frustrated translation modes along the two directions parallel to the surface with frequency ν_2, then the following expression is obtained for $\left(K_{eq}^{\ddagger}\right)'$.

$$\left(K_{eq}^{\ddagger}\right)' = \frac{2\pi m k_b T}{h^2} \left[\frac{1 - e^{\frac{-h\nu_1}{k_b T}}}{e^{\frac{-h\nu_1}{2k_b T}}}\right] \left[\frac{1 - e^{\frac{-h\nu_2}{k_b T}}}{e^{\frac{-h\nu_2}{2k_b T}}}\right]^2 e^{\frac{-E_{ads}}{k_b T}} \tag{2.11}$$

The frequency of the frustrated translational mode is defined as

$$\nu_2 = \sqrt{\frac{E_{diff}}{2m\lambda^2}} \tag{2.12}$$

where λ is the distance between two surface sites and E_{diff} is the energy barrier for diffusion. This is usually taken as 10-25% of the adsorption energy E_{ads}.

2.3.2.3 Surface coverage dependence of activation energy

When the surface coverage is low, the primary interaction of the adsorbates are with the surface atoms. As the surface coverage increases, there is increased lateral interaction of the adsorbates with each other. If the forces between the adsorbates are strong, it might significantly affect the potential energy surface around the adsorbate atoms thus leading to considerable changes to the activation energy of

the reactions [80, 371, 372].

2.3.2.4 Scattering of products

Desorption is a thermal mechanism and the products exit the surface with a MB distribution [135, 5, 367, 369]. However, if there are intermediate and elementary sub-steps involved that include energy barriers, then the desorbing gas-phase particles might have an energy distribution different from that based on the surface temperature [9]. The mean energy of the desorbing particles will be greater, but only along the surface normal direction. This is because the barrier for desorption only occurs along the surface normal direction and not along the tangential directions. Note that this desorption barrier is different from the activation energy in the Arrhenius exponent. The activation energy describes the energy barrier of the transition state (in the rate determining step), while the desorption barrier represents the energy barrier for the last elementary step of the desorption process.

Further, although the desorbing products are in thermal equilibrium with the local surface environment, this does not mean that they necessarily have energies corresponding to the bulk surface temperature. If the reaction occurs very quickly after high energy incoming particle strikes the surface, the local surface temperature might exceed the bulk surface temperature due to the presence of local hot-spots [373]. In addition, some additional energy transfer to the products might occur as a result of dissociation or bond energy of the intermediates.

2.3.3 Langmuir-Hinshelwood (LH) mechanisms

Langmuir-Hinshelwood (LH) reaction is a pure-surface mechanism (PS), where the reaction takes place entirely on the surface and the gas-phase products are completely accommodated to the surface temperature . It has three major steps namely adsorption, formation and desorption. Since the reaction takes place on the surface, all the reactants must first adsorb on the surface sites. The second

step is the formation step, where all the reactants interact on the surface to form products that are still adsorbed on the surface. Finally, the product on the surface desorbs to form gas-phase species. Each of these steps might contain many elementary sub-steps. The three steps and the final reaction for a simple CO formation on a carbon surface with adsorbed oxygen atoms is shown below.

$$O(g) + (s) \longrightarrow O(s) \tag{2.13a}$$

$$O(s) + C(b) \longrightarrow CO(s) \qquad t_f \tag{2.13b}$$

$$CO(s) \longrightarrow CO(g) + (s) \qquad t_d \tag{2.13c}$$

$$O(g) + C(b) \longrightarrow CO(g) \tag{2.13d}$$

In this system, $O(s)$, $CO(s)$ and $CO(g)$ are the reactant, surface intermediate, and product respectively. t_f and t_d are the characteristic times for formation and desorption respectively. Let τ be the time scale of interest, which may be the experimentally observable time scale or time scale related to other processes in the system, etc. An order of magnitude comparison between the reaction times (t_f and t_d) and the time scale of interest τ, results in the following four types of LH mechanisms.

1. $t_f \ll \tau$, $t_d \ll \tau$: Prompt LH mechanism
2. $t_f \sim \tau$, $t_d \ll \tau$: LH limited by formation
3. $t_f \ll \tau$, $t_d \sim \tau$: LH limited by desorption
4. $t_f \sim \tau$, $t_d \sim \tau$: LH limited by both formation and desorption

2.3.3.1 LH type 1

The first type of LH mechanism corresponds to a situation where both formation and desorption processes are extremely fast compared to the time scale of interest.

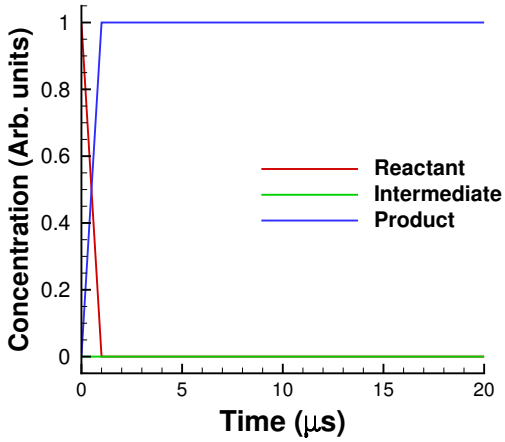

Figure 2.4: Concentration of the species as a function of time for a typical first-order LH reaction of type 1.

This implies that the surface intermediate is formed immediately after the reactants strike the surface. The desorption may be a part of the formation step or an independent process that is also very quick. The variation in the concentration of all the species are shown in Fig. 2.4. The concentration of the reactants falls rapidly to zero in a single time step (dt $= 10^{-6}$). All the reactants are instantly converted to products, and the concentration of the surface intermediate remains zero. The gas-phase product exit the surface promptly at all temperatures.

For a LH mechanism of type 1 (prompt LH mechanism), both the formation and desorption processes are rapid, leading to the collapse of Eqs. (2.13) (b) and (c) to a single step. In DSMC, this type of LH mechanism is modeled as a one step process with gas-phase reactants and gas-phase product. Since this reaction essentially becomes a gas-surface (GS) reaction, it is modeled in DSMC by specifying a probability of reaction when the reactants strike the surface.

$$O(g) + C(b) + (s) \longrightarrow CO(g) + (s) \tag{2.14}$$

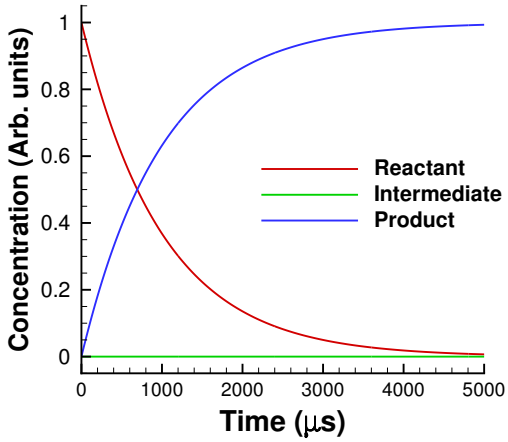

Figure 2.5: Concentration of the species as a function of time for a typical first-order LH reaction of type 2.

2.3.3.2 LH type 2

The second type of LH mechanism occurs when the time of desorption is much smaller than the time scale of interest τ, but the formation time is of the same order of τ. The formation reaction is slow and is the rate determining step (RDS) in this type of mechanism. The reactants are present on the surface for a long time before forming the surface intermediate. On the other hand, the surface intermediate forms the gas-phase products promptly since the desorption process is very rapid. Fig. 2.5 shows the variation in the concentration of all the species as a function of time. The concentration of the reactant decays either exponentially or based on a power law expression, depending on the order of the reaction. The product shows a corresponding increase with time, while the concentration of intermediate remains zero.

A LH reaction system follows the characteristics of a type 2 mechanism only for a certain temperature range. If reaction rate constant of each step follows an Arrhenius form, then the time of desoprtion and formation reduces with temperature. Thus, for a fixed time scale of interest τ, a reaction system might transition from type 2 to type 1 after a certain temperature threshold.

For a type 2 LH mechanism (LH limited by formation), only the desorption step is quick, resulting in the collapse of Eq. (2.13) (c) into Eq. (2.13) (b) and giving

rise to a two-step LH mechanism. This is similar to the form of LH mechanism used by Marschall and Maclean [3]. In DSMC, the first step (adsorption) is a GS reaction and is modeled by specifying a value for probability of the reaction when the gas-phase reactant strikes the surface. The second step is a PS reaction and is modeled using the method proposed by Molchanova *et al.,* [374]. In this approach, the rate constants (specified) and surface properties are used to compute the rates, which are then converted to a characteristic frequency and time. A time counter is used to perform the reactions based on the calculated characteristic time.

$$O(g) + (s) \longrightarrow O(s) \tag{2.15a}$$

$$O(s) + C(b) \longrightarrow CO(g) + (s) \tag{2.15b}$$

2.3.3.3 LH type 3

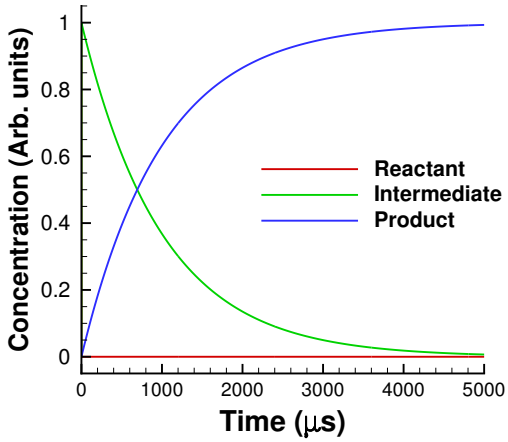

Figure 2.6: Concentration of the species as a function of time for a typical first-order LH reaction of type 3.

The third type of LH mechanism corresponds to a situation where the formation process is rapid, and the desorption time is on the same order of the time scale of interest τ. Since the formation time is very small, the surface intermediate is formed almost instantly after the reactants strike the surface. The desorption

is slow and the RDS in this type of LH mechanism. The intermediates that are formed stay at the surface for a long time before desorbing into the gas phase. The variation in the concentration of all the species are shown in Fig. 2.6. The concentration of the reactant falls rapidly to zero in a single time step to form surface intermediate. The concentration of the intermediate decays (either exponential or power law based on the order of the reaction) with time, and the product concentration shows a corresponding increase. As mentioned previously, a LH reaction system might transition from type 3 to type 1 after a certain temperature threshold.

In the case of a type 3 LH mechanism (LH limited by desorption), the formation step is quick, leading to the collapse of Eq. (2.13) (b) into Eq. (2.13) (a) and giving rise to a two-step LH mechanism again. This form of a two-step LH mechanism is, however, different from the one used by Marschall and Maclean [3]. The first step is a combination of adsorption and formation. In DSMC, this is modeled as a GS reaction by specifying a value for probability when the gas-phase reactant strikes the surface. The second step is a PS reaction and is modeled using the method proposed by Molchanova *et al.,* [374].

$$O(g) + (s) + C(b) \longrightarrow CO(s) \tag{2.16a}$$

$$CO(s) \longrightarrow CO(g) + (s) \tag{2.16b}$$

2.3.3.4 LH type 4

The fourth and the final type of LH mechanism occurs when both the desorption and formation times are on the order of the time scale of interest τ. Either of these reactions could be the RDS. Since there is no rapid process involved, the variation of the concentration of the reactant, intermediate and products are more complex. Fig. 2.7 shows the concentration of the species for a typical type 4 LH mechanism. Although the exact shape of the curves will vary widely depending

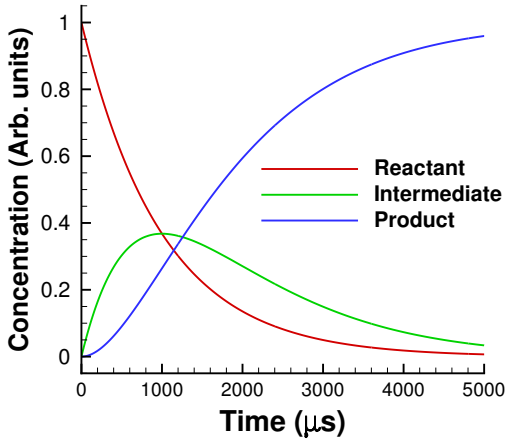

Figure 2.7: Concentration of the species as a function of time for a typical first-order LH reaction of type 4.

on the exact values of the individual rates of formation and desorption, the same general trends are observed. The reactant concentration decreases steadily based on the rate of formation. The concentration of the intermediate shows an initial increase, where the rate of formation is greater than the rate of desorption, owing to the greater concentration of reactant compared to the intermediate. As time progresses, concentration of the intermediate reaches a peak and then starts to decrease. This results from the declining formation rate (lower concentration of reactant) and increasing desorption rate (higher concentration of intermediate). The product concentration shows a monotonic increase with time, however its rate varies widely. Initially the rate is small, which increases with time to reach a peak and then starts to fall again, following the trend of concentration of the intermediate. For the purpose of validation, the concentrations of the various species obtained for a simple first-order system is compared with the analytical solution (shown below). Excellent agreement is observed between the DSMC and analytical solution, thus validating the approach.

$$R\left([O(s)]\right) = n_0\, exp(-k_f t) \tag{2.17a}$$

$$I\left([CO(s)]\right) = n_0 k_f \left(\frac{exp(-k_f t) - exp(-k_d t)}{k_d - k_f}\right) \tag{2.17b}$$

$$P\left([CO(g)]\right) = n_0 \left(1 + \frac{k_f\, exp(-k_d t) - k_d\, exp(-k_f t)}{k_d - k_f}\right) \tag{2.17c}$$

In all of the cases, the formation reactions are considered to be irreversible. If the reversibility of the formation reactions are taken into account, the analysis becomes more complicated, especially in the case of type 4 LH mechanism. Similar to the previous cases, a LH reaction system might transition from type 4 to either type 2 or 3, and finally to type 1 after certain temperature thresholds.

For a LH mechanism of type 4 (LH limited by both formation and desorption), none of the processes are rapid, hence no simplifications can be made and no steps can be collapsed. This type of reaction must modeled as a full three-step process. The first step, adsorption, is a GS reaction and the following two steps of formation and desorption are both PS reactions. These are modeled in DSMC as described previously.

$$O(g) + (s) \longrightarrow O(s) \tag{2.18a}$$

$$O(s) + C(b) \longrightarrow CO(s) \tag{2.18b}$$

$$CO(s) \longrightarrow CO(g) + (s) \tag{2.18c}$$

2.3.4 List of Gas-Surface (GS) Reactions

From the discussion above, the different types of GS reactions include adsorption (associative and dissociative), impact and adsorption-mediated dissociation, and LH mechanisms of type 1 and 3. Although LH mechanisms are PS mechanisms, the formation (and in some cases desorption) step(s) within these types of LH

mechanisms occur rapidly and are modeled together with the adsorption step. The reason for not modeling all types of LH reactions as 3 steps (adsorption, formation and desorption), adsorption-mediated desorption as 2 steps (dissociative adsorption, desorption) is that these involve some rapid processes. Accurately modeling these rapid processes within DSMC would needlessly place a restriction on the time step of the simulation. Thus whenever rapid sub-processes are present, they are not modeled as a separate step. In addition to these mechanisms, other common GS reactions are the condensation, Eley-Rideal (ER), and the Collision-induced (CI) mechanisms. Condensation reaction occurs when the gas-phase products adsorb on the surface and become a part of the bulk-phase material. ER mechanism is a direct impact mechanism where a gas-phase reactants directly reacts with surface (or bulk) species to form gas-phase products. The CI mechanism also includes gas-phase and surface reactants, however they do not undergo any reaction. The incoming gas-phase particles helps in the desorption of the adsorbed atom/molecule to form gas-phase products. The gas-phase reactant might adsorb on the surface, however, it not necessary. Table 2.2 presents the list of gas-surface (GS) reactions along with examples, which are included within this model.

Table 2.2: List of gas-surface (GS) reactions along with examples.

Symbol	Reaction type	Examples
1: AA	Associative Adsorption	$O(g) + (s) \longrightarrow O(s)$ $O_2(g) + (s) \longrightarrow O_2(s)$
2: DA	Dissociative Adsorption	$O_2(g) + (s) \longrightarrow O(s) + O(g)$ $O_2(g) + 2(s) \longrightarrow 2O(s)$
3: LH1	Langmuir-Hinshelwood type 1	$O(g) + (s) + O(s) \longrightarrow O_2(g) + 2(s)$ $O(g) + (s) + C(b) \longrightarrow CO(g) + (s)$
4: LH3	Langmuir-Hinshelwood type 3	$O(g) + (s) + O(s) \longrightarrow O_2(s) + 2(s)$ $O(g) + (s) + C(b) \longrightarrow CO(s) + (s)$
5: CD	Condensation	$C_3(g) + 3(s) \longrightarrow 3C(b) + 3(s)$
6: AMD	adsorption-mediated dissociation	$CO_2(g) + (s) \longrightarrow 2O(g) + (s) + C(b)$
7: ID	Impact dissociation	$O_2(g) + (s) \longrightarrow 2O(g) + (s)$
8: ER	Eley-Rideal	$CO(g) + O(s) \longrightarrow CO_2(g) + (s)$
9: CI	Collision Induced	$O(g) + CO(s) \longrightarrow CO(g) + O(s)$ $Ar(g) + O(s) \longrightarrow Ar(g) + O(g) + (s)$

2.3.5 List of Pure-Surface (PS) Reactions

The PS reactions that have been discussed so far include desorption, LH mechanisms of type 2 and 4. An additional common PS reaction is the sublimation reaction, the opposite of condensation reaction, where the bulk species sublimates into the gas-phase. The table below presents the list of pure-surface (PS) reactions along with examples, that is included within this model.

Table 2.3: List of pure-surface (GS) reactions along with examples.

Symbol	Reaction type	Examples
1: DES	Desorption	$O(s) \longrightarrow O(g) + (s)$ $O_2(s) \longrightarrow O_2(g) + (s)$
2: LH2	Langmuir-Hinshelwood type 2	$N(s) + O(s) \longrightarrow NO(g) + 2(s)$ $O(s) + C(b) \longrightarrow CO(g) + (s)$
3: LH4	Langmuir-Hinshelwood type 4	$N(s) + O(s) \longrightarrow NO(s) + (s)$ $O(s) + C(b) \longrightarrow CO(s) + (s)$
4: SB	Sublimation	$3C(b) + 3(s) \longrightarrow C_3(g) + 3(s)$

2.4 Modeling of Gas-Surface (GS) Reactions in DSMC

The GS reactions in DSMC is performed by computing the probability of a reaction when a particle strikes the surface. Thus these GS reactions are performed as a part of the *move* kernel within te DSMC structure. This section presents detailed information about modeling some common GS reactions in DSMC. This includes calculations of reaction probability from macroscopic rate constants and surface properties, physically consistent multi-step method for modeling multiple GS reactions without bias. Additional GS reactions and their modeling are presented in Appendix B.

2.4.1 Adsorption

As described previously, there are different pathways through which the particle adsorbs on a surface. The probability of adsorption varies widely based on the

exact pathway. However, the model provided by Kisliuk [4, 365] accounts for most of these pathways by varying the equilibrium constant (K_{eq}) for the adsorption of the intermediate. The Langmuir model can also be obtained as a special case within Kisliuk's model.

$$P_{ad} = S^{\alpha}(\theta) \tag{2.19}$$

where the sticking coefficient $S^{\alpha}(\theta)$ is calculated using the following equation.

$$\frac{S^{\alpha}(\theta)}{S(0)} = \frac{(1 + K_{eq})(1 - \theta)^{\alpha}}{1 + K_{eq}(1 - \theta)^{\alpha}} \tag{2.20}$$

Hence, the input parameters for an associative adsorption reaction are the sticking coefficient at zero surface coverage (S_0) and the equilibrium constant for the adsorption of the intermediate (K_{eq}).

This adsorption probability includes all the possible processes by which the incoming particle forms a bond with the surface. This does not provide information regarding the nature of the bond or the composition of the particle after it adsorbs. In order to obtain this information, the exact adsorption-mediated reaction process must be identified.

2.4.2 Adsorption-mediated GS reactions

Adsorption-mediated reactions are those that involve adsorption as the first step in the reaction mechanism, for example, associative and dissociative adsorption; LH mechanisms of type 1 and 3; and condensation. Hence the probability of these reactions is calculated as the product of the reaction probability and adoption probability.

$$P_{tot} = P_{ad} * P_{reac} \tag{2.21}$$

2.4.2.1 Associative Adsorption

The probability for the associative adsorption of species A (shown below) is directly determined by:

$$A + (s) \longrightarrow A(s), \tag{2.22}$$

$$P_{AA} = P_{ad} * k_{AA} \tag{2.23}$$

where P_{ad} is the adsorption probability of A species, and k_{AA} is the rate constant for the associative adsorption reaction.

Hence, the only input parameters for an associative adsorption reaction is the rate constant k_{AA}.

2.4.2.2 LH type 1

A LH mechanism of type 1 involves gas-phase reactants and gas-phase products. A representative second-order LH type 1 reaction is shown below.

$$A(g) + (s) + B(s) \longrightarrow AB(g) + 2(s) \tag{2.24}$$

The probability of this reaction is calculated as:

$$P_{LH1} = P_{ad}(A) * k_{LH1} * \frac{N_{B_s} F_N}{S_p} \tag{2.25}$$

Here N_{B_S} is the number of adsorbed B (DSMC) particles on the surface, F_N is the number of real particles represented by one DSMC particle, S_p is the surface area. $P_{ad}(A)$ is the adsorption probability of A species, and k_{LH1} is the rate constant for the LH type 1 reaction. The thermal desorption scattering model described in Section 2.6.2 can be adequately used to account for all the above mentioned features.

2.4.2.3 LH type 3

Modeling of LH type 3 mechanism is simpler since all the products are adsorbed species. A representative first-order LH type 3 reaction involving bulk-species is shown below.

$$A(g) + (s) + M(b) \longrightarrow AM(s) \tag{2.26}$$

The probability of this reaction is computed in a similar manner:

$$P_{LH3} = P_{ad}(A) * k_{LH3} \tag{2.27}$$

k_{LH1} is the rate constant for the LH type 3 reaction. Since the concentration of the bulk-species is treated as unity, it does not enter into the calculation of reaction probability.

Since the products remain adsorbed on the surface and do not desorb immediately, they will attain thermal accommodation with the equilibrium surface temperature. The desorption of these products are handled via the desorption reaction (Section 2.5.1.1). Hence, for LH type 3 mechanism only the rate constant of the reaction is specified.

2.4.3 Sequence of performing GS reactions without bias

The exact sequence of performing GS reactions is very important in order to avoid any bias and also to remain consistent with the physics of the surface reactions. The GS reactions are performed in DSMC by specifying a probability. In many cases, the individual probability or the cumulative probability of all the various possible reactions might be greater than 1.

In order to handle the case when cumulative probability becomes greater than 1, the pathways through which the cumulative probability might become greater than 1 is analyzed. There are several possible reactions when a species strikes the surface, and these possible reactions vary based on whether the particle is

an atom or a molecule. For adsorption reactions (associative and dissociative), a probability is directly specified and hence these values cannot exceed unity. The other possible reactions when an atom/molecule strikes the surface, include ER, LH1, CI, etc. An atom striking the surface can encounter either an site which contains an adsorbed atom (ER and CI reactions) or an empty site (adsorption and LH1). Hence, in this manner, all the GS reactions could be classified into two types: empty-site and filled-site reactions.

$$\begin{array}{lcl} AA & O(g) + (s) \longrightarrow O(s) & empty\ site \\ LH1 & O(g) + (s) + C(b) \longrightarrow CO(s) + O(s) & empty\ site \\ ER & O(g) + O(s) \longrightarrow O_2(g) + (s) & filled\ site \\ CI & O(g) + O'(s) + C(b) \longrightarrow CO'(s) + O(s) & filled\ site \end{array} \tag{2.28}$$

Following this thought, the total probability of a GS reaction can be split into two factors, first, the gas-phase atom/molecule must strike an appropriate site (either filled or empty), and secondly, the conditions required for this particular reaction must be satisfied.

Total Prob. = Prob. of striking an appropriate site * Prob. of reaction (after striking the site)

The first step of a GS reaction is striking an appropriate site. Once a particular site is encountered, the sum of probabilities of the various possible events (including reactions, adsorption, impulsive scattering, etc.) must be equal to 1, since some event has to occur. Hence, in order to accurately model these reactions without bias, both of these types must be normalized separately. Also it is reasonable to suppose that both these individual probabilities must be lesser than or equal to 1.

Prob. of encountering a filled site = θ (surface coverage)

Prob. of encountering an empty site = 1 - θ

The cumulative probability of all the filled-site reactions, that involve an atom striking a site with another adsorbed particle should not exceed θ. Hence, if the cumulative probability of all filled-site reactions exceeds the value of θ, then all the probabilities are normalized by the value of (sum(filled-site reactions probs)/θ). After this normalization, the cumulative probability will be equal to θ. In the same manner, this process is repeated for the empty-site reactions, except the use (1-θ) instead of θ for normalization. In this manner, both the sets of reactions (empty and filled site) are normalized separately and not together.

However, in the previous approach, it was assumed that for the filled-site reactions, the gas-phase reactants must exactly strike the site where the other reactant is adsorbed. However, this might not be necessarily true. For example, it might be sufficient for the gas-phase reactant to strike an adjacent site. In this case, the probability of striking an appropriate site for a filled site reaction can be represented as:

Prob. of striking an appropriate site = c * θ

where c is a constant which can be greater than 1. The value of c will be equal to 5 for the adjacent-site case described above. The total probability then becomes

Total Prob. = c * θ * Prob. of reaction (after striking the site)

Since, a first-order rate equation is represented as being linearly proportional to the reactants, and the value of c is not necessarily known, it is combined into the probability of reaction (rate constant). Hence, the probability of reaction can then have a value greater than 1. In general, gas-surface reactions are complex and might proceed through several intermediates (or precursors). This is readily seen from the Kisliuk's model for adsorption (Section 2.3.1.2). Currently in DSMC, the probabilities are calculated from macroscopic rates that do not account for the detailed reaction pathway and only represent the overall rate. Thus

the conditions for the elementary rates (or probabilities) should not be imposed. The only condition that should be imposed is that the final probabilities are less than or equal to 1.

Given this, the normalization should not be performed for the two types of reactions (filled and empty-site) separately, but together. However, the case of adsorption (consisting of sticking coefficient) must be considered separately, since adsorption is a necessary first step in many of the reactions (for example LH1), and is not completely independent. Thus, the total adsorption probability represents the sum of probabilities of all the processes which involve adsorption as a first step (adsorption-mediated GS reactions), and is not only restricted to the probability of particles staying adsorbed and later desorbing from the surface in the same form. This adsorbed complex is representative of all possible forms (functional groups) by which the atom/molecule can be adsorbed on the surface. When the particle adsorbs on the surface, the exact mechanism (adsorption-mediated) it undergoes is chosen from the list of possible pathways based on the reaction rates.

With this adsorption model, the following sequence of reactions is proposed.

1. Calculate probability of total adsorption using the Kisliuk's model (Section 2.4.1).

2. Calculate the probability of direct impact reactions as specified in Section B.2.

3. Compute the cumulative probability $P_{ads} + sum(P_{DI})$ and normalize if it exceeds 1.

4. Now, the probability of scattering without undergoing any reaction (impulsive scattering) is calculated: $P_{scatter} = 1 - P(step\,3)$

5. Use a random number to determine the outcome of this collision.

6. Perform the reaction and/or scattering for impulsive and direct impact reactions.

7. If adsorption, calculate the probability of all possible adsorption-mediated GS reactions (Section 2.4.2) and normalize to 1.

8. Draw a second random number to decide and perform the exact adsorption-mediated GS reaction.

Note that two different normalizations are performed. The first normalization is over all the reactions (adsorption and direct-impact) and ensures that the total probability of all possible pathways sum to unity. The second normalization is performed within adsorption-mediated GS reactions since their sum must be equal to the total adsorption probability P_{ads}.

2.5 Modeling of Pure-Surface (PS) Reactions in DSMC

This section presents detailed information about modeling some common PS reactions in DSMC. Unlike GS reactions, PS reactions cannot modeled by specifying a probability value. A PS reaction is performed by determining the time between two consecutive events [374]. For a process P, with frequency ν_P, the characteristic time, which is defined as the time between two consecutive events of P, can be calculated as:

$$t_P = -\frac{ln(Rn)}{\nu_P} \tag{2.29}$$

where Rn is a random number in the range (0,1]. This section presents the methods to obtain the characteristic frequencies of the various reactions and provides the details on how to model multiple PS reactions without bias. These PS reactions are performed within each time step by looping over all the surface elements. This can be performed in parallel with the collisions in the gas-phase. Additional PS reactions and their modeling are presented in Appendix C.

2.5.1 Computing Characteristic Frequency

2.5.1.1 Desorption

In order to model desorption reaction, the time between two desorption reactions is computed from the reaction rate constant of the desorption process.

$$A(s) \longrightarrow A + (s). \tag{2.30}$$

If the rate of this desorption reaction is given by:

$$\frac{dn_{A(s)}}{dt} = -k_{des} n_{A(s)}, \tag{2.31}$$

where k_{des} is the desorption reaction rate constant and $n_{A(s)}$ is the surface number density of the adsorbed species $A(s)$. Although here it is assumed that the rate of desorption is linearly proportional to the surface coverage, this might always be the case (Section 2.3.2). The characteristic frequency of this desorption process is

$$\nu_{des} = k_{des} N_{A(s)}. \tag{2.32}$$

The time through which the particle remains on the surface before desorption may be calculated using the characteristic frequency [374]:

$$\tau_{des} = -\frac{log(Rn)}{\nu_{des}}, \tag{2.33}$$

where Rn is a uniform random number in the range (0,1]. The desorption reaction is performed using the time counter algorithms based on the current value of the frequency and characteristic times. For a desorption mechanism, the rate constant k_{des} and the scattering model parameters for the desorbing products must be given as input. The scattering of the desorbing products can be captured using the thermal desorption model (Section 2.6.2).

2.5.1.2 LH type 2

In a LH surface reaction mechanism, all the reactants adsorb on nearby surface sites and undergo reaction to form products that desorb into the gas phase. For a LH reaction involving two distinct reactants A and B of the form:

$$A(s) + B(s) \longrightarrow AB(g) + 2(s). \tag{2.34}$$

The reaction rate for the above reaction is given by:

$$\frac{dn_{A(s)}}{dt} = \frac{dn_{B(s)}}{dt} = -k_{LH} n_{A(s)} n_{B(s)}. \tag{2.35}$$

Similar to the case of desorption, the frequency of the LH reaction can be calculated as:

$$\nu_{LH} = k_{LH} N_{A(s)} N_{B(s)} \frac{F_N}{S_p}, \tag{2.36}$$

where S_p is the area of the surface element and F_N is the number of real particles represented by one simulated particle in DSMC. The frequency for the LH recombination reactions between the same reactant species, described by the mechanism:

$$A(s) + A(s) \longrightarrow A_2(g) + 2(s), \tag{2.37}$$

can be shown to be [374]:

$$\nu_{LH} = k_{LH} \frac{N_{A(s)} \left(N_{A(s)} - 1\right)}{2} \frac{F_N}{S_p}. \tag{2.38}$$

LH surface reactions that involve a bulk species as one of the reactants, become pseudo first-order since the concentration of the bulk species is treated as unity:

$$A(s) + M(b) \longrightarrow AM(g) + (s). \tag{2.39}$$

For such reactions, the characteristic frequency can be derived as:

$$\nu_{LH} = k_{LH} N_{A(s)}. \tag{2.40}$$

Finally, the characteristic time between two LH reactions (for all types) is given by:

$$\tau_{LH} = -\frac{log(Rn)}{\nu_{LH}}. \tag{2.41}$$

Hence, for a LH type 2 reaction the rate constant k_{LH2} and the desorption barrier E_b should be specified. The flux PDF and angular distribution of the products for a LH type 2 reaction desorb based on the surface temperature and the desorption barrier of the particular species, similar to the desorption reaction.

2.5.2 Time-counter algorithm for modeling PS reactions

2.5.2.1 Basic time counter algorithm

For modeling other PS reactions in DSMC, a time counter method is used. The PS reactions that occur on the surface element during the time step Δt are consecutively performed at the end of each time step. For a single PS reaction, the following iterative process is used [374].

Algorithm 1 Simple Molchanova

```
procedure PS REACTIONS
    τ_LH = τ_LH + dt
    while τ_LH > 0 do
        Perform the reaction
        τ_LH ← τ_LH − t_LH
        update ν_LH
        t_LH = −ln(Rn)/ν_LH
    end while
end procedure
```

τ_{LH} is the time counter that is used to perform the simulations. ν_{LH} is updated after every reaction owing to the change in the concentration of the reactants,

and a new value for t_{LH} is computed. Note that this process is correct only in the case of a single reaction. The algorithm for accurately modeling multiple PS reactions (using the time counter method) without bias is described in detail in Section 2.5.3.

2.5.2.2 Extension to multiple reactions

The approach described in Section 2.5.2 was verified to reproduce the theoretical (or analytical) expression for a single PS reaction [374]. However, the extension of this approach for multiple reactions is not straightforward. Simply, using the same methodology and sequentially performing the various reactions introduces a bias towards the initial reactions.

For example, consider the following case with two possible LH reactions occurring simultaneously on a carbon surface filled with adsorbed oxygen atoms.

$$\begin{aligned} 2O(s) &\longrightarrow O_2(g) + 2(s) \\ 2O(s) + C(b) &\longrightarrow CO_2(g) + 2(s) \end{aligned} \tag{2.42}$$

Performing the two reactions sequentially in the manner described above leads to the following result for the flux and rate for each product, shown in Fig. 2.8. The surface is initially filled with adsorbed oxygen, which then undergo the aforementioned LH reactions (according to the specified rate constants) to form product O_2 and CO_2. The analytical solution is also plotted alongside for comparison. In this case, the rate constants for the two reactions were set equal to each other. Since both the LH reactions are second order, it is expected that the flux and rate of both the reactions are the same, as seen from the analytical solution. However, the DSMC solution obtained using Molchanova's approach with sequential ordering of reactions shows discrepancies in comparison with the analytical solution. The first reaction (O_2 formation) is favored over the second reaction (CO_2 formation), leading to a bias. Both these reactions lead to depletion of adsorbed O atoms, which tends to decrease the rate of both the reactions. Since all possible

O_2 formation reactions within a time step are performed first, before considering the CO_2 formation reaction, the rates of O_2 reaction is consistently higher leading to higher flux compared to CO_2. In this manner, the sequential handling of multiple reactions with Molchanova's method leads to a bias towards the initial reactions.

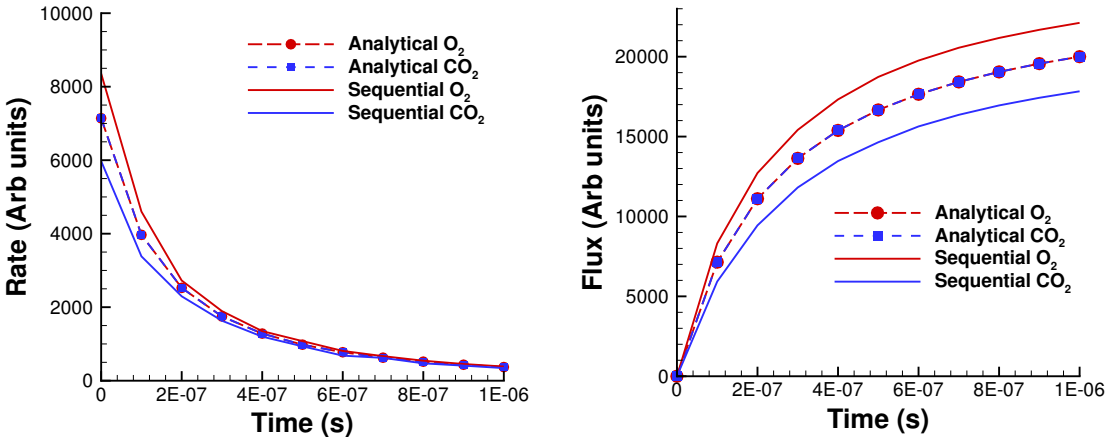

(a) (b)

Figure 2.8: (a) Rate of formation and (b) total flux of products as a function of time obtained from the analytical solution and DSMC simulation using Molchanova's method with sequential handling of reactions and a relatively large time step size.

In the case where the time step size of the simulation is much smaller compared to the reaction time scales, the observed bias between the multiple reactions decreases as shown in Fig. 2.9. This figure shows the comparison between the analytical solution and the DSMC simulations for the same case described above, but with a much smaller time step size. In this scenario, the frequency of each reaction is not high enough for a single reaction to be repeated several times within one time step. Thus, the change in concentration of adsorbed oxygen atoms due to one particular reaction is negligible compared to the total concentration. This ensures that the reaction rate is not appreciably affected by the particular sequence in which the reactions are performed and thus leads to reduction in bias. However, reducing the time step size to remove the bias is not viable solution in

DSMC. In many cases, the reaction rates at the surface might be extremely high, placing a large restriction on the time step size. This leads to an unnecessary increase in the computational requirements and restricts the total run time of the simulation.

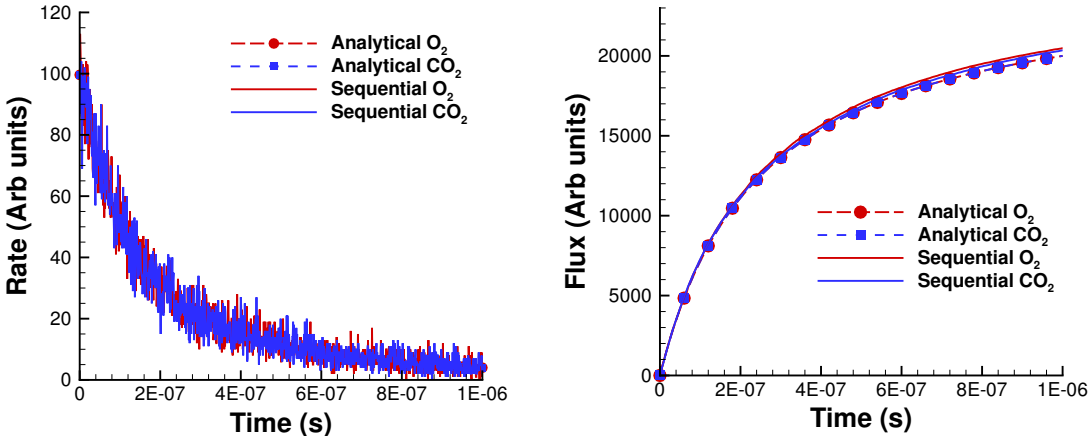

(a) (b)

Figure 2.9: (a) Rate of formation and (b) total flux of products as a function of time obtained from the analytical solution and DSMC simulation using Molchanova's method with sequential handling of reactions and a relatively small time step size.

This section describes two methods to remove the bias introduced by sequential handling of multiple reactions within Molchanova's approach [374]. The first method retains the framework of performing the reactions, while altering the order of reactions to remove the bias. The second method provides a more elegant approach of performing the reactions, similar to the one followed in kinetic Monte Carlo (kMC) simulations [375].

2.5.3 Time-counter algorithms without bias

2.5.3.1 Algorithm A

In this algorithm, the order of the various possible reactions are altered to ensure that there is no bias introduced while performing the reactions. The reactions are

not performed sequentially in a pre-determined order, however are chosen based on their rates, after each reaction is performed. Higher the rate of a reaction, greater its frequency and larger probability of occurring. At any instant, the total count of a reaction within the time step is determined by the product of τ (time counter) and ν (frequency). In addition to capturing the dependence on frequency, it also reduces the probability of reaction that have already occurred within the particular time step. When a reaction is performed, the value of that particular time counter τ is decremented, thus reducing the probability of the reaction. In other words, the probability of all the reactions are adjusted such that within a single time step, the relative selectivity of each reaction is exactly satisfied.[1]

Algorithm 2

```
1:  procedure ALGORITHM A
2:      for i ← 1 to Number of reactions do
3:          τ_LH(i) = τ_LH(i) + dt
4:      end for
5:      sum = 0
6:      while (1) do
7:          for i ← 1 to Number of reactions do
8:              update ν_LH(i)
9:              t_LH(i) ← −ln(Rn)/ν_LH(i)
10:             sum ← sum + round(τ_LH(i) ∗ ν_LH(i))
11:         end for
12:         if sum == 0 then break
13:         end if
14:         for i ← 1 to Number of reactions do
15:             prob(i) ← round(τ_LH(i)∗ν_LH(i))/sum
16:         end for
17:         Choose one reaction randomly based on probability values
18:         Perform the reaction
19:         τ_LH ← τ_LH − t_LH
20:     end while
21: end procedure
```

This algorithm updates the value of ν_{LH} of all the reactions after each reaction.

[1]For example, lets say that the probability of 2 events A and B is both 0.5. For each set of 10 events, if the count of events A and B is exactly 5, then it is said that the relative selectivity of each event is exactly satisfied.

And each reaction is chosen based on the updated value of its count ($\tau * \nu$), thus leading to a system without bias regardless of the time step size. A more complex reaction set with four possible LH reactions (shown below) of varying orders and rate constants is chosen to showcase the validity of the present approach.

$$\begin{aligned} O(s) &\longrightarrow O(g) + (s) \\ O(s) + C(b) &\longrightarrow CO(g) + (s) \\ 2O(s) &\longrightarrow O_2(g) + 2(s) \\ 2O(s) + C(b) &\longrightarrow CO_2(g) + 2(s) \end{aligned} \tag{2.43}$$

Figs. 2.10 and 2.11 present the comparison of the analytical solution with the DSMC simulation results obtained using algorithm A for a relatively small and large time step size respectively.

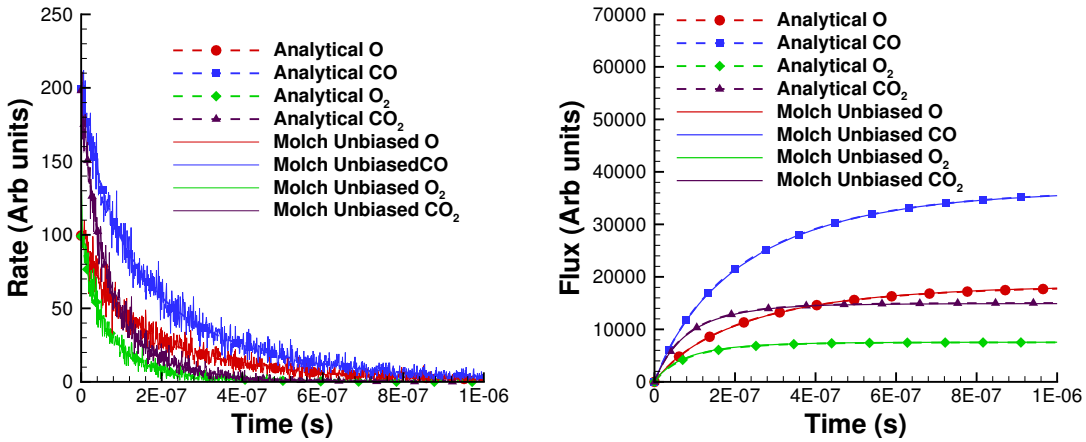

(a) (b)

Figure 2.10: (a) Rate of formation and (b) total flux of products as a function of time obtained from the analytical solution and DSMC simulation using algorithm A and a relatively small time step size.

2.5.3.2 Algorithm B

In the previous algorithm, a separate time counter was utilized for each of the reaction. Instead of this, a single time counter (for each surface element) can be

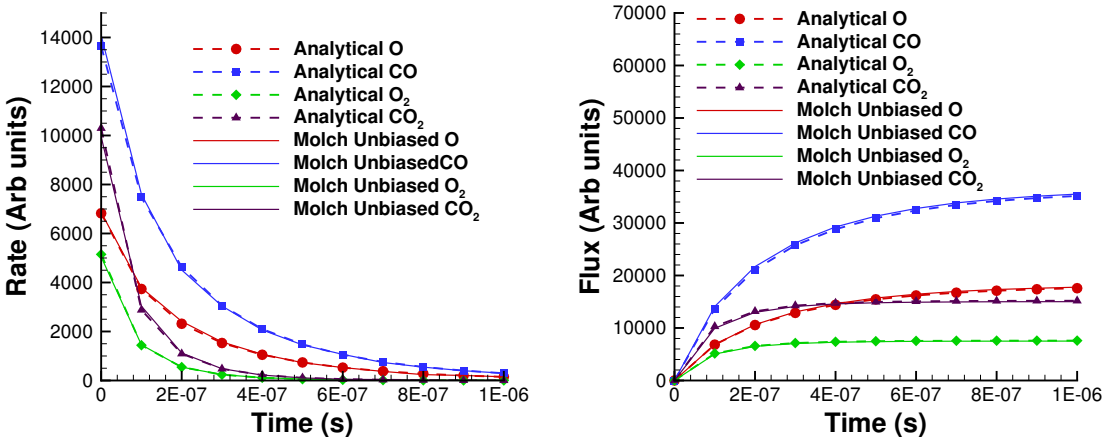

(a) (b)

Figure 2.11: (a) Rate of formation and (b) total flux of products as a function of time obtained from the analytical solution and DSMC simulation using algorithm A and a relatively large time step size.

used to accurately perform multiple LH reactions without bias. This algorithm closely resembles the standard approach using in kinetic Monte Carlo (kMC) simulations [375]. Similar to the previous approach, the order of the reaction is not pre-determined. However, the probability of each reaction is determined based solely on the frequency of each reaction (ν), and not the count ($\tau * \nu$). This algorithm is detailed below.

Note the expression for t_{LH} is based on the sum of all the reaction frequencies and remains unchanged regardless of the particular reaction that is carried out. Remember that the characteristic time between two consecutive events of a particular LH reaction is given by:

$$t_{LH}(i) = -\frac{log(Rn)}{\nu_{LH}(i)} \tag{2.44}$$

Extending this, the characteristic time between any two LH reaction can be written as:

$$t_{LH} = -\frac{log(Rn)}{\sum_i \nu_{LH}(i)} \tag{2.45}$$

Algorithm 3

procedure ALGORITHM B
  $\tau_{LH} = \tau_{LH} + dt$
  while $tau_{LH} > 0$ **do**
    $sum = 0$
    for $i \leftarrow 1$ to Number of reactions **do**
      update $\nu_{LH}(i)$
      $sum \leftarrow sum + \nu_{LH}(i)$
    end for
    for $i \leftarrow 1$ to Number of reactions **do**
      $prob(i) \leftarrow \frac{round(\nu_{LH}(i))}{sum}$
    end for
    Choose one reaction randomly based on probability values
    Perform the reaction
    $t_{LH} \leftarrow \frac{-ln(Rn)}{sum}$
    $\tau_{LH} \leftarrow \tau_{LH} - t_{LH}$
  end while
end procedure

Hence, regardless of the reaction performed, the characteristic time value is calculated in a similar manner, and is used for decrementing the common time counter. The adoption of such a combined characteristic time allows the use of a single time counter for multiple reactions (on each surface element). Since the probability of the reaction is only based on its frequency (and not the count), the probabilities are not influenced by the number of previous occurrences of each reaction within a time step. Thus, in this algorithm, the relative selectivity of each reaction is only statistically (not exactly) satisfied.[2] Similar to the previous approach, the DSMC simulations performed using the kMC approach provides excellent agreement with the analytical solutions regardless of the time step size as shown in Figs. 2.12 and 2.13.

In conclusion, the approach outlined by Molchanova *et al.,* [374] for performing LH reactions cannot be directly extended to the case of multiple reactions. It was shown that a simple sequential handling of multiple reactions can lead to a

[2]For example, lets say that the probability of 2 events A and B is both 0.5. For each set of 10 events, if the count of events A and B is not exactly 5, but on an average 5. It could be (6,4); (7,3); (4,6); (3,7), etc. If this is the case, then it is said that the relative selectivity of each event is statistically satisfied.

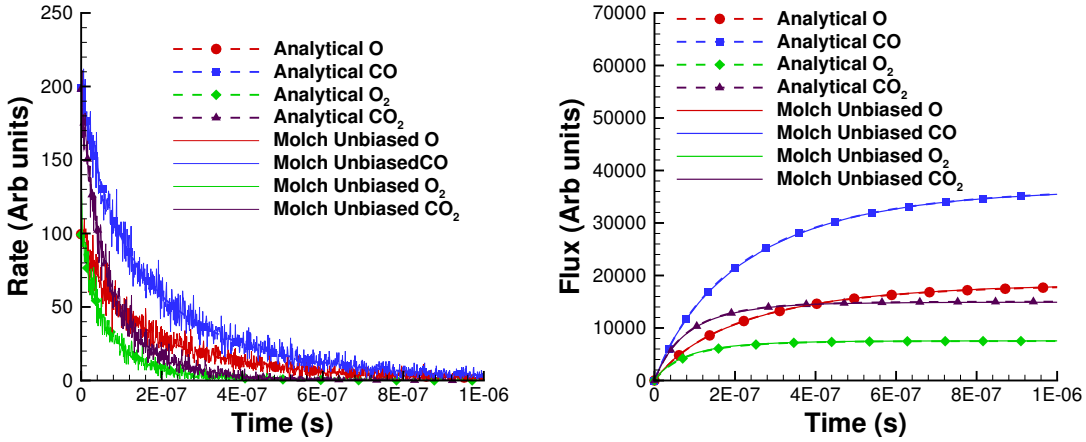

(a) (b)

Figure 2.12: (a) Rate of formation and (b) total flux of products as a function of time obtained from the analytical solution and DSMC simulation using algorithm B and a relatively small time step size.

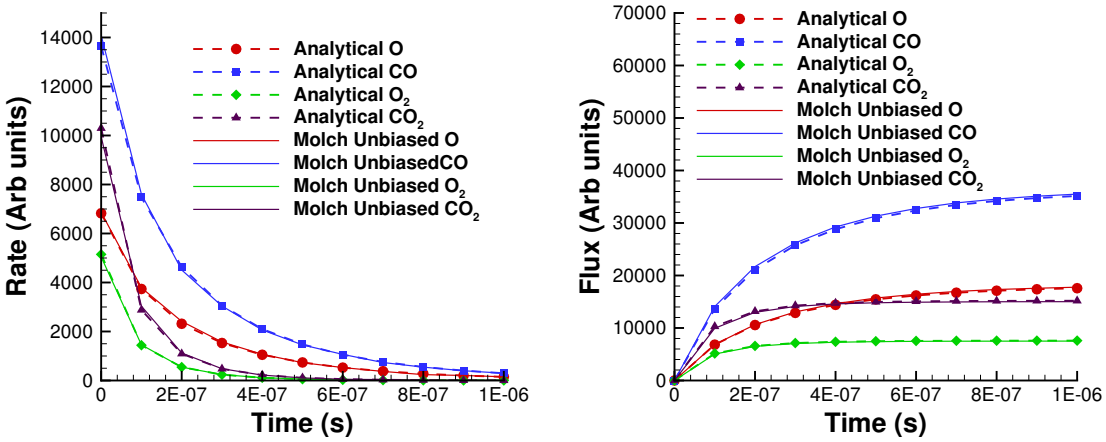

(a) (b)

Figure 2.13: (a) Rate of formation and (b) total flux of products as a function of time obtained from the analytical solution and DSMC simulation using algorithm B and a relatively large time step size.

system bias towards initial reactions, depending on the time step size. In order to eliminate this bias, two algorithms were proposed. The first approach termed as "unbaised Molchanova" involves changing the order of the reactions while the methodology to perform the reactions remains similar to the method proposed by Molchanova *et al.,* [374]. The second approach is inspired by direct method of

Gillespie [375] employed in kinetic Monte Carlo simulations and alters both the order of the reactions and methodology of performing them. Both the approaches were shown to reproduce analytical results for a multi-reaction system regardless of the time step size. The first approach exactly satisfies the relative selectivity of the multiple reactions, while the second approach statistically satisfies it. Depending on the particular application and requisite statistical properties of the system, an appropriate approach can be chosen. In the absence of any preference, the second approach is recommended owing to the (relatively) lower memory requirements and computational cost.

2.6 Scattering models in DSMC

When a particle strikes the surface, it can either adsorb, undergo a direct impact reaction, or scatter impulsively (without undergoing any reaction) from the surface. If the energy of the incoming particles is low (thermal energies, i.e., comparable to the temperature of the gas), then the scattering of the particle could be reasonably modeled using the CLL model [301, 302]. However, if the particles strike the surface with super or hyper-thermal velocities, the CLL model cannot be used to predict the energy and angular distribution of the scattered products. Hence, a non-thermal and impulsive scattering models are developed and implemented in DSMC to account for the scattering of particles with super and hyper-thermal incident energies respectively. In addition, there is absence of models in DSMC to describe the scattering of the desorbed products formed on the surface. Hence, a new model called the thermal desorption model is also developed and described in this section. Finally, in many instances, a combination of scattering models may be required for representing the scattering of the same species over a range of conditions. This is described in Appendix D.

2.6.1 CLL model

Of various phenomenological models for gas-surface interactions, the CLL model [301] appears to be most comprehensive. This model satisfies detailed balance (reciprocity) and produces physically reasonable velocity and angular distributions of the scattered particles. And unlike the Maxwell's model, it provides a continuous variation from specular reflection to diffuse reflection with full thermal accommodation.

In the original model, two accommodation coefficients for the normal and tangential directions (α_n, α_t) are employed. Each of these quantities can take a value between 0 and 1. Specular reflection is achieved by using the values {0,0}, while complete thermal accommodation with the surface and cosine angular distributions is obtained using {1,1}. There is smooth variation of both the energy and angular distribution for values in between these limits.

In addition to this spectrum having these two extreme ends, Lord [302] has proposed a way to take into account other scenarios such as fully and partially diffuse scattering with incomplete energy accommodation. This can reproduce a lobular distribution using the eccentricity factor e. Further, extension of the CLL model was also proposed to handle internal degrees of freedom, described using continuous and discrete energy levels, including anharmonic distribution.

The implementation of the CLL model within the current model takes 5 inputs for translational mode. These are the normal and surface accommodation coefficient (α_n, α_t), the accommodation coefficients for internal energies: rotational, vibrational $(\alpha_{rot}, \alpha_{vib})$ and the eccentricity parameter e.

The eccentricity parameter is used to capture partially diffuse scattering, independent of the level of energy accommodation. The range of e is [0,1]. A value of 1 implies a fully diffuse scattering (with a cosine distribution), and the distribution becomes more lobular as the value decreases. Specifying 0 for the value of e implies specular scattering at the same angle of incidence, but with partial or complete energy accommodation. Each additional degree of freedom (rotational

or vibrational) needs an additional accommodation coefficient as input.

2.6.2 Thermal desorption model

As the name suggests, the thermal desorption model can be used to describe the scattering of desorbing atom/molecule. Usually, the desorbing particle are fully accommodated to the surface temperature and desorb based on a MB distribution and a cosine angular distribution. However, certain processes on the surface might alter these standard distributions. Some common processes which are captured within this model are described below.

2.6.2.1 Desorption energy barrier

Due to the nature of the interaction between the products and the surface, the desorption of the products might have an energy barrier. For a surface desorption process, this desorption barrier exists only in the normal direction [135, 9, 376, 377]. Thus, only the products having enough energy (in the normal direction) to overcome the barrier will be able to desorb from the surface. This alters the velocity distribution of the observed products along the surface normal direction and thus leads to the distortion of the speed distribution [376].

$$E_{norm} = k_b T_s + E_b \qquad E_{tngt} = k_b T_s \tag{2.46}$$

k_b is the Boltzmann constant, T_s is the surface temperature and E_b is the energy of the desorption barrier. Fig. 3.5 (a) shows a representative flux PDF of a thermal process with and without a desorption barrier. In the presence of a desorption barrier, the flux PDF is shifted towards the right of a MB distribution. The angular distributions, which represent the ratio of the normal to the tangential velocities, are also altered as a result of the desorption barrier. The angular distributions are peaked more towards the normal and are often described by a cosine power law distribution ($cos^n\theta$).

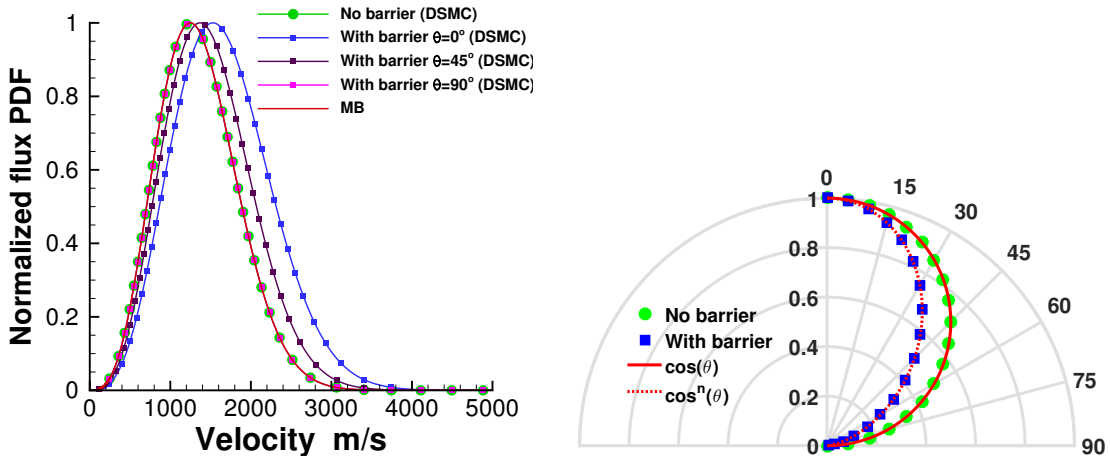

(a) (b)

Figure 2.14: (a) Representative flux PDF distributions of products formed via a thermal mechanism with and without a desorption barrier from a smooth surface for a hyperthermal beam. The distributions are plotted at angle $\theta = 0, 45, 90$ for the case with the desorption energy barrier. (b) Representative in-plane angular distributions of products formed via a thermal mechanism with and without a desorption barrier from a smooth surface (n = 1.5).

In order to obtain the cosine power law distribution in DSMC, the tangential velocities of desorbing molecules must be based on the surface temperature, and the normal velocity component must be drawn from a Boltzmann distribution based on a different temperature given by:

$$T_{norm} = T_s \left(1 + \frac{E_b}{k_b}\right). \tag{2.47}$$

The value of the desorption barrier E_b for a given cosine power law distribution ($cos^n\theta$) can be obtained as [376]:

$$E_b = \left(\frac{n-1}{2}\right) k_b T_s. \tag{2.48}$$

In the presence of the energy barrier, the final VDF/SDF will depend on the polar angle. The analytical form of the distribution can be computed as:

$$f(v) \propto v^2 exp\left(-\frac{mv^2}{2k_b}\left(\frac{cos^2\theta}{T_n} + \frac{sin^2\theta}{T_t}\right)\right) \tag{2.49}$$

2.6.3 Impulsive scattering model

When particles having super or hyper-thermal velocities strike the surface, their scattering patterns are very different from those in the thermal regime [273]. The final energy distribution of the particles exhibit dependence on the incoming energy, angle of incidence and reflection, temperature of the surface, interaction potential, etc.

2.6.3.1 VDF

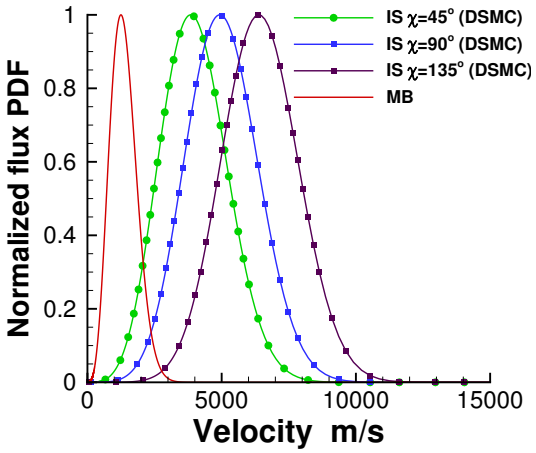

Figure 2.15: Representative flux PDF distributions of impulsively scattered (IS) atoms at deflection angles $\chi = 45, 90, 135$ from a smooth surface for a hyperthermal beam.

The velocity distribution of the IS component can be reasonably approximated using a Gaussian distribution with a mean u_0 and a variance α following Rettner [147]. These two are treated as free parameters in the DSMC model that can be adjusted to match the IS component of the experimental distributions.

$$f_{IS}(u) \propto u^2 \, exp\left(-\frac{(u-u_0)^2}{2\alpha^2}\right) \tag{2.50}$$

2.6.3.2 Angular dependence of VDF parameters: Soft-sphere scattering model

The dependence of the scattered particle energy distribution on the incident energy and angle can be captured using the soft-sphere scattering model. At such high energies, the projectile interacts with the surface in the limit of atomic collisions [273]. Hence, this kinematic model is based on a treatment of soft-sphere scattering , in which a gas-phase, soft-sphere projectile, with an incidence translational energy of E_i, undergoes an inelastic collision with a soft sphere on the surface [312]. The average final energy of the particles is given by:

$$<E_f> = E_i \left(1 - \frac{2\mu}{(\mu+1)^2}\left[1 + \mu sin^2\chi + \frac{E_{int}}{E_i}\left(\frac{\mu+1}{2\mu}\right) - cos\chi\sqrt{1-\mu^2 sin^2\chi - \frac{E_{int}}{E_i}(\mu+1)}\right]\right) \tag{2.51}$$

Here, μ is the mass ratio of the gas ans surface species. E_{int} is the energy transfered to the internal energy. This becomes zero in the case of hard-sphere scattering. The deflection angle χ is defined as:

$$\chi = 180^o - \theta_i - \theta_f \tag{2.52}$$

θ_i and θ_f are the incidence and final angle of the scattered particle with respect to the surface normal. There are two parameters in this function μ and E_{int}/E_i, which can be adjusted to match the experimental observations.

2.6.3.3 Angular distribution

The angular distributions for impulsively scattered particles usually follow a lobular scattering with a peak on the opposite side of the surface normal from the incident beam [273, 9]. The peak angle might be greater than the specular angle. The lobular pattern can be modeled using a cosine power law decay.

$$N(\theta) \propto cos^n(\theta - \theta_{peak}) \tag{2.53}$$

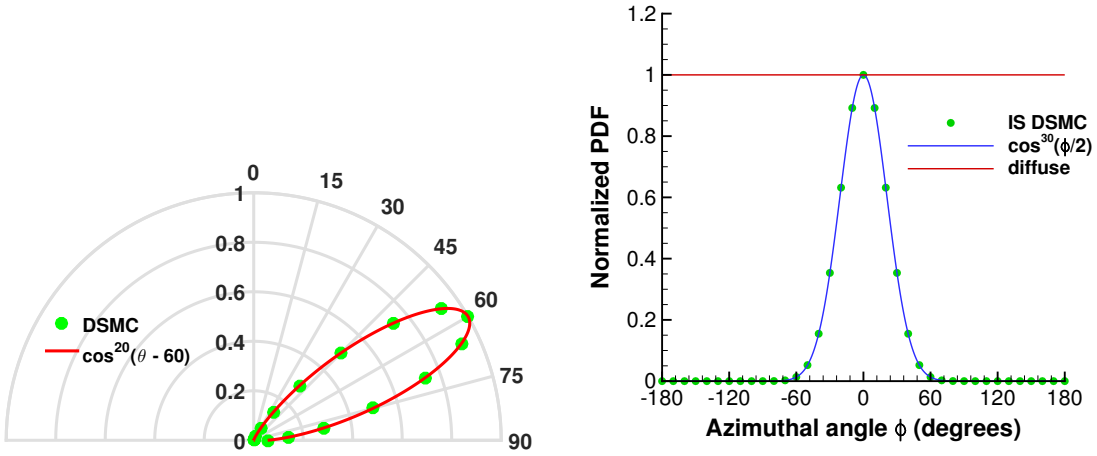

(a) (b)

Figure 2.16: Representative angular distributions of products formed via impulsive scattering (IS) of a hyperthermal beam from a smooth surface. (a) Distribution in the plane containing the surface normal and the incident beam (in-plane): lobular distribution along the polar angle θ with $\theta_{peak} = 60^o$ and $n = 20$). (b) Distribution out of the plane containing the surface normal and the incident beam (out-of-plane): cosine power decay along the azimuthal angle ϕ with $m = 30$.

θ_{peak} is the location of the peak and the value of n determines the width of the distribution. Again both of these parameters can be chosen to match the experimental data. Fig. 2.16 (b) shows a lobular angular distribution for $\theta_{peak} = 60^o$ and $n = 10$.

The azimuthal angular distribution of the IS atoms is not expected to be uniform. Following the work of Glatzer *et al* [255], a cosine power law decay is used to approximate the out-of-plane scattering distribution.

$$N(\phi) \propto cos^m\left(\frac{\phi}{2}\right) \tag{2.54}$$

The factor of 2 is introduced to ensure that the function remains positive within the range of the azimuthal angle: $(-\pi, \pi]$. In many cases, it is observed that the decay rate of the product flux on either side of the θ_{peak} is different [5, 255, 273, 10]. Additional options to capture these types of distributions are presented in Appendix F.

2.6.4 Non-thermal scattering model

Non-thermal scattering model is a generic model similar to the IS model described above but has more flexibility in terms of parameters to handle the wide range of cases where the products that scatter without accommodating to the surface temperature. It is noted that the CLL model can also be used to represent the non-thermally scattered particles, but this model provides higher flexibility.

2.6.4.1 VDF

The velocity distribution is represented using Gaussian distribution with a mean u_0 and a variance α following Rettner [147] similar to the IS model. u_0 and α are both free parameters which can be adjusted to match the experimentally observed distributions. However, unlike the IS model, u_0 is directly taken as an input instead of computing it based on the soft-sphere scattering model. In addition, there is no angular dependence of the VDF parameters.

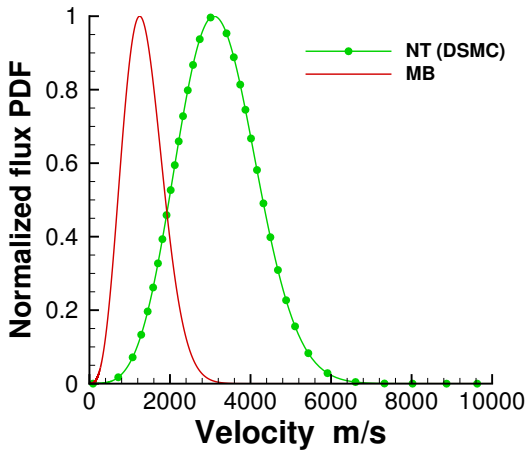

(a)

Figure 2.17: Representative flux PDF distributions of non-thermally (NT) scattered atoms from a smooth surface for a superthermal beam.

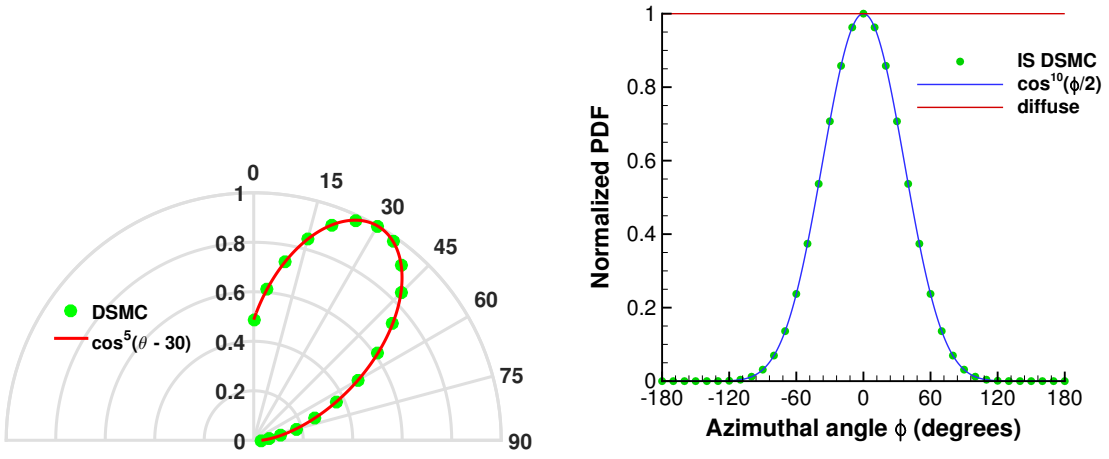

(a) (b)

Figure 2.18: Representative angular distributions of products formed via non-thermal (NT) scattering of a superthermal beam from a smooth surface. (a) Distribution in the plane containing the surface normal and the incident beam (in-plane): lobular distribution along the polar angle θ with $\theta_{peak} = 30^o$ and $n = 5$). (b) Distribution out of the plane containing the surface normal and the incident beam (out-of-plane): cosine power decay along the azimuthal angle ϕ with $m = 10$.

2.6.4.2 Angular distribution

Similar to the IS model, the polar angular distribution is expected to follow a lobular distribution represented using a cosine power law decay.

$$N(\theta) \propto cos^n(\theta - \theta_{peak}) \tag{2.55}$$

θ_{peak} is the location of the peak and the value of n determines the width of the distribution. Again both of these parameters can be chosen to match the experimental data. Unlike the IS model, here the peak of the polar distribution is expected to be smaller than the specular angle.

The azimuthal angular distribution is also represented using a cosine power law decay with its peak at an angle of zero following Glatzer *et al* [255].

$$N(\phi) \propto cos^m\left(\frac{\phi}{2}\right) \tag{2.56}$$

The factor of 2 is introduced to ensure that the function remains positive within the range of the azimuthal angle: $(-\pi, \pi]$. Although the particles are scattered non-thermally, it is possible that the angular distribution might follow a diffuse distribution: cosine in polar direction and uniform in azimuth direction. This can be obtained by setting $\theta_{peak} = 0$, polar cosine power (n) as one and azimuth cosine power (m) as zero. Additional options to capture these types of distributions are presented in Appendix F.

2.7 Summary

In this chapter, the formulation and implementation of a general finite-rate surface chemistry framework in DSMC have been described. The approach involves stochastically modeling the various competing reaction mechanisms occurring on a set of active sites. Within this framework, multiple surface phases can be specified allowing for the representation of composite materials similar to the formulation proposed by Marschall and Maclean for CFD [3]. Further each surface phase can contain multiple site sets which can be used to present heterogeneous surface materials like SiC and h-BN.

The framework includes a comprehensive list of surface reaction mechanisms including adsorption, desorption, Eley-Rideal (ER), and different types of Langmuir-Hinshelwood (LH) mechanisms. It is possible to model both catalytic (oxygen formation) and surface altering (material removal by oxidation) reaction mechanisms. Based on the presence of gas-phase species in the reactants, the reaction mechanisms are classified as gas-surface (GS) or pure-surface (PS) reactions. Since these two classes of reaction mechanisms have to be modeled as a part of different kernels within the DSMC framework, they are treated distinctly.

GS reactions are performed when the gas-phase particles strike the surface as a part of the *move* kernel. The modeling of GS reactions within DSMC involves the computation of the probability for each of the possible reactions. These probabilities are calculated from the specified reaction rate constant, properties of the

incident gas-particle and the surface. Since the probabilities are obtained from rates, it is possible that the individual or cumulative probabilities exceed unity. In order to avoid any bias in such scenarios, a physically consistent multi-step procedure is presented for obtaining the reaction probability values.

PS reactions are carried out by looping over all the surface elements in parallel with the gas-phase collisions. DSMC modeling of PS reactions involve computing a characteristic frequency for each reaction. This characteristic frequency is a function of specified rate constants and surface properties. When multiple PS reactions are present, it is possible to introduce bias within the system. Two different algorithms for performing multiple PS reactions without bias were proposed and shown to accurately match the analytical solutions.

This chapter also presents various scattering models for accurately modeling both reactive and non-reactive scattering at a wide variety of regimes and scenarios. The different models available within this framework include CLL, thermal desorption, impulsive and non-thermal scattering models. In addition, this framework also allows for combining different scattering models to describe the scattering over a range of conditions. For each reaction, recommended models are proposed, but the framework is flexible to incorporate any specified model.

Chapter 3

Construction of Finite-Rate Surface Chemistry Models

3.1 Overview

Pulsed hyperthermal beam experiments performed at high vacuum conditions can be used to elucidate the gas-surface interactions at the molecular level. This chapter describes an approach recently developed for the construction of a finite rate carbon oxidation model from pulsed hyperthermal beam scattering experiments [6]. Each of the steps outlined in Chapter 2 are elaborated, with the carbon oxidation model as an example to illustrate the applicability of this general approach. This approach can be applied to analyze surfaces of different types (metallic/non-metallic), initial states (empty/pre-adsorbed), and also experimental setups with multiple gas-phase reactants within a pulsed hyperthermal/supersonic beam.

This chapter is organized as follows: Section 4.5.1 provides an outline of the pulsed hyperthermal beam experiments. This section also describes the setup of direct simulation Monte Carlo (DSMC) used for simulating the full hyperthermal beam experiments, including the TOF and angular distributions. DSMC is then used to analyze the different components of the experimental distributions that correspond to the various surface mechanisms (Section 3.3). The procedure to compute the total fluxes of each surface reaction product from the experimental distributions (both TOF and angular data) is outlined in Section 3.4. Section 3.5 describes the methodologies to derive the rate constants of the identified reaction mechanisms. First, the steady-state beam approximation is studied and the errors associated with this approximation are analyzed and presented in Section 3.5.1. A

general calibration methodology for the transient rate calculation is proposed and investigated in Section 3.5.2. Finally, the conclusions are provided in Section 3.6.

3.2 Experimental setup

The analysis outlined in the following sections is developed for pulsed beam experimental data. In these experiments, a pulsed hyperthermal beam is focused on the material surface of interest, which is placed within a high vacuum chamber. The gas-phase reactants strike the surface with energy characteristic of the beam at a prescribed incidence angle. Upon impact, the particles can adsorb, undergo direct impact surface reactions, or scatter non-reactively. The scattered products are detected and measured using a mass spectrometer. The number density or flux information of the surface scattered products is collected as a function of time (TOF) at various angles in-plane and out-of-plane of the beam. These TOF distributions which are obtained at different scattering angles are then integrated to compute the angular flux distributions. The surface can be empty or pre-adsorbed with one or more reactants, while the incident beam may also contain multiple chemical species.

For the range of surface temperatures considered here, the incident particle energy from the beam is much greater than the fully accommodated energy from the surface. Thus, there is marked energy difference between the products that are impulsively scattered and those formed via thermal mechanisms (based on the surface temperature), which can clearly be distinguished in a TOF distribution. The TOF distributions provide a wealth of information regarding the time scales associated with reaction and desorption of reactively scattered products. This is especially important for developing chemistry models that is capable of predicting the surface reactions over a wide range of conditions, which may be considerably different from the experimental conditions. Experimental data can be acquired at various surface temperatures, incident energies and angles, in order to obtain a comprehensive picture of the reaction system of interest. Details regarding such

pulsed molecular beam experiments may be found in the literature [5, 7, 378].

3.3 Identifying reaction mechanisms from TOF distributions

Although the TOF distributions can aid in distinguishing processes with disparate time scales, identifying the reaction mechanisms from the TOF distributions is not straightforward. Often, there is significant overlap of these timescales resulting in a superposition of several reaction mechanisms within the TOF distribution. In order to identify and isolate the effects of different surface reaction mechanisms, a detailed understanding of the form of TOF distributions corresponding to these different mechanisms is essential. To this effect, numerical simulations of the molecular beam scattering from a smooth surface are performed under a range of surface and beam conditions of the candidate surface processes using DSMC. This parametric study is instrumental in identifying the reaction mechanisms at the surface corresponding to the observed experimental data.

3.3.1 Non-reactive or impulsive scattering

The particles incident upon the surface may not interact reactively with the surface, leading to inelastic (or elastic) scattering. The probability of inelastic or impulsive scattering (IS) can be significant even for atoms/molecules with large adsorption enthalpies owing to the high velocities in a hyperthermal beam. The interaction time with the surface for the impulsively scattered atoms is so short that they do not achieve thermal equilibrium, and hence these atoms have translational energies that are significantly higher than the average energy of a Maxwell-Boltzmann (MB) distribution associated with the surface temperature [135, 136, 5, 312]. The IS component velocity distribution can be expressed

using a displaced Gaussian functional form [147]:

$$f_{IS}(u) \propto u^2 \, exp\left(-\frac{(u-u_0)^2}{2\alpha^2}\right). \tag{3.1}$$

The parameter u_0 is the mean and the α is the variance of the distribution. These two parameters are treated as free parameters within the model and can be tuned to match the IS component of the experimental TOF distribution. The IS atoms can be easily identified within the TOF distribution by a sharp peak at times much shorter than the MB distribution peak as shown in Fig. 3.1 (a). The in-plane angular distribution of the IS atoms is usually peaked at angles larger than the specular angle (away from the normal) [5, 273, 135, 312]. The particles tend to have greater accommodation along the surface normal compared to the tangential direction. This causes the angular distribution to shift from the specular angle in the direction away from the surface normal. The distribution also tends to be highly peaked with rapid fall off from the peak angle. A representative IS angular distribution is shown in Fig. 3.1 (b).

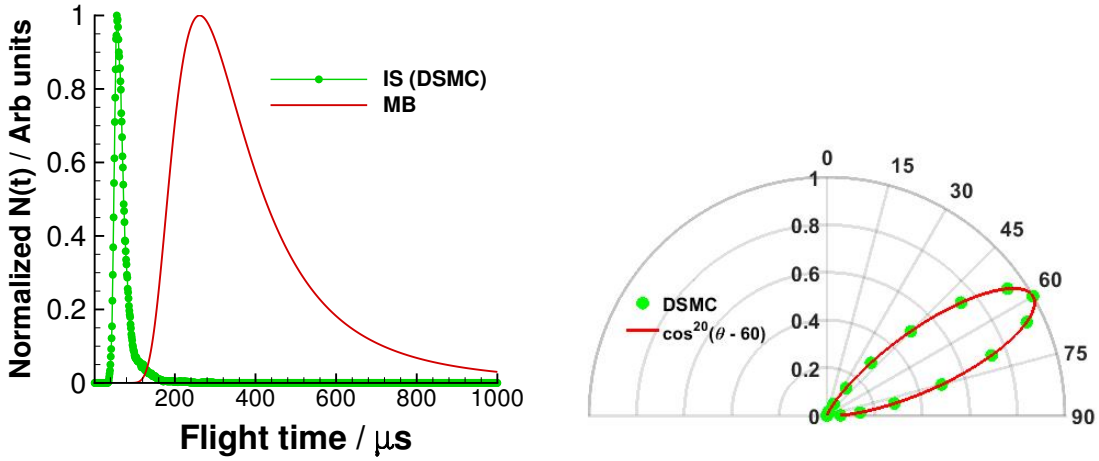

(a) (b)

Figure 3.1: Representative (a) TOF and (b) in-plane angular distribution of IS products scattered from a smooth surface for a hyperthermal beam. In Fig. 3.1 (b), θ is the final angle of the scattered products.

3.3.2 Adsorption: direct and indirect pathways

When a particle from the beam collides with the surface, it can either adsorb, undergo direct impact reactions or scatter impulsively from the surface. The probability of adsorption is determined by two factors: the surface coverage (θ) and the sticking coefficient (S_0). The adsorption probability is linearly proportional to the sticking coefficient.

The dependence of the adsorption probability on the surface coverage varies based on the dynamic pathway through which the adsorption reaction occurs: direct and indirect adsorption as described previously in Section 2.3.1. For direct adsorption, the adsorption probability is a linear function of the surface coverage, while in the case of indirect adsorption, non-linear behavior is observed. The experimental trends in the adsorption probability with surface coverage (function of temperature) can be used to identify the adsorption pathway and compute the subsequent rates.

3.3.3 Eley-Rideal mechanism

The Eley-Rideal mechanism is a non-thermal direct impact mechanism. This results from the fact that the products formed through the Eley-Ridel mechanism are formed immediately after the gas phase reactant strikes the surface, and the interaction time is not long enough for thermal equilibration with the surface [135, 136, 379, 380]. The products have translational energies that are significantly higher than the average MB distribution, but whose energies are much lower than those of the impulsively scattered (IS) atoms, as shown in Fig. 3.2 (a). Similar to IS atoms, the velocity distribution of the ER products are modeled as a Gaussian distribution (Eq. (3.1)), where the mean u_0 and variance α are treated as free parameters to fit the observed TOF distribution [147]. The in-plane angular distribution of the ER products do not follow a particular distribution and are reported in literature to vary based on the reaction. The only consistent feature is that a peak in angular distributions occurs between the normal and the specular

angle [147, 381] as shown in Fig. 3.2 (b).

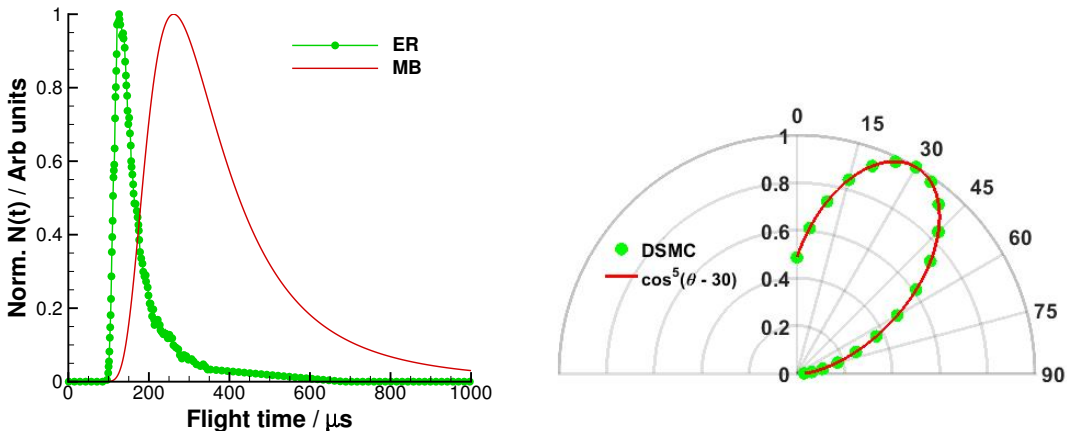

Figure 3.2: Representative (a) TOF and (b) in-plane angular distribution of products formed via Eley-Rideal (ER) mechanism from a smooth surface for a hyperthermal beam. In Fig. 3.2 (b), θ is the final angle of the scattered products.

3.3.4 Collision Induced mechanism

A CI mechanism is similar to an ER mechanism as both involve gas-phase and surface adsorbed reactants. However, the two reactants within the CI mechanism do not chemically react with each other. The energy from the collision of the gas-phase reactant induces desorption of adsorbed atoms/molecules from the surface, and hence these reactions usually involve high-speed particles (super-/hyperthermal velocities) [373, 382, 383, 135]. The incident particle may or may not adsorb onto the surface. If the incident particle does not adsorb, its scattering will be similar to an IS particle. The TOF or velocity distribution of the desorbing particles usually follows a MB distribution at time t=0, while the angular distributions is described by the cosine law [384, 385]. However, if a desorption energy barrier or additional energy transfer mechanisms are present, they can alter the shape of both angular and TOF distribution of the desorbing particle (Section 3.3.5.2).

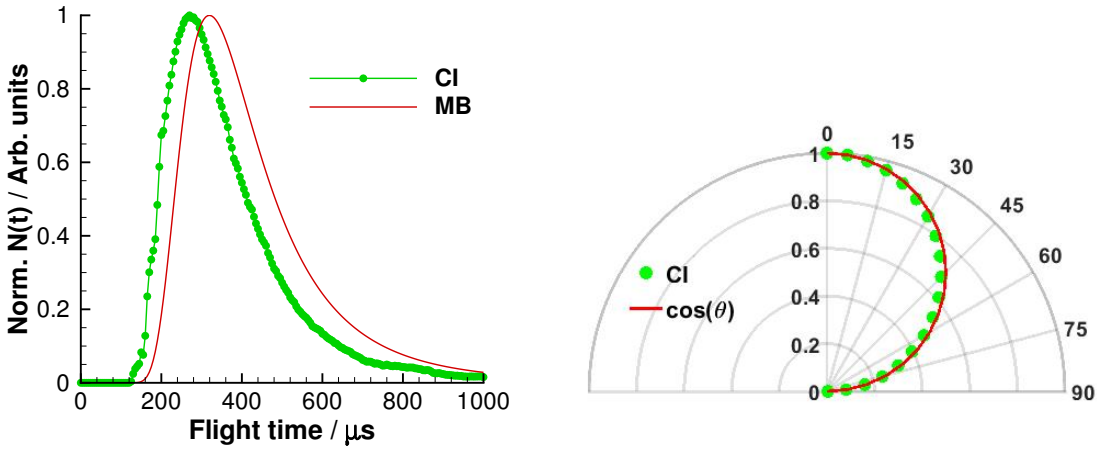

(a) (b)

Figure 3.3: Representative (a) TOF and (b) in-plane angular distribution of products formed via collision induced (CI) mechanism from a smooth surface for a hyperthermal beam. In Fig. 3.3 (b), θ is the final angle of the scattered products.

3.3.5 Desorption

Desorption is a thermal mechanism and the products exit the surface with a MB distribution [135, 5, 367, 369]. However, since the reactants are all adsorbed species, this mechanism is not directly dependent on the beam. Hence, the products are not formed immediately after the beam hits the surface, if the reaction rate is relatively low (corresponding to a relatively low surface temperature) and *do not follow a MB distribution at time t=0.* The desorption of the products into the gas phase occurs over an extended period of time, leading to a cumulative MB distribution over that time period. If the surface were continuously replenished with adsorbed reactants, the TOF signal would be constant with time. However, for a pulsed beam, the TOF signal of these reactions will be based on a convolution of MB distribution with an exponential or power decay depending on the order of the reaction as shown in Fig. 3.4 (a) [5]. As the rate constant increases (corresponding to increasing temperature), the final TOF distribution shifts closer to the MB distribution at time t=0. When the reaction rate is relatively high (corresponding to a relatively high surface temperature), the products are formed almost immediately after the beam collides with the surface and they

follow a MB distribution at time t=0 (Fig. 3.4 (c)). Regardless of the rate of the reaction, the angular distribution of the products follow a cosine distribution (shown in Fig. 3.4 (d)) provided that the species has no desorption barrier.

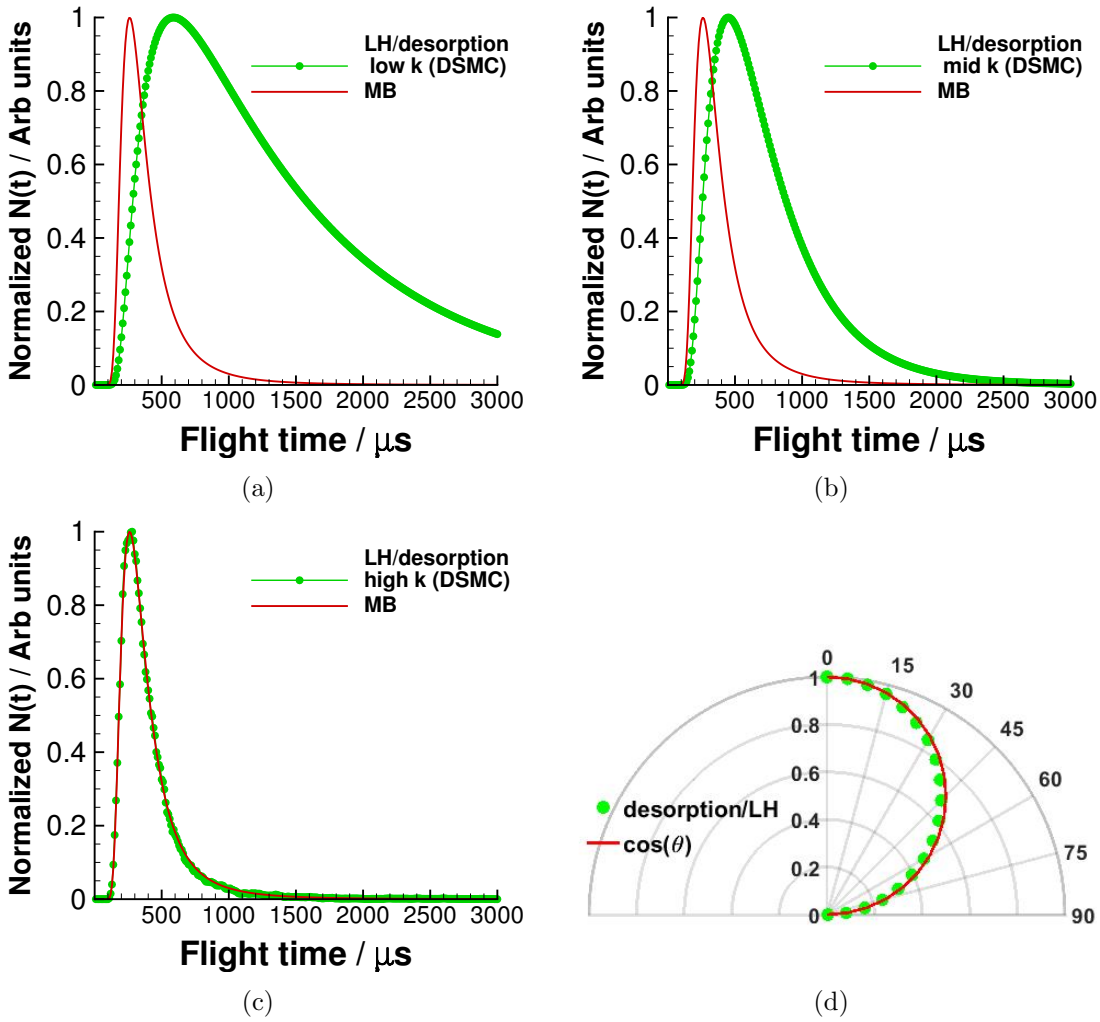

Figure 3.4: Representative TOF distributions of products formed from a smooth surface for a hyperthermal beam via desorption and LH type 2 mechanism with (a) relatively low reaction rate, (b) intermediate reaction rate and (c) relatively high reaction rate. (d) Representative angular distribution of products formed via desorption and LH type 2 mechanism from a smooth surface. In Fig. 3.4 (d), θ is the final angle of the scattered products.

3.3.5.1 Desorption Energy barrier

The presence of a desorption energy barrier will alter the TOF distribution from a MB distribution [135, 386]. Fig. 3.5 (a) shows a representative TOF distribution of a thermal process with and without an energy barrier. In a system with an energy barrier, the TOF distribution of the desorbing product is shifted left from a MB distribution. The angular distribution, which is determined by the proportion of the normal to the tangential velocity is also altered due to the energy barrier. The angular distribution is much more peaked towards the normal and follows a cosine power distribution ($cos^n\theta$) [135, 376].

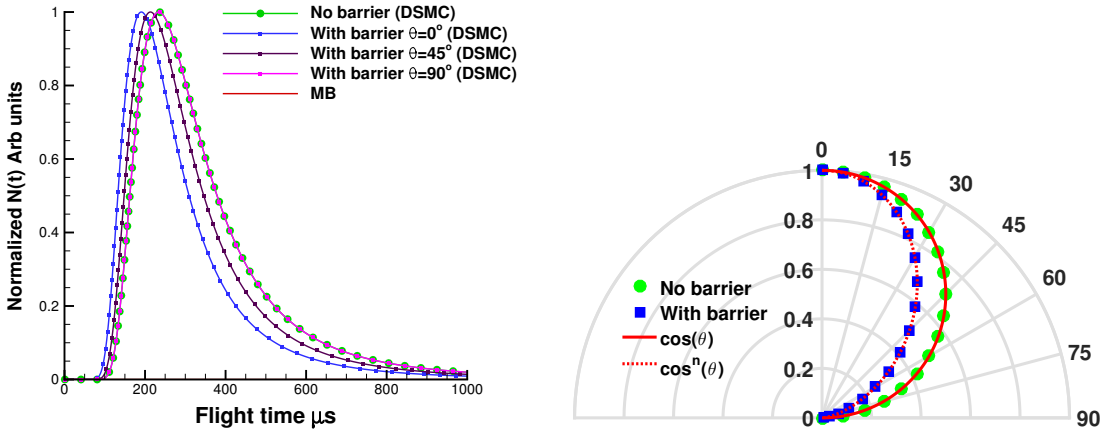

(a) (b)

Figure 3.5: Representative (a) TOF and (b) in-plane angular distribution of products formed via a thermal mechanism with and without an energy barrier from a smooth surface for a hyperthermal beam. In Fig. 3.5 (b), θ is the final angle of the scattered products.

3.3.5.2 Additional energy transfer

Besides the desorption barrier, there are several other energy transfer mechanisms that can alter the observed distributions of the desorbing product. In a CI mechanism, usually prominent in a high energy hyperthermal beam leads to the formation of local hot-spots Another energy transfer pathway is due to dissociation or adsorption bond energy corresponding to the incident particle, causing

the product to desorb with superthermal energies [384, 385]. Although these mechanisms cause the TOF distribution to be different from a MB distribution at time t=0, the "extra" energy does not show a preference to the normal/tangential directions or a dependence on the azimuthal angle, and hence the angular distribution will be a cosine distribution (Fig. 3.6).

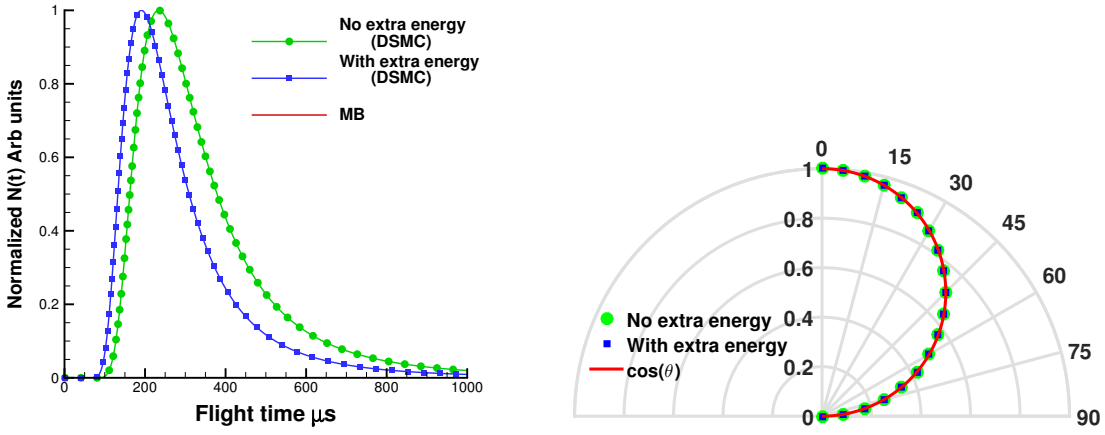

(a) (b)

Figure 3.6: Representative (a) TOF and (b) in-plane angular distribution of products formed via a thermal mechanism with and without additional energy transfer from a smooth surface for a hyperthermal beam. In Fig. 3.6 (b), θ is the final angle of the scattered products.

3.3.6 Langmuir-Hinshelwood mechanism

As described in Section 2.3.3, Langmuir-Hinshelwood mechanisms can be characterized into four types. The variation of the species concentration and the corresponding TOF distribution of the products for all the four types of LH mechanisms are shown in Fig. 3.7. In the case of LH-1 reaction, the gas-phase products exit the surface promptly at all temperatures and the TOF distribution follows a Maxwell-Boltzmann (MB) distribution at time t=0 corresponding to the surface temperature as shown in Fig. 3.7 (a). For a LH-2 mechanism, although the gas-phase products exit the surface immediately after they are formed, the formation step is not instantaneous and follows a decay rate equation. Thus, the observed

TOF distribution does not follow a MB distribution, but a convolution of MB distribution and the corresponding decay rate equation as shown in Fig. 3.7 (b). In the case of LH-3 mechanism, since the desorption occurs slowly, the TOF distribution of the gas-phase product follows a convolution of MB distribution at time t=0 and the corresponding decay rate equation as shown in Fig. 3.7 (c). Finally, for a LH-4 reaction, owing to the time-varying rate of the gas-phase product desorption, the TOF distribution has a complex form as shown in Fig. 3.7 (d).

3.3.6.1 Distinguishing between different types of LH reaction mechanisms from molecular beam data

It is observed that the TOF distribution for a LH-2 and LH-3 mechanism have the same form. Hence, the TOF distribution alone is not enough to distinguish between type 2 and type 3 LH mechanisms if there is only one LH reaction. However, the existence of a parallel reaction system with two or more LH reactions can be used to gain further insight into the exact type of the LH mechanism utilizing only the TOF distribution.

Consider a simple system of two first-order parallel reactions with the same reactant R, and having different surface intermediates (I_1 and I_2) and products (P_1 and P_2) with corresponding rate constants as shown in Fig. 3.8. If the system of reactions are of type 2 (LH limited by formation), *i.e.,* formation rates (k_{f1}, k_{f2}) are slow and desorption rates (k_{d1}, k_{d2}) are high, then the concentration of each species would follow the trends shown in Fig. 3.9 (a). The concentration of both the intermediates are zero, and the decay rate of the reactant is determined by the sum of k_{f1} and k_{f2}. The selectivity of products formed is determined by the ratio of k_{f1} and k_{f2}.

$$R = n_0 \exp(-(k_{f1} + k_{f2})t), \tag{3.2a}$$

$$\frac{P_1}{P_2} = \frac{k_{f1}}{k_{f2}}. \tag{3.2b}$$

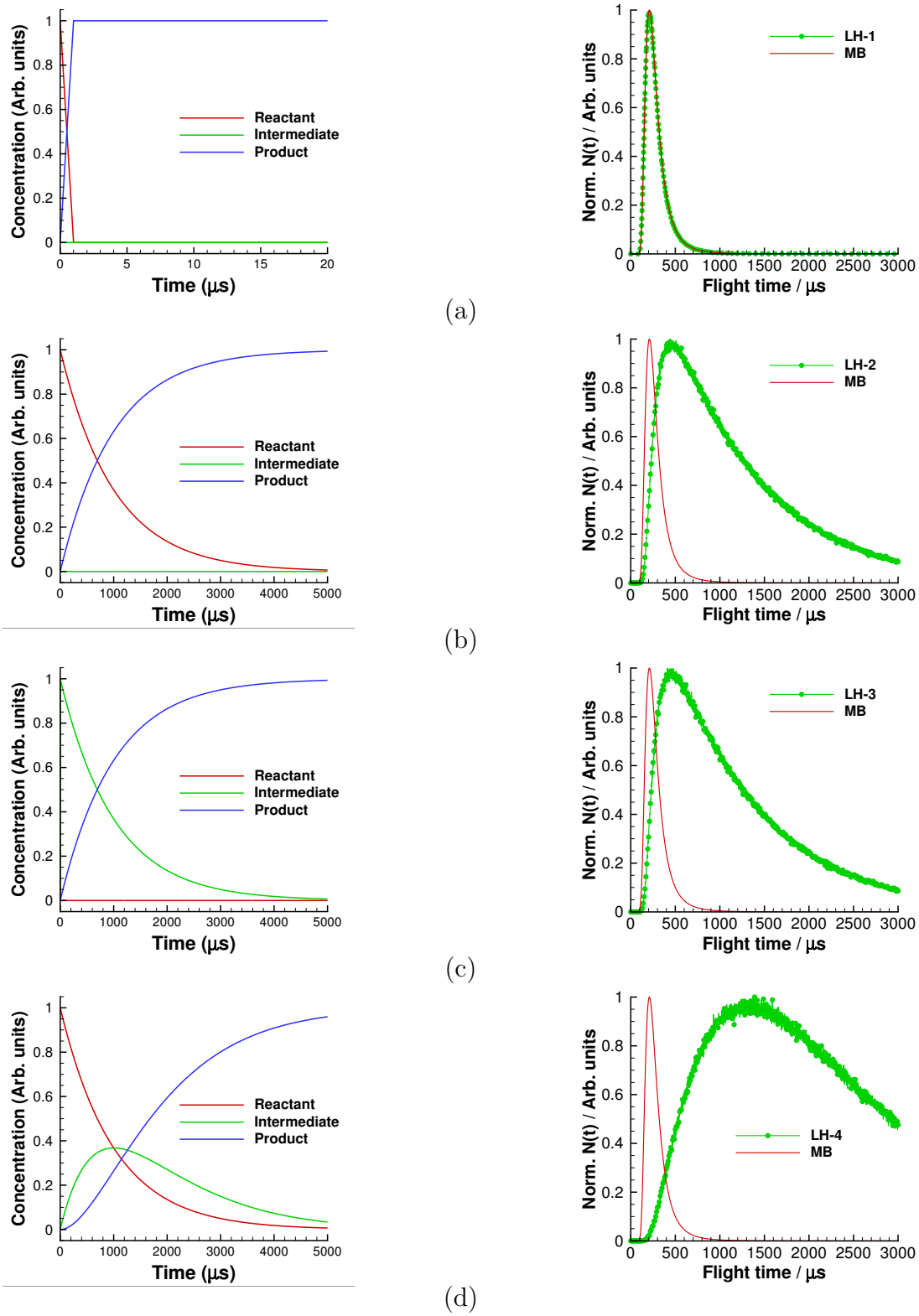

Figure 3.7: Concentration of the species as a function of time (left) and normalized TOF distribution of the product (right) for a typical LH reaction of type 1, 2, 3, and 4.

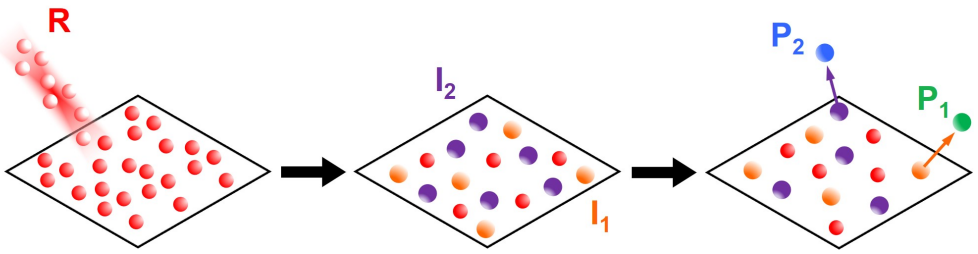

Figure 3.8: System of two parallel reactions with same reactant R, and having different surface intermediates (I_1 and I_2) and products (P_1 and P_2)

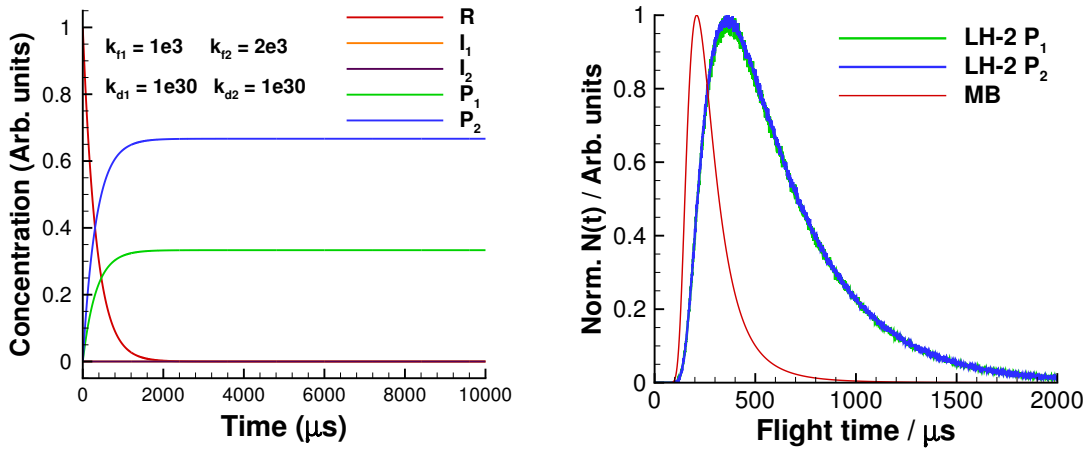

(a) (b)

Figure 3.9: (a) Concentration of the species as a function of time, (b) TOF distribution of the products (normalized independently) for a typical LH type 2 parallel reaction system shown in Fig. 3.8.

If the LH reaction system is of type 2, the values of k_{f1} and k_{f2} can be determined by the rate of decay of the reactant and the relative concentration of the products using Eq. (3.2).

The TOF distribution of both products (normalized independently) are shown in Fig. 3.9 (b). The distributions follow a convolution of MB distribution at time t=0 and exponential decay (first-order). Since the product formation rate is determined by the same reactant concentration, the TOF distribution of the products are aligned exactly.

If the reaction system follows a LH-3 mechanism (LH limited by desorption), *i.e.,* formation rates (k_{f1}, k_{f2}) are high and desorption rates (k_{d1}, k_{d2}) are low, then

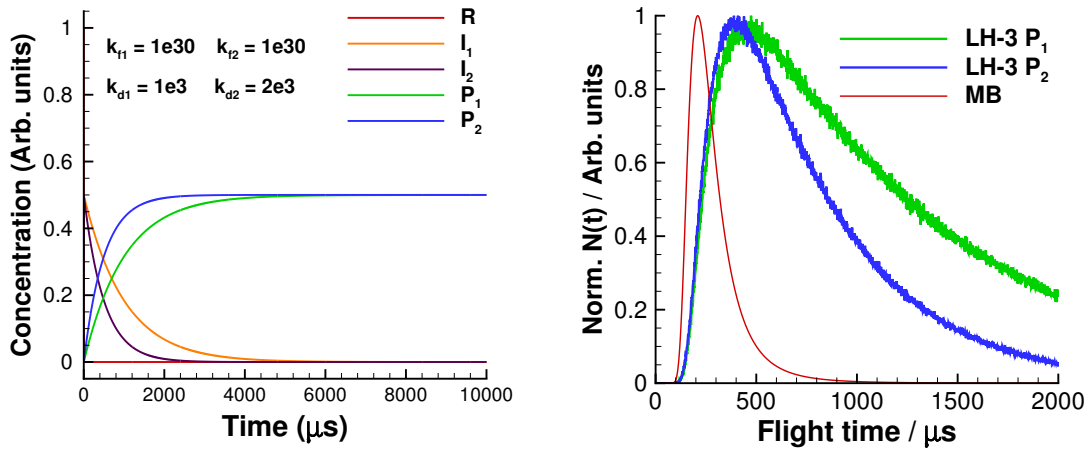

(a) (b)

Figure 3.10: (a) Concentration of the species as a function of time, (b) TOF distribution of the products (normalized independently) for a typical LH type 3 parallel reaction system shown in Fig. 3.8.

the variation of the concentration with time of each species would be very different from the previous case. This is shown in Fig. 3.10 (a). The reactant immediately forms the surface intermediates and its concentration instantaneously falls to zero. The concentration of both intermediates slowly decay over time (exponential in this case), while the products show a corresponding increase. The TOF distribution of products (normalized independently) are presented in Fig. 3.10 (b). Similar to the LH-2 mechanism, the TOF distributions follow the convolution of MB distribution and an exponential decay (first-order). However, the TOF distribution of the products from the type 3 mechanism is not the same. This results due to the fact that the formation rate of the products are based on the concentration of their respective intermediates, rather than the concentration of the reactant. This key difference between the decay rates of the products can be used to *distinguish the products formed via LH-2 or LH-3 mechanisms.*

Similar to the LH-2 mechanism, the final relative concentration of the products is determined by the ratio of k_{f1} and k_{f2} (Eq. (3.2)(b)). If the system of LH reactions are of type 3, the values of k_{f1} and k_{f2} can be determined by the ratio of the concentration of the products to the total influx of reactants. The decay

rate of the two products can be used to determine the value of desorption rates k_{d1} and k_{d2}, respectively.

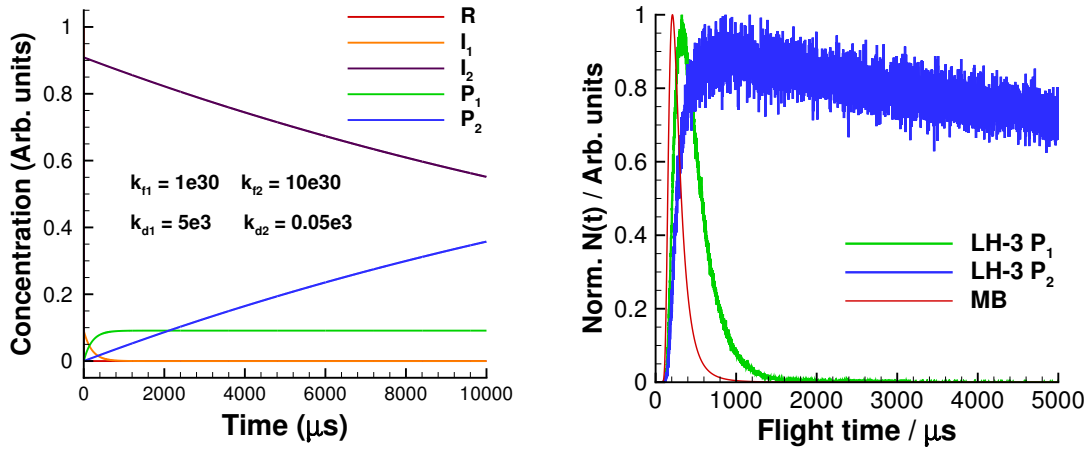

(a) (b)

Figure 3.11: (a) Concentration of the species as a function of time, (b) TOF distribution of the products (normalized independently) for a typical LH type 3 parallel reaction system shown in Fig. 3.8 with disparate rates.

It is important to keep in mind that the desorption rates do not reflect the total concentration of the products, but rather the rate at which these products are observed in the gas-phase. Hence, a reaction with higher decay rate does not necessarily imply that the total concentration of that particular product is higher. The final concentration of the products is determined exclusively by the formation rates. This can be seen more clearly from Fig. 3.11. The rate of desorption of reaction 1 is ten times greater than that of reaction 2. Thus, a higher amount of product 1 is initially observed from the TOF distribution (Fig. 3.11 (b)). However, the distribution dies off quickly in comparison with reaction 2. Hence, the total final concentration (obtained from integrating the TOF distribution) of product 2 is higher than that of product 1. In fact, the final concentration of product 2 will be ten times greater than of product 1, as can be inferred from the ratio of the corresponding formation rates (Eq. (3.2)(b)).

3.3.7 Decomposition of the TOF distributions

The total TOF distribution obtained from the experiments will often have significant overlap of the product distribution from various mechanisms. However, the techniques outlined at the beginning of this section can be used to identify and isolate the different mechanisms. The different components comprising the total TOF distribution are identified in Fig. 3.12. Component I is IS made up of inelastically or impulsively scattered atoms, which have the greatest energy and the shortest flight time. The non-thermal (NT) mechanisms (ER and HA) form products that constitute component II. The mechanisms which produce thermal products immediately after the beam strikes the surface are mainly concentrated in component III. LH-1 and CI mechanisms fall under this category. Finally, the slowly desorbing products resulting from desorption and LH mechanisms of type 2, 3 and 4 are present in component IV.

Although the exact procedure for decomposing the TOF data will vary from one system to another, the procedure outlined here has recently been employed in Swaminathan-Gopalan *et al* [6], and is briefly described with the intent of providing a guideline. In the first step, it is noted that all the distributions except for the slow component decay rapidly to zero and are not present at long times. Thus, the profile of the slow portion is determined promptly by fitting to the TOF distribution at long times. In the next step, the thermal (TD) component of the TOF distribution is identified. The desorption of the thermal products is based on a MB distribution at time t=0 and are preferentially scattered towards the surface normal following a cosine law. Both the velocity and angular distribution of the TD products might be altered due to the existence of an energy barrier for desorption. The polar angular distributions can be used to calculate the energy barrier by fitting to a cosine power law. The energy barrier value can then be used to compute the modified TD velocity distribution [6].

Once the slow and thermal components have been captured, the component of the TOF distribution containing the impulsively scattered particles is char-

acterized. A displaced Gaussian profile (Eq. (3.1)) can be used to describe the distribution of velocity for the IS component. There are two variable parameters: mean u_0 and variance α. Due to the hyperthermal energies of the particles, the IS particle collision with the surface belongs in the structural regime [273]. In this regime, the soft-sphere scattering model [312, 387, 5] can be utilized to compute the mean energy of the inelastically scattered particles. The exact procedure to obtain the free parameters (variance and soft-sphere model parameters) from the experimental data has been outlined in Ref. [6].

At last the portion between the peaks of IS and TD, termed as non-thermal (NT), is characterized. The reason for analyzing this NT portion towards the end is because of the several pathways through which this component could be produced: (i) direct non-thermal reactions like ER or HA, (ii) local hot-spots on the surface leading to superthermal energies of TD products [373], (iii) additional energy transfer due to bond breaking [384], (iv) multiple bounces of the IS atoms on the surface resulting in high energy loss [291]. The profile of the velocity and angular distribution of this TOF portion may be used to identify the exact pathway. The displaced Gaussian functional form (Eq. (3.1)) can be used to represent the velocity distribution similar to the IS part. Again, the procedure to determine the fitting parameters from the experimental data can be found in Ref. [6].

3.4 Computing total product fluxes

Once the TOF distributions have been decomposed, the total product flux from each of the mechanisms must be computed in order to calculate the rate constants of the reactions. First, the fluxes must be computed from the TOF distributions at each angle, then these fluxes must be integrated over the angular distributions to obtain the final product fluxes.

The TOF distribution detected using a mass spectrometer can either record the number density [388, 312, 5] or the flux [389] of the products as a function of time.

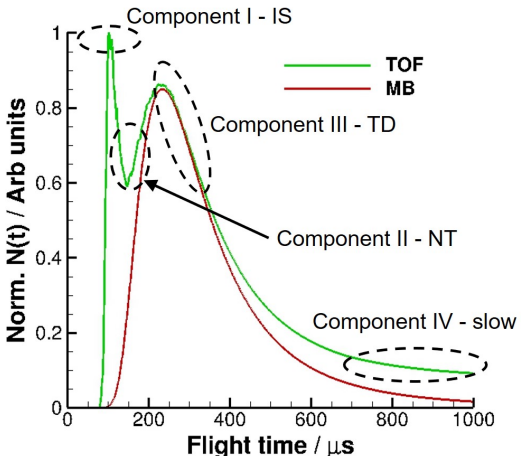

(a)

Figure 3.12: Decomposition of a sample TOF distribution into four regions namely IS, NT, TD, and slow.

If the flux distribution is measured, it can directly be integrated over the length of time between two pulses to obtain the integrated flux of the reaction products at that particular angle. However, if the number density is measured, then these must be converted to a flux distribution before integration. In order to obtain the flux or intensity distribution ($I(t)$) from the number density distribution ($N(t)$), the following formula is usually employed [5, 177, 181, 390]:

$$I(t) = \frac{N(t)}{t}. \tag{3.3}$$

However, this formula only applies for the products that scatter or desorb from the surface immediately after the beam strikes. If the products desorb slowly over a period of time, this density-to-flux conversion is not applicable since the time t is not only indicative of the time needed for the particle to reach the detector from the surface. The time t also includes the diffusion, formation and residence times of the slowly desorbing products. In order to obtain the flux distribution of the slowly desorbing products, first the desorption rate constant is determined by fitting the convolution of the MB number density distribution at time t=0 and the decay rate equation to the experimental distribution. The flux distribution

is then given by the convolution of the MB flux distribution at time t=0 and the decay rate equation (with the rate constant determined in the previous step) according to:

$$\begin{aligned} \text{number density} \quad & f(u) \propto u^2 exp\left(\frac{m}{2k_bT_s}u^2\right) \quad f(t) \propto \frac{1}{t^4} exp\left(\frac{m}{2k_bT_s}\frac{d^2}{t^2}\right), \\ \text{flux} \quad & f(u) \propto u^3 exp\left(\frac{m}{2k_bT_s}u^2\right) \quad f(t) \propto \frac{1}{t^5} exp\left(\frac{m}{2k_bT_s}\frac{d^2}{t^2}\right). \end{aligned} \tag{3.4}$$

Within the experimental setup, the detection of products desorbing very slowly over extended periods of time is challenging owing to the difficulty in distinguishing their low signal from the background noise.

This becomes especially important at low temperatures when the reaction rate constants are lower. In addition, the sampling window in the experiments during which the TOF data is collected may not cover the entire time between the beam pulses [5, 177, 181, 390], thus further increasing the fraction of products that goes undetected. Hence, care must be taken so that the sum of all the desorbing product fluxes account for the entire incident flux from the beam. Another important consideration, especially when multiple products are involved, is the mass sensitivity of the detector. Typically, the detector efficiency is higher for larger masses [388]. Thus, this mass sensitivity factor of the detector must be taken into account for obtaining accurate fluxes from experimental data.

Integration of the TOF distribution provides the fluxes at a particular reflected angle. This must be repeated for each angle to compute the angular distribution. Typically, these measurements are carried out over a limited number of angles in the plane of the beam (and the surface normal) [384, 147, 5, 177, 181, 390]. Both the in-plane and out-of-plane distributions is required for each mechanism to obtain the total fluxes of the products from the TOF integrated fluxes at different angles. The polar (in-plane) angular distribution of the TD products is characterized by a cosine law, while the azimuthal (out-of-plane) distribution is usually uniform. However, this can be altered due to the presence of energy barriers and

additional heat transfer mechanisms. The angular distributions of other direct impact reaction mechanisms and inelastically scattered species must be explicitly determined either in the current or previous experiments or theoretical studies. While integrating the distributions over the angles, it is important to use analytical or functional forms and perform the integration over the complete range of angles: $[0, \pi/2]$ for in-plane, and $(-\pi, \pi]$ for out-of-plane angle.

3.5 Computing the rate constants

In this section, methodologies to compute the rate constants for all the surface reactions identified in the TOF and angular distributions are described. First, the rate constant of desorption reactions can be directly determined from fitting the TOF distributions of the slowly desorbing products. As described previously, the form of the slowly desorbing product TOF distribution follows a convolution of MB distribution at time t=0 and the decay rate equation. The best fit to the slow component of the experimental TOF distribution with the analytical form gives the desorption rate constants. It is important to note that the desorption reactions need not necessarily be first order reactions [367, 369]. Further, their order might vary with coverage of the different species on the surface.

Once the rate constant of desorption reactions have been computed, the final step is to obtain the Gas-Surface (GS) reaction rate constants. The GS reactions are comprised of all reactions which contain gas-phase and surface (or bulk) reactants. This includes direct impact reactions (ER, HA) as well as some thermal mechanisms such as CI, LH-1, LH-3 formation, etc. In order to obtain these rate constants, usually the steady-state approximation is used to estimate the surface conditions to simplify the analysis [33, 144, 145, 391, 392, 146]. With this approximation, the analytical solution for the rate constant values can be computed directly from the steady state equations for the product fluxes, surface coverage and site conservation equation. However, this approach neglects the transient characteristic of the pulsed beam, in which the surface conditions still vary widely

over the course of a pulse. For instance, based on the temporal location of each particle within the pulse, the surface coverage it encounters will vary, thereby leading to different reaction rates After the system has reached steady state (where "steady-state" refers to a long exposure of the surface to the pulsed beam prior to the acquisition of the experimental data) the incoming particles at the start of each pulse will experience the same surface coverage at time t=0. As the pulse progresses, the surface coverage increases till the end of the pulse. Then, the desorption of the particles from the surface leads to steady decrease in surface coverage till the next pulse. By the start of the next pulse, the surface coverage recovers to the value at t=0 and this cycle continues. This is in complete contrast to the steady-state approximation, where it is assumed that each particle experiences identical surface conditions, thus neglecting the variations in the surface within the duration of the pulse.

3.5.1 Steady-state approximation

First, a study is conducted to quantify the errors introduced by the steady-state approximation using a baseline surface reaction system with the given mechanisms and rate constants as shown in Table 4.1. These mechanisms and rate constants are taken as the baseline values which serve as the standard for comparison to assess the accuracy of the steady-state assumption vs. pulsed beam approach for determining the model rate constants. DSMC simulations of a pulsed hyperthermal beam of O atoms directed at the surface of interest are performed at various temperatures, and the final compositions of the products that are observed at steady state are shown in Fig. 3.13. The frequency of the pulse is 2 Hz, and the flux is 5×10^{18} O atoms/m^2/s. The width of the pulse is approximately 20 μs, and the total site density on the surface (Φ) is taken as 6×10^{18} m^{-2}. These compositions are then given as input to the steady-state approximation to compute the rate constants, which are then compared with the baseline rate constant values in Table 4.1.

Table 3.1: Sample reaction system used for assessing the steady-state approximation and the pulsed-beam calibration methodology

Reaction Mechanism	Rate	Rate constant	Units
$O(g) + (s) \longrightarrow O(s)$	$k_1[O(g)][s]$	$\frac{1}{4B}\sqrt{\frac{8k_bT}{\pi m_O}}$	$\frac{m^3}{mols}$
$O(s) \longrightarrow O(g) + (s)$	$k_2[O(s)]$	$\frac{2\pi m_O k_b^2 T^2}{Bh^3} 1.5 \times 10^{-15} e^{\frac{-5000}{T}}$	$\frac{1}{s}$
$O(g)+C(b)+(s) \longrightarrow CO(g)+(s)$	$k_3[O(g)][s]$	$\frac{1}{4B}\sqrt{\frac{8k_bT}{\pi m_O}} 2e^{\frac{-2287}{T}}$	$\frac{m^3}{mols}$
$O(g)+O(s)+C(b) \longrightarrow CO_2(g)+(s)$	$k_4[O(g)][O(s)]$	$\frac{1}{4B}\sqrt{\frac{8k_bT}{\pi m_O}} 0.8e^{\frac{-100}{T}}$	$\frac{m^3}{mols}$
$O(g) + O(s) \longrightarrow O_2(g) + (s)$	$k_5[O(g)][O(s)]$	$\frac{1}{4B}\sqrt{\frac{8k_bT}{\pi m_O}} 1.5e^{\frac{-1200}{T}}$	$\frac{m^3}{mols}$

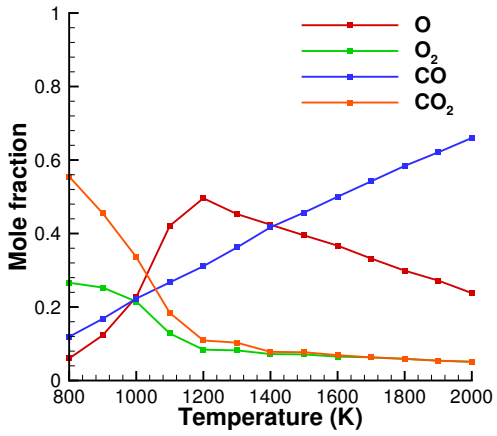

(a)

Figure 3.13: Mole fractions of the products obtained using a hyperthermal pulsed beam for the system in Table 4.1.

The list of equations included within this study are shown below:

$$\begin{aligned}
\frac{d[O(g)]}{dt} &= +[O(g)] - k_1[O(g)][(s)] + k_2[O(s)] - k_3[O(g)][(s)] \\
&\quad - k_4[O(g)][O(s)] - k_5[O(g)][O(s)], \\
\frac{d[CO(g)]}{dt} &= k_3[O(g)][(s)], \\
\frac{d[CO_2(g)]}{dt} &= k_4[O(g)][O(s)], \\
\frac{d[O_2(g)]}{dt} &= k_5[O(g)][O(s)], \\
[O(s)] + [(s)] &= \Phi.
\end{aligned} \tag{3.5}$$

As described in the previous section, the desorption rate constant (k_2) can be directly obtained from the TOF distributions. Hence assuming that the values of k_1 and k_2 are known, the reaction rate constants of k_3, k_4, and k_5 are computed using the above equations with the product fluxes (Fig. 3.13) as input. The percent error between the computed rate constant values and the baseline values from Table 4.1 are plotted in Fig. 3.14 (a). Significant discrepancies are observed between the rate constants. Major differences are observed at higher temperatures, when the surface coverage is very low at steady state. The errors in rate constants k_3 and k_5 are identical owing to the similar dependence of the corresponding products on the surface coverage. These errors also reach very high values at high temperatures as a result of low product fluxes. In order to understand the impact of the differences in the computed rate constants, the steady-state rate constant values are used to perform DSMC simulations of the pulsed hyperthermal O beam. The product fluxes obtained from the rate constants computed using the steady-state approximation are compared with the baseline product fluxes (Fig. 3.13) and the errors are plotted in Fig. 3.14 (b). The errors in the mole fractions of O_2 and CO_2 reach values greater than 100%, while the error in CO reaches a maximum value of 25%. Due to the coupled nature of the reaction system, the errors in O flux also reach 100% at higher temperatures.

Using the steady-state approximation is analogous to assuming a continuous beam, in which the particles are continuously incident on the surface. In a pulsed beam, however, all the particles strike the surface in a very short period of time (20-100 μs). In the remaining time between pulses, in which the scattered product information is collected, there are no particles from the beam colliding with the surface as shown in Fig. 3.15 (a). Thus for a given overall incident flux, the continuous beam experiences a much smaller instantaneous flux spread uniformly throughout the time between pulses, while the pulsed beam has a much greater flux incident over a short amount of time (duration of the pulse). Fig 3.15 (b) presents the corresponding variation with time of the surface coverage values under both of these beams. The surface upon which the continuous beam is incident

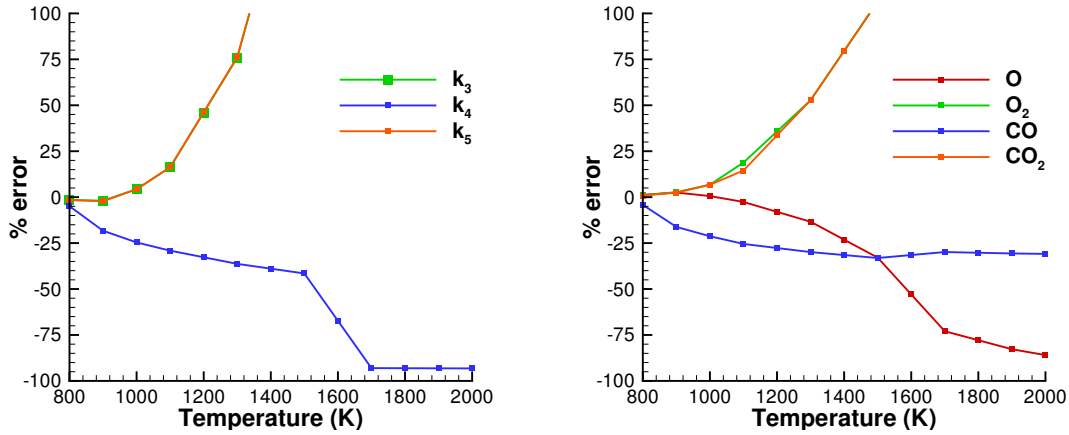

(a) (b)

Figure 3.14: (a) Percent error in rate constants derived using the steady-state approximation compared with the baseline values in Table 4.1 (b) Percent error in mole fractions obtained using the rate constants derived from steady-state approximation.

has a surface coverage value that is time invariant. However, within the pulsed beam setup, the surface experiences a sharp increase in the coverage as the pulse progresses. Once the pulse is completed, the surface coverage value drops gradually as the adsorbed particles slowly desorb from the surface. This difference in the time evolution of the surface coverage is the reason for the observed differences between the final product fluxes. Hence, analyzing the experimental data using the steady-state approximation will lead to over/under prediction of finite rate chemistry at the surface.

3.5.2 Proposed calibration methodology

In the previous section it was established that the steady-state approximation leads to significant errors in the predicted products fluxes and the transient nature of the pulsed beam must be considered. However, this is not straightforward since the rate constant information is not directly available, but must be determined from experimental product flux data. Here a general methodology to precisely compute the rate constants from pulsed molecular beam data is developed.

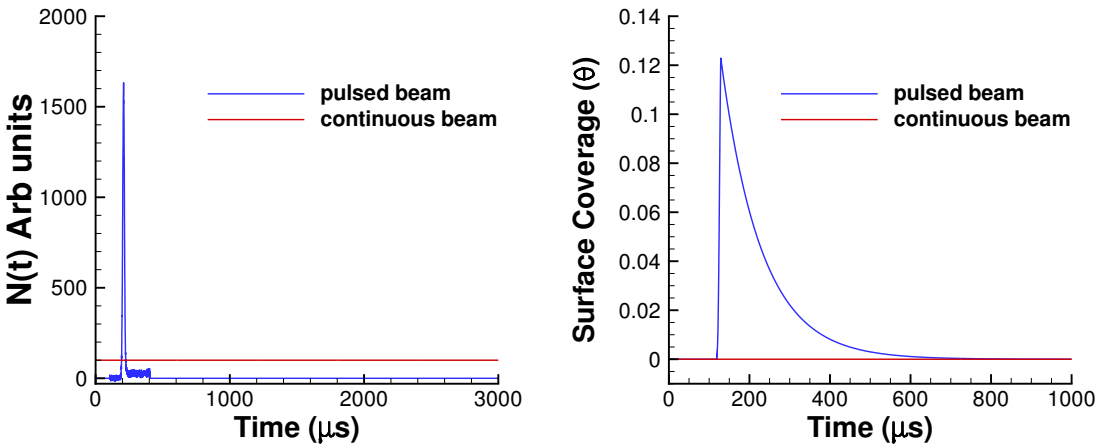

(a) (b)

Figure 3.15: (a) Number density of particles incident on the surface and (b) surface coverage (θ) of adsorbed atoms as a function of time for a continuous and a pulsed beam.

At a given temperature, the rate constant of a reaction is simply a constant value. The instantaneous rate (or probability in DSMC) is then determined solely by these rate constant values and the current surface conditions. Thus, for each temperature, the problem breaks down to finding the value of these constants for each reaction mechanism for which the final product compositions reproduce the experimentally observed values. In order to construct this calibration problem, the initial values are prescribed for each rate constant, and the complete beam simulations are carried out in DSMC to obtain the final product composition formed via each reaction mechanism. The error is then defined as the difference between the resulting composition and the experimental composition. The goal of the calibration procedure is to minimize this error by calibrating the reaction rate constant values. This process is then repeated at each temperature to obtain the reaction rate constants, which can then be fitted to any form (preferably Arrhenius). A major advantage of such an approach is that no assumption is made about the surface coverage; rather, it is obtained as a result of this calibration procedure. This is of particular importance since the experimental determination of surface coverage is challenging, and it is also expected to widely vary over

a range of temperatures. However, this procedure does require as an input the maximum available adsorption sites per unit area of the surface material.

Since the objective function to be minimized (*i.e.,* the error between the DSMC and experimental product composition) cannot be explicitly expressed in a functional form, heuristic or meta-heuristic algorithms like the particle swarm optimization algorithm [393, 394] is ideally suited for this calibration problem. In addition, this algorithm can search over very large multi-dimensional spaces of candidate solutions, which is required for this calibration process. Furthermore, the particle swarm algorithm is stochastic in nature and is shown to consistently converge to the global minimum [395].

This methodology is applied to the sample system described in the previous section. Initial values are guessed for the three rate constants (k_1, k_2, and k_3). The product composition corresponding to these guess values are computed and compared with the baseline values (Fig. 3.13). Based on the error between these product fluxes, the guess values are updated. This process continues until the error between the two sets of product fluxes falls below the specified threshold. The rate constant obtained from this methodology is compared to the baseline rate constants (Table 4.1) and the errors are plotted in Fig. 3.16 (a). Excellent agreement is observed between the sets of rate constants and the maximum error is around 0.5%. The corresponding errors in the mole fractions are shown in Fig. 3.16 (b) and as expected the maximum errors are less than 0.3%.

3.6 Summary

A general approach for constructing finite rate surface chemistry models using pulsed hyperthermal beam experimental data has been presented, which is of great interest in a broad range of fields. First, detailed DSMC simulations of various reaction mechanisms for a wide range of conditions are performed to obtain the TOF and angular distributions. This step is crucial in understanding and interpreting the experimental data and isolating the effects of different mechanisms

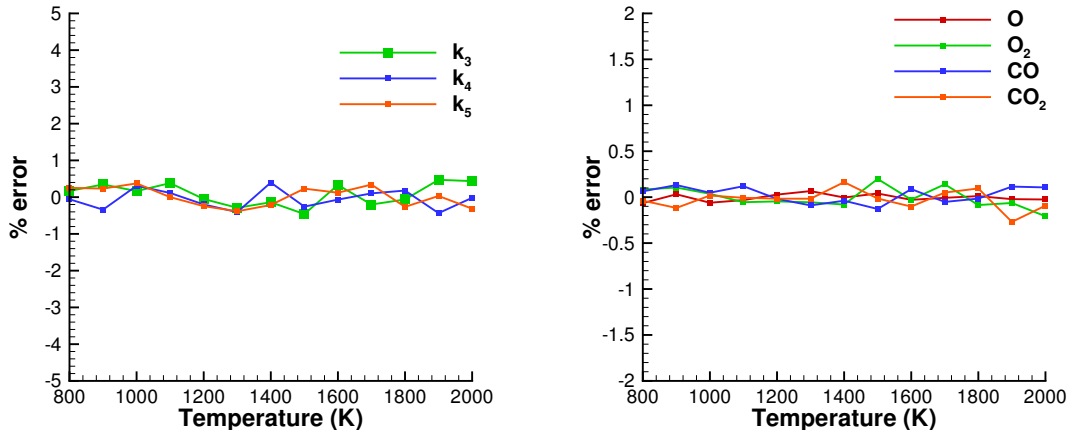

(a) (b)

Figure 3.16: (a) Percent error in rate constants derived using the calibration methodology and (b) Percent error in mole fractions obtained using the rate constants derived from the calibration methodology.

contained in the pulsed beam experimental data. The Langmuir-Hinshelwood mechanisms were categorized into four types based on the comparison of time scales for formation and desorption steps with the system time scale. The characteristics of each type of mechanism were analyzed in detail and a method to identify and distinguish between them using only the experimental TOF data is provided. A new procedure to accurately compute the total integrated flux of the products, specifically the slowly desorbing species from the TOF and angular distribution is described.

The final and most crucial step of this approach is the development of a general methodology to accurately derive the rate constants of the identified surface reaction mechanisms under transient (pulsed beam) conditions. An analysis of the commonly used steady-state approximation revealed significant differences in terms of both the rate constants and total product composition, specifically when the surface coverage at steady state is low. Modulation of the beam into short pulses inherently introduces a transient component which must be accounted for in order to reliably obtain the rates. Within the proposed methodology, the changing surface conditions are explicitly considered while computing the product fluxes.

The fitting procedure uses particle swarm optimization to systematically search through the rate constant parameter space in order to match the final product composition with the experimental values. In addition, the surface coverage of the different species is readily obtained as output and are consistent with the experimental product fluxes. This procedure is performed at each temperature, and the computed rate constant values can be expressed as a function of temperature in any desired form.

Chapter 4

Application to Vitreous Carbon

4.1 Overview

The novel approach described in the previous chapter is applied to construct a detailed surface chemistry model for oxidation of vitreous carbon. The applicability of the TOF decomposition procedure, total product flux computation, and transient rate calculation methodology is demonstrated by applying it to actual experimental data of Murray *et al.* [5].

Although the final objective of this effort is to simulate the oxidation and recession of FiberForm®, an appropriate gas-surface interaction model for the carbon surface (i.e., the individual fibers) is first established without the added complexity introduced by simulating the full FiberForm® microstructure. Vitreous carbon was chosen as the template for developing the surface reaction model, owing to the similarity of carbon and FiberForm® [5] in terms of their characteristic chemical structure and sp^2 bonding. Thus, the aim of this study is to establish an appropriate model for the oxidation of vitreous carbon guided by surface scattering data from the recent molecular beam experiments [5].

The contents of this chapter are organized as follows: a brief description of the experimental setup and measured quantities, including the experimental TOF and angular distributions, as well as the product fluxes, is presented in Section 4.2. In Section 4.3 a detailed analysis of the experimental TOF data is presented, and the major reaction mechanisms at the vitreous carbon surface are identified. The procedure used to obtain the corresponding rate constants of the reaction mechanisms is outlined in Section 4.4. Finally, a comparison of the simulated

and experimental TOF and angular distributions and the total product fluxes is presented in Section 4.5, followed by the conclusions in Section 4.6.

4.2 Molecular beam experimental data

In this section, the TOF and angular distribution data obtained from experiments of Murray *et al.* [5] are presented, which are used to construct and validate the DSMC model. The details of the experiment and analysis of the scattered products have been discussed at length by Murray *et al.* [5]. Here, some key observations are described for completeness. A hyperthermal O/O_2 beam with a nominal velocity of 7760 ms^{-1}, and a mole ratio of approximately 93% $O(^3P)$ ($\sim$5 eV) and 7% $O_2(^3\sum_g^-)$ ($\sim$10 eV), is directed at a vitreous carbon surface with an incidence angle (θ_i) of 45. The vitreous carbon sample employed in this experiment was Grade 22 SPI-Glas^{TM} vitreous carbon obtained from SPI, Inc. The sample had dimensions of 25 mm $\times$ 7 mm $\times$ 1 mm, and was prepared with a mixture of trichloroethylene and ethanol prior to the experiments. The surface temperature of the sample was controlled by resistively heating the material, and was determined by fitting the TOF data to a Maxwell-Boltzmann distribution characterized by the surface temperature. First, the number densities of the species are collected as functions of the flight time (TOF distribution) and scattering angle in the plane defined by the surface normal and the beam. The TOF distributions are then converted to energy distributions ($P(E_T)$), which may be integrated to obtain the angular flux distributions. It is noted that the scattered product distributions obtained in this study are specific to vitreous carbon. In this study, the TOF distributions were collected over the full range of final angles (θ_f) at 5 increments for surface temperatures of 800 and 1875 K only. At the intermediate temperatures, the TOF distributions are obtained at a single angle θ_f of 45.

A total of four chemical species are detected as scattered products, including O and O_2, which are supplied by the beam, and CO and CO_2, which are formed at

the surface. Representative TOF distributions for O and CO at two temperatures (800 K and 1875 K) are shown in Figs. 8, 11 and 12 of Murray *et al.* [5]. The O and O_2 TOF distributions have a peak at very short times corresponding to impulsively scattered (IS) products. The interaction time of the IS products with the surface is very brief, such that this population does not achieve thermal equilibrium with the surface. These products scatter with energies slightly below that of the incident beam energy, and show up at early times in the TOF distribution.

A second population of scattered products is observed at later times in the TOF distributions, corresponding (for example) to the second peak in the O and first peak in the CO TOF distributions in Figs. 8, 11 and 12 of Murray *et al.* [5]. A considerable amount of information may be gained from analysis of these products; a brief introduction is provided here, followed by a more detailed discussion in Section 4.3. First, it is noted that these products can be fit to a Maxwell-Boltzmann (MB) distribution based on the surface temperature, and include O, CO and CO_2 products. This implies that these products are formed via thermal mechanisms and are completely accommodated to the surface temperature. Second, these products may desorb from the surface in a number of different ways. Products that desorb immediately after the beam pulse (at t=0 ms) and that follow a MB distribution are referred to as thermally desorbed (TD) products; again, these include O, CO, and CO_2, and make up the majority of the detected TOF distribution following the IS products. Products may also desorb from the surface at later times, resulting in a distribution component that is not captured by a TD description. For example, if the surface reaction products are formed by a relatively slow process whose rate is governed by the surface temperature, then the products will desorb from the surface based on the decay rate equation of the formation reaction since the beam is the only source of oxygen on the surface. In this case, the final observed TOF will be a convolution of the MB distribution and the specific decay rate equation (exponential for a 1^{st} order reaction, linear inverse for a 2^{nd} order reaction, etc.). As will be discussed in Section 4.3, this behavior is observed for O and CO products, which make up the majority of the

long tail in the detected TOF distribution. Lastly, these products may desorb over an energy barrier, which is evident in the shape of the scattered product angular distributions (Figs. 8 and 11 of Murray *et al.* [5]). Angular distributions of products that thermally desorb in the absence of an energy barrier follow a cosine distribution. The angular distributions of O, CO and CO_2 are observed to follow a cosine power law distribution, which is characteristic of a desorption barrier. As a final remark, the scattering characteristics of O_2, which constitutes only 7% of the beam by mole fraction are nearly identical to that of the IS O atoms [5]. Furthermore, it is apparent that the TOF distributions and total flux of O_2 were observed to be constant across the entire temperature range. Considering that there is only 7% O_2 in the beam and that O_2 has a low sticking coefficient on the surface, it was assumed that the contribution to the CO and CO_2 signal from O_2 reactions is minimal.

The temperature dependence of the CO flux also exhibits a hysteresis, whose magnitude is dependent upon the rate of change of temperature (Fig. 4 of Murray *et al.* [5]). The model introduced by Poovathingal *et al.* [33] was constructed from the data corresponding to a rapid change in temperature (red data points in Fig. 4(c) of Murray *et al.* [5]), with the idea that this would better represent the surface conditions in a hypersonic flow environment. The current work, on the other hand, employs data obtained from a slow surface temperature variation (blue data points in Fig. 4(c) of Murray *et al.* [5]), which are more appropriate for the steady state conditions targeted in this work.

4.3 Analysis of Experimental Data

4.3.1 Missing flux

Products that desorb very slowly from the surface over long periods of time would be difficult to detect since their signal cannot be distinguished from the background noise, especially at a mass-to-charge ratio m/z=28 (CO^+). The fraction

of slowly desorbing products that are not detected becomes especially significant at low temperatures, since the rate of desorption is reduced with decreasing temperature. In addition, the experimental sampling window within which the TOF data are collected extends 10 ms from the beginning of the beam pulse (t=0 ms), and the time between beam pulses is 500 ms. Thus, some of the scattered products that desorb very slowly from the surface are not captured within this sampling window, particularly at low temperatures. This is evident, for example, in the long tail of CO products at 800 K extending from t=1.0 ms in Fig. 12 of Murray *et al.* [5].

Fig. 4.1 shows the total oxygen/oxide product flux measured by the experiments over the 10 ms sampling window as a function of surface temperature. If all products are desorbed from the surface and detected within this window, the total flux should be constant, since the same beam setup was used to perform the experiments over this range of temperatures. At temperatures above T=1700 K, the total flux reaches an asymptote, indicating that the entire incident beam flux is captured within the experimental sampling window, owing to sufficiently rapid desorption. At temperatures below T=1700 K, up to half of the oxygen/oxide product flux is "missing", or is not detected within this sampling window. Assuming that this high-temperature asymptote in the detected total oxygen flux is equal to the total incident beam flux (i.e., the incident flux is reflected/desorbed and thus detected within 10 ms), the value of the "missing" oxygen flux at low temperatures may be determined. This additional mass balance analysis is one of several features that distinguishes the current model from the previous PSMM model, which equated the incident beam flux to the IS and TD product fluxes only.

4.3.2 Surface Coverage

An important parameter that affects the rate of surface reactions is the oxygen atom coverage. Although surface coverage is not explicitly measured during the

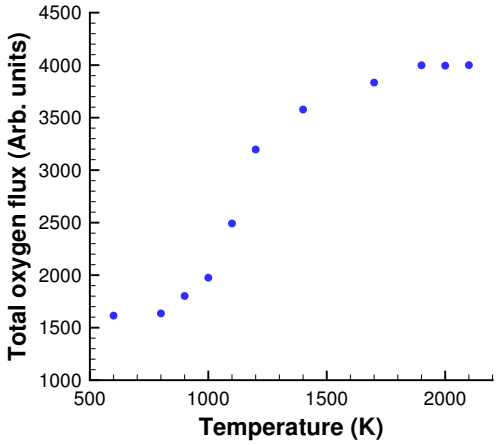

Figure 4.1: Total relative oxygen/oxide product flux (O + CO + 2*O_2 + 2*CO_2) based on analysis of the experimental data as a function of temperature.

experiments, the qualitative behavior of surface coverage as a function of temperature can be inferred from other experimentally measured quantities.

The CO and CO_2 product fluxes in Fig. 4 (c) and Fig. 4 (d) of Murray *et al.* [5] exhibit strong temperature dependencies. The CO_2 flux is substantial at the lowest temperature, but it decreases rapidly with increasing temperature and falls below detectable limits above 1000 K. Based on the theoretical study by Sun *et al.*, it is believed that the reduction in CO_2 flux is the result of decreasing surface coverage. Sun *et al.* showed that additional adsorbed oxygen atoms are necessary in order for the formation of CO_2 to be kinetically and thermodynamically favored. The formation of CO_2 must be an activated process; thus, following from the study by Sun *et al.*, the constant decrease in CO_2 production with surface temperature implies a competition between loss of adsorbed oxygen and reaction to form CO_2. This competition is especially pronounced because of the low flux of the incident O-atom beam. In a similar way, Sun *et al.* also showed that the formation of CO is promoted by adsorbed O atoms, so an analogous competition is also occurring in the formation of CO, leading to an apparent rise and fall of the CO product flux as the surface temperature is increased. The reactions that lead to CO_2 are more sensitive to surface O-atom coverage, because more O atoms are required to form the product. Therefore, the CO_2 flux is expected to drop quickly

with temperature as the probability of O atom desorption increases. Indeed, the observed temperature dependencies of the CO and CO_2 product fluxes is consistent with the rapid rise in the flux of desorbed O atoms with temperature, as seen in Fig. 4 (a) of Murray *et al.* [5]).

With this set of observations and the evidence regarding surface coverage, the consistency of the inferred surface coverage with the other observed experimental quantities is considered, starting with scattered O atoms. Fig. 4.2 shows the temperature variation of the IS and TD O atom flux. The TD flux increases with temperature, consistent with a decreasing surface coverage. The IS O atom flux is approximately constant across the temperature range. A high surface coverage at low temperatures would imply that relatively few sites are available for *direct* adsorption, assuming that the surface is Langmuirian, and the majority of incident atoms, unable to adsorb directly, would reflect as IS products. Thus for a Langmuirian surface, the IS O atom flux should exhibit a decrease with temperature, as more sites become available for direct adsorption with decreasing coverage. This is clearly not the case in the observed IS product flux (Fig. 4.2). There is, however, evidence that the oxygen adsorption on carbon follows an *indirect* adsorption pathway, in which the incident atom initially forms a precursor that moves freely along the surface, until it chemisorbs on a suitable site [396, 397, 398, 399]. The *indirect* adsorption pathway captures the (constant) IS atom flux as a function of temperature observed experimentally, and is modeled using Kisliuk's formulation for which the sticking coefficient remains constant with surface coverage. It is important to note that the other finite rate models discussed in Section 1.2.1 use a direct adsorption pathway. This indirect adsorption pathway is consistent with the observed variation of TD products with surface coverage, and is also consistent with an IS O atom flux that is independent of surface coverage. It is also noted that the assumption regarding surface coverage is consistent with the observed hysteresis of the CO flux, which is discussed in G.

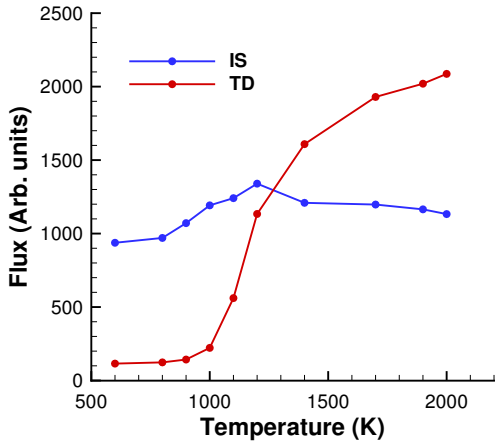

Figure 4.2: Variation of IS and TD fluxes of O (based on analysis of experimental data from Murray *et al.* [5]) measured at $\theta_f = 45$ scattered from a vitreous carbon surface following bombardment with the O/O_2 beam at $\theta_i = 45$.

4.3.3 Surface Reaction Mechanisms

The mechanisms considered in the present surface interaction model include adsorption, desorption and Langmuir-Hinshelwood (LH) mechanisms. Identification of these mechanisms is based on careful analysis from both the TOF and angular distribution data of the detected products, as well as a mass balance analysis to account for long-desorption time products that are not detected in the experiments at low temperatures. The surface reaction mechanisms elucidated from the features of the TOF distributions are presented in the sections below. These mechanisms, along with the mass balance analysis (to account for the "missing oxygen" flux), are used to construct the surface chemistry model.

4.3.3.1 Prompt thermal mechanisms

The TD products, which include O, CO, and CO_2 are observed at all temperatures, and are represented in the current model by a (prompt) LH1 reaction mechanism. There has been theoretical evidence suggesting that CO and CO_2 formation and desorption into the gas phase are promoted by neighboring adsorbed oxygen atoms [80]. The presence of these neighboring atoms stabilizes the

intermediates in the formation of these products, making the reactions thermodynamically favorable. Adsorbed oxygen is therefore included in the CO LH1 mechanism in this model. This results in a prompt CO reaction rate that is proportional to the concentration of the adsorbed oxygen on the surface. Evidence of this dependence was observed (in a separate experiment) as a time-dependent reduction in the TD component of the CO TOF distribution (Fig. H1 (d)). Details of this experiment are provided in H. Adsorbed oxygen is included in the prompt LH1 mechanism for CO_2. The corresponding prompt mechanisms (A4, A5, A6) are listed in Table 4.1.

4.3.3.2 Slow mechanisms

Both O and CO TOF distributions contain a long tail component at low and intermediate temperatures (Figs. 8 and 11 of Murray *et al.* [5]), which can be captured by a convolution of a MB distribution and a first order decay. These products are formed as a result of a relatively slow first-order reaction whose rate is governed by the surface temperature. The rate of formation and desorption of these products is relatively slow at low temperatures, and these products are detected at longer times in the TOF distributions. As the temperature increases, the formation/desorption become faster, and these products are detected at progressively earlier times in the TOF distributions. At high temperatures, these products desorb immediately, and the resulting TOF distribution of the detected products is captured by a MB distribution (based on the surface temperature) of particles desorbing from the surface at time t=0 ms. It is important to note that the slow O may have contributions from both surface processes correlated with the beam pulse and experimental artifact (slow effusion of O atoms from the source chamber after the beam pulse and subsequent non-reactive scattering from the surface), and so the slow O atom rate employed in this model is considered an *upper limit* of any slow chemical process. This slow component of O is represented by a simple desorption process (mechanism B1 in Table 4.1).

Next, the long tail of the CO TOF distributions is considered, guided by analysis of the detected products in the TOF distribution (up to 10 ms). The LH mechanism describing the slow CO products may be either formation-limited (LH2) or desorption limited (LH3). It is not possible to determine the type of LH mechanism from the CO TOF distribution alone. In this case, however, there is a parallel system of reactions in which both slow O(g) products and slow CO(g) products are formed from the same reactant, adsorbed oxygen O(s). If formation is the limiting step, then both the rate of slow O(g) and slow CO(g) are determined by the concentration of O(s). This will result in both products having the same decay rate (i.e., the decay rate of O(s)). If, on the other hand, the LH mechanism is desorption-limited, the rates of both products are driven by two different surface species desorption rates. In this case, O(s) dictates the decay rate of slow O(g), while the LH intermediate CO(s) will determine the decay rate of slow CO(g). From the TOF distributions, it is clearly observed that the decay rate of slow CO(g) is different from that of slow O(g). The formation of the CO(s) intermediate at the surface is fast, but the desorption is relatively slow compared to slow O(g), as evident in the decay rates (Fig. 11 of Murray *et al.* [5]). The slow CO(g) is thus modeled as a LH3 mechanism. Similar to TD CO, the formation reaction of slow CO also includes an adsorbed O atom which promotes the reaction, consistent with the findings of Sun *et al.* [80]. It is important to note that the LH intermediate need not be a CO molecule bound to the surface. Although this is possible, it is unlikely since CO is typically not strongly bound to the carbon surface [400, 401, 402]. It is more likely that the adsorbed O is present in the form of a functional group (lactone, semiquinone, etc.) on the surface and desorbs from the surface as CO [400, 396]. This is referred to as the incipient CO, and for ease of comprehension it is expressed in the reactions as CO(s). This slow CO mechanism is listed as CO{a} (A2, B2) in Table 4.1.

4.3.3.3 Very slow mechanisms

Although the long distribution tail in the CO TOF is well-captured by the slow CO{a} mechanism for times up to t=1.5 ms, it cannot account for the low-amplitude CO signal detected at much larger times (up to 10 ms). It is also noted that such a signal was not observed for the other products, and this low-amplitude CO signal presumably extends to significantly longer times. Recalling the opening discussion of this section, the total oxygen/oxide product flux measured by the experiments at temperatures below 1700 K indicates that up to half of the oxygen/oxide product flux is "missing", or is not detected in the experiments. In fact, Marchon *et al.* have shown indirect evidence for slow desorption of CO products from thermally programmed desorption experiments involving O_2 adsorption on graphite [403]. Yang and Wong [83, 86] have also shown direct evidence for slow removal of carbon from a graphite surface using transmission electron microscopy experiments. However, since the identity of the volatile products at lower temperatures cannot be determined, it is assumed that all of the missing O-atom flux is in the form of CO. This assumption allows for closure of the model through a mass balance analysis in which the incident beam flux is assumed to be equal to the sum of missing and detected oxygen/oxide flux. This assumption will be updated as more experimental data becomes available regarding the product distribution resulting from the slow removal of carbon. Thus, a second mechanism for slow CO products referred to as CO{b} is included in the model.

Under the assumptions of this model, the CO{b} products are also formed from reactions involving adsorbed oxygen O(s), through a LH3 mechanism. Following the discussion in Section 4.3.3.2, this implies that the CO{b} intermediate is a different chemical species than the CO{a} intermediate, both of which have their own distinct desorption times. The formation reaction of CO{b} again consists of an adsorbed O atom similar to TD CO and CO{a}. It is noted that the oxygen present at the surface as the CO{b} intermediate is also available to promote

other reactions until it desorbs. The combination of the LH3 CO{a} mechanism (up to t=1.5 ms) and the LH3 CO{b} mechanism (much longer times) properly captures the long distribution tail in the observed CO TOF (up to t=10 ms) in a way that is consistent with the mass balance constraint necessary for model closure. The corresponding set of mechanisms for the formation and desorption of CO{b} (A3, B3) are listed in Table 4.1.

4.3.3.4 Non-thermal mechanisms

Both CO and CO_2 contain a small non-thermal (or super-thermal) component in the respective TOF distributions. These non-thermal products represent a population of particles that leave the surface faster than the TD products (including an energy barrier) immediately following the beam pulse. The in-plane angular distributions of the non-thermal components are well described by a cosine power law distribution, and are indicative of a thermal process. Thus, the non-thermal component for both CO and CO_2 is modeled as a small portion of the prompt LH1 mechanism (A5, A6 in Table 4.1).

In the O TOF distribution, a small non-thermal component is also observed which lies in between the IS and TD populations; that is, the non-thermal component is slower than the IS products but faster than the TD products. Similar to the case of CO and CO_2, this non-thermal component could be formed from a thermal process. However, since some of the oxygen from the beam is scattered non-reactively, this non-thermal component could also be a result of multiple bounces on the atomically rough surface [291, 404]. This component is modeled as a small portion of both the IS and prompt LH1 mechanism (A4 in Table 4.1).

4.3.3.5 Final set of reaction mechanisms

Table 4.1 summarizes the nine major reaction mechanisms that are elucidated from the experimental TOF distributions. The reaction mechanisms include adsorption of O, LH3 formation of CO{a} and CO{b}; LH1 formation of O, CO,

and CO_2; desorption of O, and LH3 desorption of CO{a} and CO{b}. The first six reactions are gas-surface reactions, which involve the atoms from the incident beam pulse as reactants. The last three reactions are pure surface reactions, independent of the beam pulse. It is important to note that reactions A1, A4, and B1 are common with the PSMM model [33], however the rates are different between the models (discussed in the next section).

The LH1 or prompt LH mechanisms are responsible for the observed TD products in O, CO, and CO_2. In addition, a small component of these products has super thermal energies and corresponds to non-thermal products in the TOF distributions. The LH1 formation of CO and CO_2 involve additional adsorbed atoms, denoted by O′(ads). The adsorption/desorption and LH3 mechanisms are responsible for the slow products observed in the TOF distributions of O and CO. These products are formed immediately after they strike the surface (adsorption and LH3 formation), followed by delayed desorption of these species. Thus these products are represented as a two-step process: adsorption/LH3 formation and desorption/LH3 desorption. The two types of CO that are formed through LH3 mechanisms are indicated as CO{a} and CO{b}, and the CO{b} comprises the missing flux in the TOF distributions at lower temperatures.

As a final remark, it is noted that the LH1 mechanism may be clearly identified in the TOF distributions. Although the LH2 and LH3 mechanisms can be reasonably inferred from the experimental observations, the exact form of the mechanism is almost impossible to obtain. Further, these reactions may involve multiple elementary sub-steps. Since the focus of this work is to develop a macro/mesoscale surface chemistry model for carbon surface oxidation, the simplest mechanisms that can reasonably capture the experimental observations are selected for the model.

Table 4.1: Set of reactions modeled in DSMC for O/O_2 hyperthermal beam

Gas-surface (GS) reactions		Pure-surface (PS) reactions	
A1. LH3 O{a} formation	$O(g) + (s) \longrightarrow O\{a\}(s)$	B1. LH3 O{a} desorption	$O\{a\}(s) \longrightarrow O(g) + (s)$
A2. LH3 CO{a} formation	$O(g) + (s) + C(b) + O'(s) \longrightarrow CO\{a\}(s) + O'(s)$	B2. LH3 CO{a} desorption	$CO\{a\}(s) \longrightarrow CO(g) + (s)$
A3. LH3 CO{b} formation	$O(g) + (s) + C(b) + O'(s) \longrightarrow CO\{b\}(s) + O'(s)$	B3. LH3 CO{b} desorption	$CO\{b\}(s) \longrightarrow CO(g) + (s)$
A4. LH1 O formation	$O(g)(IS) + (s) \longrightarrow O(g)(TD) + (s)$		
A5. LH1 CO formation	$O(g) + C(b) + O'(s) \longrightarrow CO(g) + O'(s)$		
A6. LH1 CO_2 formation	$O(g) + (s) + O(s) + C(b) + 4O'(s) \longrightarrow CO_2(g) + 2(s) + 4O'(s)$		

4.4 Computing the finite rates

In this section, the reaction rates for all of the surface mechanisms described in the previous section are computed. There are three steps involved in this process:

1. Decomposition of the TOF distributions into contributions from each reaction mechanism.

2. Calculation of total product fluxes as a function of temperature from experimental data at the 45 angle.

3. Calculation of surface reaction rate constants constrained by experimental flux values.

4.4.1 Decomposition of TOF distributions

First, the long tail portion of the TOF distribution is fit since the other components rapidly decay and do not contribute to the fluxes measured at long times. Recall that the long tail is observed only for the O and CO products. The shapes of these distributions are described by a convolution of the MB distribution and a decay rate specified for each process. These mechanisms are first order and follow an exponential decay, and so the rate constants of the slow processes are obtained directly from the fitting. These are shown as the "slow" product curves in Fig. 4.3.

Next, the thermally desorbed (TD) part of the distribution is fit for O, CO, and CO_2 products. In the presence of a desorption energy barrier, the TD products

have angular distributions that follow a cosine power law dependence. In addition, the shape of the TD TOF component is shifted to the left (towards shorter times). The value of the energy barrier is obtained from the cosine power law fit of the angular distributions [187, 190]. From this the directional temperatures can be calculated and the final shape of the TD distribution (MB distribution at t=0 ms + energy barrier fit) can be obtained.

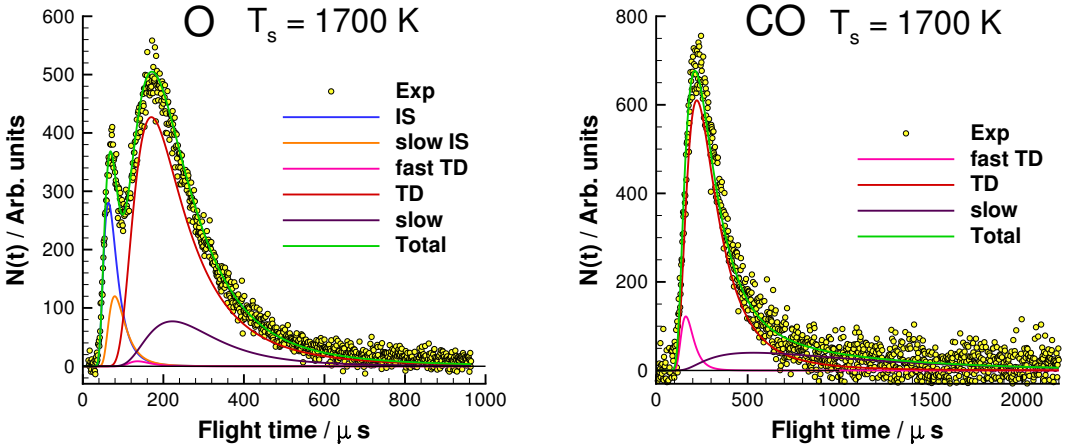

(a) (b)

Figure 4.3: Decomposition of the experimental [5] TOF distribution of (a) O and (b) CO at 1700 K into individual components, based on flux contributions from IS, slow IS, fast TD, TD, and slow processes.

For CO, the decomposition of the TOF distribution into TD and slowly desorbing components is straightforward, since the long-tail distribution remains distinct and can be easily isolated from the TD components for all temperatures examined. However, isolating the TD component in the O TOF distribution is complicated by the fact that at high temperatures, the desorption rate constants become high enough that the slowly desorbing, long-tail component of the distribution effectively merges with the TD component. It then becomes impossible to distinguish between the TD and slow processes for these high-temperature cases. At temperatures below 1700 K, however, the slowly desorbing component remains distinct from the TD flux, allowing for the characterization of both rate constants. The TD rate constants from the lower temperature ranges are fit to an appropriate

functional form and extended to the high temperature range. This information allows the product fluxes of the slow processes to be isolated across the entire temperature range. The TD + energy barrier components are shown as the "TD" product curves in Fig. 4.3.

The impulsively scattered portion of the distribution (for O products only) is captured next. The velocity distribution of the IS component is modeled as a weighted Gaussian distribution with a mean u_0 and a variance α (Eq. (3.1)) The value of α is adjusted to match the width of the IS distribution. A single value was found to be sufficient to capture the IS part of the O TOF data (*i.e.,* α is a constant and does not depend on temperature or the final angle at which the TOF was collected). The value of u_0 is determined using the soft-sphere scattering model [312, 387]. The inelastic scattering of the hyperthermal beam particles at the surface corresponds to the structural regime [273], in which the atomistic structure of the surface becomes important. This model contains two free parameters: the effective surface mass m_s, and the internal excitation fraction E_{int}/E_i (Eq. (2.51)).Due to the high incident energy of the O atoms, the thermal vibrations of the surface have little effect on the energy transfer during the collision. Consequently, these parameters exhibit little or no variation with temperature. The IS component is shown as the "IS" product curve in Fig. 4.3 (a).

Finally, the non-thermal part of the TOF distribution is analyzed. The non-thermal component appears between the IS and the TD peaks and is classified as either "slow IS"or "fast TD" products. It is noted that these products represent a relatively small portion of the total observed product flux. These products are considered to be a result of: (i) products formed via thermal mechanisms, but desorbing with super-thermal energies as a result of local hot-spots [373], or transfer of bond energy of the intermediates [384]; (ii) impulsively scattered particles that lose a large fraction of energy due to multiple collisions with the surface [291].

As discussed previously, the non-thermal component for CO and CO_2 is expected to be a result of a thermal mechanism (LH1) having a super-thermal

component (termed as "fast TD"), since the angular distributions follow a cosine power law distribution. It is noted that the fast TD products have characteristics similar to the products desorbing over an energy barrier, and are identified as the high energy population of the products not captured by the energy barrier fit.

The same functional form as that of the IS distribution (Eq. (3.1)) is used to fit the fast TD component. However, both the α and u_0 parameters were obtained directly by fitting the TOF distribution, without using the soft-sphere scattering model (since these products do not correspond to the structural regime). Once again, it is found that a single value of α was able to capture the width of the distribution for the entire range of temperatures and final angles. On the other hand, u_0 was found to be a constant with final angle, but exhibited a variation with the temperature which was captured by a linear fit with two parameters. The fast TD flux was found to be a constant fraction of the TD flux across the temperature range, thus supporting the hypothesis that the non-thermal population is a super-thermal subset of the prompt LH1 mechanism.

The non-thermal components of the O TOF distribution consist of both "slow IS" and "fast TD". Again the functional form of the IS distribution (Eq. (3.1)) is used to fit the non-thermal components. The slow IS components are first identified as the low energy tail population in the first peak of the O TOF distribution that is not captured by the IS fit. The fast TD products are again identified as the high energy population not captured by the TD + energy barrier fit. For both the slow IS and fast TD, the parameter α is again found to be constant and u_0 exhibits a linear variation with temperature, consistent with the result for CO fast TD products. The resulting decomposition of the angular distributions for O at 800 K is shown in Fig. 4.4. The IS flux follows a lobular distribution highly peaked at an angle greater than the specular angle. The angular distribution of both slow IS and fast TD products is that of a cosine power law distribution. This is expected for the fast TD products since they are a subset of a thermal mechanism. However, this is also reasonable for the slow IS products because, although the roughness of the surface and multiple bounces might not lead to

complete energy accommodation, it can result in randomization of the reflected particle angle toward a cosine distribution. This is the case of partial energy accommodation with diffuse scattering described by Lord [301]. Fig. 4.3 shows the full decomposition of the experimental TOF distribution of O at 1700 K into IS, slow IS, fast TD, TD (with desorption barrier), and slow processes.

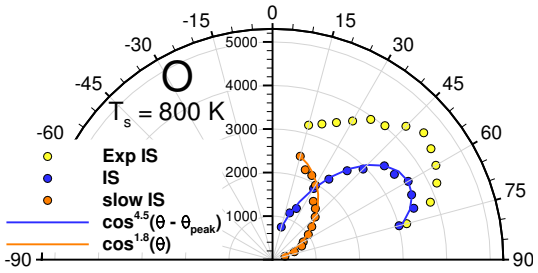

Figure 4.4: Decomposition of the experimental IS angular distribution into IS and slow IS. The IS distribution follows a lobular distribution with a peak at an angle higher than the specular angle, and is fit well by cosine power decay about the peak. The slow IS distribution can be represented by a cosine power law with maximum along the surface normal.

4.4.2 Obtaining total product fluxes

The TOF and flux data derived from the molecular beam experiments are limited to the plane defined by the beam and the surface normal, thus out-of-plane scattering information is not available. However, the total flux of products scattered from the surface *in all directions* is required for the calculation of the surface reaction rate constants. The angular distributions from $15° < \theta_f < 75°$ obtained in-plane are available at 800 and 1875 K [5], while at the intermediate temperatures, the data is available only at θ_f=45. A procedure similar to that of Poovathingal *et al.* [33] is adopted, in which the experimental data at θ_f=45 is used to scale the angular distributions for the intermediate temperatures, and out-of-plane scattering is approximated using an appropriate azimuthal scattering dependence.

Briefly, the in-plane angular distributions of products at intermediate tempera-

tures are approximated based on the measurements obtained at 800 and 1875 K. All the products except IS (slow IS, fast TD, TD, and slow) exhibit a cosine power law distribution, which was used to obtain the value of the desorption barrier [190]. The resulting desorption barrier exhibits a small temperature dependence which was linearly fit over the intermediate temperatures. The angular distributions of the IS, non-thermal (slow IS and fast TD), TD, and slow particles are considered separately for fits over the intermediate temperatures, to ensure that the temperature-dependent behavior of each class of products is captured. This is in contrast to Poovathingal *et al.* [33], in which the complete angular distribution (with contributions from all products) was used for a temperature-piece-wise representation of the angular distribution at intermediate temperatures; the complete angular distribution at 800 K was used up to 1100 K, and the distribution at 1875 K was used above 1100 K.

We next consider the treatment of the out-of-plane scattering, since this information is not available from the experiments. The thermal products are known to be distributed uniformly and do not exhibit an azimuthal angular dependence. However, it is expected that the flux of IS O atoms varies significantly with the azimuthal angle. In the PSMM model, a uniform azimuthal distribution was assumed for the IS O atoms. In the current work, a cosine power law decay is used to approximate the out-of-plane scattering distribution following Glatzer *et al.* [255]. The normalized angular distributions for each of the reactively scattered products at the low and high temperatures are computed and presented in Table 4.2. This information can then be used along with the data at a 45 final angle to determine the total flux of each of the products at the intermediate temperatures. It is noted that similar out-of-pane angular distributions were used in the work of Poovathingal *et al.* [33] for the reactively scattered products.

The total fluxes of each of the different species cannot still be directly compared to each other owing to the mass sensitivity of the detector. Larger molecules generate a higher intensity signal, thus a scaling factor must be used in order to make consistent comparisons. Finally, the mass balance analysis is employed for

Table 4.2: Expressions for the normalized angular distributions of scattered products.

Species	600-1000 K	1100-2000 K
IS O	8.2752 $\times 10^{-4}\cos^{4.5}(\theta - \theta_{peak})$	8.2752 $\times 10^{-4}\cos^{4.5}(\theta - \theta_{peak})$
slow IS O	6.3465 $\times 10^{-4}\cos^{1.8}(\theta)$	6.1945 $\times 10^{-4}\cos^{1.746}(\theta)$
fast TD O	4.9584 $\times 10^{-4}\cos^{1.555}(\theta)$	4.7799 $\times 10^{-4}\cos^{1.463}(\theta)$
TD O	4.9584 $\times 10^{-4}\cos^{1.555}(\theta)$	4.7799 $\times 10^{-4}\cos^{1.463}(\theta)$
LH3 O{a}	4.9584 $\times 10^{-4}\cos^{1.555}(\theta)$	4.7799 $\times 10^{-4}\cos^{1.463}(\theta)$
fast TD CO	5.1661 $\times 10^{-4}\cos^{1.662}(\theta)$	5.1428 $\times 10^{-4}\cos^{1.65}(\theta)$
TD CO	5.1661 $\times 10^{-4}\cos^{1.662}(\theta)$	5.1428 $\times 10^{-4}\cos^{1.65}(\theta)$
LH3 CO{a}	5.1661 $\times 10^{-4}\cos^{1.662}(\theta)$	5.1428 $\times 10^{-4}\cos^{1.65}(\theta)$
TD CO_2	4.8206 $\times 10^{-4}\cos^{1.484}(\theta)$	-

the missing oxygen flux. The flux of oxygen/oxide products that desorb slowly can be obtained by using the following steady-state equation:

$$N_{\mathrm{O,beam}} = N_{\mathrm{O-IS,NT,TD,slow}} + N_{\mathrm{CO,CO\{a\}-NT,TD,slow}} + 2 \times N_{\mathrm{CO_2-NT,TD}} + N_{\mathrm{missing}} \quad (4.1)$$

Using this equation, it is assumed that at steady state, the surface conditions do not change and the incoming flux from the incident beam is equal to the outgoing flux. With this assumption, the value of N_{missing} can be calculated, which includes all oxygen/oxide products not captured by the experimental TOF distributions and includes the possibility for contributions to the long-tail from beyond the 10 ms sampling window. The value of $N_{\mathrm{O,beam}}$ is first determined using the total product fluxes (the asymptotic value discussed earlier in Section 4.3) at the highest temperatures. Substituting $N_{\mathrm{missing}} = 0$, the value of $N_{\mathrm{O,beam}}$ is computed. N_{missing} was found to be significant especially at very low temperatures, where it constituted up to 60-75% of the total flux.

The total relative fluxes obtained from the scaling of the 45 in-plane data, using the current interpretation of the experimental data as described in Section 4.3 and Section 4.4.1, are shown in Fig. 4.5. It is noted that the CO_2 relative flux is very small compared to the experimental CO_2 flux shown in Fig. 4 (d) of Murray *et al.* [5]. This difference is the result of two factors. First, the detection

efficiency of the mass spectrometer is biased by the mass of the detected particle as mentioned previously. In this case, the apparent flux of CO_2 is larger than the actual flux. Secondly, the relative flux is further reduced by the inclusion of the missing flux.

In what follows, these derived experimental data are referred to as analyzed experimental data. Comparisons of this model with the analyzed experimental results, and with the PSMM, Park, ZA and Alba models are presented in Section 4.5.1 and Section 4.5.2 respectively.

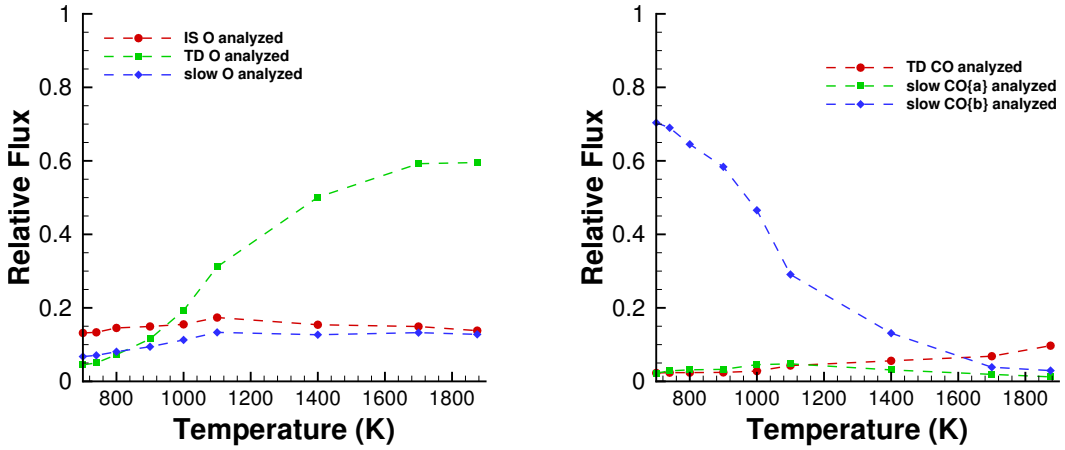

(a)

(b)

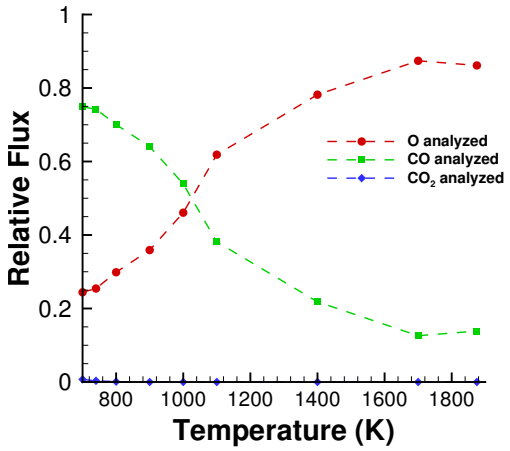

(c)

Figure 4.5: Mole fractions of surface interaction products as obtained from analysis of experimental data for (a) different types of O, (b) different types of CO, and (c) total flux of O, CO and CO_2. The CO_2 relative flux in (c) is very small compared to both O and CO.

4.4.3 Computing the reaction rate constants

As stated previously, the rate constants of O desorption and CO{a} LH3 desorption can be directly determined from the fits to the long-tail distributions in the TOF data. These values are obtained at each temperature and then fitted to an appropriate form as a function of temperature. The method for determining surface temperature is discussed in detail in Murray *et al.* [5]. For CO{a}, the rate constants are described using a simple Arrhenius form. The rate constants of O desorption are fit to the following expression obtained from transition state theory (TST) [405] as proposed by Zhluktov and Abe [36]:

$$k_{des,O} = A_{des} T_s^2 \, exp\left(-\frac{E_{des}}{RT_s}\right). \tag{4.2}$$

The desorption rate of CO{b} cannot be determined in this manner since it is not captured in the experimental TOF distributions. However, the total flux of CO{b} is known (N_{missing}). During steady state, at time t=0, the surface contains some concentration of adsorbed CO{b} atoms (N_{steady}). During the beam pulse, the quantity of CO{b} formed is N_{missing} such that the concentration on the surface is now $N_{\text{steady}} + N_{\text{missing}}$. After the pulse ends, the particles slowly desorb over the next 0.5 s to finally reach a concentration of N_{steady} at the beginning of the next pulse. Thus, the value of the rate constant can be directly computed using the first-order rate equation.

$$\frac{N_{\text{steady}}}{N_{\text{missing}} + N_{\text{steady}}} = exp(-k_{des,CO\{b\}} * 0.5) \tag{4.3}$$

The value of N_{steady} at each temperature is consistent with the expected variation of surface coverage (Section 4.3.2) and admits Arrhenius forms for the reaction rate constants.

After obtaining the rates for the desorption reactions, the reaction rates of the prompt LH1 and LH3 formation reactions are calculated. The PSMM model obtained rates using a steady-state approximation for the surface conditions during

the beam pulse. Although the experimental measurements are obtained at steady state (in which the sample has been exposed to the beam for a long time prior to the data acquisition), the use of a pulsed beam nevertheless introduces a transient nature to the process. The local surface conditions change significantly *during* the pulse. For instance, each atom/molecule within a pulse will experience a different surface coverage depending on its temporal position within the pulse, and this value will continue to increase as the pulse progresses. After the pulse ends, the particles slowly desorb and the surface coverage steadily decreases until the beginning of the next pulse. However, in the steady-state analysis, each atom/molecule is assumed to experience identical surface conditions, which does not capture the variations within the pulse. The difference between pulsed beam and steady-state analysis was found to be as high as 30% for some conditions [187]. Hence, in order to determine the reaction rate constants, the pulsed nature of the beam needs to be taken into account. The methodology proposed by Swaminathan-Gopalan *et al.* [187, 190] is employed, which captures the transient nature of the beam to provide the accurate surface reaction rate constants. The final error associated with the fitting process was approximately 1%.

The sticking coefficient for adsorption was also treated as a fitting parameter and was allowed to vary freely (within physical limits of 0 and 1). The sticking coefficient converged to a value between 0.84 and 0.86 across the entire temperature range. Hence, a value of 0.85 (average) was used for the sticking coefficient. It is noted that the value of the sticking coefficient will have a strong dependence on the incident energy of the atoms/molecules. This value of 0.85 is applicable only at the incident energy of 5 eV at which the experiments were performed. The value of the sticking coefficient is expected to increase with decreasing beam energy, approaching unity for sufficiently low beam energies.

Consistent with previous works [36, 400, 33], the rate constant of LH3 O{a} formation is taken to be unity. All the other rate constants from the different

Table 4.3: Reaction rate constants in the new finite rate model.

Type	Mechanisms	Reaction	Rate constant (k)	Units
Adsorption	Adsorption	$O(g) + (s) \longrightarrow O(ads)$	$\frac{1}{\Phi} * \frac{1}{4}\sqrt{\frac{8k_bT_g}{\pi m}} * 0.85$	$m^3\ mol^{-1}\ s^{-1}$
Adsorption-mediated GS reactions	LH3 O{a} formation	$O(ads) \longrightarrow O\{a\}(s)$	1	s^{-1}
	LH3 CO{a} formation	$O(ads) + C(b) + O'(ads) \longrightarrow CO\{a\}(s) + O'(ads)$	$\frac{1}{\Phi} * 153.0\ exp(-\frac{4172.8}{T_s})$	$m^2\ mol^{-1}\ s^{-1}$
	LH3 CO{b} formation	$O(ads) + C(b) + O'(ads) \longrightarrow CO\{b\}(s) + O'(ads)$	$\frac{1}{\Phi} * 71.2\ exp(-\frac{1161.2}{T_s})$	$m^2\ mol^{-1}\ s^{-1}$
	LH1 O formation	$O(ads) \longrightarrow O(TD)(g) + (s)$	$20.9\ exp(-\frac{2449.3}{T_s})$	s^{-1}
	LH1 CO formation	$O(ads) + C(b) + O'(ads) \longrightarrow CO(g) + (s) + O'(ads)$	$\frac{1}{\Phi} * 1574.9\ exp(-\frac{6240.0}{T_s})$	$m^2\ mol^{-1}\ s^{-1}$
	LH1 CO_2 formation	$O(ads) + O(s) + C(b) + 4O'(ads) \longrightarrow CO_2(g) + 2(s) + 4O'(ads)$	$\frac{1}{\Phi^5} * 536.3\ exp(-\frac{655.6}{T_s})$	$m^{10}\ mol^{-1}\ s^{-1}$
PS reactions	LH3 O{a} desorption	$O\{a\}(s) \longrightarrow O(g) + (s)$	$0.05\ T^2\ exp\left(-\frac{3177.2}{T_s}\right)$	s^{-1}
	LH3 CO{a} desorption	$CO\{a\}(s) \longrightarrow CO(g) + (s)$	$4485.5\ exp\left(-\frac{1581.4}{T_s}\right)$	s^{-1}
	LH3 CO{b} desorption	$CO\{b\}(s) \longrightarrow CO(g) + (s)$	$1.2\ exp\left(-\frac{2251.6}{T_s}\right)$	s^{-1}

temperatures are fitted to a standard form of a gas-surface reaction [3]:

$$k_{LH} = A_{LH}\, exp\left(-\frac{E_{LH}}{RT_s}\right) \tag{4.4}$$

The final reaction mechanisms of the finite rate model and their rate constant expressions and values are summarized in Table 4.3. The reactions are generally classified as adsorption, adsorption-mediated, gas-surface (GS) or pure-surface (PS). The quantity Φ appearing in the expressions for the rate constants in Table 4.3 is the surface site density. A value of 3.5×10^{19} m^{-2} was used for the surface site density of carbon in this work [36, 406]. Since the fast TD and slow IS are subsets of TD and IS respectively, they are not considered as separate reactions, but rather included within TD and IS. An appropriate fraction of the products undergoing TD or IS reactions are scattered based on the identified energy distributions of the subset group (Section 4.4.1). Since all reaction mechanisms involve adsorption as a first step, the rates of these mechanisms are not affected by the incident velocity of the beam particles.

It is noted that the rate constants of all the reactions may be reasonably represented using an Arrhenius form. These rates can then be converted to reaction probabilities for use in DSMC. A complete description of the DSMC surface chemistry model implementation (including the conversion of rates to reaction prob-

abilities) can be found in Swaminathan-Gopalan *et al.* [188]. It is important to note that the adsorption probability does not imply that the particle that adsorbs on the surface will later desorb as O(g). This is because adsorption is treated as an initial step for several mechanisms (LH1, LH3, etc.) within the DSMC surface chemistry framework consistent with the physics. Thus, the adsorption probability represents the sum of probabilities of all the processes which involve adsorption as a first step (adsorption-mediated GS reactions), and is not only restricted to the probability of particles staying adsorbed and later desorbing from the surface in the same form. O(ads) is representative of all possible forms (functional groups) by which O can be adsorbed on the surface: O{a}, CO{a}, and CO{b}. When the particle adsorbs on the surface, the exact mechanism it undergoes is chosen from the list of possible pathways based on the reaction rates [188].

4.5 Results

4.5.1 Comparison with Experiment

Comparisons between the experimental TOF and angular distributions, and relative product fluxes analyzed from experimental data, with DSMC simulations using the finite rates in Table 4.3 and the energy barrier values obtained from angular distribution fits in Table 4.2 are shown in Figs. 4.6, 4.7, and 4.8. The DSMC TOF distributions are shown in Fig. 4.6 for O and CO products at (a) 800 K, (b) 1000 K, and (c) 1700 K, alongside the experimental TOF data.

The direct comparison of the DSMC TOF distributions with the experimental data requires a scaling factor, which has two components. The first component is for adjusting the total flux and is the ratio of the total incident flux of the experiments ($N_{\mathrm{O,beam}}$ computed in Section 4.4.2) and that used in DSMC. The second component is a result of the mass sensitivity of the detector as discussed in Section 4.4.2.

The current model shows excellent agreement with the experimental data. All

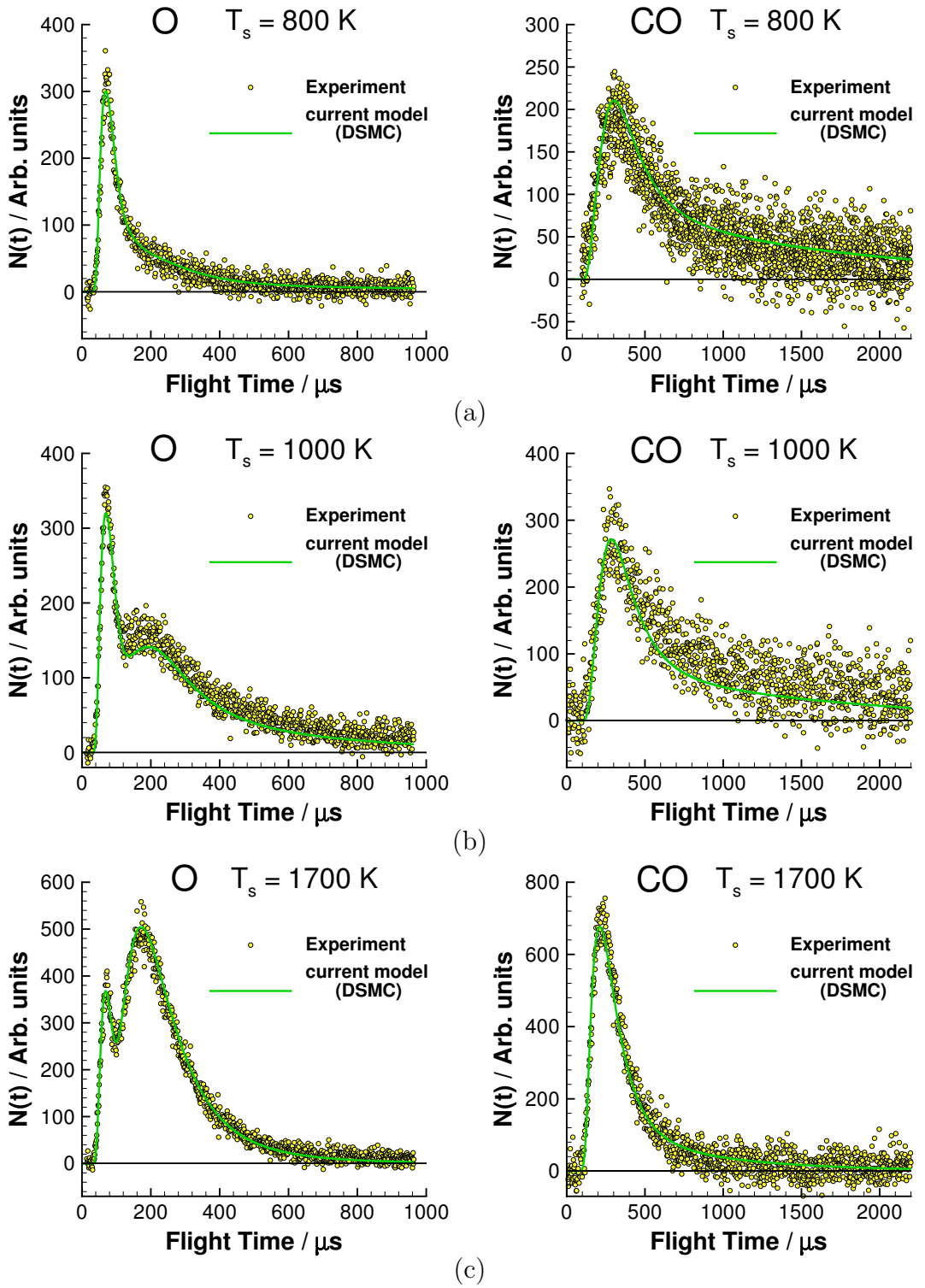

Figure 4.6: Comparison of TOF distributions at $\theta_f = 45$ of O (left) and CO (right) obtained from DSMC with the current finite rate model and the experiment [5] at (a) 800 K, (b) 1000 K, and (c) 1700 K following bombardment with the O/O_2 beam at $\theta_i = 45$.

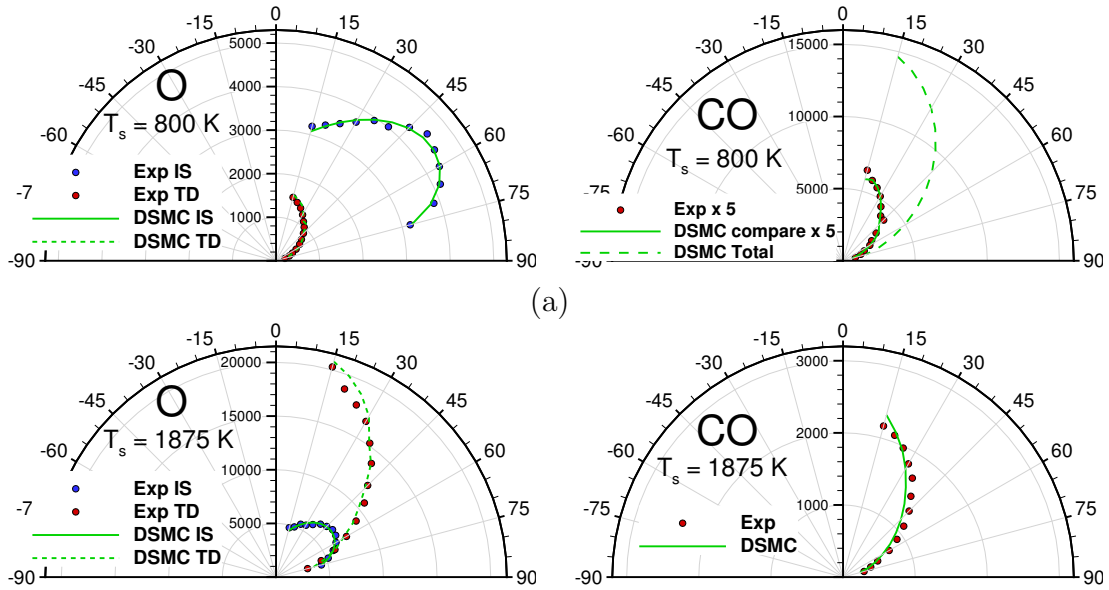

Figure 4.7: Comparison of angular distributions for O (left) and CO (right) obtained from DSMC with the current finite rate model and the experiment [5] at (a) 800 K and (b) 1875 K following bombardment with the O/O_2 beam at $\theta_i = 45$. For CO at 800 K (a, right), DSMC compare is the flux computed in DSMC corresponding to the detected experimental products. It is plotted for the purpose of direct comparison with the experimental data. Both the DSMC compare and experimental data are multiplied by a factor of 5 for sake of visibility. DSMC total is the total flux of CO computed in DSMC including the missing CO flux.

features in the TOF distributions are properly captured by the DSMC simulation with the current model. The observed improvement (c.f. Swaminathan-Gopalan [107]) in the current model over the simulation results obtained with the PSMM finite rate model for O is due to the modified rates, which capture both the TD and long-tail components of the TOF distributions. The new finite rate mechanism (B2 in Table 4.1) introduced in the current model captures the detected long tail in the CO TOF distribution, which is most prominent at 800 K (Fig. 4.6 (a) right). Although the current model includes the "missing" flux which accounts for a significant portion (60-75%) at lower temperatures, the computed TOF distributions overlap almost exactly with the experimental data. This is because the CO{b} signal is 2-3 orders of magnitude lower than the signals of the other types of CO. Although its magnitude is lower, the signal extends for the entire time range of 500 ms, while all the other signals decay to zero after 2-3 ms. Thus, the persistence of the signal rather than the magnitude is responsible for the large CO{b} flux. Hence the TOF distribution with and without missing CO{b} flux will essentially look identical.

Additionally, the angular distributions, which are incorporated using simple models and curve fits in the DSMC simulation, reproduce the appropriate behavior (Fig. 4.7), as expected. The angular distribution of the missing CO{b} flux could not be determined from the experiments. However, since it is produced through a thermal mechanism, the angular distribution of CO{b} is modeled as a cosine distribution with energy barrier assumed to be equal to the values of CO{a}.

Finally, the comparison between the experimental and DSMC product fluxes is shown in Fig. 4.8. The relative flux of scattered O and CO product components are plotted as a function of temperature in Fig. 4.8 (a,b). At low temperatures, IS O atoms are the most abundant (Fig. 4.8 (a)). It is noted that the IS component predicted by the model is nearly constant with temperature (in agreement with the analyzed experimental data), which is a consequence of the *indirect* adsorption pathway adopted in this model. The TD component is the most abundant product above 1000 K, which is a result of the increase in the rate constant with

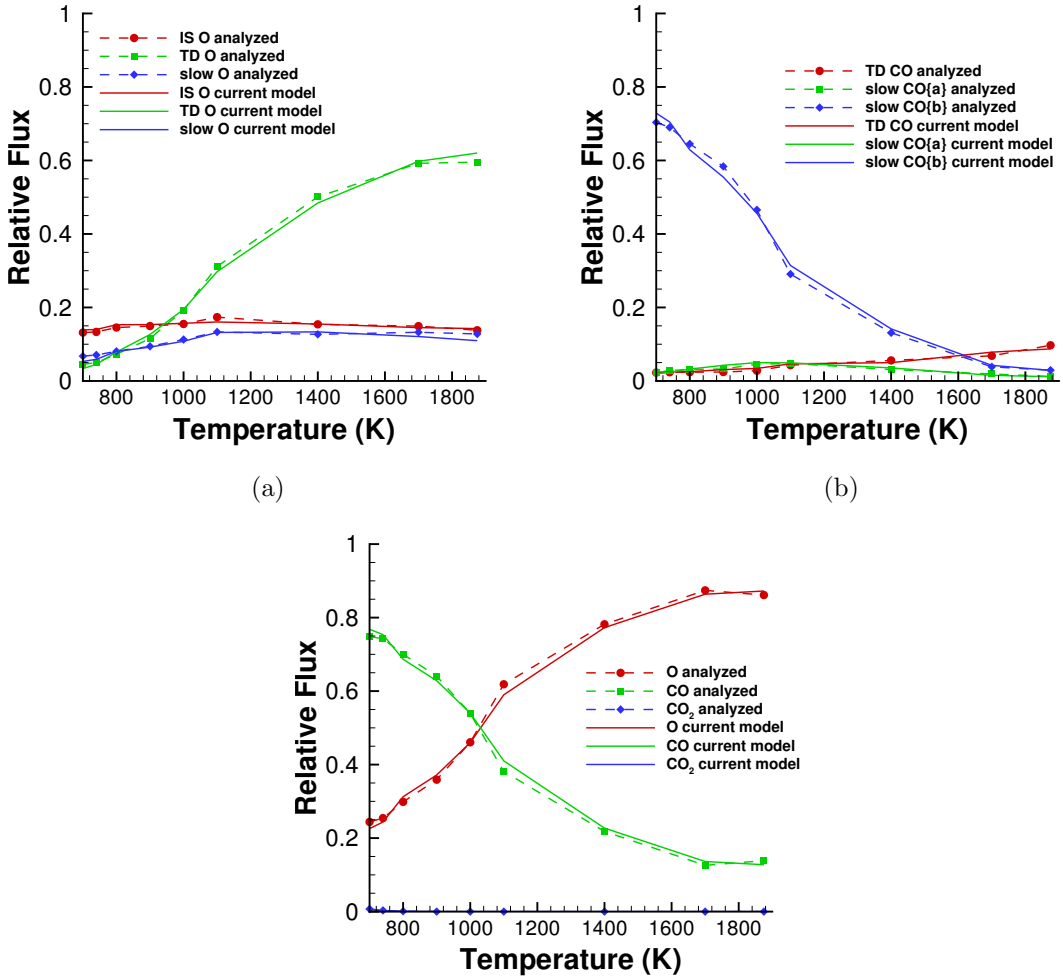

Figure 4.8: Comparison of mole fractions of surface interaction products between analyzed experimental data and DSMC (using the current finite rate model) for (a) different types of O, (b) different types of CO, and (c) total fluxes of O, CO, and CO_2.

temperature and a reduction in surface coverage. In Fig. 4.8 (b), slow CO{b} is the major reaction product from the surface interaction, accounting for up to 70% of the total CO produced at low temperatures. It is noted that in Fig. 4.7, the flux of the detected CO (which does not account for the "missing flux") is lower at 800 K compared to 1875 K. However, with the addition of the missing CO{b}, the total flux at 800 K is higher compared to 1875 K consistent with Fig. 4.8 (c). The flux of CO{b} steadily decreases with temperature, due to the reduction in surface coverage.

Fig. 4.8 (c) compares the total relative fluxes of O, CO and CO_2 as a function of temperature. The CO_2 relative flux is very small compared to both O and CO even at low temperatures where the surface coverage is high. It is noted that the trends in the O and CO relative fluxes are primarily driven by the behavior of the TD O and the slow CO{b} products as a function of temperature.

4.5.2 Comparison with Previous Carbon Oxidation Models

In this section, the current model is compared with previous carbon oxidation models available in the literature including PSMM [33], ZA [36], Alba [128], and Park model proposed by Chen and Milos [38]. Each of these models is implemented in DSMC and is used to simulate the hyperthermal molecular beam experiments according to the conditions outlined in Section 4.2, but with a pure O atom beam. In the ZA model, only the case of the immobile desorption mechanism is considered for O atom desorption. Multiple activation energies are also provided for different reactions within the original ZA model [36]. In such cases, the activation energies consistent with those of the Alba model [128] are used. Fig. 4.9 presents the mole fractions of the surface interaction products (O, O_2, CO, and CO_2) obtained from the DSMC simulations employing the previous models (PSMM, ZA, Alba, Park) and the current model.

For atomic oxygen (Fig. 4.9 (a)), the previous models predict relatively high mole fractions at low temperatures due primarily to impulsively scattered O

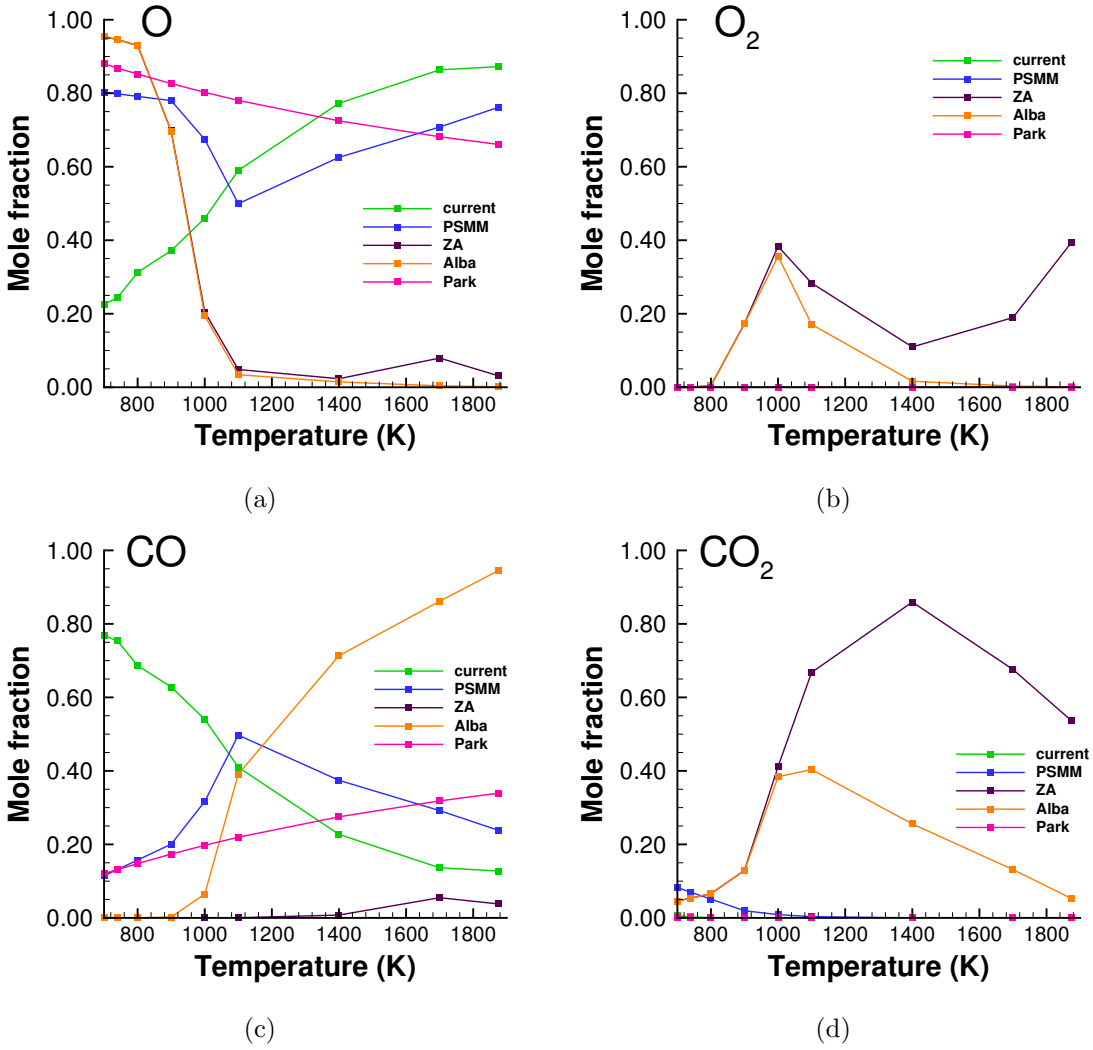

Figure 4.9: Comparison of mole fractions of surface interaction products between current model and PSMM, ZA, Alba and Park models for (a) O, (b) O_2, (c) CO, and (d) CO_2. All results are obtained using DSMC and correspond to the molecular beam experimental conditions (with effective beam pressure of 4.75×10^{-5} Pa).

atoms. This is a consequence of a *direct* adsorption pathway that is adopted by these models, where IS O atoms are the dominant scattered O product due to a high surface coverage. An *indirect* adsorption pathway in DSMC allows for the definition of a sticking coefficient in the model that is independent of surface coverage. In the ZA and Alba models, there is a sharp decline after 900 K and the flux becomes negligible after 1100 K. The Park model shows a monotonic decrease with temperature, but O continues to be the dominant product throughout the temperature range. The PSMM model shows an initial decline with temperature, but at 1100 K this trend is reversed and the mole fraction of O increases due to the increasing desorption rate of O. The current model shows a monotonic increase of O with temperature. It is noted that above 1100 K, only the PSMM and current model are able to capture the increase in mole fraction with temperature as indicated by the experimental data. The experimental data used in the PSMM model to compute the product fluxes were not corrected for the mass sensitivity of the detector (i.e., large molecules generate a higher intensity signal). The offset of the PSMM model prediction from the current model and experimental data above 1100 K is likely due, in part, to this mass sensitivity correction. Correcting for this would shift the O distribution upward, in closer agreement to the experimental data. The PSMM, Park, and the current model do not predict any formation of O_2 (Fig. 4.9 (b)), while mechanisms in the ZA and Alba models produce O_2 from the surface recombination of O.

Figure 4.9 (c) shows the variation of CO mole fraction with temperature. A number of important observations can be made from these comparisons. First, for temperatures below 1100 K, the CO mole fractions predicted by the current model differ significantly from those predicted by the PSMM model. This difference in the CO flux at low temperatures is attributed to the missing oxygen flux that has been accounted for by the formation and very slow desorption of CO{b} in the current model. Second, it is noted that the PSMM model prediction features a peak (or maximum) in the CO mole fraction versus temperature at 1100 K. This peak occurs as a result of a competition between CO formation and O desorption.

CO formation (which is an activated process) and subsequent desorption results in an initial increase in CO flux with temperature. As the temperature rises, surface coverage decreases, making fewer O atoms available on the surface to participate in CO formation, either to promote the reaction or to combine with carbon. This results in a decrease in CO flux at higher surface temperatures, and thus the CO reaction probability passes through a maximum. A number of previous experimental and theoretical studies have demonstrated that carbon oxidation is an activated process, and the reaction probability passes through a peak based on the mechanisms outlined above [407, 185, 408, 403]. It is also noted that the location of this peak (in terms of temperature) is dependent upon the oxygen atom partial pressure in the gas phase. These studies indicate that a decrease in pressure shifts the CO flux peak to lower temperatures. Based on the very low effective pressure of the beam (4.75×10^{-5} Pa), the current model predicts a peak in the CO product flux at a temperature of 700 K. For the temperature range in Fig. 4.9, the near monotonic decrease in CO product flux corresponds to the decay just after the peak, due to a decrease in surface coverage (and hence fewer O atoms available to participate in CO formation).

This decrease in the CO flux is primarily driven by the LH3 CO{b} mechanism (up to 1600 K, see Fig. 4.8(b)). Although the identity of the missing oxygen flux is not known from the current molecular beam experiments, it is reasonably assumed that this flux exits the surface in the form of slow CO. Future experiments involving a continuous O-atom beam under steady-state conditions would be useful to confirm the identity of the missing flux.

Finally in the case of CO_2, the ZA and Alba models show significant production at intermediate and high temperatures with CO_2 being the dominant product in the ZA model. The Park model does not have a reaction that produces CO_2. PSMM, the current model, and the experiments show a decrease with temperature. Within the PSMM model, this decrease is due to a positive exponent in the CO_2 production rate (negative activation energy). However, the current model has a positive activation energy and the decreasing trend is a result of the

sharply declining surface coverage and the four adsorbed O atoms (to promote the reaction) present in the CO_2 formation reaction (Table 4.3).

4.5.3 Discussion

The finite rate model outlined in Table 4.3 presents of a number of reaction mechanisms, activation energies and characteristics that may be compared to the literature values and models for carbon oxidation by atomic oxygen. It is first noted that the current model and the PSMM model feature the same mechanisms for O desorption (LH3 O desorption in Table 4.3), but with different activation energies. The PSMM model suggests an activation energy for O desorption of 3.8 eV, similar to that of the ZA model. This is approximately twice the desorption activation energy predicted by density functional calculations for the binding energy of an O atom to a graphene or graphite surface (1.92 eV), suggested separately by Sun *et al.* [80] and Sorescu *et al.* [82]. The energy of 1.92 eV corresponds to the binding energy of the O atom adsorbed at a C-C bridge site on graphite forming a spin-singlet epoxide structure [82]. The same study by Sorescu reports a spin-triplet epoxide structure with a binding energy of 0.38 eV, which is similar to the desorption activation energy for LH3 O (0.27 eV) suggested by the current model. In addition, the triplet structure is shown to be less stable than the singlet state, which is consistent with the low fraction of LH3 O predicted in the current model. The more stable singlet O chemisorbed on the surface most likely undergoes reactions to form gasification products of CO/CO_2 similar to the model predictions.

The fraction of TD O steadily increases with temperature. Mechanical interaction mechanisms that could possibly lead to the formation of TD O atoms such as multiple collisions, penetration, thermal roughening were excluded due to inconsistency with other observed experimental data [5]. This could be a result of a precursor (possibly physisorbed) rapidly desorbing before forming a stable state at the surface consistent with the Kisliuk model (Section 4.3.2). Further, these

products would be accommodated with the surface temperature and their fraction would also be expected to increase with thermal energy at the surface.

The mechanism for the TD formation of CO is also consistent with the PSMM model. The activation energies of the LH1 CO mechanism and the PSMM CO mechanism are in very good agreement: 0.4 eV (PSMM) and 0.53 eV (current model, LH1 CO), and also compare well with the values of 0.5-0.6 eV reported in the literature [80]. The activation energies of other two components of CO (0.36 and 0.1 eV formation; 0.15 and 0.2 eV desorption) are much lower than the different values available in the literature from theoretical studies [113, 101, 122, 114, 115, 116, 123]. Physically, these low values could be a result of the hyperthermal beam energies as observed by Nicholson *et al* [88]. However, as mentioned previously, the mechanisms involving the formation and desorption of CO/CO_2 presented in this work are not elementary, but effective processes; and the rate constants are obtained as fit to experimental data. As an example, increasing the number of catalytic atoms within the present model (CO and CO_2 formation reactions) would lead to the increase in fitted activation energies since the surface coverage decreases rapidly with temperature. Further, the mole fraction of CO_2 and some components of the CO actually decrease with temperature most likely resulting from competition of multiple pathways (that are in general ignored within the theoretical calculations). It is also shown that these energy barrier values are highly dependent on many factors including neighboring groups, geometry of surface sites, spin configuration [111, 118, 100, 126, 124, 396]. Hence it is more appropriate to compare the characteristics of the mechanisms and the products rather than the quantitative values of the activation energies.

Desorption of CO from carbon surfaces are known to primarily occur from semiquinone and carbonyl functional groups [111, 101, 123, 116, 126]. Other possible pathways include carboxyl and ether, are usually present at mainly higher temperatures [122, 100]. In comparison with the carbonyl structure, the semiquinone functional group is reported to be more stable [101, 111, 113]. In the current model, there are three different components of CO. CO{b} has a very low des-

orption rate and is strongly bound to the surface. The desorption rate of CO{b} only gradually increases with temperature and is strongly bound even at high temperatures; similar to the desorption processes involving a semiquinone group. However its formation rate is very high at low temperatures and decreases rapidly with temperature. Decreasing surface coverage could be a direct and indirect (through increasing activation energies [101, 118, 100]) cause for the observed decrease in CO{b}. Within the model, the apparent activation energy (value in the exponent) is assumed to be constant, hence the indirect effect of the surface coverage is captured by the addition of catalytic O′ atoms. The desorption rate of CO{a} is higher than that of CO{b}, however it is still somewhat tightly bound to the surface and does not desorb immediately after the beam strikes; thus showing characteristics similar to desorption process involving carbonyl group intermediates. The desorption rate of CO{a} shows significant increase with temperature, while its formation rate is low across the entire temperature range. TD CO forms and desorbs immediately after the beam strikes the surface (desorption could be part of the formation process). TD CO is the only CO component that shows a steady increase with temperature and is mainly present at higher temperatures, striking a resemblance with CO desorption proceeding via carboxyl/ether groups [122, 100]. The indirect surface coverage dependence of TD CO is explicitly observed in the experiments consistent with the theoretical predictions [80, 101, 118, 100].

Finally, the prompt mechanism of CO_2 formation is present only at low temperatures and rapidly falls to zero with increasing values; consistent with TPD spectra [89, 90, 91, 409] and theoretical calculations [100, 122]. The rapid decrease of CO_2 could be a result of decreasing stability of an intermediate with temperature in comparison to other pathways [100, 122] or the indirect effect of surface coverage. Within the model, these effects are captured as low values of apparent activation energies (leading to slow increase of rate constant with temperature) and the additional catalytic O′ atoms.

4.5.4 Sensitivity analysis

Within the vitreous carbon model developed in this chapter, there is an interplay of several GS and PS reactions. In addition there is non-negligible errors present within the different development stages of this model. Thus, in order to analyze the effect of each of the different reactions on the final products, a sensitivity analysis is performed. Similar to the so-called Campbell's degree of rate control [410], a sensitivity factor X is defined as follows:

$$X_i = \frac{\Delta r/r}{\Delta k_i/k_i} \tag{4.5}$$

This sensitivity factor X is defined for each reaction i. k_i is the rate constant of the reaction, while r is the quantity of interest. The sensitivity factor measures the ratio of the relative change in the quantity of interest to the relative change in the reaction rate constant. There exists several quantities of interest, but from the viewpoint of TPS design, the most important quantity is the total amount of carbon removed from the material.

$$r = \chi_{CO} + \chi_{CO_2} \tag{4.6}$$

For the current study, all the rate constants are increased by 10%, such that $\Delta k_i/k_i$ is 0.1. Simulations with the modified rate constants were performed using the same experimental setup in DSMC for the entire temperature range. The results of this study are shown in Fig. 4.10.

Fig. 4.10 (a) presents the sensitivity factor as a function of temperature for three O formation reactions. All these values are negative since the formation of CO and CO_2 decreases when the O formation rate constants are increased. The magnitude of the sensitivity factor for the O adsorption probability is constant across the range of the temperatures, while those for TD O and slow Oa increase with the temperature consistent with their corresponding mole fraction variations (Fig. 4.8 (a)). The rate of carbon removal is most sensitive to the O adsorption

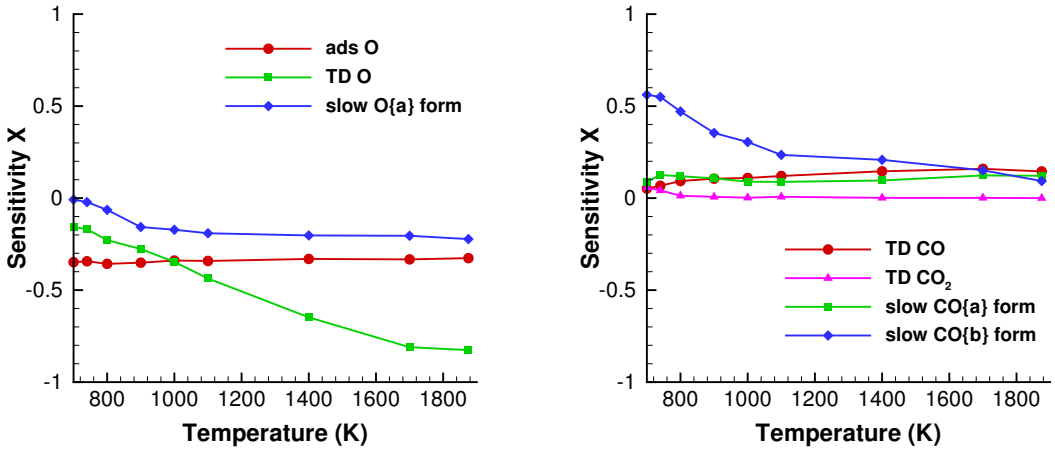

(a)

(b)

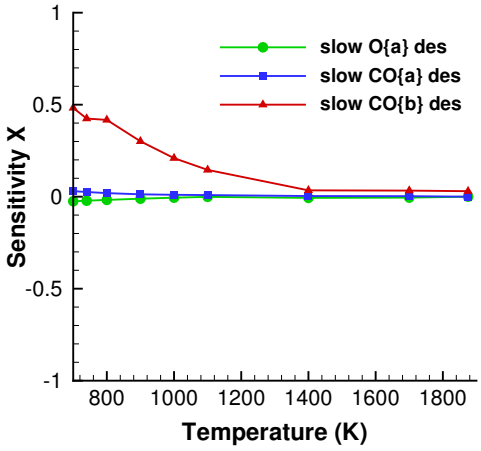

(c)

Figure 4.10: Comparison of mole fractions of surface interaction products between analyzed experimental data and DSMC (using the current finite rate model) for (a) different types of O, (b) different types of CO, and (c) total fluxes of O, CO, and CO_2.

rate at lower temperatures, while at higher temperatures it is most sensitive to the TD O rate constant.

The sensitivity factors for the formation reactions of CO and CO_2 are plotted in Fig. 4.10 (b). Similar to the case of O, the sensitivity factors mirror the mole fraction variation with temperature for each of the components (Fig. 4.8 (b)). The sensitivity factor for CO_2 is very small at lower temperatures and quickly falls to zero. The sensitivity factors for TD CO and slow COa are consistently low across the entire temperature. The rate of carbon removal is highly sensitive to the COb formation rates at lower temperatures, but the sensitivity reduces with increasing temperature.

Finally, Fig. 4.10 (c) shows the sensitivity factor for the desorption reaction of Oa, COa, and COb. In general, the effect of the desorption rate constants on the net rate of carbon removal decreases with temperature. At lower temperatures the surface is closer to saturation, thus changes in the desorption rates will significantly affect the number of available adsorption sites and thereby the final products. This effect decreases at higher temperature since the surface is no longer near saturation. Consistent with the previous cases, the temperature variation of the sensitivity factor magnitude follows the corresponding mole fraction variations, with COb desorption rate having the highest sensitivity factor (among other desorption reactions).

4.6 Summary

DSMC simulations of hyperthermal oxygen scattering on a vitreous carbon surface have been conducted to model TOF and angular distributions in comparison with recent experimental data. The purpose of this study was to construct a surface chemistry model in DSMC that captures observed features in the experimental TOF and angular distribution data.

The most notable information gained from this analysis and current interpretation of the experimental data included: (i) the inclusion of slow products in the

TOF distributions, namely slowly desorbing O and CO products, into the current model, (ii) the inclusion of the "missing flux" of scattered oxygen products that were not detected in these experiments. The missing flux accounts for approximately 60-75% of the total oxygen/oxide flux at low temperatures. Although both O and CO products exhibit a long distribution tail in the TOF data, the identity of the missing flux was determined to be CO (referred to as CO{b}). This was based on the observation that the long distribution tail (slow O component) in the TOF is not evident at high temperatures, as this component merges with the TD products due to an increased desorption rate.

From the analysis of the experimental data, a surface chemistry model is proposed which consists of nine major surface reactions, and physically consistent forms for these mechanisms were inferred. The rate constants of all the mechanisms were represented using an Arrhenius form, and activation energies compare well with previous values reported in the literature.

Simulations performed using the proposed finite rates within the DSMC surface chemistry model provided excellent agreement with the experimental TOF and angular distributions, and with the analyzed experimental fluxes. The CO_2 flux is negligible compared to both O and CO at all temperatures in agreement with the PSMM model. However, the current model predicts CO to be the major reaction product at low temperatures primarily through the formation of the strongly bound CO{b}. The current model predicts a peak in the CO flux at a temperature of 700 K. Thus, for the experimental temperature range spanning 600-1875 K, the CO product flux predicted by the current model corresponds to the decay just after the peak and shows a near monotonic decrease with temperature. The flux of O increases and becomes the dominant product at higher temperatures.

Part II

Gas-Surface Interactions in FiberForm

Chapter 5

Scattering within Porous Fibrous Network

5.1 Overview

This chapter focuses on the carbon based ablator known as FiberForm®, a rigid preform made of rayon-derived carbon fibers used as a precursor of the NASA's Phenolic Impregnated Carbon Ablator (PICA). Although several finite-rate reaction models exist for the air-carbon system,[37, 36, 35] recent studies performed by Candler *et al.,*[129, 130] showed considerable difference between the different models. Furthermore, the study stated that careful validation against experimental measurements are required to improve the accuracy of the models. In addition, all of these models only contain macroscopic information while the kinetic solvers require additional information regarding the microscopic interactions. In order to obtain high-fideltiy solutions in the rarefied regions near the surface, additional information regarding the microscopic interactions like the sticking coefficients, energy barriers, angular scattering distributions, etc., is essential.

The current work is a part of a larger effort to develop a kinetic-based simulation tool for carbon preform ablators. Owing to the complicated fibrous microstructure of carbon preform, it is very difficult to isolate the effect of geometry from the surface reactions in the final observed experimental data of the scattered products. Hence, a study was first carried out to establish a gas-surface interaction model based on the analysis of beam scattering experiments on vitreous carbon [107]. The main aim of the current study is to investigate the validity of applying the vitreous carbon surface chemistry model to carbon preform. Thus, simulations of the molecular beam scattering experiments were carried out with a detailed

FiberForm® microstructure, where the gas-surface interaction on fibers was based on the surface chemistry model developed for the vitreous carbon in Chapter 4. These results were then compared with the FiberForm® experimental data.

The detailed microstructure of the material was obtained directly from X-ray microtomography (micro-CT) imaging of a sample of the FiberForm® material. Micro-CT volumes were used as computational samples in PuMA. The surface was discretized as triangulated elements, using a threshold-based segmentation. This realistic representation of the FiberForm® microstructure captures the actual reactive surface area of the material and also distinguish the effects of surface kinetics and microstructure geometry.

This chapter is organized as follows. A brief description of the molecular beam experiments and the corresponding modeling in PuMA is provided in Section 5.2. Section 5.3 describes the micro-tomography procedure used to obtain the FiberForm® samples. The non-reactive argon beam scattering on FiberForm® is presented in Section 5.4. The extension of the VC model to FiberForm® and comparison with the corresponding FiberForm® experimental results is presented in Section 5.5. Finally, the conclusions and future work are summarized in Section 5.6.

5.2 Methodology

5.2.1 Molecular Beam Experiments

Recent molecular beam experiments performed by Minton and co-workers have presented many details regarding the reaction products generated at the FiberForm® surface [1], and a summary is provided. A hyperthermal O/O_2 beam composed of roughly 92% O and 8% O_2 (mole ratio), was directed at a FiberForm® sample at incident angle of 45 degrees. The number density distribution as a function of arrival time at the detector, N(t), for the products exiting the surface were collected at various final angles that were in the plane of the beam and the surface normal.

These distributions are referred to as time-of-flight (TOF) distributions. Angular flux distributions can be derived by properly integrating the TOF distributions at every final angle. The angular distributions were obtained at two temperatures of 1023 K and 1623 K. The TOF data was collected at fixed final angle of 45 degrees for various temperatures ranging from 1023 K to 1823 K.

5.2.2 PuMA Modeling

The Porous Microstructure Analysis (PuMA) software [411, 412] was used in this study to simulate the beam experiments. PuMA is a suite of tools for the analysis of microstructural data, including material properties and material response simulations. For this study, a custom particle method was implemented and parallelized in the PuMA software to simulate the transport of reactant and product particles, particle-surface collisions, adsorption and surface chemistry of adsorbed particles. Similar to DSMC, each PuMA particle represents a large number of real particles. However, unlike DSMC, PuMA does not model the particle-particle collisions explicitly. It uses random walk statistics (based on Poisson distribution) to perform particle collisions based on the input mean free path. Thus, PuMA framework has a significant speed increase compared to traditional DSMC solvers, though the application is limited to regimes where particle-particle collisions can be ignored (free-molecular regime), or can be modeled based on random walk statistics (e.g. diffusion). The vacuum conditions in the experiments results in negligible particle-particle collisions [106], thus making PuMA an ideal choice for modeling these experiments. At higher particle densities, particle-particle collisions will become important and DSMC must be used to model the system.

In PuMA simulations, the domain is set up to mimic the experimental configuration. The frequency of the pulse is 2 Hz and the beam spot diameter is 1.3 mm. Thus, in the PuMA simulations, the particles were released at regular intervals of 0.5 s from a 1.3 mm diameter circular region (source). In the experiments, all the particles within a pulse were released over a very short interval of time, hence the

PuMA model assumes the emission of all the particles to occur at the same instant. Beam particle velocities were drawn from a Gaussian distribution fitted to the experimental data obtained from the TOF distribution. The surface reactions in PuMA are modeled using the detailed surface chemistry framework developed by Swaminathan-Gopalan *et al* [188, 413]. The maximum number of adsorbed O atoms was restricted by the surface site density of carbon which was taken as 3.5 $\times$ 10^{19} atoms/m^2 following the recommendation of Zhluktov and Abe [36] and Alba [35]. This value was derived based on the inter-atomic distances between carbon atoms in a pristine sample assuming a smooth surface.

5.3 FiberForm® Microstructure

FiberForm® is a rigid material with average porosity varying between 85 and 92%. Its microstructure is characterized by fibers preferentially aligned at about $\pm 15^{\circ}$ with one of the planes (that perpendicular to the direction of compression during manufacturing). The arrangement of the fibers provides the material transverse isotropic properties, with the highest insulation capabilities (lowest thermal conductivity) in the "through-thickness" (TT) direction. The characteristic mean pore diameter of FiberForm® ranges between 50 and 80 μm, and the average fiber diameter is about 10 μm.

In order to produce a digital representation of the materials microstructure for use in PuMA, micro-CT images were acquired using the 3D X-ray microscope (Xradia 520 Versa, ZEISS, Pleasanton, CA) of the Stanford Nano Shared Facilities at Stanford University. A 3 mm cylindrical sample of FiberForm® was extracted by cutting a material billet along the principal manufacturing direction. The sample was placed onto the tomography setup and aligned with the axis of rotation of the stage. Radiographs were collected setting the X-ray source at a voltage of 50 kV and a current of 80 μA. A 4× magnification lens was used, and the positions of detector and X-ray source were adjusted to achieve a pixel size of 1.651 μm. This ensured that the sample fit entirely into the field of view. In addition, the

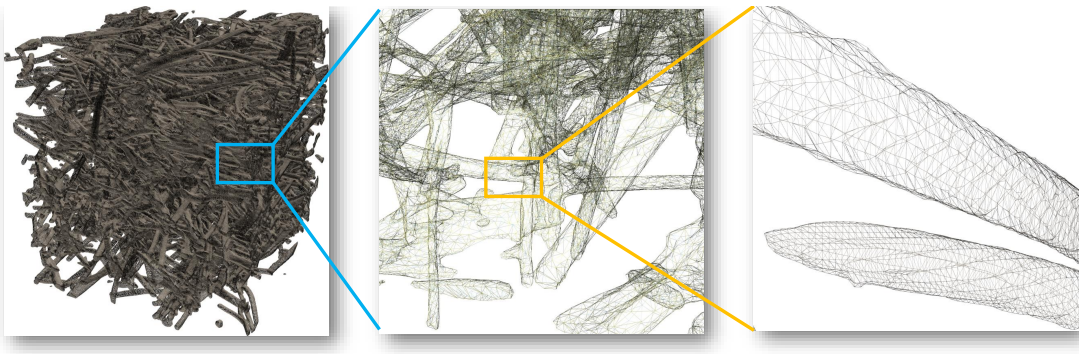

Figure 5.1: Triangulated image of a FiberForm® sample obtained from X-ray imaging using microtomography.

selected pixel size was found to provide a suitable resolution of the FiberForm® microstructure during previous investigations [414]. The tomography reconstruction was performed using the instrument reconstruction software. It should be noted that the sample used for imaging is not the same as the one used in the molecular beam experiments. However, the material used in the experiments and that imaged with micro-tomography are contemporary versions of FiberForm® which have comparable porosity and similar micro-structural features.

The PuMA computational domain was prepared by first scaling the dataset by a factor of 0.5, resulting in a voxel size of 3.302 μm, then by extracting a 0.5 mm thick slab from the reconstructed dataset. Subsequently, the images were thresholded in correspondence of the local minimum in their bimodal gray-scale histogram. The iso-surface was then discretized into a fine set of triangles using a marching cubes algorithm, implemented in PuMA [104]. Fig. 5.1 shows an example of a FiberForm® micro-tomography and two views of the triangulated surface of the fibers at increasing level of detail. The actual 3 mm diameter puck used for the PuMA simulations is shown in Fig. 5.2. The surface of the computational domain is discretized with approximately 16 million triangles.

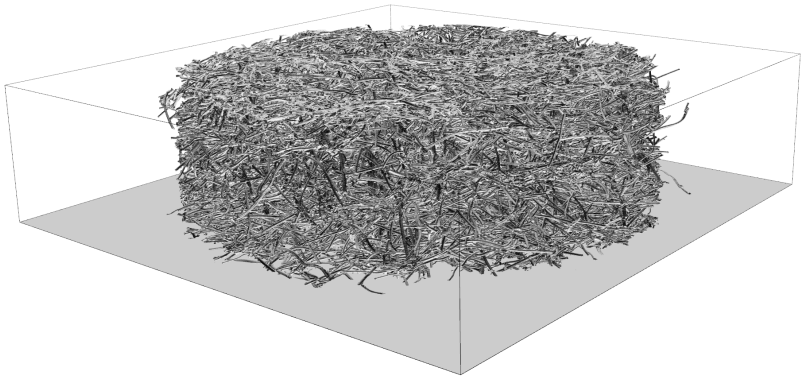

Figure 5.2: Computational surface used for the simulation. The surface comprises roughly 16 million triangles. The FiberForm® sample has a diameter of 3 mm.

5.4 Argon Scattering on FiberForm®

For the Ar scattering from FiberForm, the scattering parameters obtained from vitreous carbon experiments were used. However, in the case of vitreous carbon, the Ar atoms do not undergo multiple collisions with the surface. Hence, information regarding the interaction of high energy (hyperthermal energy) Ar with the surface can only be obtained from the vitreous carbon experiment. Due to the porous nature of FiberForm, particles are expected to bounce around and undergo multiple collisions with the surface. Upon repeated interaction with the surface, the particles attain thermal energies. The details of the scattering are expected to vary widely when the energy of particles are lower (thermal energies) [415]. The interaction of thermal Ar with the carbon surface was modeled using the Cercignani-Lampis-Lord (CLL) model [301, 302]. The scattering model was shifted from impulsive to CLL based on a specified energy threshold of 2 eV. Particles with energy greater than this threshold value were scattered impulsively, while the particles with lower energies were scattered based on the CLL model. The values for the normal and tangential accommodation coefficients for the CLL model and the energy threshold were modified to obtain the best possible agreement with the experimental data. As for the vitreous carbon, since the experiments do not provide out-of-plane data, a cosine power law decay was used to

approximate the out-of-plane scattering distribution following Glatzer *et al.*[255]

Figures 5.3 and 5.4 show the comparison of the experimental and PuMA TOF and angular distributions for Ar scattering on FiberForm® at 1623 K, following bombardment with the Ar beam at θ_i=45°. In comparison to the Ar scattering on vitreous carbon [5], it is noticed that the Ar scattering on the FiberForm® surface is vastly different. No thermal component was observed in the signal for vitreous carbon scattering, while roughly half of the FiberForm® signal was thermally accommodated to the surface temperature. In addition, the angular distribution of the IS component was much broader for the FiberForm® compared to the vitreous carbon. From the PuMA simulations, it was identified that the sole reason for the thermal accommodation of Ar in FiberForm® was due to the multiple collisions with various fibers. The gas-phase collisions between the Ar atoms are extremely negligible and do not contribute towards the thermalization process.

Fig. 5.5 shows a histogram plot of the fraction of particles scattered from the surface against the number of surface collisions. The last bin represents the number of particles that underwent 20 or more collisions before being scattered from the surface. This shows that a significant number of particles undergo a large number of collisions, resulting the thermalization of the particles. Gas-phase collisions were found to be negligible as a result of the low pressures of the experimental setup. Accumulation of the particles caused by trapping inside the microstructure was not observed despite the complex geometry.

The TOF plots correspond to a final angle of 45°. It can be seen that the general agreement between the experimental and numerical results is very good, despite the number of approximations used. All the features of the experimental TOF distribution such as the IS, NT and TD shapes, peak values and locations are captured by the PuMA results. Excellent agreement is also observed in the case of the angular distributions for both the IS and TD portions. The IS angular distribution includes both the fast IS and the NT portions. This distribution is very flat owing to the fact that the NT portion is close to a cosine distribution.

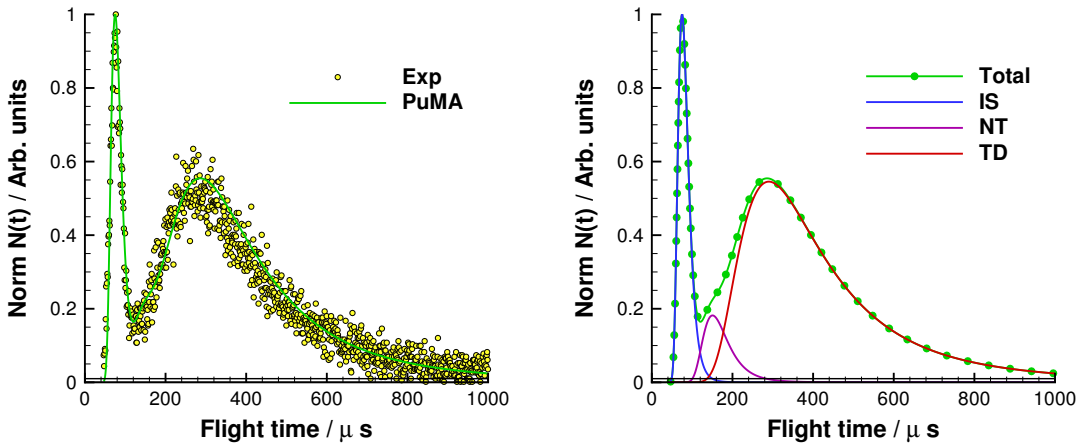

Figure 5.3: TOF for Ar scattering from FiberForm® surface at incident and final angles of 45° at 1623 K. The left plot shows the comparison between the experimental and simulation results. The right plot shows the decomposition of the PuMA results into IS and TD.

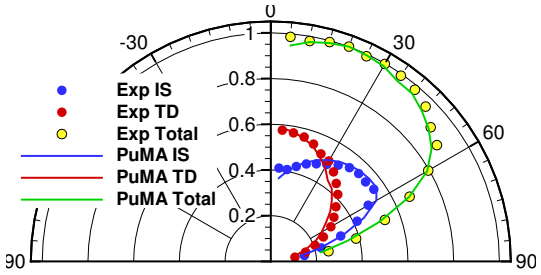

Figure 5.4: Comparison of experimental and PuMA results for flux integrated angular distributions for Ar scattering from a FiberForm® surface at an incident angle of 45° and final angles between 5 and 80°, at 1623 K.

5.5 Oxygen Scattering on FiberForm®

For the O scattering from FiberForm®, the reactive and non-reactive scattering parameters obtained from vitreous carbon experiments were used. However, in the case of vitreous carbon, the O atoms do not undergo multiple collisions with the surface. Hence, only the information regarding the interaction of high energy (hyperthermal energy) O with the surface can be obtained from the vitreous carbon experiment. Due to the porous nature of FiberForm®, particles are expected to bounce around and undergo multiple collisions with the surface. Upon repeated interaction with the surface, the particles attain thermal energies. The

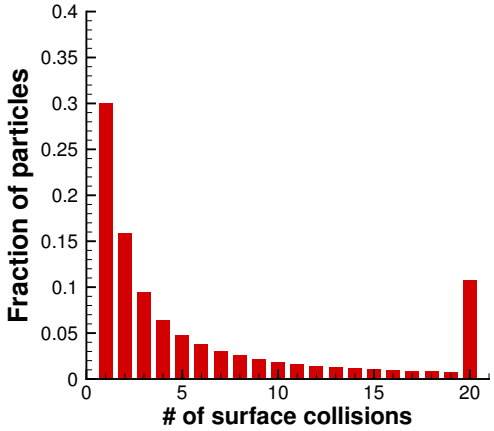

Figure 5.5: Histogram showing the fraction of the particles scattered from the surface vs the number of surface collisions. The last bin represents the fraction of particles that underwent 20 or more collisions before exiting the surface.

details of the non-reactive scattering are expected to vary widely when the energy of particles are lower (thermal energies) [415]. The interaction of thermal O with the carbon surface was modeled using the Cercignani-Lampis-Lord (CLL) model [301, 302]. The appropriate scattering model (impulsive to CLL) is selected based on a specified energy threshold of 2 eV for the incident particle energy prior to a surface collision. Particles with energy greater than this threshold value were scattered impulsively, while the particles with lower energies were scattered based on the CLL model. The values for the normal and tangential accommodation coefficients for the CLL model and the energy threshold were modified to obtain the best possible agreement with the experimental data. The reaction probabilities of hyperthermal O atoms were used for the thermal O atoms, except for the initial adsorption probability. This is a reasonable approximation since the products of all the reaction mechanisms are thermal, and are independent of the incident energy [34]. The adsorption probability of the thermal O atoms was taken as unity following the work of Zhluktov and Abe [36] and Alba [128]. It was also assumed that all species other than O (CO and CO_2) undergo only non-reactive collisions with the surface.

Figure 5.6 shows the experimental and numerical TOF distributions for O and

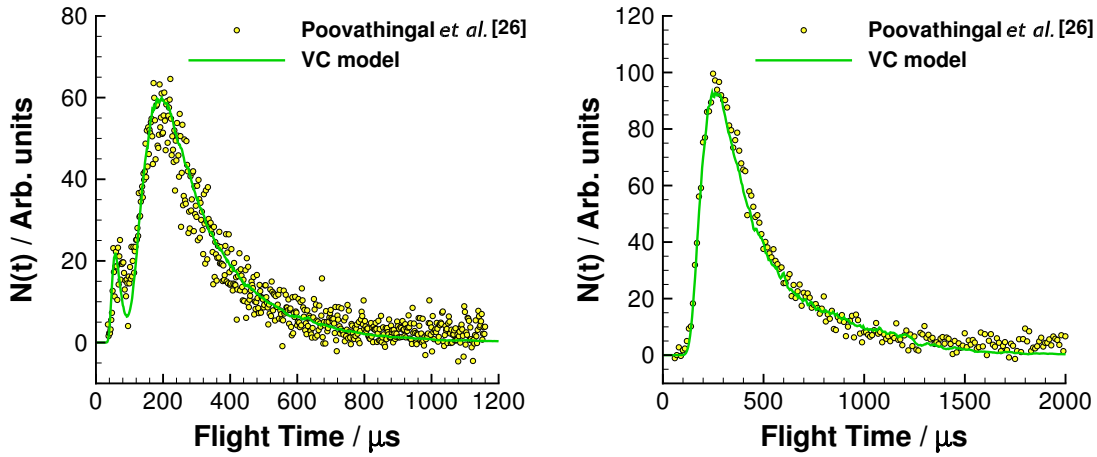

Figure 5.6: TOF obtained from PuMA simulations (using the VC model [6]) and experiments [1] of (a) O and (b) CO scattering from a FiberForm® surface at incident and final angles of 45° at 1623 K.

CO, respectively, at 1623 K and a final angle of 45°. It can be seen that a majority of the O and CO scatter from the surface with thermal energies, which is in good agreement with the experimental distributions. When compared with TOF distributions for vitreous carbon experiments at similar temperatures,[5, 107] it can be seen that the fraction of TD atoms in the signal has increased from vitreous carbon to FiberForm®. This is expected since an O atom is likely to experience multiple surface collisions when penetrating the porous FiberForm® material and therefore more likely to become thermally accommodated with the surface. In the case of vitreous carbon, the average number of surface collisions experienced by an O atom is likely to be close to 1 due to its non-porous nature. Fig. 5.7 shows a histogram plot of the fraction of particles scattered from the surface against the number of surface collisions. The last bin represents the number of particles that underwent 20 or more collisions before being scattered from the surface. This shows that a significant number of particles undergo a large number of collisions, resulting in the thermalization of the particles. Approximately half of the atoms undergo more than one collision with the surface with about 5% being trapped for a relatively long time (undergoing more than 20 collisions). Gas-phase collisions were found to be negligible as a result of the low pressures of the experimental

setup. Accumulation of the particles caused by trapping inside the microstructure was not observed despite the complex geometry. In the case of CO, both vitreous carbon and FiberForm® show that CO is almost exclusively a TD product at these high surface temperatures.

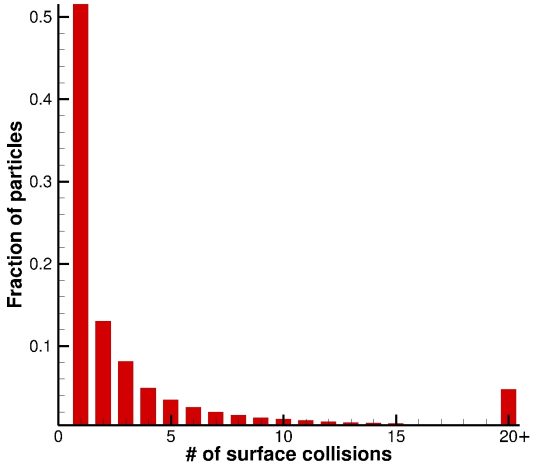

Figure 5.7: Histogram showing the fraction of the particles scattered from the surface vs the number of surface collisions. The last bin represents the fraction of particles that underwent 20 or more collisions before exiting the surface.

Additionally, Fig. 5.8 shows the experimental and numerical angular distributions for O and CO, respectively, at 1623 K. When compared with angular distributions for vitreous carbon experiments at similar temperatures,[5, 107] the shapes and relative IS/TD ratio are consistent with the observations from the previous paragraph. However, one important difference between the two materials is that the relative CO to O flux increased in the case of FiberForm®. This difference is also attributed to the multiple collisions experienced by the oxygen atoms within FiberForm®. An O atom has a finite probability of reacting with the surface to form CO, while the nascent CO is assumed to scatter non-reactively. Hence, a greater number of collisions with the surface increases the effective probability of CO formation.

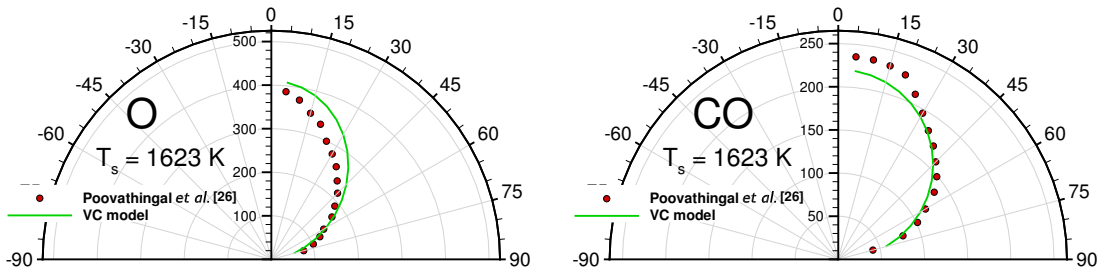

Figure 5.8: Angular distribution obtained from PuMA simulations (using the VC model [6]) and experiments [1] of (a) O and (b) CO scattering from a FiberForm® surface at incident and final angles of 45° at 1623 K.

5.6 Summary

PuMA software was used to perform simulations of molecular beam scattering experiments of hyperthermal O striking a FiberForm®, which is a common component of an ablative TPS. X-ray micro-tomography was used to obtain the detailed microstructure of FiberForm®, which was employed within the PuMA simulations to capture the effect of the complex porous and fibrous geometry. The finite-rate surface chemistry model recently constructed from the molecular beam scattering experiments on vitreous carbon [5] was applied to each fiber of the FiberForm® material.

First, the effect of microstructure was investigated by studying the non-reactive scattering of Ar off the FiberForm® sample. A significant portion of the Ar particles were thermally accommodated to the surface temperature, unlike the case of vitreous carbon where all the particles were impulsively scattered. Multiple collisions with the different fibers, resulting from the porous nature of FiberForm® was found to be solely responsible for the thermalization of Ar. The effect of gas-phase collisions was negligible. Good agreement was observed between the simulations and experiments of Ar beam scattering. The discrepancies are attributed mainly

to the differences in the microstructure of the samples used in the experiments and simulations.

The reactive interaction on FiberForm® was investigated by modeling the atomic oxygen beam scattering experiments. Comparison between the experimental and PuMA time-of-flight (TOF) distributions of both O and CO at 1623 K showed good agreement. In comparison with the vitreous carbon experiments, the fraction of TD O atoms were significantly higher in the case of FiberForm®. Multiple collisions with the different fibers, resulting from the porous nature of FiberForm® was found to be responsible for the thermalization of the O atoms, while the effect of gas-phase collisions was negligible. In addition, a larger relative CO to O flux is observed for the case of FiberForm® in comparison with vitreous carbon. This was again attributed to the multiple collisions of the O atoms within FiberForm®. The CO atoms only undergo non-reactive scattering, while the interaction of O atom with the surface can result in the formation of CO with a finite probability, thus increasing the number of surface collisions and resulting in a higher effective CO formation rate.

The details of the microstructure is crucial in determining the final composition (O/CO) and energy distributions (IS/thermal) of the gas-surface interaction products. The properties of the microstructure such as porosity and fiber diameter will govern the number of collisions each particle undergoes with the surface before exiting the FiberForm® and thereby the properties of the scattered products. Hence, it is crucial to account for the detailed microstructure in order to accurately model the gas-surface interactions. However, kinetic-based mesoscale methods, which can capture the microscopic details of FiberForm®, become intractable at the macroscopic scales and cannot be used to describe the flowfield around a spacecraft. Thus, effective surface interaction models which can be employed directly within macroscopic simulation methods like Computational Fluid Dynamics (CFD) and material response codes are necessary.

Chapter 6

Effective Surface Oxidation Model for FiberForm

6.1 Overview

Although the recently developed VC model accurately captures the carbon oxidation at the mesoscopic scale, it requires the detailed microstructure of the FiberForm®. Thus, it can only be employed directly within the kinetic mesoscale solvers like DSMC and PuMA. In addition, employing the detailed microstructure in the simulations is also computationally very expensive. In the case of macroscopic solvers like CFD, which does not account for the microstructure of the FiberForm®, direct application of the VC model would result in erroneous predictions. Therefore, carbon oxidation model which includes the effect of both the surface oxidation as well as the inherent microstructure of the FiberForm® is required for use within CFD [416]. These models effectively capture the complete interaction of oxygen within the microstructure (including multiple collisions) within one single collision against a flat plate, and thereby termed as effective models.

The effective model described above will be a function of both the microstructure properties (such as porosity) and the gas inflow properties (such as the number density and flux). Porosity has been identified as one of the most important properties to represent the microstructure and significantly affect the behavior of FiberForm®. Thus, this work studies the variation of the effective model rate constant with the porosity. Future work will explore the effect of other microstructure and gas-inflow properties.

This chapter is organized a follows. A description of the modeling in PuMA

to obtain the product fluxes is provided in Section 6.2. Section 6.3 describes the procedure for the computation of the effective rates from the product fluxes. The development of the effective surface oxidation model as a function of the fibrous carbon porosity is discussed in Section 6.4. Finally, the conclusions are summarized in Section 6.5.

6.2 Computing Product Fluxes

In order to analyze the effect of porosity on the effective rates, the product fluxes is required as a function of porosity. However, the experiments of FiberForm® described in the previous chapter were performed only for a single porosity. Hence, product fluxes at different values of porosities need to be calculated first.

The PuMA simulation domain is configured to be similar to the experimental setup, but the "experimental" sample is replaced with samples of varying porosity to obtain the changing product fluxes. The frequency of the pulse and the beam diameter is maintained at 2 Hz and 1.3 mm respectively. The initial velocity distribution of the particles were captured accurately by drawing from the experimental distributions, and all the atoms within a single pulse are released simultaneously. The gas-surface and pure-surface reactions in PuMA are modeled using the detailed surface chemistry framework developed by Swaminathan-Gopalan *et al* [188, 413]. The surface site density on each of the carbon fiber surface was taken as 3.5×10^{19} atoms/m^2 following the recommendation of Zhluktov and Abe [36] and Alba [35]. The simulations were carried out for a hundred pulses with a million PuMA particles in each pulse in order to obtain sufficiently smooth statistics in the final distributions. The average porosity was varied from 85-92% over a 1mm^3 sample consistent with the range observed in virgin FiberForm® [414]. The temperature range was taken from 800 to 2000 K.

Fig. 6.1 shows the O and CO (mole fraction) composition as a function of temperature at two different FiberForm® porosities of 85% and 91%. At higher porosities, greater mole fractions of CO and less amounts of O are observed. This

is due to the greater penetration of the incoming beam atoms into the microstructure leading to more collisions with the surface. As mentioned previously the CO collisions with the surface only leads to non-reactive scattering, while the O atom interactions with the surface have a finite probability of reacting to form CO. Hence greater the number of collisions with the surface, higher is the probability of CO formation. The effect of the differences in the collision histogram is more pronounced at higher temperatures when the probability of CO formation during a single collision is smaller. At lower temperatures, there is a very high probability of CO formation when the O atom strikes the surface. Once CO is formed, the subsequent collisions with the surface are non-reactive and the differences in the collision histogram at varying porosities has a small effect on the final composition. However, at higher temperatures, where the CO formation probability in a single collision is small, the effect of the differences in the collision histogram is more significant on the final product fluxes.

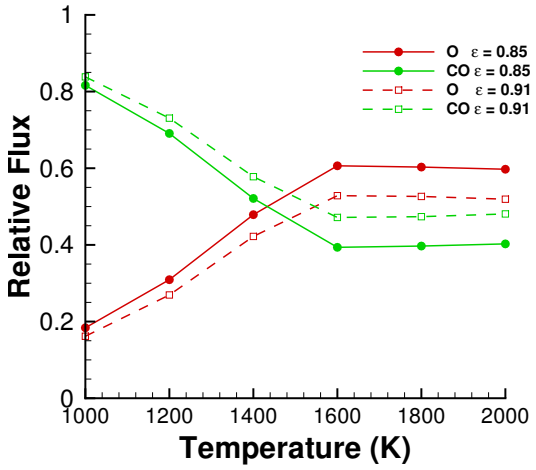

Figure 6.1: Mole fractions of surface interaction products obtained from PuMA using the vitreous carbon model for total fluxes of O and CO at two different porosities of 85% and 91%.

6.3 Computing Effective Rates

The goal of the effective model introduced in this work is to simultaneously capture the effect of the microstructure in addition to the surface chemistry by defining an effective rate for these processes. The reaction mechanisms and form of the effective model are assumed to be the same as that of the original VC model. This is a valid approximation since the occurrence of multiple collisions within the microstructure does not fundamentally alter the mechanism of the surface reactions [416]. Further, the rate constants for the desorption reactions are retained from the VC model since the desorption process is also unaffected due to the multiple collisions on the FiberForm® surface.

In order to derive the GS rate constants within the effective model, they are computed first at each porosity independently. These rate constants are then fitted to a polynomial expression to obtain the Arrhenius pre-exponential factor and energy as a function of porosity.

For fitting the GS rate constants at each porosity, a similar procedure that was used to derive the VC model outlined in Swaminathan-Gopalan *et al.*[187, 190] is employed. Briefly, initial guesses for the different rate constants were assumed, and the surface reactions during the full beam simulations were carried out. The molecular beam is modeled to strike a flat carbon FiberForm® surface without the detailed microstructure similar to the way it is treated within CFD. The product fluxes obtained using these guess values are compared to the FiberForm® experimental and PuMA data, and the corresponding errors are computed. Based on these errors, the initial guess values are modified in a systematic manner using the particle-swarm algorithm [393, 394]. This procedure is repeated until the error values reach below a specified threshold.

While fitting the GS rate constants at each porosity, it is observed that the Arrhenius energy E was constant across the porosity range for each of the reactions. This is reasonable since the parameter E within the Arrhenius expression (Eq. 6.1) describes the variation of the rate constant with the temperature. Thus,

this parameter is unaffected by the presence of multiple collisions and thereby the porosity [416]. Thus, only the pre-exponential factor A of the Arrhenius form varies with the collision histogram and is a function of the porosity.

$$k = f(\Phi) * A\, exp(-E/T) \tag{6.1}$$

The rate constant values thus obtained inherently account for the detailed interaction within the microstructure since they reproduce the multiple collisions within the FiberForm® microstructure by assuming a single collision with a flat plate.

6.4 Results

In this section, the effective rates for atomic oxygen scattering from FiberForm® derived using the methodology outlined in the previous sections is presented. First, the effective rates obtained from the experiments at a single porosity is presented, with comparisons of TOF and angular distributions and product fluxes. Finally, the effective rates constructed at different porosities are fitted to a polynomial functional form.

6.4.1 Effective rates: Comparison with Experiments

As mentioned previously, the experiments were performed for a single FiberForm® microstructure. The VC model applied to the full microstructure of PuMA was able to reproduce the experiments (Section 5.5). Now, this experimental data is used to construct the effective rates assuming a single collision of the atomic oxygen at the surface. The final rate constant values and the mechanisms in the effective model are provide in Table 6.1. All the reaction mechanisms and the desorption rate constant remain the same as in the VC model. CO_2 was observed only at the lowest temperature in the FiberForm® experiments and this data was

Table 6.1: Reaction rate constants in the effective oxidation model developed from FiberForm® experiments [1].

Type	Mechanisms	Reaction	Rate constant (k)	Units
Adsorption	Adsorption	$O(g) + (s) \longrightarrow O(ads)$	$\frac{1}{\Phi} * \frac{1}{4}\sqrt{\frac{8k_bT_g}{\pi m}} * 0.892$	$m^3\ mol^{-1}\ s^{-1}$
Adsorption-mediated GS reactions	LH3 O{a} formation	$O(ads) \longrightarrow O\{a\}(s)$	1	s^{-1}
	LH3 CO{a} formation	$O(ads) + C(b) + O'(ads) \longrightarrow CO\{a\}(s) + O'(ads)$	$\frac{1}{\Phi} * 8337.8\ exp(-\frac{10360.8}{T_s})$	$m^2\ mol^{-1}\ s^{-1}$
	LH3 CO{b} formation	$O(ads) + C(b) + O'(ads) \longrightarrow CO\{b\}(s) + O'(ads)$	$\frac{1}{\Phi} * 57.83\ exp(-\frac{2908.9}{T_s})$	$m^2\ mol^{-1}\ s^{-1}$
	LH1 O formation	$O(ads) \longrightarrow O(TD)(g) + (s)$	$7.85\ exp(-\frac{6154.6}{T_s})$	s^{-1}
	LH1 CO formation	$O(ads) + C(b) + O'(ads) \longrightarrow CO(g) + (s) + O'(ads)$	$\frac{1}{\Phi} * 964555.3\ exp(-\frac{16574.0}{T_s})$	$m^2\ mol^{-1}\ s^{-1}$
PS reactions	LH3 O{a} desorption	$O\{a\}(s) \longrightarrow O(g) + (s)$	$0.05\ T^2\ exp\left(-\frac{3177.2}{T_s}\right)$	s^{-1}
	LH3 CO{a} desorption	$CO\{a\}(s) \longrightarrow CO(g) + (s)$	$4485.5\ exp\left(-\frac{1581.4}{T_s}\right)$	s^{-1}
	LH3 CO{b} desorption	$CO\{b\}(s) \longrightarrow CO(g) + (s)$	$1.2\ exp\left(-\frac{2251.6}{T_s}\right)$	s^{-1}

not enough to derive a rate constant for CO_2 production reaction mechanism.

Figures 6.2, 6.3, and 6.4 compare the TOF, angular distribution and the final product fluxes for both O and CO obtained from the effective model (PuMA simulations) and the experiments. Excellent agreement is observed between the effective model and the experiments for each of the quantities. Further, all the features within the TOF and angular distributions are captured by the effective model thus providing validation of the model. This effective model may thus be used as a smooth-wall BC for use in CFD solvers.

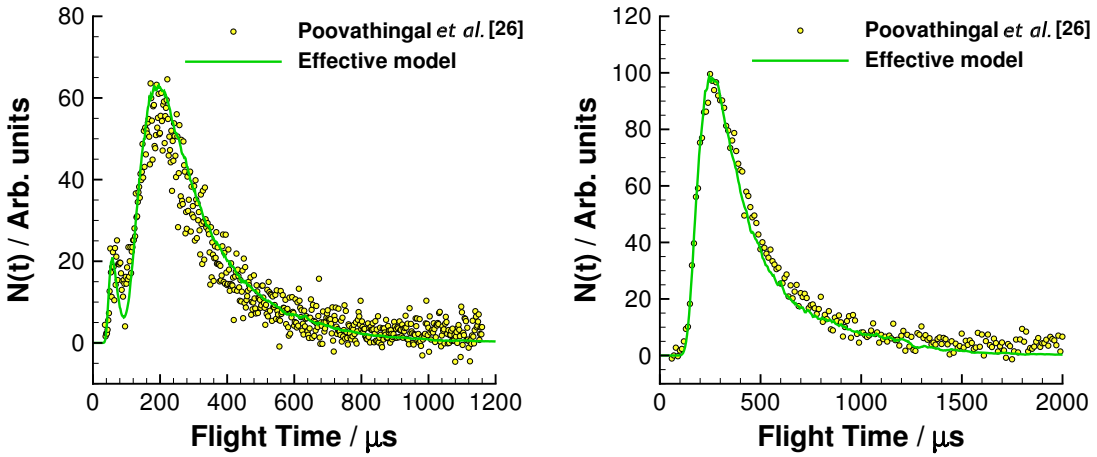

Figure 6.2: TOF obtained from PuMA simulations (using the effective model in Table 6.1) and experiments [1] of (a) O and (b) CO scattering from a FiberForm® surface at incident and final angles of 45° at 1623 K.

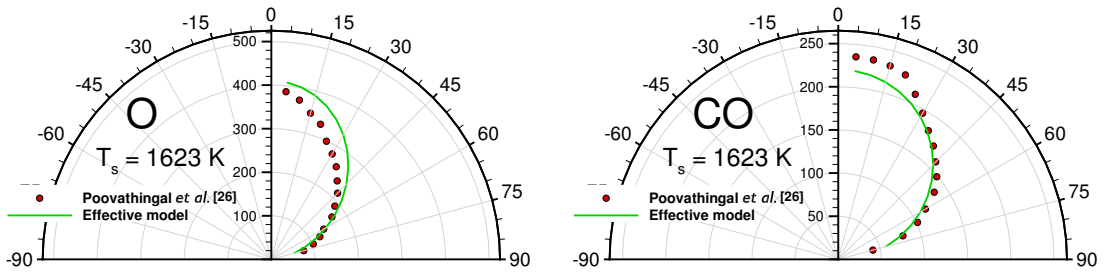

Figure 6.3: Angular distribution obtained from PuMA simulations (using the effective model in Table 6.1) and experiments [1] of (a) O and (b) CO scattering from a FiberForm® surface at incident and final angles of 45° at 1623 K.

6.4.2 Effective rates: Function of Porosity

Next, the PuMA data obtained from simulating the atomic oxygen beam scattering from FiberForm® microstructures of varying porosity is used to improve and expand the effective carbon oxidation model described in the previous section. First, the effective rates are constructed using the particle-swarm algorithm [393, 394] independently at each porosity. As mentioned previously, the Arrhenius pre-exponential factor was the only parameter that exhibited a variation with the porosity. Thus the pre-exponential factor A from these effective rates are then fitted to a polynomial form. A second degree polynomial was found to sufficiently capture the variation across the porosity (ϵ) range for all the different GS reactions.

$$A = a_0 + a_1 * \epsilon + a_2 * \epsilon^2 \tag{6.2}$$

Table 6.2 presents the Arrhenius form parameters and the coefficients of the second degree polynomial fit for all the GS reactions in the carbon oxidation effective model for FiberForm®.

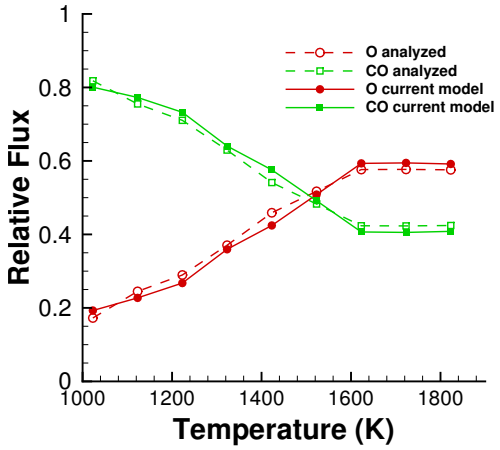

Figure 6.4: Final product fluxes obtained from PuMA simulations (using the effective model in Table 6.1) and analyzed from experimental data [1] of O and CO scattering from a FiberForm® surface at 1623 K.

Table 6.2: Reaction rate constants in the effective oxidation model developed from FiberForm® experiments [1] and PuMA data.

Mechanisms	Reaction	Rate constant $k = f(\Phi) * A * exp(-E/T)$				
		$f(\Phi)$	$A = a_0 + a_1 * \epsilon^1 + a_2 * \epsilon^2$			E
			a_0	a_1	a_2	
Adsorption	$O(g) + (s) \longrightarrow O(ads)$	$\frac{1}{\Phi} * \frac{1}{4}\sqrt{\frac{8k_bT_g}{\pi m}}$	+1.335E−1	+1.583E+0	−8.177E−1	0
LH3 O{a} formation	$O(ads) \longrightarrow O\{a\}(s)$	1	1	0	0	0
LH3 CO{a} formation	$O(ads) + C(b) + O'(ads) \longrightarrow CO\{a\}(s) + O'(ads)$	$\frac{1}{\Phi}$	−7.343E+4	+1.636E+5	−7.997E+4	+1.036E+4
LH3 CO{b} formation	$O(ads) + C(b) + O'(ads) \longrightarrow CO\{b\}(s) + O'(ads)$	$\frac{1}{\Phi}$	−5.093E+2	+1.134E+3	−5.547E+2	+2.909E+3
LH1 O formation	$O(ads) \longrightarrow O(TD)(g) + (s)$	1	+6.298E+1	−1.151E+2	+5.943E+1	+6.155E+3
LH1 CO formation	$O(ads)+C(b)+O'(ads) \longrightarrow CO(g)+(s)+O'(ads)$	$\frac{1}{\Phi}$	−8.495E+6	+1.892E+7	−9.251E+6	+1.657E+4

6.5 Summary

In this chapter, the molecular beam experimental data on FiberForm® and VC model applied to FiberForm® are used to construct effective oxidation models. These effective models capture the effects of the microstructure without explicitly modeling them, and thus can be used directly within CFD.

PuMA software was used to perform simulations of molecular beam scattering experiments of hyperthermal O striking a FiberForm®, which is a common component of an ablative TPS. X-ray micro-tomography was used to obtain the detailed microstructure of FiberForm®, which was employed within the PuMA simulations to capture the effect of the complex porous and fibrous geometry. The finite-rate surface chemistry model recently constructed from the molecular beam scattering experiments on vitreous carbon [5] was applied to each fiber of the FiberForm® material. This was used to obtain the product fluxes of oxygen scattering from FiberForm® at various porosities different from the experiments.

At higher porosities, greater mole fractions of CO and less amounts of O (up to 10% of the total product flux) were observed. This is due to the greater penetration of the incoming beam atoms into the microstructure leading to more collisions with the surface resulting in greater mole fraction of CO. The effect of the differences in the collision histogram is more pronounced at higher temperatures when the probability of CO formation during a single collision is smaller. At lower temperatures, there is a very high probability of CO formation when the O atom strikes the surface. Once CO is formed, the subsequent collisions with the surface are non-reactive and the differences in the collision histogram at varying porosities has a small effect on the final composition. However, at higher temperatures, where the CO formation probability in a single collision is small, the effect of the differences in the collision histogram is more significant on the final product fluxes.

The experimental and PuMA data are used to construct the effective model. The effective model reaction mechanisms are assumed to be the same as that of

the VC model, as well as the desorption rate constant values. This is a valid approximation since multiple collisions within the microstructure does not fundamentally alter the mechanism of the surface reactions, or the desorption process. CO_2 was observed only at the lowest temperature in the FiberForm® experiments and this data was not enough to derive a rate constant for CO_2 production reaction mechanism.

Particle-swarm algorithm was used to obtain the rate constants of the gas-surface reactions within the effective model at each porosity. The fitting process yielded constant values (different value for each of the reaction) for the Arrhenius energy value for the range of porosities examined here. This is reasonable since the Arrhenius parameter E describes the variation of the rate constant with the temperature, and is unaffected by the presence of multiple collisions and thereby the porosity. Thus, only the Arrhenius pre-exponential factor A varies with the collision histogram and is a function of the porosity.

Simulations performed using the constructed effective rates with a flat plate provided excellent agreement with the experimental TOF and angular distributions, and with the analyzed experimental fluxes. This effective model also provides excellent agreement with the PuMA data for the whole porosity range of interest. Thus, this effective model can be directly used within the CFD solvers.

Part III

Non-reactive surface interaction of molecules

Chapter 7

O_2 scattering from carbon surface: Molecular Dynamic simulations

7.1 Overview

Although classic MD simulations are equipped to accurately model the translational degrees of freedom of the molecule, their classical nature prevents the accurate modeling of internal energies. Using quasi-classical methods to represent the internal energies of the systems within MD, leads to the so-called Molecular dynamics/Quasi-classical trajectory (MD-QCT) technique [417, 418, 419, 420]. This method can be used to model accurate post-reaction and post-collision molecular internal energy distributions [421, 422, 423, 424, 425, 426].

The aim of the current work is to investigate the gas-surface interaction of O_2 molecule with a carbon surface. Molecular dynamics/Quasi-classical trajectory (MD-QCT) simulations using interaction potentials derived from *ab-initio* methods are used to perform gas-surface scattering. The ro-vibrational energies of the scattered molecule are characterized and the resultant distributions are obtained for desired initial configurations of the gas-surface system. These simulations are used to provide an atomic-level understanding of the energy transfer dynamics and mechanisms for energy transfer to the translational, rotational and vibrational degrees of freedom of the O_2 molecule [426]. Only non-reactive (inelastic) collisions between O_2 and the graphite surface are considered in the present work.

The contents of this chapter are organized as follows. The simulation methodology, initial conditions, and potentials for the MD-QCT calculations performed in this work are presented in Section 7.2. Section 7.3 compares the MD-QCT results with the experimental data of Murray *et al.,* [7] of O_2 scattering from

graphite. The results of this study and the final energy (translational, rotational, and vibrational) and angular distributions for a wide range of initial conditions are provided in Section 7.4. These results are presented for two incident parameters of translational energy (Section 7.4.1) and surface temperature (Section 7.4.2). Finally, the conclusions are summarized in Section 7.5.

7.2 Simulation Methodology

The MD-QCT simulations in this study were performed using LAMMPS MD package [427]. The carbon-carbon (C-C) and carbon-oxygen (C-O) atom interactions are modeled using the ReaxFF potential. ReaxFF potential is an empirical potential which has a general form for an extensive list of inter-molecular interaction [428].

$$E_{system} = E_{bond} + E_{over} + E_{under} + E_{val} + E_{pen} + E_{tors} + E_{conj} + E_{vdWaals} + E_{Coulomb}. \tag{7.1}$$

The various parameters within this form are parameterized against an extensive quantum chemical database. The value of the parameters used in this study are taken from Shin *et al.* [429]. The C-C bond parameters used in this work were recently re-parameterized to better capture the properties of the solid carbon phase [430]. The ReaxFF potential and the corresponding set of parameters were chosen because they can capture both short and long range bonds within solid carbon [431] as well as the reactive interaction between the carbon and oxygen atoms [432].

Although the ReaxFF parameter set used in the current study can be used for describing the interaction between the oxygen atoms (O-O), it was not constructed to capture the ro-vibrational energies within the O_2 system. Thus, the O_2 diatomic potential constructed by Bytautas *et al.,* [433, 434] using *ab-initio* calculations is used. This potential has been shown to accurately reproduce the experimental

ro-vibrational spectra of O_2 [434]. The even-tempered Gaussian functional form is used to represent the potential. The parameters a_k, α, and β have been fitted to capture the ro-vibrational spectra accurately.

$$E(r) = \sum_{k=1}^{7} a_k \, exp\left(-\alpha\beta^k r^2\right). \tag{7.2}$$

The representative 3D simulation domain is shown in Fig. 7.1. A single layer of carbon atoms at the bottom are fixed in the computational domain frame of reference. The next bottom layer and a thin layer (one atom thick) on all the four sides of the surface are thermostatted. This models the energy dissipation to the surrounding atoms and also ensures that the dissipated energy does not re-enter into the simulation domain due to the periodic boundary conditions. The temperature of the thermostat atoms were controlled using Berendsen thermostat [435]. Both the characterization of the scattered O atom internal states, and the initialization of the O atom velocities for a given internal energy state are performed as described in Ref. [436]

The second-order velocity-verlet scheme is used for time-integration, and a time step of 0.1 fs was used during the entire course of the simulation. The carbon surface system is first equilibrated to the particular temperature for a time of 1 ps. Following this, the O_2 molecule is introduced within the domain according to the specific initial conditions (translational, rotational, vibrational energy of the molecule and polar angle of incidence). Both the azimuthal angle and the location of impact is chosen randomly. The impact location is selected within a region one-sixth of the unit cell at the center of the domain due to the six-fold symmetry of the carbon lattice. The cutoff of the C-O interaction potential is 8 Å and hence the molecule is initially placed at 10 Å above the surface ensuring that there is no interaction at the beginning of the simulation. The simulation is performed until one of the two stopping criteria is satisfied: (i) the molecule reaches a height of 10 Å from the surface upon reflection, (ii) the simulation time exceeds 10 ps after the molecule has struck the surface. If the molecule is still

near the surface after 10 ps, the molecule is said to be trapped on the surface. A total of 5000 trajectories were performed for each of the cases shown below to obtain the reported final distributions.

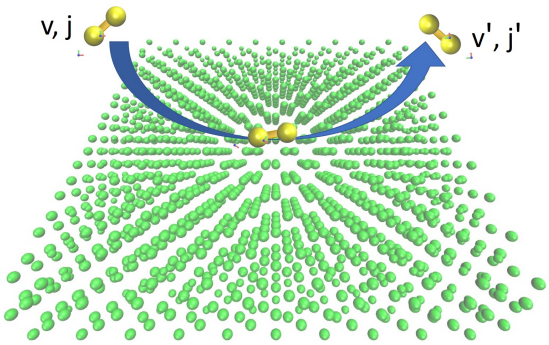

Figure 7.1: Schematic illustration of the side view of the 3D simulation setup.

7.3 Comparison with experiments

In a recent study by Murray *et al.,* [7], the reactive and non-reactive scattering of hyperthermal O and O_2 on a graphite surface was studied. The incident O_2 molecules had an energy of about 10 eV and were directed at the surface at an angle of 45°. The final reactive and non-reactive products were measured as a function of time (TOF distributions) at various angles in the plane of incident beam. These TOF distributions are then integrated to obtain the angular distributions.

O_2 interaction with the surface was revealed to be almost completely non-reactive, thus validating the non-consideration of the reactive interactions in the present work. Further, it was observed in the experiments that almost all of the scattered O_2 had hyperthermal energies, indicating that the incident O_2 molecules do not undergo multiple collisions and thermalize with the surface, consistent with the results of the MD simulations.

Figure 7.2 shows the comparison between the current MD simulations and the experimental data of Murray *et al.,* [7]. The peak of the distribution occurs

around 55°, consistent with the super-specular scattering (final distribution peak is greater than the incident angle) usually observed at hyperthermal incident energies for single collision events. The collision time is so small that there is almost no change in the molecule energy in the tangential direction to the surface. The energy of the molecule along the direction perpendicular to the surface reduces due to the inelastic nature of the collision, thus resulting in super-specular scattering. Excellent agreement is observed between the simulations and the experiments. Both the location of the peak and the width of the distribution from the simulations are consistent with the experiments. This validates the use of MD potentials used in the current work for performing inelastic scattering simulations.

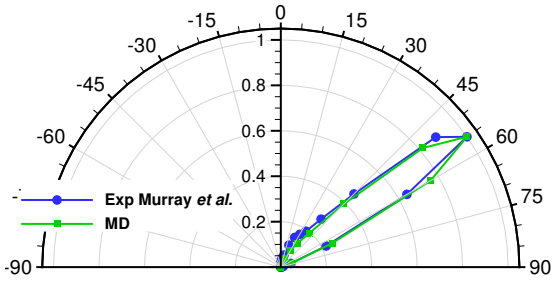

Figure 7.2: Comparison of in-plane angular distribution of O_2 scattered from a graphite surface with an incident energy $E_{tr,i}$ 10 eV and incident angle $\theta_i = 45°$ obtained from MD simulations with the experimental data of Murray *et al.*, [7].

7.4 Results

Four quantities of interest were analyzed, namely the final translational energy, rotational and vibrational state distributions, as well as the polar angular distributions. These quantities are very important in predicting both the transport properties and the gas-phase reaction rates near the surface. First, the effect of

initial translational energy on the final distributions of the four properties were investigated, followed by the effect of surface temperature.

7.4.1 Effect of Initial Translational Energy

In this section, the effect of initial translational energy of the molecule on the quantities of interest is discussed. For this study all the other initial parameters were kept constant. Both the rotational and vibrational states were taken as ground state ($j_i = 0$, $v_i = 0$). The angle of incidence (θ_i) was kept at 45°, and the surface temperature (T_{surf}) at 1000 K.

A range of initial translational energies from 0.01-10 eV were studied, however for the sake of brevity only three distributions are presented. These distributions are representative and are sufficient to showcase the trends observed within the range of energies that were investigated. Fig. 7.3 shows the normalized final distributions for all the quantities of interest for $E_{tr,i} = 0.5, 3, 8$ eV. Fig. 7.3(a) presents the final translational energy distributions. As expected the location of the peak increases with increasing $E_{tr,i}$. However, the fraction of translational energy lost in the collision also increases with $E_{tr,i}$. In addition, it is also observed that the final distribution broadens for higher initial translational energies.

The final polar angular distributions are shown in Fig. 7.3(b). In all of these cases, super-specular scattering is observed where the peak of the angular distributions is greater than the incident angle [271, 292, 5]. This is characteristic of the structural and transitional regime scattering where the interaction time with the surface is short and complete thermal accommodation does not occur. The interaction of the molecule with the surface is much greater in the normal direction in comparison to the tangential direction. Hence, the decrease in energy/velocity in the normal direction is higher, resulting in super-specular scattering. It is also observed that the width of the distribution decreases with greater $E_{tr,i}$. This might seem to be in apparent contradiction with the increased width observed for the final translational energies as $E_{tr,i}$ increases. However, detailed analysis reveals

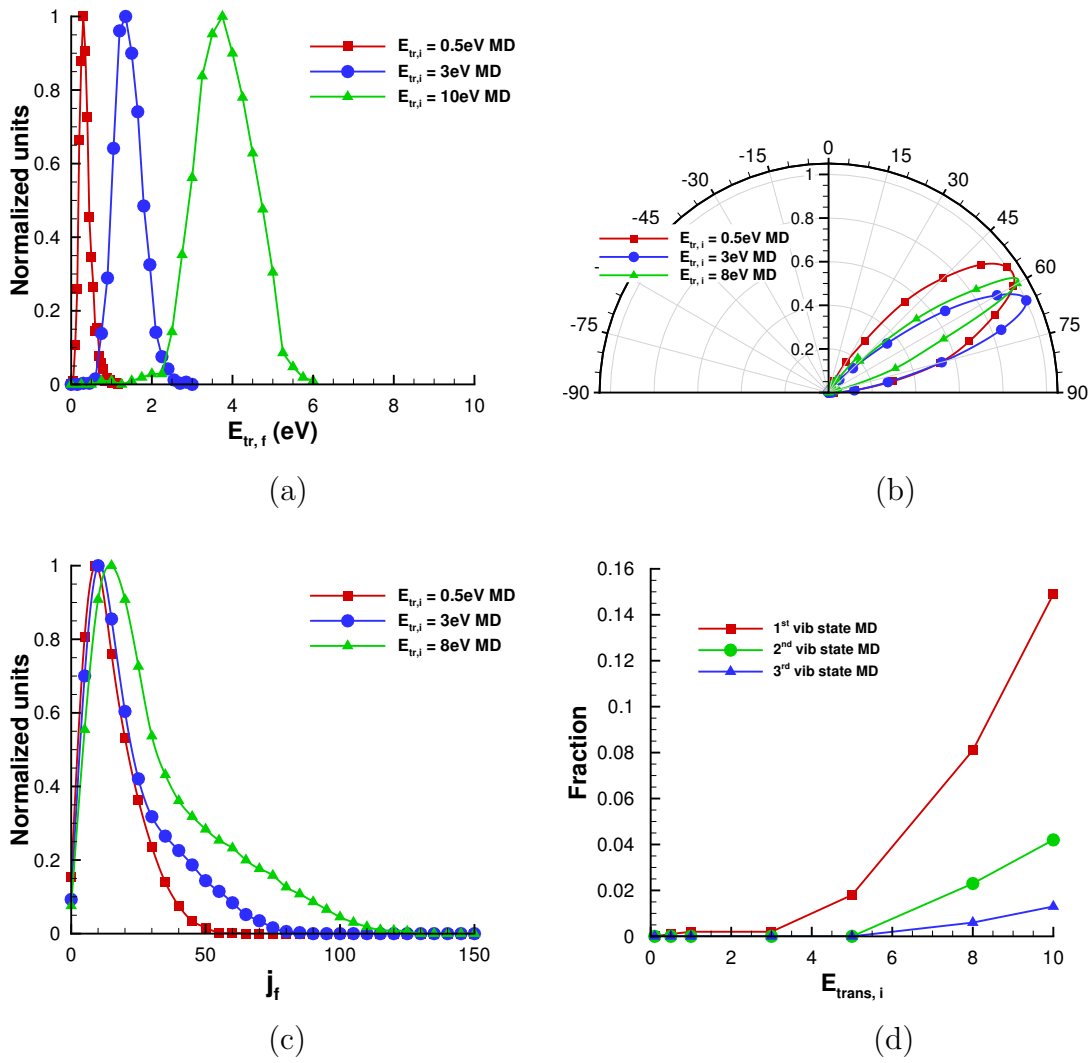

Figure 7.3: Final normalized distribution of (a) translational energy, (b) polar angle, (c) rotational state, and (d) vibrational state of scattered O_2 molecules obtained using MD-QCT simulations for three initial translational energies of 0.5, 3, and 10 eV. For the vibrational state, the transition probability is presented rather than the distributions. The other initial parameters of the incident O_2 molecule were kept constant at $j_i = 0$, $v_i = 0$, $\theta_i = 45°$, and $T_{surf} = 1000$ K.

that the fraction of the distribution width to the initial value tends to decrease with higher value of $E_{tr,i}$. Since the polar angle is the ratio between velocities along different directions, the observed variation of the distribution is consistent with the final translational energy and polar angle.

Fig. 7.3(c) describes the final rotational state distributions of the scattering O_2 molecule. The distribution shows an initial increase and a peak followed by a

decay at higher states; similar to a Boltzmann distribution. However, the tail of the observed distribution is much higher than that of a Boltzmann distribution, resulting in a characteristic bimodal distribution observed in gas-surface scattering [293]. As the initial translation energy increases, it is observed that the higher rotational states are more excited leading to higher peak value and greater width in the distribution.

For the final vibrational state distribution, since the excitations to higher excited levels are very small, the fraction of molecules transitioning to higher vibrational states (up to third) is plotted rather than the distribution (Fig. 7.3(d)). As expected, the transition probability is higher for lower vibrational states. The transition probabilities also show an increase with increasing $E_{tr,i}$. However, significant transitions are observed only for energies greater than 3 eV. This suggests that the primary mechanism of vibrational excitation is transfer from the translational energy of the incident gas particle rather than transfer from the surface. This is consistent with the fact that the first vibrational excited state of O_2 (for j=0) is 0.2 eV ($\sim$2260 K) higher than the ground state. However, it is important to emphasize that vibrational excitations were observed at lower translational energies although in much smaller probabilities ($\sim$0.001). Since many reactions in the gas-phase are vibrationally favored, even such low excitation probabilities might be significant. Considerably higher number of trajectories are required to accurately compute these excitation probabilities (above the statistical noise), and will be explored as part of the future work.

Finally, it is observed that the distributions predicted by the MSS theory are in very good agreement with the MD-QCT simulations. Some discrepancies between the distributions are observed, especially in the case of the angular distributions, however, this might be a result of statistical noise in the MD-QCT data. The theory reasonably captures almost all of the trends both qualitatively and quantitatively including the rotational and vibrational state distributions.

7.4.2 Effect of Surface Temperature

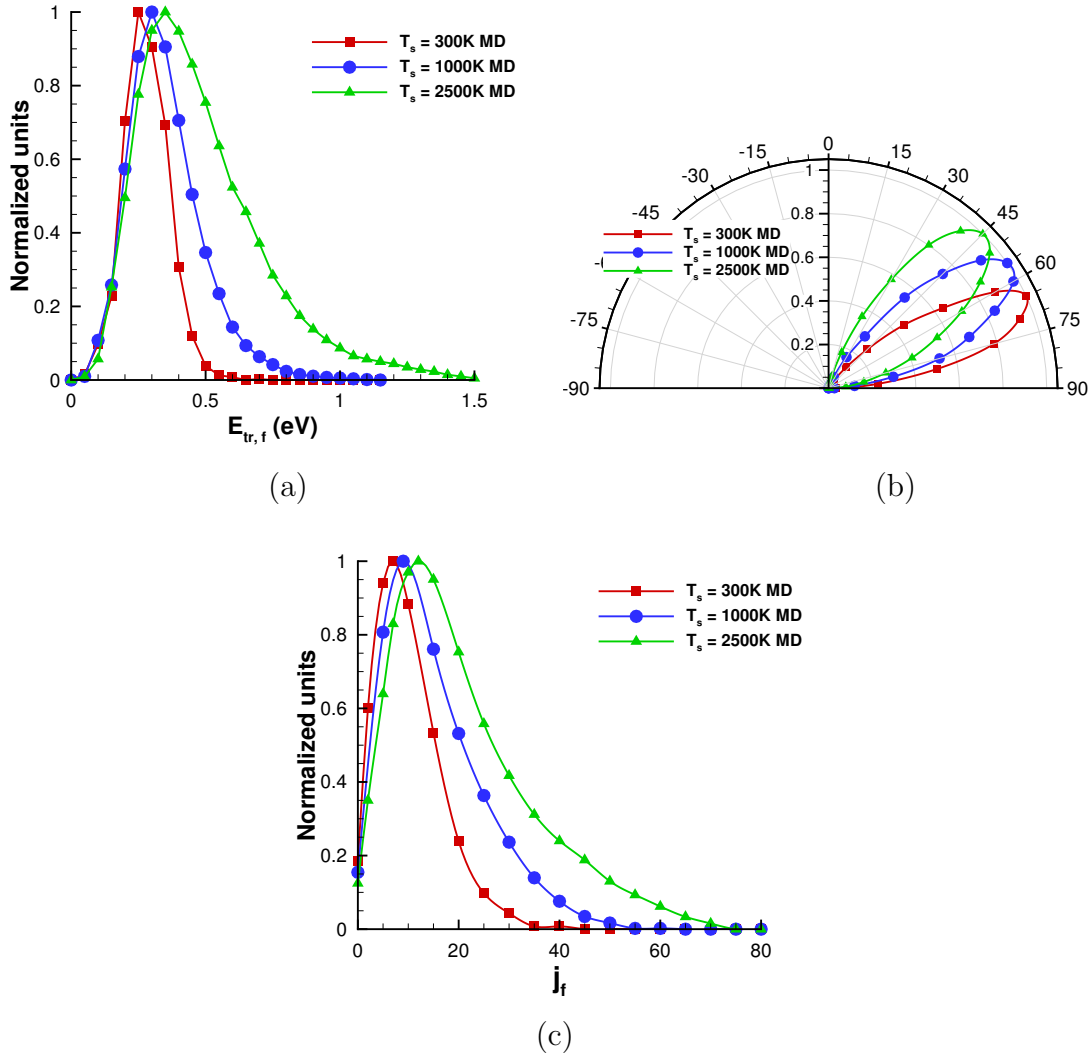

Figure 7.4: Final normalized distribution of (a) translational energy, (b) polar angle, and (c) rotational state of scattered O_2 molecules obtained using MD-QCT simulations for three surface temperatures of 300, 1000, and 2500 K. The other initial parameters of the incident O_2 molecule were kept constant at $E_{tr,i} = 0.5$ eV, $j_i = 0$, $v_i = 0$, and $\theta_i = 45°$.

The effect of surface temperature on the final distributions of various properties are investigated next. Similar to the previous study, all the initial parameters other than the surface temperature were kept constant. Again, only the ground rotational and vibrational states are considered ($j_i = 0$, $v_i = 0$), while the angle of incidence was taken as 45°, and the translational energy was kept constant at

0.5 eV.

The surface temperature was varied from 300-2500 K, spanning the range of temperatures typically encountered within carbon heat shields during atmospheric (re)entry. Similar to the previous study, only three distributions are presented that are representative and showcase the trends. Fig. 7.4 presents the final distributions for the properties of interest for the surface temperature of 300, 1000, and 2500 K. As mentioned previously, the vibrational excitations at $E_{tr,i}$ of 0.5 eV, although observed, were scarce and could not be resolved above the statistical noise and is not presented for this study. The final translational energy distributions for various surface temperatures are shown in Fig. 7.4(a). The average value of the energy increases with temperature and so does the peak and width of the distribution. The variation of the final translational energy (and other properties) with the surface temperature indicates that the system is in thermal or transition regime.

Fig. 7.4(b) presents the final polar angular distributions of the scattered O_2 molecule. No super-specular scattering is observed at lower surface temperatures, but the distributions moves towards the normal as the surface temperature increases. Greater the surface temperature, larger the vibration of molecules on the surface resulting in higher transfer of energy to/from the surface. This is the reason for the shift of the angular peak towards the normal and the broadening of the distribution (tending to a cosine distribution).

The final distribution of the rotational energy states are shown in Fig. 7.4(c). Similar to the previous study, it is observed that the rotational distributions follow a bi-modal distribution, however the deviation from the Boltzmann distribution was less significant. This suggests that the energy transfer mechanisms from the surface and from the initial translational energy are both significant. As the temperature of the surface increases, the peak of the distribution and its width increases due to greater energy transfer from the surface as discussed previously.

7.5 Summary

The MD-QCT simulations were performed using the ReaxFF potential for the C-C and C-O interactions while the O-O interactions were modeled using the accurate *ab-initio* potential designed to capture the ro-vibrational states accurately. A range of initial translational energy of the molecule and the surface temperature is considered to elucidate the dependence of the scattered molecule properties on these parameters.

The peak final translational energy and the width of the distribution increased with the initial translational energy. It was also observed that the fraction of translational energy lost during the collision increases, as well as a broadening of the final distribution with increasing energy. In the case of angular distributions, super-specular scattering was observed due to the high energies and low interaction time with the surface. The peak of the angular shows non-monotonic trend with initial translational energy while the width increases. For the final rotational energy state distribution, bi-modal distributions were observed with both the peak value and the width of the distribution increasing with increasing $E_{tr,i}$. The transition probabilities to excited vibrational states increased with $E_{tr,i}$, and these values were higher for lower states. The transition probabilities for energies below 3 eV were small and were not resolved above the statistical noise.

For a fixed initial translational energy and varying surface temperature, the final translational energy peak and width also showed an increase with surface temperature. In the case of angular distributions, the super-specular nature of the scattering becomes less prominent with increase in surface temperature. Shifting of the peak towards the surface normal and increased broadening of the distribution were also observed with rise in temperature. The final rotational energy state distributions were bi-modal in nature, but the deviation from Boltzmann distribution was less significant compared to the initial translational energy variation study. This suggests that the energy transfer mechanisms from the surface and from the initial translational energy of the molecule are both significant.

Chapter 8

O_2 scattering from carbon surface: Molecule Surface Scattering Theory

8.1 Overview

In the present work, a rigorous theoretical model based on gas-phonon interactions at the surface is used to describe detailed scattering of gas atoms/molecules from the surface [280]. During the collision, energy transfer occurs both between and within the sub-systems (substrate and gas particle). The current model considers several such mechanisms including multi-phonon processes, translational and internal mode (rotational and vibrational) excitations. The translational and rotational modes of the gas particle are treated classically within this framework while the quantum mechanical nature of the vibrational modes are taken into account.

This model provides a state-resolved description of the scattered particles through the evaluation of the detailed scattering kernels and transition matrix. Thus, this framework provides a powerful alternative to full molecular dynamic simulations to compute various surface interaction quantities such as accommodation coefficients, internal mode excitation probabilities, etc. Further, since this framework describes gas-surface interactions at a microscopic level, it can be extended to describe the systems in strong non-equilibrium, which are frequently encountered in high speed re-entry flows and nano-scale devices.

The contents of this chapter are organized as follows. The detailed description of the molecule surface scattering (MSS) theory employed in the current work is provided in Section 8.2. The calibration of the free parameters within the MSS theory using the MD data from the previous chapter is presented in Section 8.3.

The variation of the free parameters with the incident molecule energy and surface temperature is discussed in Section 8.4. Finally, the conclusions are summarized in Section 8.5.

8.2 Theory

In order to describe the scattering of the incident gas atoms/molecules from the surface, the theory by Manson [280] is used. In this theory, the state-to-state transition rate, w is given by the generalized Fermi-Golden rule [280].

$$w(\boldsymbol{p_f}, \boldsymbol{I_f}, q_{gf}, \boldsymbol{p_i}, \boldsymbol{I_i}, q_{gi}) = \left\langle \left\langle \frac{2\pi}{\hbar} \sum_{n_f} \left|\tau_{fi}^2\right| \delta\left(\varepsilon_f - \varepsilon_i\right) \right\rangle \right\rangle \tag{8.1}$$

This describes the rate of transition of the incident gas particle from an initial translational momentum $\boldsymbol{p_i}$, angular momentum $\boldsymbol{I_i}$, and the vibrational excited quantum number q_{gi} for the g^{th} mode to a final state of $\boldsymbol{p_f}$, $\boldsymbol{I_f}$, and q_{gf}. The angular brackets denote the ensemble average, and $\varepsilon_{(i,f)}$ is the total energy of the system (gas particle plus surface) before and after the collision. τ_{fi} is the transition matrix and $[n_f]$ are all the possible final states.

The translation and rotational modes are treated classically while the vibrational mode is treated quantum mechanically. In this semi-classical limit, the transition rate can be written as [283]

$$\begin{aligned} w(\boldsymbol{p_f}, \boldsymbol{I_f}, q_{gf}, \boldsymbol{p_i}, \boldsymbol{I_i}, q_{gi}) = \frac{1}{\hbar^2} \left|\tau_{fi}^2\right| \int_{-\infty}^{\infty} dt \Big\{ & \exp\left[-i(E_f - E_i)t/\hbar\right] \\ & \times \exp\left[-2W\right] \times \exp\left[Q(t)\right] \Big\} \end{aligned} \tag{8.2}$$

where $\exp\left[-2W\right]$ is the generalized Debye-Waller factor, $E_{(i,f)}$ is the initial/final energy of the incident gas particle, and $Q(t)$ is the time-dependent correlation function. Several mechanisms are involved in the energy transfer during the collision process such as phonon creation/annihilation, and rotational and vibrational

excitations. Treating each of these processes as independent, the transition rate ca nbe expressed in terms of the various scattering kernels [284].

$$w(\boldsymbol{p_f}, \boldsymbol{I_f}, q_{gf}, \boldsymbol{p_i}, \boldsymbol{I_i}, q_{gi}) = \frac{1}{\hbar^2} \left|\tau_{fi}^2\right| \int_{-\infty}^{\infty} dt \Big\{ K_T(t, T_s) K_R(t, T_s) K_V(t, T_s) \times \exp\left[-i(E_f^T - E_i^T + E_f^R - E_i^R + E_f^V - E_i^V)t/\hbar\right] \Big\} \tag{8.3}$$

$E_{(i,f)}^T$, $E_{(i,f)}^R$, and $E_{(i,f)}^V$ represent the initial/final translational, rotational and vibrational energies of the gas particle. K_T, K_R, and K_V are the scattering kernels for the translational, rotational and vibrational modes respectively, describing the different energy exchange process. The evaluation of these scattering kernels finally yields the complete description of the gas-surface interaction process through the state-to-state transition rate.

Within the semi-classical limit the scattering kernels for the translational and rotational energies can be generally expressed as [283]

$$K_T(t, T_s) = \int_{-\infty}^{\infty} d\boldsymbol{R} \times \exp\left[i\boldsymbol{K}.\boldsymbol{R}\right] \times \exp\left[-2W_T\left(\boldsymbol{p_f}, \boldsymbol{p_i}\right)\right] \times \exp\left[Q_T(\boldsymbol{R}, t)\right] \tag{8.4}$$

$$K_R(t, T_s) = \int_{-\infty}^{\infty} d\theta_z \times \exp\left[i l_z \theta_z/\hbar\right] \times \exp\left[-2W_R\left(\boldsymbol{I_f}, \boldsymbol{I_i}\right)\right] \times \exp\left[Q_R(\theta_z, t)\right] \tag{8.5}$$

$2W_{(T,R)}$ and $Q_{(T,R)}$ are the translational/rotational contributions to the Debye-Waller factor and time correlation functions respectively. $\boldsymbol{K}$ is the phonon wave vector parallel to the surface and $\boldsymbol{R}$ is the position vector on the surface. l_z and θ_z are the components of the angular momentum and rotation respectively.

The scattering kernel of the vibrational modes is expressed as [284]

$$K_V(t,T_s) = \sum_{\kappa,\kappa'=1}^{N_A} \left\{ \exp\left[i(\boldsymbol{p_f}.\Delta\boldsymbol{r}^f_{\kappa,\kappa'} - \boldsymbol{p_i}.\Delta\boldsymbol{r}^i_{\kappa,\kappa'})/\hbar \right] \right\} \times \exp\left[Q^p_{V,\kappa,\kappa'}(\boldsymbol{p_f},\boldsymbol{p_i},t) \right] \times \exp\left[-\left(W^p_{V,\kappa}(\boldsymbol{p_f},\boldsymbol{p_i}) + W^p_{V,\kappa'}(\boldsymbol{p_f},\boldsymbol{p_i}) \right) \right] \tag{8.6}$$

Here N_A is the number of atoms in the incident gas molecule and m_k is the mass of the κ^{th} molecular atom. The position of the κ^{th} atom of the molecule just before the collision (i) and just after the collision (f) is given by $\boldsymbol{r}^i_\kappa(t) = \boldsymbol{r}^i_\kappa(0) + \boldsymbol{u}^i_\kappa(t)$. The term $\Delta\boldsymbol{r}^{(i,f)}_{\kappa,\kappa'}$ is the relative displacement of the k^{th} atom before and after the collision with the surface. The vibrational displacement relative to $\boldsymbol{r}^i_k$ due to the internal model, decomposed into cartesian components denoted by β, is

$$u^\beta_k(t) = \sum_{j=1}^{N_v} \sqrt{\frac{\hbar}{2N_v m_k \omega_j}}\, \tilde{e}\,(\kappa,j|\beta) \left\{ a_j \exp\left[-i\omega_j t\right] + a^\dagger_j \exp\left[i\omega_j t\right] \right\} \tag{8.7}$$

where N_v is the total number of internal modes, a_j and $a^\dagger_j$ are, respectively, the annihilation and creation operators for the j^{th} mode of frequency ω_j , and $\tilde{e}\,(\kappa,j|\beta)$ is the polarization vector that is obtained from a normal modes analysis of the molecule. Again, $W_{V,\kappa,\kappa'}$ and $Q_{V,\kappa,\kappa'}$ are the vibrational contribution of the Debye-Waller factor and the generalized correlation function respectively.

The classical limits of the generalized correlation functions for the translational and rotational models for a non-corrugated surface are obtained using perturbation expansions over small times and space around the point of collision resulting in the following expressions [280].

$$Q_T(\boldsymbol{R},t) = 2W_T(\boldsymbol{p_f},\boldsymbol{p_i}) - \frac{i}{\hbar}\Delta E^T_0 - \frac{t^2}{\hbar^2}\Delta E^T_0 k_b T_s - \frac{\Delta E^T_0 k_b T_s R^2}{2\hbar^2 v^2_R} \tag{8.8}$$

$$Q_R(\theta_z, t) = 2W_R\left(\boldsymbol{I_f}, \boldsymbol{I_i}\right) - \frac{i}{\hbar}\Delta E_0^R - \frac{t^2}{\hbar^2}\Delta E_0^R k_b T_s - \frac{\Delta E_0^R k_b T_s \theta_z^2}{2\hbar^2 \omega_R^2} \tag{8.9}$$

Here, v_R is the weighted average of the phonon velocities parallel to the surface and ω_R is the weighted average of the frustrated rotational angular velocities of the surface molecules along the surface normal. $\Delta E_0^{(T,R)}$ are the translational/rotational recoil energies defined as [284]

$$\Delta E_0^T = \frac{\left(\boldsymbol{p}_f - \boldsymbol{p}_i\right)^2}{2M_s} \tag{8.10}$$

$$\Delta E_0^R = \frac{l_x^2}{2I_{xx}} + \frac{l_y^2}{2I_{yy}} + \frac{l_z^2}{2I_{zz}} \tag{8.11}$$

In these equations, M_s and I_{jj} are the effective substrate mass and moment of inertia along the principal directions. Now, the full quantum mechanical expression for the generalized displacement-correlation function of the vibrational state of the molecule can be written as [284]

$$\begin{aligned} Q^p_{V,\kappa,\kappa'}\left(\boldsymbol{p}_f, \boldsymbol{p}_i, t\right) = \sum_{\alpha,\alpha'=1}^{3} p_\alpha p_{\alpha'} \sum_{j=1}^{N_v} \Bigg[& \frac{1}{2N_v \hbar \omega_j \sqrt{m_\kappa m_{\kappa'}}} \tilde{e}\left(\kappa, j|\alpha\right) \tilde{e}^*\left(\kappa', j|\alpha'\right) \\ & \left\{ n\left(\omega_j\right) \exp\left[i\omega_j t\right] + \left[n\left(\omega_j\right) + 1\right] \exp\left[-i\omega_j t\right] \right\} \Bigg] \end{aligned} \tag{8.12}$$

where $n\left(\omega_j\right)$ is the Bose-Einstein function and N_v is the total number of vibrational modes. ω_j is the frequency of j^{th} vibrational mode and the $\tilde{e}(\kappa, j|\alpha)$ is the polarization vector which can obtained from a normal mode analysis of the molecule.

In the internal-mode correlation function $Q^p_{V,\kappa,\kappa'}\left(\boldsymbol{p}_f, \boldsymbol{p}_i, t\right)$ can be further expanded to

$$\exp\left\{Q^{p}_{V,\kappa,\kappa'}\left(\boldsymbol{p}_f,\boldsymbol{p}_i,t\right)\right\}=\prod_{j=1}^{N_v}\sum_{\alpha_j=-\infty}^{\infty}\left\{I_{|\alpha_j|}\left(b_{\kappa,\kappa'}(\omega_j)\right)\left[\frac{n(\omega_j)+1}{n(\omega_j)}\right]^{\alpha_j/2}\exp\left(-i\alpha_j\omega_j t\right)\right\} \tag{8.13}$$

where $I_{|\alpha_j|}(z)$ is the modified Bessel function of integer order α_j and argument z. The argument of the modified Bessel function above is given by

$$b_{\kappa,\kappa'}(\omega_j)=\sum_{\alpha,\alpha'=1}^{3}p_\alpha p_{\alpha'}\frac{1}{N_v\hbar\omega_j\sqrt{m_\kappa m_{\kappa'}}}\tilde{e}\left(\kappa,j|\alpha\right)\tilde{e}\left(\kappa',j|\alpha'\right)\sqrt{n(\omega_j)\left[n(\omega_j)+1\right]} \tag{8.14}$$

Substituting the expressions for the correlation functions into the transition rate equation and integrating, the following results can be obtained for a non-corrugated surface [272]

$$\begin{aligned}w(\boldsymbol{p_f},\boldsymbol{I_f},\boldsymbol{p_i},\boldsymbol{I_i})=&\frac{1}{S_{uc}\hbar^2}\left|\tau^2_{fi}\right|\exp\left[-\frac{2v_R^2\boldsymbol{P}^2}{4k_bT_s\Delta E_0^T}\right]\exp\left[-\frac{2\omega_R^2 l_z^2}{4k_bT_s\Delta E_0^R}\right]\\&\times\left(\frac{2\pi\hbar^2v_R^2}{k_bT_s\Delta E_0^T}\right)\left(\frac{2\pi\hbar^2\omega_R^2}{k_bT_s\Delta E_0^R}\right)^{1/2}\left(\frac{\pi\hbar^2}{k_bT_s\left(\Delta E_0^T+\Delta E_0^R\right)}\right)^{1/2}\\&\times\sum_{\kappa,\kappa'=1}^{N_A}\left\{exp\left[\frac{i\left(\boldsymbol{p_f}.\Delta\boldsymbol{r}^f_{\kappa,\kappa'}-\boldsymbol{p_i}.\Delta\boldsymbol{r}^i_{\kappa,\kappa'}\right)}{\hbar}\right]\right.\\&\times exp\left[-W^p_{V,\kappa}\left(\boldsymbol{p_f},\boldsymbol{p_i}\right)\right]exp\left[-W^p_{V,\kappa'}\left(\boldsymbol{p_f},\boldsymbol{p_i}\right)\right]\\&\times\prod_{j=1}^{N_v}\sum_{\alpha_j=-\infty}^{\infty}\boldsymbol{I}_{|\alpha_j|\left(b_{\kappa,\kappa'}(\omega_j)\right)}\left[\frac{n\left(\omega_j\right)+1}{n\left(\omega_j\right)}\right]^{\alpha_j/2}\\&\left.\times\exp\left[-\frac{\left(E_f^T-E_i^T+E_f^R-E_i^R+\Delta E_0^T+\Delta E_0^R+\hbar\sum_{s=1}^{N_v}\alpha_s\omega_s\right)^2}{4k_bT_s+\left(\Delta E_0^T+\Delta E_0^R\right)}\right]\right\}\end{aligned} \tag{8.15}$$

The transition rate for the full molecule system with non-negligible vibrational transitions is given by Eq. (8.15). This is actually expressed as a product over

all normal modes labeled by j and a summation over the excitation quantum number denoted by α_j . To obtain the discrete transition rate to a particular internal mode final state or combination of states, one takes the corresponding $(j, \alpha_j)^{th}$ term of the above equation.

The dominant feature is the Gaussian-like function containing the three different modes of energy exchange (phonons, rotations, and internal molecular vibrations) together with the recoil terms from phonons ΔE_0^T and from rotational exchange ΔE_0^R . The width of the Gaussian-like function varies as the square root of the temperature and the sum of the two recoil energies. This is not a true Gaussian because of the momentum dependencies of the recoil energies. There are also Gaussian-like functions in the exchange of parallel momentum $\boldsymbol{P}$ and perpendicular angular momentum l_z that arise from retaining the correct momentum conservation conditions for a smooth surface. increased, the maximum intensity of the Gaussian-like function decreases in order that the total integral over final states remains constant

In many cases, such as where the incident molecular energy and the surface temperature are not large compared to the energy of molecular vibrational excitations, the expansion of Eq. (8.15) to only single quantum excitations is sufficient [284]:

$$
\begin{aligned}
w(\boldsymbol{p_f}, \boldsymbol{I_f}, \boldsymbol{p_i}, \boldsymbol{I_i}) =& \frac{1}{S_{uc}\hbar^2} \left|\tau_{fi}^2\right| \exp\left[-\frac{2v_R^2 \boldsymbol{P}^2}{4k_b T_s \Delta E_0^T}\right] \exp\left[-\frac{2\omega_R^2 l_z^2}{4k_b T_s \Delta E_0^R}\right] \\
&\times \left(\frac{2\pi\hbar^2 v_R^2}{k_b T_s \Delta E_0^T}\right)\left(\frac{2\pi\hbar^2 \omega_R^2}{k_b T_s \Delta E_0^R}\right)^{1/2}\left(\frac{\pi\hbar^2}{k_b T_s\left(\Delta E_0^T + \Delta E_0^R\right)}\right)^{1/2} \\
&\times \sum_{\kappa,\kappa'=1}^{N_A}\left\{ exp\left[\frac{i\left(\boldsymbol{p_f}.\Delta \boldsymbol{r}_{\kappa,\kappa'}^f - \boldsymbol{p_i}.\Delta \boldsymbol{r}_{\kappa,\kappa'}^i\right)}{\hbar}\right]\right. \\
&\times exp\left[-W_{V,\kappa}^p\left(\boldsymbol{p_f}, \boldsymbol{p_i}\right)\right] exp\left[-W_{V,\kappa'}^p\left(\boldsymbol{p_f}, \boldsymbol{p_i}\right)\right] \\
&\times \left\{\exp\left[-\frac{\left(E_f^T - E_i^T + E_f^R - E_i^R + \Delta E_0^T + \Delta E_0^R\right)^2}{4k_b T_s + \left(\Delta E_0^T + \Delta E_0^R\right)}\right]\right. \\
&+ \sum_{\alpha,\alpha'=1}^{3} p_\alpha p_{\alpha'} \sum_{j=1}^{N_v}\left[\frac{1}{2N_v\hbar\omega_j\sqrt{m_\kappa m_{\kappa'}}}\tilde{e}\left(\kappa, j|\alpha\right)\tilde{e}^*\left(\kappa', j|\alpha'\right)\right. \\
&\times \left(n(\omega_j)\exp\left[-\frac{\left(E_f^T - E_i^T + E_f^R - E_i^R + \Delta E_0^T + \Delta E_0^R - \hbar\omega_j\right)^2}{4k_b T_s + \left(\Delta E_0^T + \Delta E_0^R\right)}\right]\right. \\
&\left.\left.\left.\left. + \left[n(\omega_j) + 1\right]\exp\left[-\frac{\left(E_f^T - E_i^T + E_f^R - E_i^R + \Delta E_0^T + \Delta E_0^R + \hbar\omega_j\right)^2}{4k_b T_s + \left(\Delta E_0^T + \Delta E_0^R\right)}\right]\right)\right\}\right.
\end{aligned}
\tag{8.16}
$$

Further, for a molecule whose vibrational levels are far apart such that there is negligible vibrational transitions due to the interaction with the surface (rigid molecule), the transition rate can be simplified to [272]:

$$
\begin{aligned}
w(\boldsymbol{p_f}, \boldsymbol{I_f}, \boldsymbol{p_i}, \boldsymbol{I_i}) =& \frac{1}{S_{uc}\hbar^2} \left|\tau_{fi}^2\right| \left(\frac{2\pi\hbar^2 v_R^2}{k_b T_s \Delta E_0^T}\right)\left(\frac{2\pi\hbar^2 \omega_R^2}{k_b T_s \Delta E_0^R}\right)^{1/2}\left(\frac{\pi\hbar^2}{k_b T_s\left(\Delta E_0^T + \Delta E_0^R\right)}\right)^{1/2} \\
&\times \exp\left[-\frac{2v_R^2 \boldsymbol{P}^2}{4k_b T_s \Delta E_0^T}\right] \exp\left[-\frac{2\omega_R^2 l_z^2}{4k_b T_s \Delta E_0^R}\right] \\
&\times \exp\left[-\frac{(E_f^T - E_i^T + E_f^R - E_i^R + \Delta E_0^T + \Delta E_0^R)^2}{4k_b T_s\left(\Delta E_0^T + \Delta E_0^R\right)}\right]
\end{aligned}
\tag{8.17}
$$

Furthermore, for the molecules for which the rotational transitions are also negligible and for atoms, the transition rate consists of only translational energy terms, and can be defined as [437]

$$w(\boldsymbol{p}_f, \boldsymbol{p}_i) = \frac{2\hbar v_R^2}{S_{uc}} \left|\tau_{fi}^2\right| \left(\frac{\pi}{k_b T_s \Delta E_0^T}\right)^{3/2} \times \exp\left[-\frac{(E_f^T - E_i^T + \Delta E_0^T)^2 + 2v_R^2 \boldsymbol{P}^2}{4k_b T_s \Delta E_0^T}\right] \tag{8.18}$$

The form factor τ_{fi} is the transition matrix of the interaction potential taken between the incoming and final state of the system (substrate plus gas particle). A commonly used approximation that has been successful in numerous calculations [438, 439, 440, 437, 272, 283, 284] is the Born hard repulsive wall limit which simplifies the expression of the scattering form to the following [437].

$$\tau_{fi} = \frac{2p_{iz}p_{fz}}{m} \tag{8.19}$$

Now, the transition rate expressed in Eq. (8.15) can be directly evaluated for given initial conditions. In order to obtain the quantities related to the final distribution of the scattered gas particles from MD-QCT calculations, this transition rate must be connected to the differential reflection coefficient (DRC). DRC gives the fraction of the incident particles that have energy in the interval of dE_f^T centered around E_f^T and are scattered into a final solid angle of the detector $d\Omega_f$. This is proportional to the transition rate and is calculated by dividing with the incident flux parallel to the surface and multiplying with the density of the final states available [284].

$$\frac{d^3R}{d\Omega_f dE_f^T}\left(\boldsymbol{p}_f, \boldsymbol{I}_f, \boldsymbol{p}_i, \boldsymbol{I}_i\right) = \frac{L^4}{(2\pi\hbar)^3}\frac{m^2|\boldsymbol{p}_f|}{p_{iz}} w\left(\boldsymbol{p}_f, \boldsymbol{I}_f, \boldsymbol{p}_i, \boldsymbol{I}_i\right) \tag{8.20}$$

Finally, in order to be able to compare with the experiments directly, the detector efficiency must be accounted for. If the experiments measure the flux of the products, this efficiency is unity, while for an equipment measuring the number density, the efficiency is directly proportional to the time spent within the detector volume. High speed particles are less likely to be detected, while slower particles are easier to capture. Thus, in order to obtain the distributions that can be directly compared to the experiments, a correction is applied [272].

$$\left(\frac{d^3R}{d\Omega_f dE_f^T}\right)_{corr} = \left(\frac{d^3R}{d\Omega_f dE_f^T}\right) \times \frac{1}{\sqrt{E_f^T}} \tag{8.21}$$

This DRC can be converted to a distribution of time to obtain the TOF distributions. In order to obtain the angular distributions, the DRC must be averaged over the final energy and angular momentum.

8.3 Calibration with MD results

There are a total of five "free" parameters within the MSS theory: (i) effective surface mass M_s, (ii) average phonon velocity v_R, (iii) effective moment of inertia of the surface I_s, (iv) average frustrated rotational angular velocity ω_R, and (v) effective surface reduced mass μ_s. The values for these parameters can be assumed to be the equal to the properties of a single surface atom. But this approach has shown to be inadequate in predicting the experimental distribution [437, 272, 441, 442]. Physically, the incoming atom/molecule will interact with more than a single surface atom. Even in the case of hyperthermal scattering from highly corrugated surface, the neighboring surface atoms determine the motion of the interacting surface atom, and thus the incident gas particle. Thus, these parameters must be computed as an effective value for the entire surface. Such computations are usually highly complex, and these parameters are varied to obtain the best fit to the experimental data [437, 272, 441, 442].

The values for these parameters are computed by obtaining the best fit to the MD results that were presented in the previous chapter. The least square method is used for the fitting process. Generally it was observed that the parameters M_s and v_R predominantly affect the translational and angular energy distributions, while having a small effect on the rotational and vibrational distributions. This is consistently observed for the other parameters as well: I_s and ω_R for rotational distributions and μ_s for vibrational distributions. Although cross term effects are present in the system, they are negligible. The parameter ω_R was found to

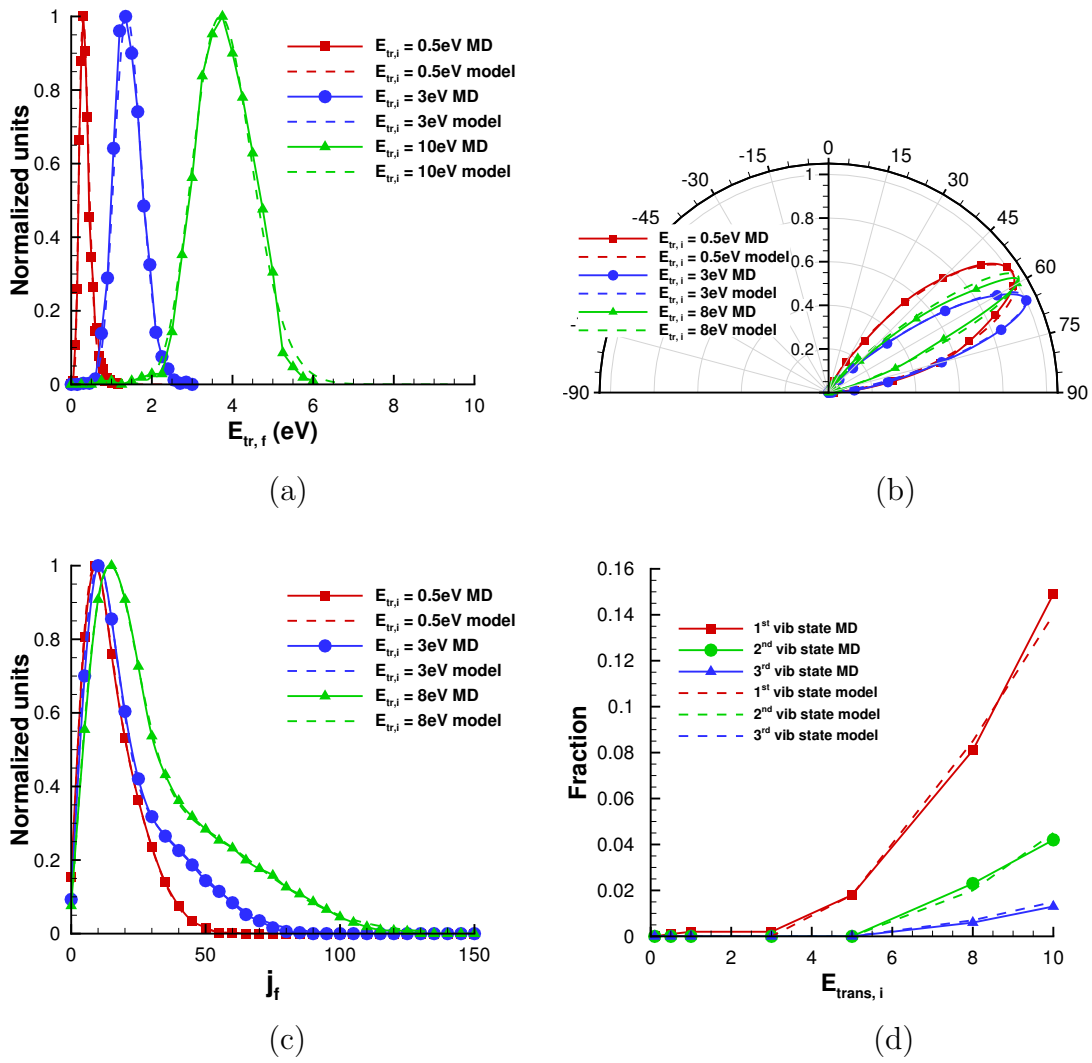

Figure 8.1: Final normalized distribution of (a) translational energy, (b) polar angle, (c) rotational state, and (d) vibrational state of scattered O_2 molecules obtained using MD-QCT simulations and MSS theory for three initial translational energies of 0.5, 3, and 8 eV. For the vibrational state, the transition probability is presented rather than the distributions. The other initial parameters of the incident O_2 molecule were kept constant at $j_i = 0$, $v_i = 0$, $\theta_i = 45°$, and $T_{surf} = 1000$ K.

have only negligible effect on all the final distributions even with large variations, consistent with the previous works [284], and thus was taken to be constant for all the cases. Finally, the fitted values for all the mass and moment of inertia parameters were observed to be greater than the values for a single surface atom consistent with the discussion above.

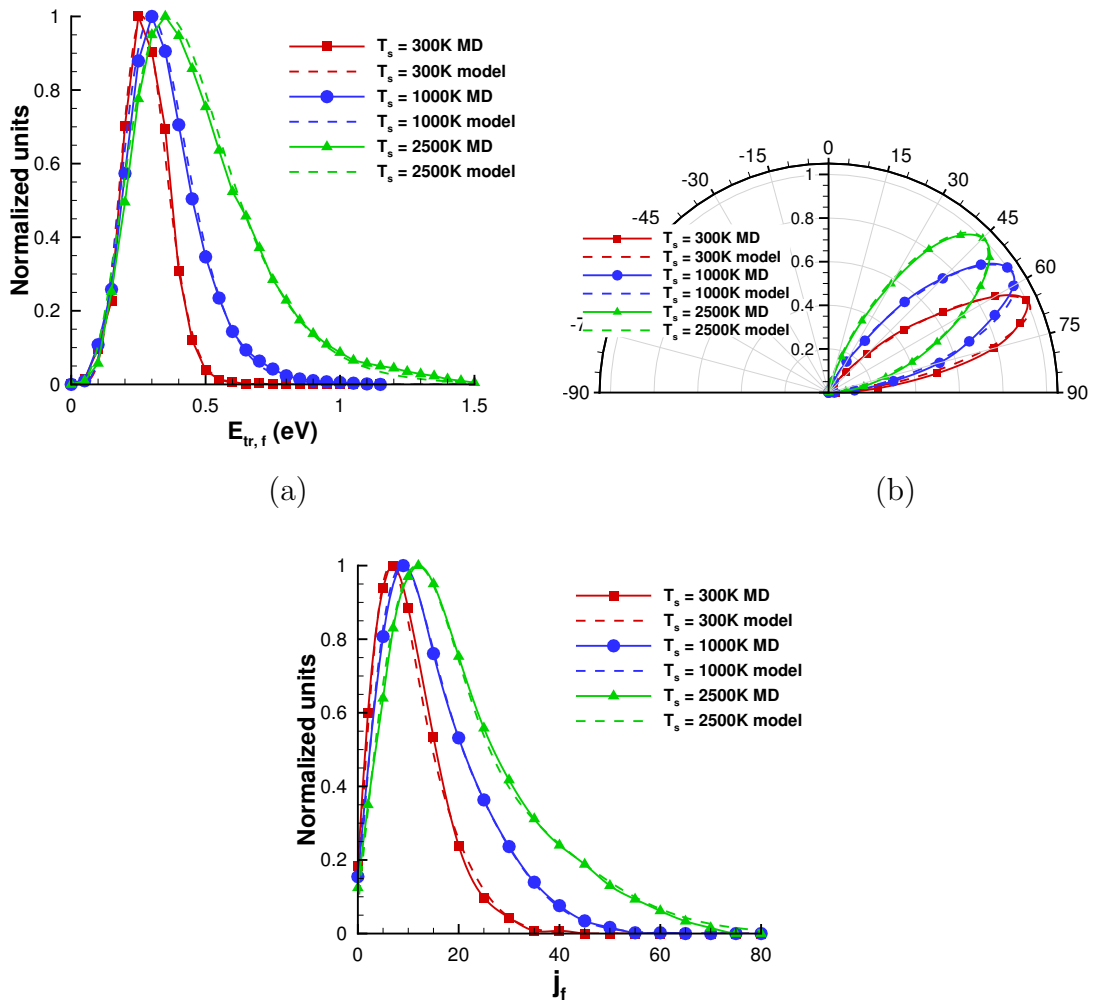

Figure 8.2: Final normalized distribution of (a) translational energy, (b) polar angle, and (c) rotational state of scattered O_2 molecules obtained using MD-QCT simulations and MSS theory for three surface temperatures of 300, 1000, and 2500 K. The other initial parameters of the incident O_2 molecule were kept constant at $E_{tr,i} = 0.5$ eV, $j_i = 0$, $v_i = 0$, and $\theta_i = 45°$.

The translational, rotational, and vibrational energy and angular distributions obtained using the fitted MSS parameters are plotted alongside the distributions obtained from MD for comparison. Fig. 8.1 presents the different distributions for varying initial incident energy of the molecule, while Fig. 8.2 shows the distributions for the different surface temperatures. Excellent agreement is obtained between the MSS and MD distributions. All of the features in the various distribu-

tions are captured by the MSS theory in thermal, structural and transition regime. The values of the "free" parameters are presented in the next section along with their variation with the initial translational energy of the molecule and the surface temperature. In addition, the physical significance of their variation is also discussed.

8.4 Discussion

8.4.1 Effect of Initial Translational Energy

First the variation of the four MSS parameters with the initial translational energy of the molecule is studied. Fig. 8.3 presents the fitted MSS parameters of effective surface mass (Fig. 8.3 (a)), average phonon velocity (Fig. 8.3 (b)), effective surface moment of inertia (Fig. 8.3 (c)), and effective surface reduced mass (Fig. 8.3 (d)) as a function of the initial molecule translational energy.

The effective surface mass M_s is observed to increase with the initial translational energy of the molecule. This is consistent with the previously observed results for the MSS theory by Manson and co-workers [437, 272, 441, 442]. As the initial translational energy of the gas particle increases, larger energy is transfered to the surface during collision. This energy is effectively dissipated over higher number of atoms, leading to an higher effective mass for the scattering event. Further, the value of the effective masses are always higher than that of a single carbon atom, since multiple surface atoms will be involved in the collision and scattering event.

A constant value for the average phonon velocity was able to consistently match the MD data for the full range of initial translational energy. The phonon velocity is a property of only the surface and thus unaffected by the variation in the initial translational energy of the molecule.

Both the effective moment of inertia and the effective reduced mass of the surface also exhibit an increasing trend with the initial translational energy of the

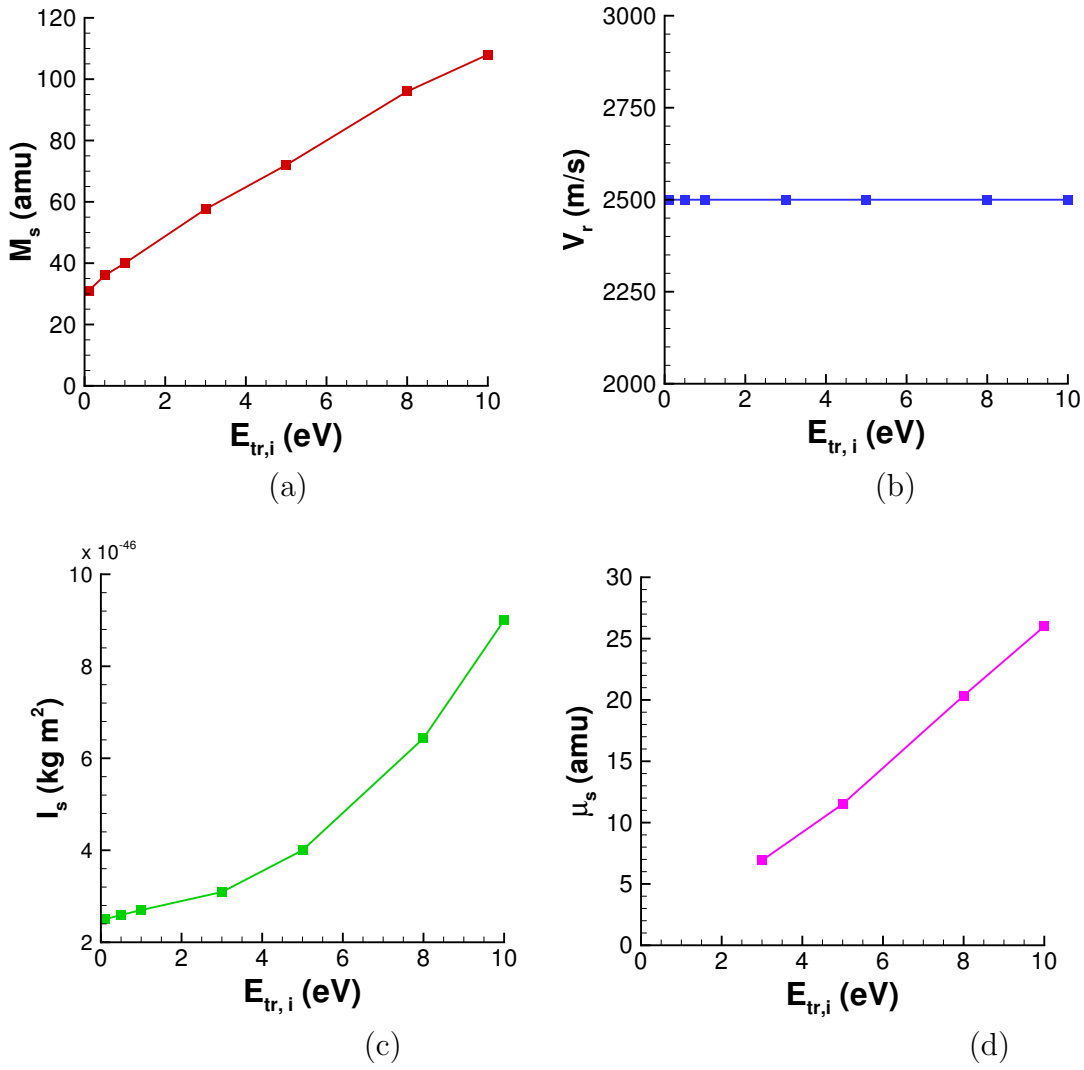

Figure 8.3: Variation of the MSS model parameters (a) effective surface mass, (b) average phonon velocity, (c) effective surface moment of inertia, and (d) effective surface reduced mass as a function of the initial translational energy of the molecule.

molecule. This is in line with the increasing final distributions of the rotational and vibrational energy of the molecules. Although the increasing internal energies are a result of transfer of energy from the translational modes, the MSS theory describes this process as a transfer from the surface to the molecule, leading to the observed increase in the effective moment of inertia and reduced mass. The values of the reduced mass could only be obtained for energies greater than 3 eV since vibrational transitions were observed only at higher energies.

8.4.2 Effect of Surface Temperature

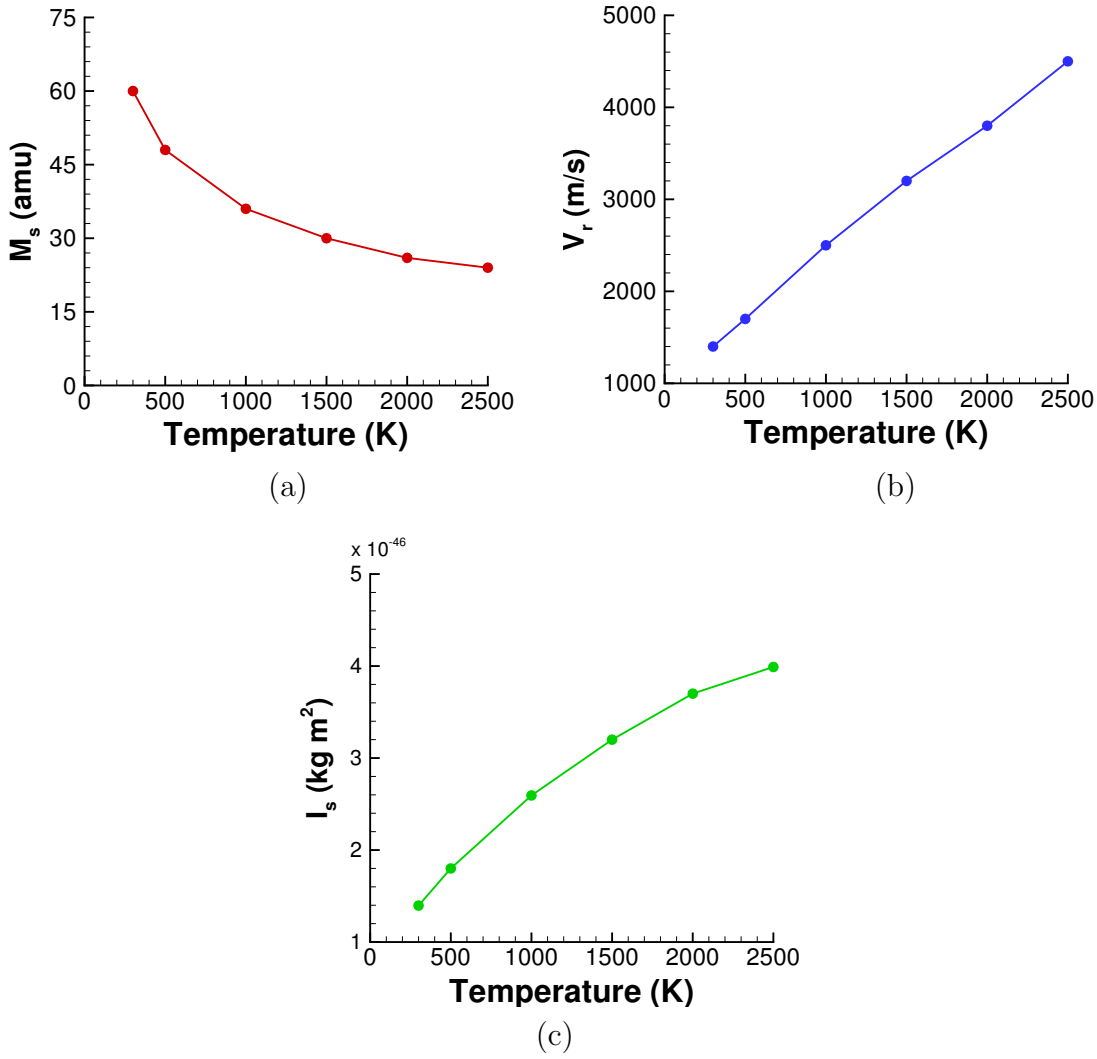

Figure 8.4: Variation of the MSS model parameters (a) effective surface mass, (b) average phonon velocity, and (c) effective surface moment of inertia as a function of the surface temperature.

The effect of the surface temperature on the various MSS parameters is studied next. Fig. 8.4 shows the fitted MSS parameters of effective surface mass (Fig. 8.4 (a)), average phonon velocity (Fig. 8.4 (b)), and effective surface moment of inertia (Fig. 8.4 (c)) as a function of the surface temperature. Since the initial translational energy of the molecules was low for these calculations, vibrational transitions were not observed for these cases, and thus the effective reduced mass

of the surface could not be computed.

The average phonon velocity of the surface is observed to increases with surface temperature, consistent with the previous discussion. However, in this case, the effective surface mass is found to decrease with the surface temperature. As the surface temperature increases, the surface atoms have greater energy, and are able to absorb more energy during the collision. This results in the collision energy being dissipated over smaller number of atoms leading to the decrease in effective surface mass.

In contrast to the effective surface mass, the effective surface moment of inertia actually increases with the surface temperature. However, this is again in line with the greater final rotational energy distributions. In this case, the transfer of energy to the rotational mode comes from the surface, and not the translational mode of the molecule. Thus, the increase in the effective moment of inertia of the surface is consistent with the physical energy transfer mechanism.

8.5 Summary

The molecule surface scattering (MSS) theory is a rigorous theoretical model based on gas-phonon interactions at the surface is used to describe the final energy (translational, rotational, and vibrational) and angular distributions for an oxygen molecule scattering from a graphite surface. The MSS model considers several such mechanisms including multi-phonon processes, translational and internal mode (rotational and vibrational) excitations. The translational and rotational modes of the gas particle are treated classically within this framework while the quantum mechanical nature of the vibrational modes are taken into account. Further, this model provides a state-resolved description of the scattered particles through the evaluation of the detailed scattering kernels and transition matrix.

Since the parameters within the MSS model are difficult to obtain, these parameters are varied to obtain the best fit to the experimental or MD data. In the present work, four "free" parameters namely effective surface mass M_s, average

phonon velocity v_R, effective surface moment of inertia I_s, and effective surface reduced mass μ_s are varied to match the MD data presented in the previous chapter. The values of the "free" parameters are presented along with their variation with the initial molecule translational energy and the surface temperature. In addition, the physical significance of their variation is also discussed.

The least square method is used for the fitting process. It was observed that the cross term effects of the all the parameters were negligible. This means that the translational parameters (M_s and v_R) only affect the translational energy (and angular) distributions, and have negligible effect on the internal energy distributions. This is consistently observed for the other parameters as well: I_s and ω_R for rotational distributions and μ_s for vibrational distributions. Excellent agreement is obtained between the MSS (with fitted parameters) and MD distributions. All of the features in the various distributions are captured by the MSS theory in thermal, structural and transition regime.

The average frustrated rotational angular velocity parameter ω_R was found to have only negligible effect on all the final distributions even with large variations and was taken to be constant for all the cases. The fitted values for all the mass and moment of inertia parameters were observed to be greater than the values for a single surface atom, since physically, the incoming atom/molecule will interact with more than a single surface atom, and multiple surface atoms will be involved in collision and scattering event.

The effective surface mass M_s is observed to increase with the initial molecule translational energy, while it was observed to decrease with increasing surface temperature. As the initial translational energy of the gas particle increases, a greater amount of energy is transfered to the surface during collision, which is effectively dissipated over larger number of atoms, leading to an higher effective mass for the scattering event. In the case of increasing surface temperature, the surface atoms have greater energy, and are able to absorb more energy during the collision. This results in the collision energy being dissipated over smaller number of atoms leading to the decrease in effective surface mass.

The average phonon velocity of the surface is observed to increases with surface temperature, and remains constant across the entire molecule translational energy range. This is consistent since the phonon velocity is a property of only the surface and thus unaffected by the variation in the initial translational energy of the molecule.

In contrast to the effective surface mass, the effective surface moment of inertia increases with both the initial translational energy of the molecule and the surface temperature. This is in line with the increasing final rotational energy distributions observed in both the cases. In the case of the initial translational energy, although the increasing internal energies are a result of transfer of energy from the translational modes, the MSS theory describes this process as a transfer from the surface to the molecule, leading to the observed increase in the effective moment of inertia. However for the temperature case, the transfer of energy to the rotational mode comes from the surface, and not the translational mode of the molecule. Thus, the increase in the effective moment of inertia of the surface is consistent with the physical energy transfer mechanism.

Finally, the effective reduced mass of the surface was computed only at higher initial translational energies (greater than 3 eV) since the vibrational transitions are observed only for these cases. Similar to the case of effective surface moment of inertia, the effective surface reduced mass also exhibits an increasing trend with the initial translational energy of the molecule. Again, this in line with the increasing final distributions of the vibrational energy, resulting in the observed increase of the effective surface reduced mass.

Part IV

Desorption from Surfaces

Chapter 9

Surface Phonon Density of States

9.1 Overview

The density and energy of phonons present at the surface is described through the phonon density of states (PDOS). The phonon density of states (PDOS) is a fundamental property of the material and the lattice, which characterizes the distribution of allowed vibrational modes. The PDOS can provide information regarding heat storage (heat capacity), energy transport (lattice thermal conductivity), gas-surface interactions,[284] and surface chemistry. The PDOS shows significant variation in the presence of adsorbates, random surface defects, and etch pits (formed due to oxidation). Thus, the surface phonon density of states (PDOS) is expected to evolve during the course of ablation.

The PDOS is an important input within the phonon-induced desorption (PID) model (described in the next chapter). The vibrational modes present in the system is greatly altered when the distribution of the substrate atoms is changed. Molecular Dynamics (MD) is used to investigate the effect of the presence of (i) adsorbates, (ii) random surface defects, (iii) etch pits (formed due to oxidation) on the PDOS of the system, and (iv) a combination of random surface defects with etch pits.

This chapter is organized as follows. The simulation methodology used to compute the phonon density of states is presented in Section 9.2. Section 9.3 describes the construction of the lattice surface with the presence of various defect configurations. The results of the MD simulations and the analysis of the PDOS of the various defect configurations are discussed in Section 9.4. Finally the summary

and conclusions are presented in Section 9.5.

9.2 Simulation Methodology

The phonon density of states were calculated using the LAMMPS Molecular Dynamics (MD) software [427] which uses parallelization through both CPUs and GPUs. The PDOS is computed through the determination of the velocity autocorrelation function (VACF).

$$VACF = \frac{< v(t).v(0) >}{< v(0)^2 >} \tag{9.1}$$

where $v(0)$ is the average velocity vector of a particle at initial time, $v(t)$ is the average velocity at time t, and ω is the frequency. The VACF is computed and stored at regular intervals during the MD simulations. The averaging within the VACF is performed over only the lattice atoms. The Fourier transform of the VACF gives the density of states for the particular system.

$$g(\omega) = \int \frac{< v(t).v(0) >}{< v(0)^2 >} e^{i\omega t} dt \tag{9.2}$$

The system was equilibrated in an isobaric-isothermal ensemble, thus all PDOS approach zero at $\omega = 0$. After equilibration, the NVE ensemble with a time step of 0.1 fs is used to gather the VACF . The average of the VACF is calculated for ten different independent cases. All PDOS calculations were performed at 1000 K and for times long enough to obtain a good frequency resolution. The standard verlet velocity scheme is used with periodic boundary conditions along the directions parallel to the surface (x and y direction). In the direction perpendicular to the surface (z direction), there is no periodic boundary condition since the aim is to simulate the surface. At the bottom of the lattice, additional 3 layers are added so as to simulate infinite solid in the negative z direction. The atoms within these additional layers are not used within the VACF calculations.

The main input within the MD simulation is the inter-atomic potential. The

carbon system has been and continues to be the focus of a large number of studies, leading to a wide array of inter-atomic potentials, developed to capture several different aspects computationally [431]. In order to choose an appropriate potential for this study, three important criteria needed to be satisfied: (i) the phonons in the system have to accurately represented, (ii) changes in the bonding between the atoms due to the presence of defects have to be accounted, and (iii) the surface atom - adatom bonding needs to be consistently modeled.

With these criteria, the reaxFF potential, a transferable bond-order dependent potential was chosen for this study to describe the C-C, C-O, and C-N interactions. Since the potential accounts for the bond-order, it is expected to capture the effects of the lattice defects reasonably well. ReaxFF potential is an empirical potential with a general form for various types of forces [428].

$$E_{system} = E_{bond} + E_{over} + E_{under} + E_{val} + E_{pen} + E_{tors} + E_{conj} + E_{vdWaals} + E_{Coulomb}. \tag{9.3}$$

The various parameters within this form are parameterized against an extensive quantum chemical database. The value of the parameters used in this study are taken from Shin *et al* [429]. The C-C bond parameters used in this work were recently re-parameterized to better capture the properties of the solid carbon phase [430]. The ReaxFF potential and the corresponding set of parameters are ideal for this study because they can capture both short and long range bonds within solid carbon [431] as well as the reactive interaction between the carbon and adsorbate atoms [432].

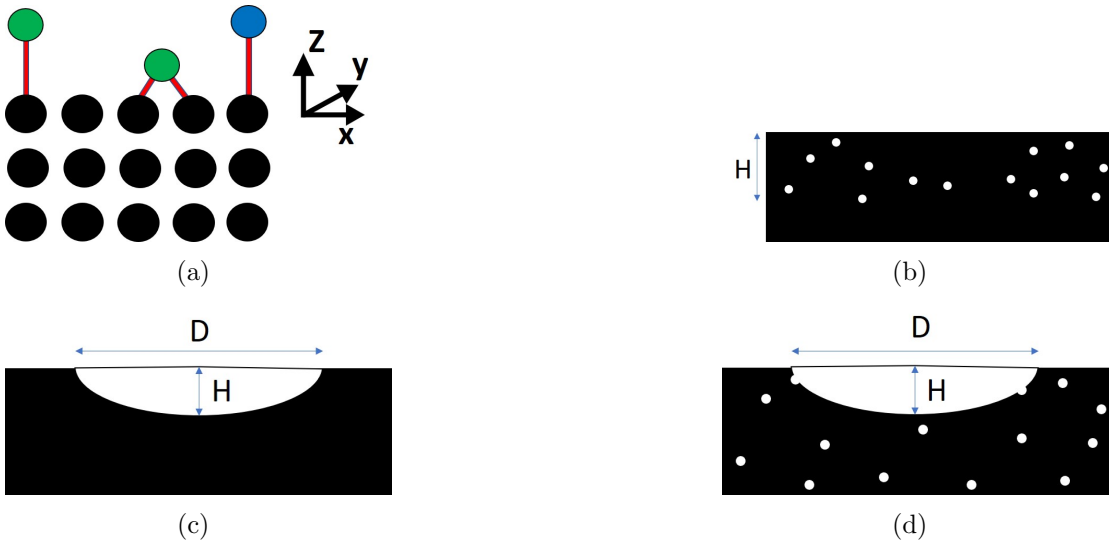

(a) (b) (c) (d)

Figure 9.1: Schematic illustration of side view of the lattice with (a) adsorbates, (b) random surface defects, (c) an etch pit, and (d) an etch pit and random surface defects.

9.3 Lattice Surface Construction

9.3.1 Adsorbates on the surface

The adsorbates are randomly placed on a pristine graphite surface at the top sites (exactly on top of the carbon atoms), and allowed to relax before the PDOS is computed (Fig. 9.1 (a)). The PDOS of surface covered with adsorbates is characterized as a function of the surface coverage at three values of 0 (empty), 0.5, and 1 (full monolayer). Since the interaction of carbon surfaces with dissociated air is the focus of this work, both oxygen and nitrogen atom adsorbates were considered.

9.3.2 Random surface roughness

For purposes of this study, the random surface defects are introduced on the graphite carbon by irradiation with low energy ions [443]. The surface defects are characterized based on the depth (height H) of the defective region and the areal density (number of defects per unit area ρ) as shown in Fig. 9.1 (b). Pristine

graphite lattice is bombarded with ions of different energies to obtain the desired defect configurations of different depths and densities.

9.3.3 Etch pits

The etch pits are formed due to oxidation processes and are ellipsoidal in shape [444]. These etch pits are characterized based on the depth (or height H) and diameter of the ellipsoid as shown in Fig. 9.1 (c). The diameter of these etch pits are usually much greater than the height (or depth). This is because the oxidation along the lateral direction is much faster than along the normal direction [444]. These etch pits are directly obtained in MD by removing the atoms within the ellipsoidal region of pristine graphite lattice.

9.3.4 Etch pits with surface roughness

In order to obtain the lattice with both etch pits and surface roughness, the ellipsoidal region of the etch pit is removed from the rough surfaces obtained from the irradiation simulations (Fig. 9.1 (d)). The effect of etch pits with random surface roughness is characterized by the size (both diameter and height) of the etch pits, while using a constant surface roughness.

9.4 Results and Discussion

9.4.1 Surface and bulk PDOS

Before investigating the effect of surface defects on the PDOS, first the difference between the surface and bulk PDOS is analyzed. Atoms at the surface have higher energies and can move more freely due to the absence of atoms above them. Fig. 9.2 presents the PDOS for surface and bulk carbon graphite lattice. The difference between them is predominantly along the surface normal (lower

energies). The surface PDOS has increased concentration of phonons at the lower energies and decreased concentration at higher energies compared to the bulk. Other characteristics such as the final peak are preserved in the surface PDOS.

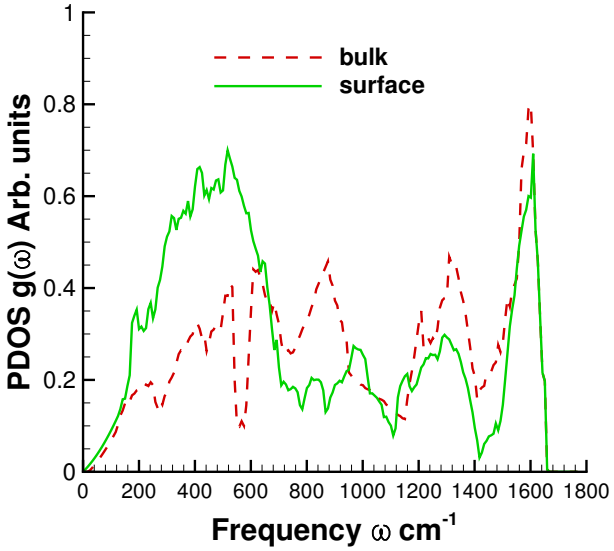

Figure 9.2: PDOS of surface and bulk carbon graphite lattice.

9.4.2 Effect of adsorbates

Next, the effect of adsorbates on the PDOS is investigated. The presence of adsorbates will alter the vibrations predominantly along the z-direction. The adsorbates are expected to have a significant effect on the PDOS since the inter-layer bonding between the carbon graphite layers is weak. The results of this study is shown in Fig. 9.3 which plots the PDOS along the surface normal (z-direction). First, it is observed that the presence of adsorbates shifts the PDOS modes towards lower frequencies. In addition, it is noticed that the PDOS peaks of the adsorbate covered lattice are also broad compared to the PDOS of empty surface.

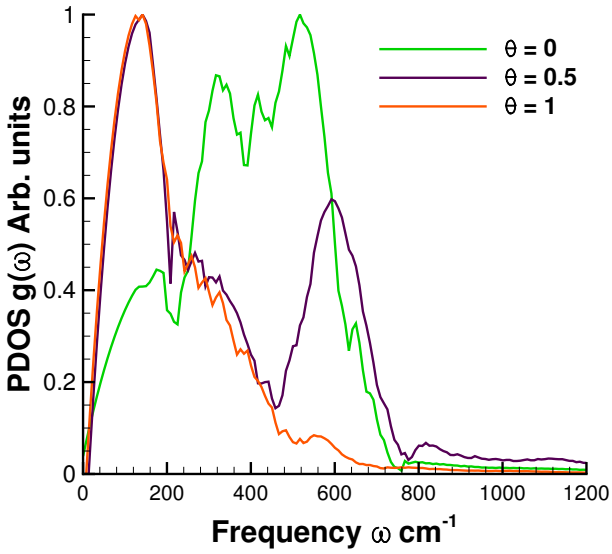

Figure 9.3: PDOS along the surface normal (z-direction) of carbon graphite surface with surface coverage of (θ) of 0, 0.5, and 1.

9.4.3 Effect of random surface defects

The effect of random defects present at and near the surface on the PDOS is investigated next. This study analyzes the effect of varying both the depth and density of the defective region on the PDOS is studied (as shown in Fig. 9.4). It is observed that the presence of defects broadens the peak within the PDOS. Additional modes at very low energies are also observed for the defective surfaces. In general, the presence of surface roughness systematically shifts the PDOS modes from higher frequencies to lower frequencies. However, additional densities at frequencies greater than the final peak of the pristine system is also observed. This is most likely a result of the close packing of defects at certain regions.

9.4.4 Effect of etch pits

The variation in PDOS due to the presence of etch pits is analyzed next. The effect of varying height and diameter of the etch pit on the surface PDOS is presented in Fig. 9.5. Although the values of D and H were limited to Angstrom scales due to the computational requirements of MD simulations, the ratio of D:H were chosen

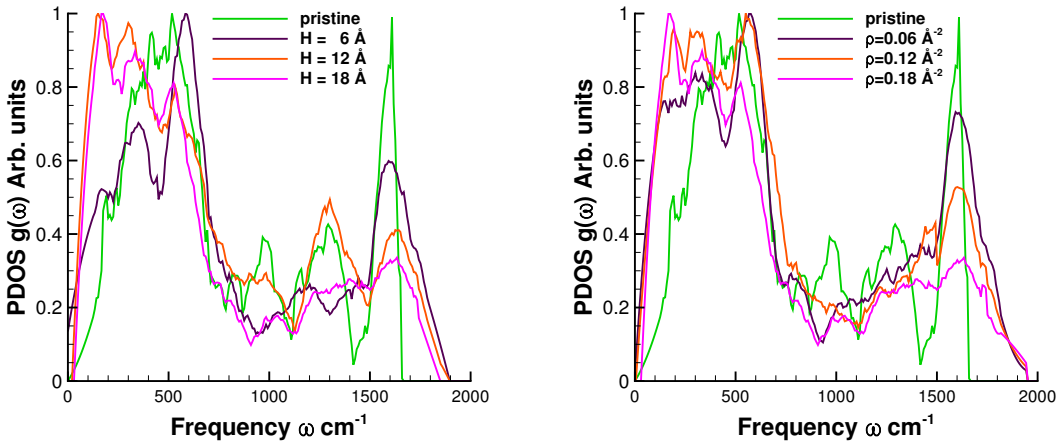

Figure 9.4: PDOS of carbon graphite surface with random surface roughness of (a) varying depths (heights) and (b) varying densities.

to be of the same range as found in the experiments [444, 445, 446]. Similar to the case of random surface defects, the presence of etch pits tend to broaden the PDOS modes and more rounded peaks are observed. Also the PDOS modes are shifted towards lower frequencies due to the etch pits. Again, additional densities at frequencies greater than the final peak of the pristine system is observed similar to the case of random surface defects. However, the PDOS is found to be insensitive to the geometry of the etch pits resulting in very similar density of states for the range of D and H values.

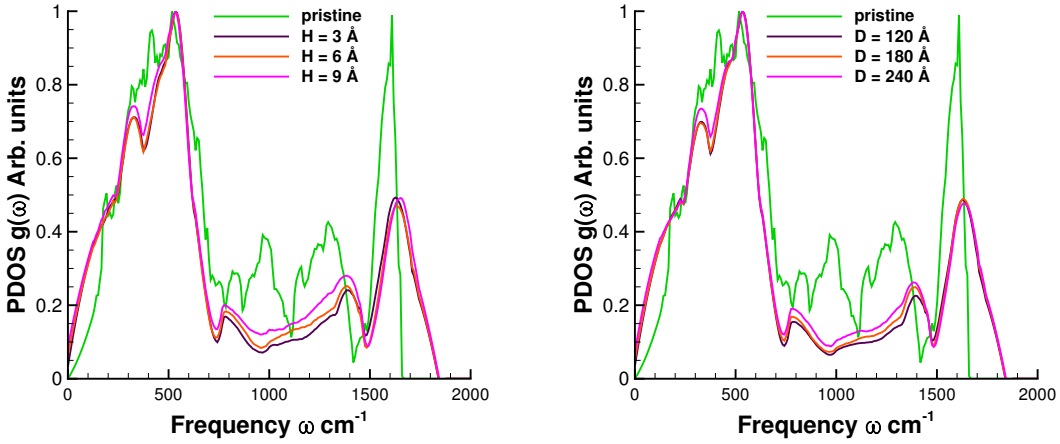

Figure 9.5: PDOS of carbon graphite surface with etch pit of (a) varying depths (heights) and (b) varying diameters.

9.4.5 Effect of etch pits with surface roughness

Finally, the effect of both the etch pits and surface roughness is studied. Fig. 9.6 shows the effect of variation in the diameter and height of the etch pit. The surface roughness was kept constant at H = 18 Å and $\rho = 18$ Å^{-1}. Similar to the previous study, the values of D and H are chosen to emulate the D:H ratio found in the experiments. First, it is observed that the effect of varying diameter and height of the etch pit has negligible influence on the final PDOS for the range studied, consistent with the previous section. In comparison to only etch pit case, it is observed that the PDOS is shifted toward even lower frequencies. The position of the first peak is similar to the case with only surface roughness, however the later peaks are not observed.

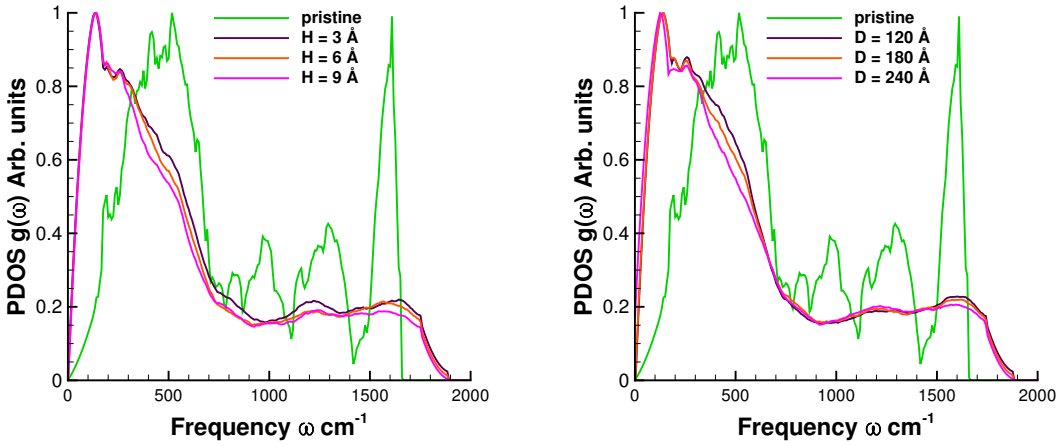

Figure 9.6: PDOS of carbon graphite surface with surface roughness and etch pit of (a) varying depths (heights) and (b) varying diameters.

9.5 Summary

The surface PDOS is an important input for describing the phonon-induced desorption process (next chapter). The results of the detailed MD study suggests that the PDOS varies widely as a result of defects present within the system. In general any kind of defect tends to broaden the phonon distributions resulting in

rounded peaks. Further, the PDOS is consistently observed to be shifted towards lower frequencies leading to lower densities at higher energies. The effect of the adsorbates is predominantly along the surface normal direction. In the case of random surface defect, the PDOS was found to be sensitive to both the presence and configuration of the defects. However, for the etch pits, the PDOS is observed to be only dependent on the presence of the etch pit and insensitive to the exact configuration. Similar consistent results are observed for the case with both surface roughness and etch pits.

Chapter 10

Phonon-Induced Desorption

10.1 Overview

Desorption of thermal products from the substrate occur through the interaction with the phonon bath on the surface. Several finite-rate reaction models exist for the air-carbon system,[37, 36, 35, 85, 6] developed using results from numerous experimental studies [447, 448, 449, 450, 144, 451, 5]. However, all of these models characterize the rate of desorption only as a function of temperature. The effect on the desorption rate due to variations in the surface phonons which is a function of the surface structure and configuration need to be characterized for these systems. A mesoscale description of the surface energetics which participate in, and promote, the desorption of surface adsorbates and oxidation products is currently lacking.

In this chapter, a rigorous theoretical model is used to describe the desorption of adsorbed atoms/molecules due to interaction with the surface phonons [349]. The adsorbate-surface interaction (oscillator) is coupled with the phonon bath leading to excitations and de-excitations along the vibrational 'ladder'. This process can be described as a random walk using the Markoffian approximation and first order master equation is solved for the probability in a given state. This random walk continues till the interaction energy becomes sufficient to break the adsorbate-surface bond leading to desorption. Traditionally simple harmonic oscillators (SHO) are used to describe the vibrational bond [8]. However, within the harmonic approximation, the bond breaking is not inherently captured and has to be imposed, typically as a vibrational threshold beyond which desorption is assumed.

In addition, the energy spacing between the oscillator levels are constant within the SHO approximation, which becomes a poor approximation particularly at the higher energy levels. Furthermore, the SHO allows only mono-quantum jumps, which again breaks down at higher energy levels. The Morse potential provides a much better approximation to the adsorbate surface bond with decreasing energy gaps at higher levels, finite probability of multi-quantum transitions and a clear threshold between the free and bound states. Thus, the Morse potential is employed within this framework to describe the adsorbate-surface interaction potential [349].

The transition matrix describing the probability of transition between the oscillator energy levels accounts for the PDOS present at the surface. The coupling of the oscillator jump with each of the phonon modes is summed to give the final transition rate. Thus, introducing a realistic PDOS within the calculation of the transition matrix ensures the accurate description of the transition rates and thereby the desorption rate. The time between successive transitions (jumps) of a particular surface-adsorbate oscillator within the vibrational ladder is known to be much higher than the characteristic vibrations of the adsorbate and surface atoms [375]. This fact allows the treatment of these transition processes as rare events and use Markoffian random walks to analyze them. The desorption process is treated as first order and a Master equation is used to derive the final rate constant [349].

This chapter is organized as follows. The theoretical framework describing the phonon-induced desorption process is presented in Section 10.2. Section 10.3 describes the process of computing the transition and desorption rates for the different systems of interest. The results of this study are discussed in Section 10.4 and the transition rates and the desorption rates of the pristine and defective systems are compared and analyzed. Finally the conclusions and summary are presented in Section 10.5.

10.2 Theory

In order to describe the desorption of adsorbed atoms/molecules from the surface due to the interaction with the phonon bath, the theory by Efrima *et al.*[349] is used. This theory begins by describing the Hamiltonian of the system which consists of three parts: lattice (l), particle (p) and interaction (I) [349].

$$H = H_l + H_p + H_I \tag{10.1a}$$

$$H_l = \hbar \sum_{\lambda} \omega_\lambda b_\lambda^\dagger b_\lambda \tag{10.1b}$$

$$H_p = K_p + \langle V(\boldsymbol{Q}; z) \rangle \tag{10.1c}$$

$$H_I = V(\boldsymbol{Q}; z) - \langle V(\boldsymbol{Q}; z) \rangle \tag{10.1d}$$

The lattice Hamiltonian is described over the phonons (λ) in the system. ω is the phonon frequency while b and $b^\dagger$ are the corresponding creation and annihilation operators. K_p is the kinetic energy of the particle, $V(\boldsymbol{Q}; z)$ is the interaction potential between the adsorbate and the surface atom, and $\langle V(\boldsymbol{Q}; z) \rangle$ is the thermal average of the lattice-particle interaction over an equilibrium phonon distribution. $\boldsymbol{Q}$ is 3N dimensional and denotes the position of the N lattice atoms and z is the position of the adsorbed particle. $H_l + H_p$ is the zero-order part of the Hamiltonian while H_I describes the fluctuations in the system. The reason for the addition of the average quantity $\langle V(\boldsymbol{Q}; z) \rangle$ is to ensure that the average of the interaction Hamiltonian is zero which avoids the buildup of secular terms in the subsequent derivation [349]. The adsorbate-surface interaction potential is described using a Morse potential:

$$V(\boldsymbol{Q}; z) = D \left\{ e^{-2\alpha(z - \boldsymbol{Q}_0 - \boldsymbol{u} - r_0)} - 2e^{-\alpha(z - \boldsymbol{Q}_0 - \boldsymbol{u} - r_0)} \right\} \tag{10.2}$$

where $\boldsymbol{Q}_0$ is the equilibrium lattice position and $\boldsymbol{u}$ is the displacement of the atoms. α and r_0 are the Morse potential parameters. The Morse potential is

an excellent approximation for the adsorbate-particle interaction since it captures bond breaking (desorption), multi-quantum jumps, and decreasing energy spacing at higher energies. Thus, the definition of the bound states and free state within the model is straightforward and the ladder climbing pathway of desorption can be captured along with multi-quantum jumps (Fig. 10.1).

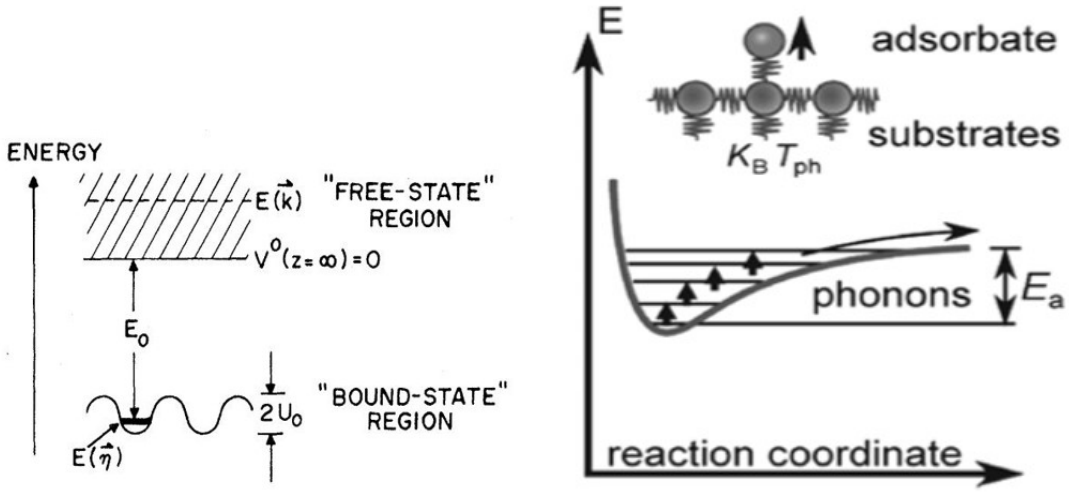

Figure 10.1: (a) Schematic showing the bound and free-state regions for an adsorbed particle [8]. (b) Ladder climbing model describing the pathway of desorption [9].

Now, the generalized master equation is presented, which describes the time evolution of the probability of the adsorbates being present in a particular state $|n\rangle$ at time t:[349]

$$\frac{\partial P_n}{\partial t} = -\sum_m W_{n\to m} P_n(t) + \sum_m W_{m\to n} P_m(t) - \int W_{n\to\epsilon} P_n(t) d\epsilon \tag{10.3}$$

The first term on the right side of the equation describes the transitions from state n to all other states, while the second term represents the all the transitions leading to the state n. The last term denotes the depletion from state n to the continuum state ϵ (desorption). Expressing $P_n(t)$ in terms of the reduced density matrix:[349]

$$P_n(t) = \langle n| \rho_r(t) |n\rangle . \tag{10.4}$$

Here, $\rho_r(t)$ is the reduced density matrix of the particle which is defined as summation over all phonon state $|Ph\rangle$:

$$\rho_r(t) = \sum_{Ph} \langle Ph| \rho(t) |Ph\rangle . \tag{10.5}$$

The density matrix $\rho(t)$ of the lattice-particle system satisfies the Liouville equation:[349]

$$\frac{\partial \rho(t)}{\partial t} = -\frac{i}{\hbar} [H, \rho(t)] \tag{10.6}$$

Now substituting the Hamiltonian and $\rho(t)$ from the previous equations, the following expression is obtained for rate of probability:[349]

$$\begin{aligned} \frac{\partial P_n(t)}{\partial t} &= \int_0^t \sum_m K_{nm}(s) P_m(t-s) \\ K_{nm}(s) &= \frac{-2}{\hbar^2} Re \left\{ \sum_k e^{i\omega_{mk}} \langle (H_I(s))_{mk} (H_I)_{km} \rangle \delta_{nm} - e^{-i\omega_{nm}s} \langle (H_I(s))_{mn} (H_I)_{nm} \rangle \right\} \end{aligned} \tag{10.7}$$

Using a Markoffian approximation, the $K_{nm}(s)$ is assumed to decay on a time scale that is small enough such that the value of $P_n(t)$ is constant, resulting in [349]

$$\int_{-\infty}^{t} K_{nm}(s) P_m(t-s) ds \cong P_m(t) \int_{-\infty}^{\infty} K_{nm}(s) ds \cong \boldsymbol{W}_{nm} P_m(t) \tag{10.8}$$

with

$$\begin{aligned} \boldsymbol{W}_{nm} &= -\delta_{nm} \sum_k W_{m\to k} + W_{m\to n} \\ W_{n\to m} &= \frac{2}{\hbar^2} Re \left\{ \int_0^{\infty} \langle (H_I(s))_{mn} (H_I)_{nm} \rangle \, exp(+i\omega_{nm}s) \right\} \end{aligned} \tag{10.9}$$

Assuming a first order master equation, $P(t)$ can be expressed as:[349]

$$P(t) = e^{\boldsymbol{W}t} P(0) \tag{10.10}$$

Using this, the average time between two successive desorption events can be calculated as:[349]

$$\langle \tau \rangle = \sum_n \int_0^\infty P_n(t) dt = \sum_n \left(\boldsymbol{W}^{-1} P(0) \right)_n \tag{10.11}$$

The desorption rate is given by the inverse of the average time.

$$k_{des} = \langle \tau \rangle^{-1} \tag{10.12}$$

Thus, all that is required now to calculate the desorption rate constants is the phonon density of states and the transition rates. There are two types of transition present in the system: bound to bound, and bound to continuum. The bound to bound transition rates can be derived as [350]:

$$\begin{aligned} W_{n\to m} =& \frac{2D^2}{\hbar^2} Re \int_0^\infty dt \, exp(i\omega_{nm} t) \\ & \Big[\left(B_{nm}^{(2)} \right)^2 exp\left(4\alpha^2 \left\langle u^2 \right\rangle \right) \left\{ exp\left(4\alpha^2 \left\langle u(t)u(0) \right\rangle \right) - 1 \right\} \\ & + 4 \left(B_{nm}^{(1)} \right)^2 exp\left(\alpha^2 \left\langle u^2 \right\rangle \right) \left\{ exp\left(\alpha^2 \left\langle u(t)u(0) \right\rangle \right) - 1 \right\} \\ & - 4 \left(B_{nm}^{(1)} \right) \left(B_{nm}^{(2)} \right) exp\left(2.5\alpha^2 \left\langle u^2 \right\rangle \right) \left\{ exp\left(2\alpha^2 \left\langle u(t)u(0) \right\rangle \right) - 1 \right\} \Big] \end{aligned} \tag{10.13}$$

The term $B_{nm}^{(j)}$ is the bound to bound matrix elements, for which a general expression can be obtained as [349]:

$$\begin{aligned} B_{nm}^{(j)} =& \frac{1}{2k} \left[\frac{\tilde{n}(2k - \tilde{n} - 1) - \bar{n}(2k - \bar{n} - 1) + 2k}{2k} \right]^{j-1} \\ & \tilde{n}! \, \Gamma(2k - \tilde{n}) \left[\frac{(2k - 2\tilde{n} - 1)(2k - 2\bar{n} - 1)}{\tilde{n}! \Gamma(2k - \tilde{n}) \bar{n}! \Gamma(2k - \bar{n})} \right]^{1/2} \end{aligned} \tag{10.14}$$

Here $\langle u(t)u(0) \rangle$ is the correlation function of surface atom displacement given

by

$$\langle u(t)u(0)\rangle = \frac{\hbar}{2M}\int_0^\infty d\omega\rho(\omega)\left|\zeta(\omega)\right|^2\left\{n(\omega)e^{-i\omega t}+\left(n(\omega)+1\right)e^{i\omega t}\right\}\frac{f\left(\Delta\right)}{\omega} \tag{10.15}$$

Here M is the mass of a lattice atom, while the quantities $\rho(\omega)$, $\zeta(\omega)$, and $n(\omega)$ are the phonon density of states, polarization, and population, respectively. The form of the function $f\left(\Delta\right)$ appearing in the above equation determined by the choice of phonon relaxation model. The Lorentzian model of phonon broadening defines

$$f\left(\Delta\right) = exp(-\Delta|t|) \tag{10.16}$$

while the Gaussian model employs

$$f\left(\Delta\right) = exp(-\Delta^2t^2/2) \tag{10.17}$$

The bound to continuum transition states can be defined in a similar manner [349]:

$$\begin{aligned} W_n =& \frac{2D^2}{\hbar^2}Re\int_0^\infty dt\, exp(i\omega_{n\epsilon}t) \\ & \left[\left(a^{(2)}(t)\right)exp\left(4\alpha^2\left\langle u^2\right\rangle\right)\left\{exp\left(4\alpha^2\left\langle u(t)u(0)\right\rangle\right)-1\right\}\right. \\ & +\left(a^{(1)}(t)\right)exp\left(\alpha^2\left\langle u^2\right\rangle\right)\left\{exp\left(\alpha^2\left\langle u(t)u(0)\right\rangle\right)-1\right\} \\ & \left.-4\left(c(t)\right)\left(B_{nm}^{(2)}\right)exp\left(2.5\alpha^2\left\langle u^2\right\rangle\right)\left\{exp\left(2\alpha^2\left\langle u(t)u(0)\right\rangle\right)-1\right\}\right] \end{aligned} \tag{10.18}$$

where the terms $a^{(j)}(t)$ and $c(t)$ are the bound to continuum matrix elements, for which a general expression can be obtained as [349]:

$$a^{(j)}(t) = \int_0^\infty d\epsilon\ exp(-i\omega_{n\epsilon}t)\ \left(B_{n\epsilon}^{(j)}\right)^2 \tag{10.19}$$

$$c(t) = \int_0^\infty d\epsilon \; exp(-i\omega_{n\epsilon}t) \; \left(B_{n\epsilon}^{(1)} B_{n\epsilon}^{(2)}\right) \tag{10.20}$$

10.3 Calculations

10.3.1 Determination of input parameters

There are three main inputs to the theoretical model described in the previous section: surface-adatom (Morse) potential parameters, the phonon relaxation time, and the phonon density of states. The inter-atomic potential needs to describe the interaction between the adatom and the entire surface and not a single surface atom. Such potential parameters are not readily available in the literature. Further, these potential parameters are highly sensitive to the configuration of the adatom on the surface. Thus, these parameters are calibrated by fitting the desorption rates from this model to experimental values (Table 4.3).

The computation of the phonon relaxation time due to phonon interaction with various processes has been performed for both pristine and defective graphite [452, 453, 454]. Although the phonon relaxation time is a function of both temperature and frequency, a single value for each pristine and defective lattice is used. The phonon density of states as computed in the previous chapter is directly used for the calculations within the theoretical model. It is important to note that this PDOS is based on a graphitic carbon lattice (with an intra-layer atomic spacing of 1.42 Åand inter-layer spacing of 3.35 Å), while the desorption rates were developed for a vitreous carbon system. The phonon density of states for the vitreous carbon is expected to be different from that of the graphitic surface. Thus, the calibration of the interatomic Morse potential parameters are required in order to match the experimental results with the PID model.

The Morse potential parameters for each of the three different adatom configuration of O{a}, CO{a}, and CO{b} are calibrated by fitting the corresponding

experimental desorption rates constants with those obtained from the theoretical model. For this calibration, the phonon density of states and phonon relaxation times corresponding to the pristine carbon system are employed. This is justified from the fact that the SEM images of the carbon sample obtained pre and post experiments showed negligible differences. Thus, it is postulated that due to the low input flux of oxygen, the carbon sample remains (nearly) topographically pristine throughout the experiments.

10.3.2 Desorption rates for defective systems

The interaction potential is expected to be sensitive to the configuration of the adatom on the surface and less sensitive to the surface configuration around the adatom. Thus, in this study, the Morse potential parameters obtained using the pristine system are used to compute the rate constants for the defective system.

As described in the previous chapter, there are many types of defects that can occur in the lattice system. For a representative defective system, the case of etch pits with surface roughness is chosen. The phonon density of states is directly obtained for such a defect configuration from the previous study. Finally, the phonon relaxation time for the defective system is obtained using the parameters presented in Ref. [452]. For the phonon relaxation, the Gaussian model is used instead of the Lorentzian following the recommendation of Hood *et al.* [350]. They observed that the transition rates predicted by the Lorentzian model were anomalously large, which is an artifact of the slower decay. Thus, the Gaussian model was used in all calculations.

10.4 Results and Discussion

The process of obtaining the Morse potential parameters by fitting the desorption rate constants of the pristine system is performed using least square method over the temperature range of interest. Fig. 10.2 presents the experimental and fitted

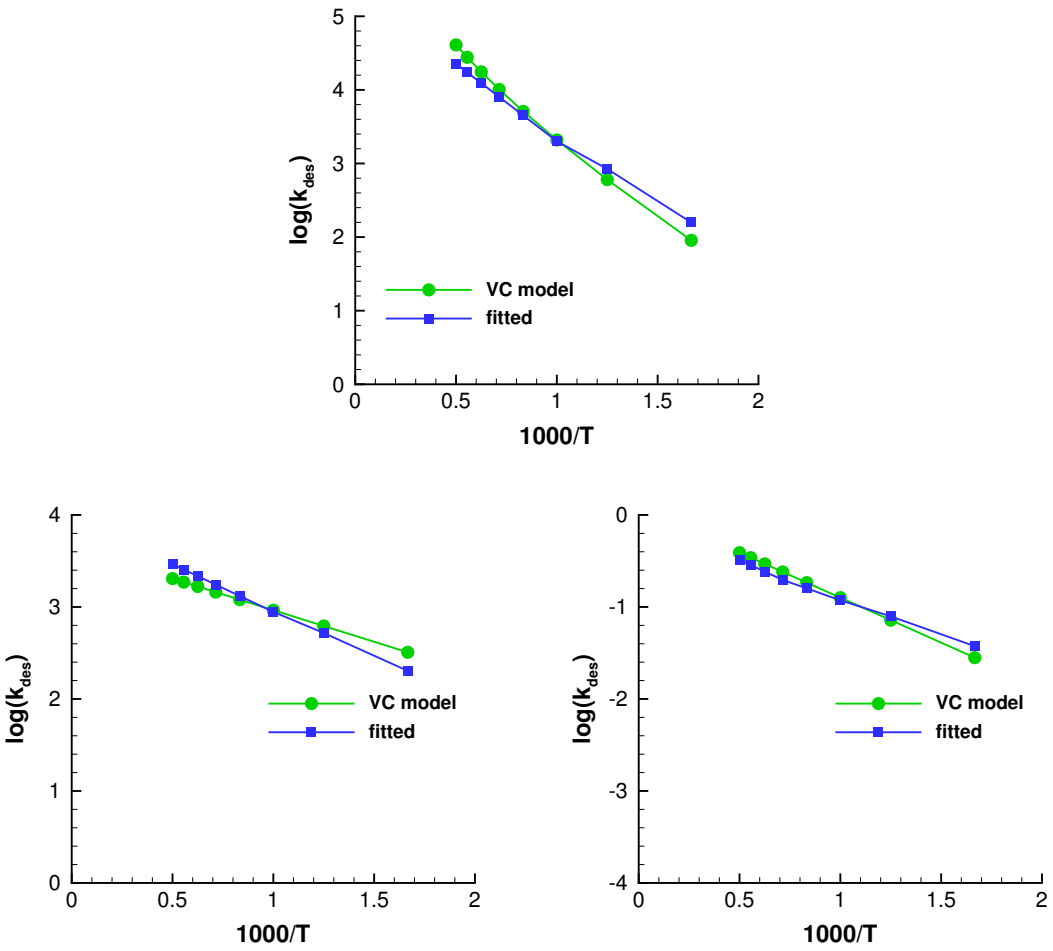

Figure 10.2: Rate constants for (a) O{a}, (b) CO{a}, and (c) CO{b} adatom systems from experiments [6] and theoretical model with a pristine carbon lattice.

rate constants for all the three adatom systems: O{a}, CO{a}, and CO{b}. The logarithm of the desorption rate constants are plotted against the inverse temperature. The experimental rate constants follow an Arrhenius form and thus forms a straight line. It is observed that the model predicts rate constants that deviate from the Arrhenius form especially at the lower temperatures, which is consistent with the results of Hood *et al.,* [350]. Nevertheless, good agreement is observed between the model (fitted) and experimental rate constants. As mentioned previously, these calculations were performed assuming a pristine lattice system. The CO{b} adatom has the strongest bond with the surface and therefore the lowest desorption rate, while O{a} has the highest desorption rate.

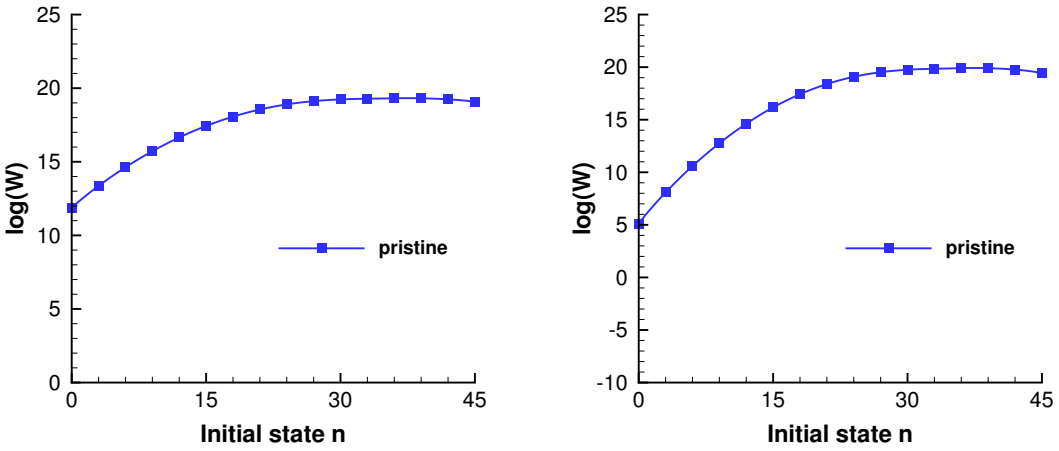

Figure 10.3: (a) Bound to bound and (b) bound to continuum transition rates between nearest neighbor oscillator states $W_{n\to n+1}$ vs bound state for the CO{b} adatom system with a pristine carbon lattice.

In order to further analyze the system, the transition rates (logarithm) between nearest neighbor oscillator states $W_{n\to n+1}$ are plotted against the initial state n for the CO{b} system. Fig. 10.3 (a) shows the bound to bound transition rates, while the bound to continuum transition rates are presented in Fig. 10.3 (b). The transition rates initially increases with the bound state n as the energy spacing between the levels decrease. At higher energy states, the transition rates reach a peak and then plateaus.

Next, the transition and desorption rates are computed and analyzed for a defective system. The phonon density of states computed in the previous chapter along with the phonon relaxation time for the defective system is used. Fig. 10.4 presents the rate constants of the defective system for all the three adatom systems: O{a}, CO{a}, and CO{b}. The experimental and fitted rate constants are also plotted for comparison. As expected, the rate constants for the defective system are consistently lower compared to the pristine system for all the three adatom configurations. Due to the presence of the defects, the phonons are increasingly scattered [455, 456, 443], thus reducing the energy transferred to the adatom leading to lower desorption rates. This effect is increasingly observed at higher temperatures, where there is a larger population of high energy phonons

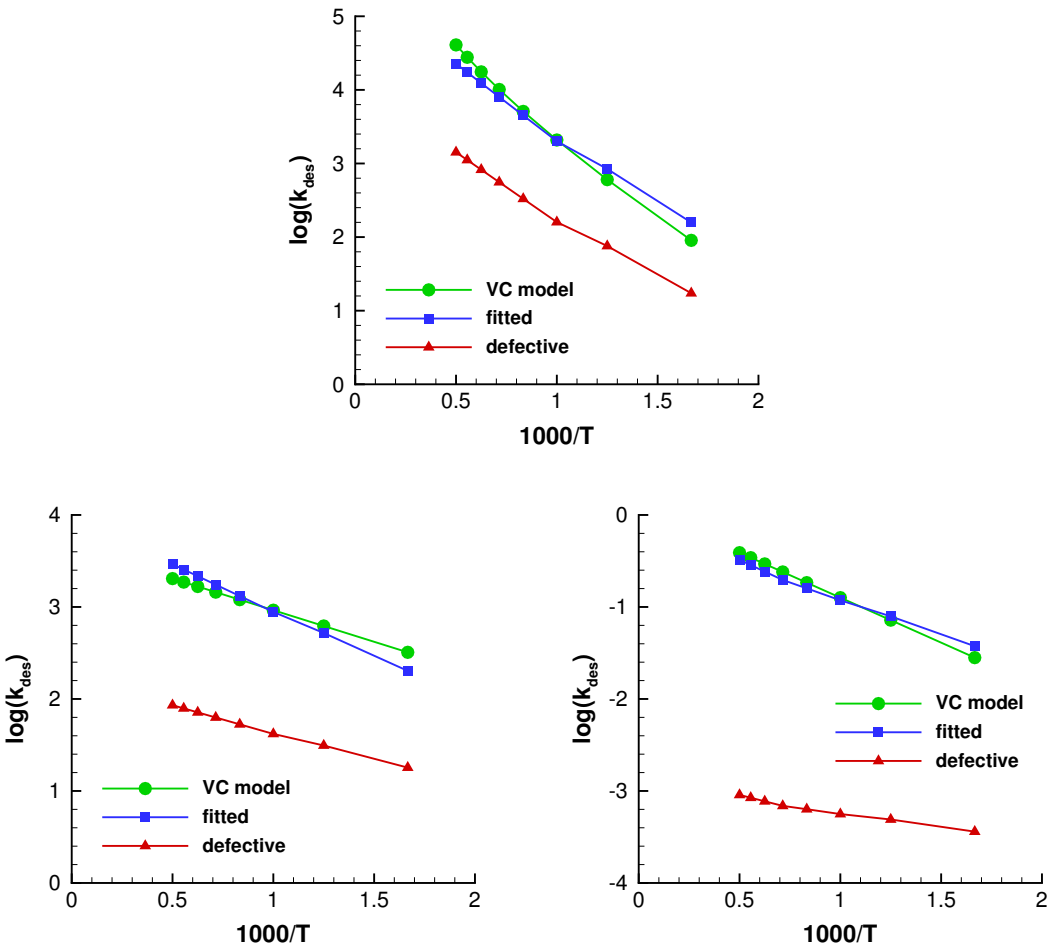

Figure 10.4: Rate constants for (a) O{a}, (b) CO{a}, and (c) CO{b} adatom systems from experiments [6] and theoretical model with a pristine and defective carbon lattice.

for the pristine system. The presence of defects scatters these phonons to lower energies, thus reducing the energy transfer to the adatom and lower desorption rates. The desorption rates for each of the system shows an order of magnitude decrease with the strongly bound CO{b} system exhibiting the greatest reduction in the desorption rates consistent with the above reasoning.

Finally, the transition rates with the pristine and defective carbon lattice for the CO{b} system is shown in Fig. 10.5. Both the bound-bound and bound-continuum transition rates between nearest neighbor oscillator states $W_{n\to n+1}$ are plotted against the initial state n. The transition rates for the defective system

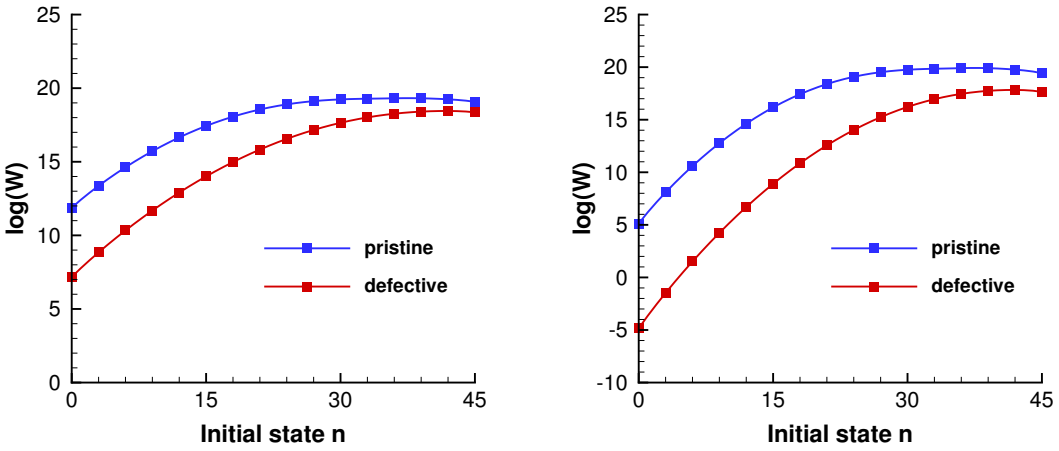

Figure 10.5: (a) Bound to bound and (b) bound to continuum transition rates between nearest neighbor oscillator states $W_{n\to n+1}$ vs bound state for the CO{b} adatom system for a pristine and defective carbon lattice.

are consistently lower than the pristine system, consistent with the observations of the desorption rates. The disparity is more significant at lower initial states where the spacing between the energy levels is higher.

10.5 Summary

A rigorous theoretical model based on the interaction of the adsorbed atoms/-molecules with the phonon bath at the surface is used to describe the desorption process of the adsorbates. The interaction of the adsorbate with the surface phonons is explicitly captured by using the PDOS of the surface. The adsorbate-surface interaction is represented using a Morse potential, which allows for the desorption process (transition from bound to free state) to be directly modeled as the interaction energy reaches beyond a threshold level described by the potential. This model is one-dimensional and considers the interaction only along the surface normal direction. The coupling of the adsorbate with the phonon bath results in adsorbate-surface bond to jump within the interaction energy ladder. Both mono and multi-quantum jumps are considered within this framework. The desorption process is treated as a Markoffian process and a first order Master equation is

used to derive the final rate constant.

This model was used to compute the transition and desorption rates for both pristine and defective systems. The phonon density of states for both the pristine and defective systems are obtained directly from MD calculations. Mathissen's rule is used to compute the phonon relaxation time for pristine and defective systems based on the phonon scattering times for each of the different scattering processes. First, the desorption rates of the pristine system is fitted against the experimental values to obtain the Morse potential parameters for each of the three observed adatoms: O{a}, CO{a}, and CO{b}. These Morse potential parameters are used along with the defective PDOS and phonon relaxation time to compute the desorption rates for the defective system. The defective system rates (both transition and desorption) were consistently lower in comparison with pristine system. This is a result of additional phonon scattering due to the presence of the defects leading to lower energy transfer to the adatom. The difference between the transition rates is more significant at lower initial states due to higher energy spacing between the levels. In the case of the desorption rates, the difference between the defective and pristine system is more significant at higher temperatures. A larger population of higher energy phonons which is present in the pristine system at higher temperatures are scattered due to the defects resulting in the greater disparity. The desorption rates for each of the system shows an order of magnitude decrease with the strongly bound CO{b} system exhibiting the greatest reduction in the desorption rates.

Chapter 11

Conclusions

In this chapter, a summary of this work is presented, with a highlight on the physical principles, novel methods, important observations, and key results. The major contributions of the current research efforts are outlined next, followed by some suggestions regarding possible areas of focus for future research directions.

11.1 Summary

11.1.1 Vitreous Carbon oxidation model

First, the formulation and implementation of a general finite-rate surface chemistry framework in DSMC is described. The approach involves stochastically modeling the various competing reaction mechanisms occurring on a set of active sites. Within this framework, multiple surface phases can be specified allowing for the representation of composite materials, and each surface phase can contain multiple site sets which can be used to present heterogeneous surface materials. The framework includes a comprehensive list of surface reaction mechanisms including adsorption, desorption, Eley-Rideal (ER), and different types of Langmuir-Hinshelwood (LH) mechanisms. It is possible to model both catalytic (oxygen formation) and surface altering (material removal by oxidation) reaction mechanisms, as well as gas-surface (GS) or pure-surface (PS) reactions.

GS reactions are performed when the gas-phase particles strike the surface as a part of the *move* kernel. The modeling of GS reactions within DSMC involves the computation of the probability for each of the possible reactions. These prob-

abilities are calculated from the specified reaction rate constant, properties of the incident gas-particle and the surface. PS reactions are carried out by looping over all the surface elements in parallel with the gas-phase collisions. DSMC modeling of PS reactions involve computing a characteristic frequency for each reaction. This characteristic frequency is a function of specified rate constants and surface properties. Two different algorithms for performing multiple PS reactions without bias were proposed and shown to accurately match the analytical solutions. This work also presents various scattering models for accurately modeling both reactive and non-reactive scattering at a wide variety of regimes and scenarios. The different models available within this framework include CLL, thermal desorption, impulsive and non-thermal scattering models. For each reaction, recommended models are proposed, but the framework is flexible to incorporate any specified model.

This detailed surface chemistry framework was used to construct a general approach for constructing finite rate surface chemistry models using pulsed hyperthermal beam experimental data. First, detailed DSMC simulations of various reaction mechanisms for a wide range of conditions are performed to obtain the TOF and angular distributions. The Langmuir-Hinshelwood mechanisms were categorized into four types based on the comparison of time scales for formation and desorption steps with the system time scale. The characteristics of each type of mechanism were analyzed in detail and a method to identify and distinguish between them using only the experimental TOF data is provided. A new procedure to accurately compute the total integrated flux of the products, specifically the slowly desorbing species from the TOF and angular distribution is described.

The final and most crucial step of this approach is the development of a general methodology to accurately derive the rate constants of the identified surface reaction mechanisms under transient (pulsed beam) conditions. An analysis of the commonly used steady-state approximation revealed significant differences in terms of both the rate constants and total product composition, specifically when the surface coverage at steady state is low. Modulation of the beam into short

pulses inherently introduces a transient component which must be accounted for in order to reliably obtain the rates. Within the proposed methodology, the changing surface conditions are explicitly considered while computing the product fluxes. The fitting procedure uses particle swarm optimization to systematically search through the rate constant parameter space in order to match the final product composition with the experimental values. In addition, the surface coverage of the different species is readily obtained as output and are consistent with the experimental product fluxes. This procedure is performed at each temperature, and the computed rate constant values can be expressed as a function of temperature in any desired form.

This general approach for constructing surface chemistry models along with the detailed surface chemistry framework was used to derive a carbon surface oxidation model. DSMC simulations of hyperthermal oxygen scattering on a vitreous carbon surface were conducted to model TOF and angular distributions in comparison with recent experimental data.

The most notable information gained from this analysis and current interpretation of the experimental data included: (i) the inclusion of slow products in the TOF distributions, namely slowly desorbing O and CO products, into the current model, (ii) the inclusion of the "missing flux" of scattered oxygen products that were not detected in these experiments. The missing flux accounts for approximately 60-75% of the total oxygen/oxide flux at low temperatures. Although both O and CO products exhibit a long distribution tail in the TOF data, the identity of the missing flux was determined to be CO (referred to as CO{b}). This was based on the observation that the long distribution tail (slow O component) in the TOF is not evident at high temperatures, as this component merges with the TD products due to an increased desorption rate.

From the analysis of the experimental data, a surface chemistry model is proposed which consists of nine major surface reactions, and physically consistent forms for these mechanisms were inferred. The rate constants of all the mechanisms were represented using an Arrhenius form, and activation energies compare

well with previous values reported in the literature. Simulations performed using the proposed finite rates within the DSMC surface chemistry model provided excellent agreement with the experimental TOF and angular distributions, and with the analyzed experimental fluxes. The CO_2 flux is negligible compared to both O and CO at all temperatures in agreement with the PSMM model. However, the current model predicts CO to be the major reaction product at low temperatures primarily through the formation of the strongly bound CO{b}. The current model predicts a peak in the CO flux at a temperature of 700 K. Thus, for the experimental temperature range spanning 600-1875 K, the CO product flux predicted by the current model corresponds to the decay just after the peak and shows a near monotonic decrease with temperature. The flux of O increases and becomes the dominant product at higher temperatures.

11.1.2 Effective carbon oxidation model for FiberForm

PuMA software was used to perform simulations of molecular beam scattering experiments of hyperthermal O striking a FiberForm®, which is a common component of an ablative TPS. X-ray micro-tomography was used to obtain the detailed microstructure of FiberForm®, which was employed within the PuMA simulations to capture the effect of the complex porous and fibrous geometry. The finite-rate surface chemistry model recently constructed from the molecular beam scattering experiments on vitreous carbon [5] was applied to each fiber of the FiberForm® material.

First, the effect of microstructure was investigated by studying the non-reactive scattering of Ar off the FiberForm® sample. A significant portion of the Ar particles were thermally accommodated to the surface temperature, unlike the case of vitreous carbon where all the particles were impulsively scattered. Multiple collisions with the different fibers, resulting from the porous nature of FiberForm® was found to be solely responsible for the thermalization of Ar. The effect of gas-phase collisions was negligible. Good agreement was observed between the

simulations and experiments of Ar beam scattering.

The reactive interaction on FiberForm® was investigated by modeling the atomic oxygen beam scattering experiments. Comparison between the experimental and PuMA time-of-flight (TOF) distributions of both O and CO at 1623 K showed good agreement. In comparison with the vitreous carbon experiments, the fraction of TD O atoms were significantly higher in the case of FiberForm®. Multiple collisions with the different fibers, resulting from the porous nature of FiberForm® was found to be responsible for the thermalization of the O atoms, while the effect of gas-phase collisions was negligible. In addition, a larger relative CO to O flux is observed for the case of FiberForm® in comparison with vitreous carbon. This was again attributed to the multiple collisions of the O atoms within FiberForm®.

The next focus was to develop an effective surface chemistry model, which inherently accounts for the microstructure of FiberForm®, and thus can be directly employed within macroscopic simulation methods like Computational Fluid Dynamics (CFD) and material response codes. In order to construct such a model for FiberForm®, the VC model was applied to the detailed microstructure of FiberForm® to obtain the product fluxes of oxygen scattering from FiberForm® at various porosities different from the experiments.

At higher porosities, greater mole fractions of CO and less amounts of O (up to 10% of the total product flux) were observed. This is due to the greater penetration of the incoming beam atoms into the microstructure leading to more collisions with the surface resulting in greater mole fraction of CO. The effect of the differences in the collision histogram is more pronounced at higher temperatures when the probability of CO formation during a single collision is smaller.

The experimental and PuMA data are used to construct the effective model. The effective model reaction mechanisms are assumed to be the same as that of the VC model, as well as the desorption rate constant values. CO_2 was observed only at the lowest temperature in the FiberForm® experiments and this data was not enough to derive a rate constant for CO_2 production reaction mechanism. Particle-swarm algorithm was used to obtain the rate constants of the gas-surface

reactions within the effective model at each porosity. The fitting process yielded constant values (different value for each of the reaction) for the Arrhenius energy value for the range of porosities examined here. Thus, only the Arrhenius pre-exponential factor A varies with the collision histogram and is a function of the porosity.

Simulations performed using the constructed effective rates with a flat plate provided excellent agreement with the experimental TOF and angular distributions, and with the analyzed experimental fluxes. This effective model also provides excellent agreement with the PuMA data for the whole porosity range of interest. Thus, this effective model can be directly used within the CFD solvers.

11.1.3 Inelastic scattering from surfaces

MD-QCT simulations were performed to study the non-reactive or inelastic scattering of O_2 molecules from carbon surfaces, with a special focus on the internal (rotational and vibrational) energy distributions. The ReaxFF potential for the C-C and C-O interactions while the O-O interactions were modeled using the accurate *ab-initio* potential designed to capture the ro-vibrational states accurately. A range of initial translational energy of the molecule and the surface temperature is considered to elucidate the dependence of the scattered molecule properties on these parameters.

The peak final translational energy and the width of the distribution increased with the initial translational energy. It was also observed that the fraction of translational energy lost during the collision increases, as well as a broadening of the final distribution with increasing energy. In the case of angular distributions, super-specular scattering was observed due to the high energies and low interaction time with the surface. The peak of the angular shows non-monotonic trend with initial translational energy while the width increases. For the final rotational energy state distribution, bi-modal distributions were observed with both the peak value and the width of the distribution increasing with increasing $E_{tr,i}$.

The transition probabilities to excited vibrational states increased with $E_{tr,i}$, and these values were higher for lower states. The transition probabilities for energies below 3 eV were small and were not resolved above the statistical noise.

For a fixed initial translational energy and varying surface temperature, the final translational energy peak and width also showed an increase with surface temperature. In the case of angular distributions, the super-specular nature of the scattering becomes less prominent with increase in surface temperature. Shifting of the peak towards the surface normal and increased broadening of the distribution were also observed with rise in temperature. The final rotational energy state distributions were bi-modal in nature, but the deviation from Boltzmann distribution was less significant compared to the initial translational energy variation study. This suggests that the energy transfer mechanisms from the surface and from the initial translational energy of the molecule are both significant.

Next, the inelastic scattering event is described using the molecule surface scattering (MSS) theory. It is a rigorous theoretical model based on gas-phonon interactions at the surface, and is used to describe the final energy (translational, rotational, and vibrational) and angular distributions for an oxygen molecule scattering from a graphite surface. The MSS model considers several such mechanisms including multi-phonon processes, translational and internal mode (rotational and vibrational) excitations. The translational and rotational modes of the gas particle are treated classically within this framework while the quantum mechanical nature of the vibrational modes are taken into account. Further, this model provides a state-resolved description of the scattered particles through the evaluation of the detailed scattering kernels and transition matrix.

Since the parameters within the MSS model are difficult to obtain, these parameters are calibrated against the MD-QCT data. In the present work, four "free" parameters namely effective surface mass M_s, average phonon velocity v_R, effective surface moment of inertia I_s, and effective surface reduced mass μ_s are calibrated to match the MD data. The values of the "free" parameters are presented along with their variation with the initial molecule translational energy

and the surface temperature.

The least square method is used for the fitting process. It was observed that the cross term effects of the all the parameters were negligible. All of the features in the various distributions are captured by the MSS theory in thermal, structural and transition regime. The average frustrated rotational angular velocity parameter ω_R was found to have only negligible effect on all the final distributions even with large variations and was taken to be constant for all the cases. The fitted values for all the mass and moment of inertia parameters were observed to be greater than the values for a single surface atom.

The effective surface mass M_s is observed to increase with the initial molecule translational energy, while it was observed to decrease with increasing surface temperature. The average phonon velocity of the surface v_R is observed to increases with surface temperature, and remains constant across the entire molecule translational energy range. In contrast to the effective surface mass, the effective surface moment of inertia I_s increases with both the initial translational energy of the molecule and the surface temperature. This was in line with the increasing final rotational energy distributions observed in both the cases. Finally, the effective reduced mass of the surface μ_s was computed only at higher initial translational energies (greater than 3 eV) since the vibrational transitions are observed only for these cases. Similar to the case of effective surface moment of inertia, the effective surface reduced mass also exhibits an increasing trend with the initial translational energy of the molecule. Again, this was in line with the increasing final distributions of the vibrational energy, resulting in the observed increase of the effective surface reduced mass.

11.1.4 Phonon-induced desorption

The surface PDOS is an important input for describing the phonon-induced desorption process. The results of the detailed MD study suggests that the PDOS varies widely as a result of defects present within the system. In general any kind

of defect tends to broaden the phonon distributions resulting in rounded peaks. Further, the PDOS is consistently observed to be shifted towards lower frequencies leading to lower densities at higher energies. The effect of the adsorbates is predominantly along the surface normal direction. In the case of random surface defect, the PDOS was found to be sensitive to both the presence and configuration of the defects. However, for the etch pits, the PDOS is observed to be only dependent on the presence of the etch pit and insensitive to the exact configuration. Similar consistent results are observed for the case with both surface roughness and etch pits.

The realistic PDOS computed with MD is used within the phonon-induced desorption (PID) model. It is a rigorous theoretical model based on the interaction of the adsorbed atoms/molecules with the phonon bath at the surface, and is used to describe the desorption process of the adsorbates. The adsorbate-surface interaction is represented using a Morse potential, which allows for the desorption process (transition from bound to free state) to be directly modeled as the interaction energy reaches beyond a threshold level described by the potential. This model is one-dimensional and considers the interaction only along the surface normal direction. The coupling of the adsorbate with the phonon bath results in adsorbate-surface bond to jump within the interaction energy ladder. Both mono and multi-quantum jumps are considered within this framework. The desorption process is treated as a Markoffian process and a first order Master equation is used to derive the final rate constant.

This model was used to compute the transition and desorption rates for both pristine and defective systems. The phonon density of states for both the pristine and defective systems are obtained directly from MD calculations. Mathissen's rule is used to compute the phonon relaxation time for pristine and defective systems based on the phonon scattering times for each of the different scattering processes. First, the desorption rates of the pristine system is fitted against the experimental values to obtain the Morse potential parameters for each of the three observed adatoms: O{a}, CO{a}, and CO{b}. These Morse potential parameters

are used along with the defective PDOS and phonon relaxation time to compute the desorption rates for the defective system.

The defective system rates (both transition and desorption) were consistently lower in comparison with pristine system. This is a result of additional phonon scattering due to the presence of the defects leading to lower energy transfer to the adatom. The difference between the transition rates is more significant at lower initial states due to higher energy spacing between the levels. In the case of the desorption rates, the difference between the defective and pristine system is more significant at higher temperatures. A larger population of higher energy phonons which is present in the pristine system at higher temperatures are scattered due to the defects resulting in the greater disparity. The desorption rates for each of the system shows an order of magnitude decrease with the strongly bound CO{b} system exhibiting the greatest reduction in the desorption rates.

11.2 Contributions

This work is focused on the development of physically consistent models for mesoscopic and macroscopic simulation of gas-surface interactions. This work considers both non-reactive and reactive interactions with a special focus on desorption. Developing a predictive surface interaction model that is applicable over a wide temperature range can be complicated owing to competing mechanisms, such as adsorption, desorption, and chemical reactions. The reaction rate constant values are also usually very sensitive to the surface conditions, temperature, pressure, etc., owing to the large disparities in the activation energies and power law dependencies. In addition, non-equilibrium phenomena is frequently encountered in the systems of interest. Thus, detailed mesoscopic models describing the fundamental interaction at the gas-surface interface is necessary for obtaining high-fidelity solutions. The aim of the work is to employ microscopic information in the form of detailed experiments, numerical simulations, and fundamental theories, as a basis to construct very general, accurate and physically realistic models. The purpose

of these investigations is to develop high-fidelity models that can be directly used in cases of non-equilibrium which is frequently encountered in the systems of interest.

This work introduces a new generalized surface chemistry framework that is comprehensive and can be applied to any mesoscopic and macroscopic simulation techniques. This framework is used to devise a general approach for constructing finite rate surface chemistry models using pulsed hyperthermal beam experimental data. This general methodology along with the detailed surface chemistry framework is used to construct a surface chemistry model for the carbon and atomic oxygen system. This model, which was developed for a flat carbon surface is extended to porous FiberForm® with stochastic and complex microstructure. Further, effective models that inherently account for the FiberForm® microstructure are also developed.

Next, the focus of this work is shifted to non-reactive gas-surface interaction of molecules. MD-QCT simulation technique and the MSS theoretical model is used to study the inelastic scattering between the molecular oxygen and carbon. Finally, the desorption process is analyzed within the framework of phonon-induced desorption model for pristine and defective surfaces. Realistic surface phonon density of states is used to investigate the variation in the desorption rates of atomic oxygen and carbon monoxide from carbon surfaces. The major efforts and contributions of this dissertation are summarized below.

- Developed a generalized surface chemistry framework incorporating a comprehensive list of reaction mechanisms, including gas-surface and pure-surface reactions as well as catalytic and surface altering mechanisms.

- Implemented the detailed surface chemistry framework into DSMC solver SPARTA and Porous microstructure analysis software PuMA.

- Developed a general methodology to derive physically consistent finite rate surface chemistry models from pulsed hyperthermal beam experimental data.

- Constructed a detailed finite rate carbon oxidation surface chemistry model with physically consistent mechanisms and precise rate constants based on the vitreous carbon experimental data.

- Formulated a novel approach to include the microstructure information within the finite-rate surface chemistry models, thus enabling the direct use of these models within continuum solvers.

- Constructed an effective surface oxidation model for FiberForm® where the rate constants are a function of porosity in addition to the surface temperature.

- Performed MD-QCT simulations of non-reactive gas-surface scattering of rotationally and vibrationally resolved O_2 on carbon surfaces; and analyzed the final energy and angular distributions for various initial conditions to elucidate the effect of the initial molecule translational energy and surface temperature.

- Utilized the MSS theory to describe the inelastic gas-surface interaction of molecular oxygen with carbon surfaces; calibrated the MSS model parameters using the final energy and angular distribution from MD.

- Performed PDOS calculations using MD on carbon surfaces to analyze and understand its dependence on the commonly encountered defects during ablation.

- Utilized the phonon-induced desorption model to study the effect of defects on the transition and desorption rates.

Although the methodologies and models described in this work are applied to particular systems, many of these approaches can either be used directly or can be easily extended in a straightforward manner to study various other systems and under different conditions.

11.3 Future Considerations

Some possible future research directions for extending the current work is presented below.

11.3.1 Vitreous carbon oxidation model

1. **New parallelization strategies for DSMC with surface chemistry** - The inclusion of the surface chemistry framework will introduce new kernels in the DSMC code and also alter some of the present kernels. Thus, the parallelization strategies used for the simple gas-phase DSMC code may need to be revised to account for inclusion of the surface chemistry framework (DSMC-SC). New parallelization strategies for DSMC-SC code for efficient simulations need to be explored.

2. **Diffusion and lateral interactions on the surface** - The current surface chemistry framework does not include the diffusion of the adsorbed particles on the surface. This process becomes important at low surface coverage at intermediate temperatures. Further, the lateral interaction between adsorbed particles is also not modeled. This becomes significant at higher surface coverages at low temperatures. Although the modeling of both the diffusion and lateral interactions are straightforward for a lattice based Monte Carlo method, the extension to surface where the lattice is not modeled requires careful consideration.

3. **Extension to continuous and subsonic/thermal beams** - The methodology described in this work for constructing surface chemistry models from molecular beam experimental data is very general and can be directly applied to analyze surfaces of different types (metallic/non-metallic), initial states (empty/preadsorbed); and also experimental setups with multiple gas-phase reactants within the beam. However, it requires the use of pulsed

hyperthermal/supersonic beam. Extension of this procedure to continuous beams as well as subsonic/thermal beams would be of great interest.

4. **Higher resolution of CO_2 fluxes and rates** - The vitreous carbon oxidation model accounts for the presence of CO_2 at low temperatures. However, the experimental data used to construct the VC model was sparse for the CO_2 mole fraction, which introduces a lot of error in the formation rate constants. Additional experimental data is required to better characterize the quantity and rate of CO_2 during the reactive interaction of oxygen with carbon surface.

5. **Reactive interaction of O_2, CO, and CO_2 with carbon surface** - The reactive interaction of molecular oxygen with carbon surface is small in comparison to atomic oxygen, but nonetheless significant. The molecular beam experiments cannot resolve such large differences in the reaction probability (between O and O_2) and therefore other experimental methods such as flow tube experiments are required to elucidate the surface reactions of O_2. In addition, the reactive interaction of the products (CO and CO_2) on carbon surfaces were not investigated as a part of the molecular beam experiments. This information is necessary to develop a comprehensive surface chemistry model accounting for all possible species reactions at the surface, which is required for the accurate simulation of the ablation process.

6. **Carbon nitradation model** - The vitreous carbon surface chemistry model describes the interaction of atomic oxygen with the carbon surface, which is the main source of ablation/recession at most of the temperature range of interest. However, another significant pathway for recension is due to interaction with atomic nitrogen. This process becomes increasingly relevant for the case of Mars atmosphere. Thus, a carbon nitradation model, similar to the oxidation model, needs to be developed.

11.3.2 Effective carbon oxidation model for FiberForm®

1. **Effect of incident flux on scattering** - In addition to the porosity, the incident flux of gas beam will affect the reactive and non-reactive interaction at the surface. In addition the gas-phase collisions also become important at higher fluxes and will further modify the final distributions and product fluxes. Thus, the effect of incident flux on the outcome of the gas-surface scattering process must be investigated.

2. **Inclusion of CO_2 products within the effective model** - Although the VC oxidation model consists of a reaction to form CO_2, it was omitted from the effective model due to the lack of sufficient FiberForm® experimental data. Additional data in the form of experiments or simulations is required for the inclusion of CO_2 formation reactions within the FiberForm® effective model.

3. **Effective model as a function of other properties** - The effective model derived in this work provides the rates as a function of a single microstructure property: porosity. The effective model will likely be a function of additional microstructure properties (other than porosity) and the gas inflow properties (such as the number density and flux). The effect of these additional parameters on the effective rates must be investigated.

4. **Effective nitradation model** - As mentioned previously, the nitradation reactions on carbon surfaces is also a significant pathway for recession. After the development of carbon nitradation model on a simple surface, it needs to be extended to FiberForm® in the form of an effective model.

5. **Effective models for carbon felts and weaves** - Although the effective model allows for direct incorporation into continuum solvers, it cannot be extended for materials other than FiberForm®. If the microstructure of the TPS material changes, the surface collision histogram is affected leading to changes in the final product fluxes and distributions. Thus, a "new"

effective model must be deveoped for each of the different TPS materials, e.g. carbon felt, weaves.

6. **Recession modeling in DSMC** - Within the current framework, the surface is treated as an infinite sink or source where any amount of bulk species can be added or removed. However, in reality this is not the case. For example, recession of ablative material from the surface exposed to extreme environments is one of the major properties required for the efficient design of TPS materials. Recession/addition on the surface due to mass loss/deposit should be incorporated into DSMC.

11.3.3 Inelastic scattering from surfaces

1. **Study azimuthal angle distributions** - The final polar angular and translational, rotational, and vibrational distributions of the scattered molecules obtained from MD-QCT simulations were studied and analyzed. Additional quantities of interest include the out-of-plane or azimuthal angular distributions.

2. **Effect of initial polar angle, rotational and vibrational levels** - In this work, the MD-QCT technique was used to investigate the effect of initial molecule translational energy and surface temperature on the final distributions of the molecule. It would be very interesting to investigate the effect of the initial polar angle as well as the initial rotational and vibrational levels on the final distributions.

3. **Effect of initial conditions at different scattering regimes** - There are three scattering regimes namely thermal, transition and structural. The physics of the scattering process varies widely in each of the different regimes. The effect of the initial conditions on the final distributions were investigated at a single translational energy of 0.5 eV in the thermal regime. However,

it is possible and likely that these effects on the final distributions will vary based on the scattering regime, and thus warrants further investigation.

4. **Study of collision dynamics** - Although the overwhelming majority of O_2 surface collisions encountered in this work were single collision events, other scenarios such as multiple collisions, trapping, and dissociation were observed. The study of particle trajectory and the relative probability of these events would be of great value and interest.

5. **Comparison to phenomenological models** - A wide variety of phenomenological models exist to describe the inelastic scattering process. A comparison of the MD-QCT data with the existing models would provide insight into the applicability, limitations and validity of these models.

6. **Additional gas molecules of interest** - The oxygen molecule was chosen as a representative gas owing to its importance in the ablation process. Other gas molecules of interest from the viewpoint of the hypersonic community include N_2, NO, CO, CO_2, CN, and CH_4. The extension of the current procedure to investigate these additional gases of interest is straightforward, however, it is subject to the availability of accurate interaction potentials for MD.

7. **Additional surfaces of interest** - Carbon is one of the most commonly used TPS material over a range of different space agencies. Other TPS materials include silica and ceramic composites. Study of inelastic interaction of earth and mars atmospheric gases with these surfaces is required. Again, this procedure is straightforward, but limited by the availability of accurate MD potentials.

8. **Functional form for the variation of MSS model parameters** - The variation of the "free" parameters within the MSS theory with the initial conditions was studied in this work. Functional forms which can be used to

fitting these parameters would be quite useful, especially when this model is used within mesoscopic and macroscopic simulation techniques.

9. **Full quantum treatment of the rotational/ro-vibrational states** - Currently the MSS theory treats the translational and rotational modes in continuum while the vibrational mode is modeled quantum-mechanically. Highly non-equilibrium conditions occurring in some physical situations of interest, sufficiently distort the rotational energy distribution of particles, thus causing the continuum description of the rotational mode to be inadequate. In such cases, the rotational modes or further the rovibrational modes must be treated quantum mechanically. Thus the current MSS theoretical framework must be extended to accurately model these types of systems.

10. **Implementation of MSS model within mesoscopic solvers** - The MSS model is very robust and versatile and can capture all of the features in the various distributions in thermal, structural and transition regime. Thus, it would be of great interest to implement this model into mesoscopic solvers such as DSMC and PuMA.

11.3.4 Phonon-induced desorption

1. **Coupled effect of different types of defects on the PDOS** - The effect of the various configurations of different types of defects on the surface PDOS of the system was investigated individually. However, these defects often occur together on the surface. Thus, the combined effect of these different types of defects on the PDOS must be investigated.

2. **Inclusion of internal energy modes in the PID model** - Currently the PID model describes the adsorbate as a single particle and does not account for the internal structure of the adsorbate (in the case of a molecule). The internal degrees of freedom need to be included as a part of the particle

Hamiltonian to accurately describe the energy transfer processes, which in turn affects the transition and desorption rates.

3. **Three dimensional PID model** - Within the PID model, the interaction of a gas atom with only a single solid-surface atom is considered, and the motion of the adatom and the substrate atoms parallel to the surface is either neglected or assumed to be unchanged. It is possible that these assumptions cause an overestimation of the transition probabilities and also cannot accurately predict the angular distributions. Thus, a full three dimensional formulation of the adsorbate-surface interaction process is necessary for accurate transition probabilities, desorption rates, and prediction of final distributions.

4. **Final rotational and vibrational distributions from PID model** - The translational energy of a desorbing molecule tends to follow a Maxwell-Boltzmann (MB) distribution. Thus, it is likely that the internal energy modes also follow an MB distribution. However, if the spacing between the internal energy levels is large, then the quantum transition to higher energy states might be restricted leading to deviation from the MB distribution. Furthermore, it is observed that the peak of the carbon PDOS occurs at a frequency of 1600 cm^{-1}, which is very close to the vibrational frequency of the CO bond (2000 cm^{-1}). This could result in resonant transfer of energy from the surface phonons directly to the vibrational model of CO leading to excited vibrational states in the desorbing molecules. Thus the current PID model must be extended to characterize and provide the final internal energy distributions of the desorbing molecule.

Appendices

Appendix A

Additional types of surface reactions

A.1 Dissociation

Dissociation reactions on the surface can be of two types: (i) adsorption-mediated and (ii) impact dissociation [457, 458]. In the adsorption-mediated pathway, the surfaces act as catalysts to promote dissociation reactions which are the first step of many industrial processes. The gaseous molecule adsorbs on the surface and undergoes dissociation with all the products desorbing back into the gas-phase. The first step is dissociative chemisorption followed by the products rapidly desorbing into the gas-phase.

In the impact dissociation pathway, the surface acts similar to the second colliding species in a gas-phase dissociation reaction. The incoming gas-phase molecule dissociates upon impact on the surface. The adsorption-mediated pathway is much more common on the surfaces in comparison to the impact pathway. Representative dissociation reactions through both the pathways are shown below.

$$\begin{array}{ll} \textit{Adsorption mediated dissociation} & \textit{Impact dissociation} \\ O_2(g) + (s) \longrightarrow O_2(s) & \\ O_2(s) + (s) \longrightarrow 2O(s) & O_2(g) + (s) \longrightarrow 2O(g) + (s) \\ 2O(s) \longrightarrow 2O(g) + 2(s) & \end{array} \tag{A.1}$$

A.2 Collision-Induced (CI) mechanism

A collision-induced (CI) mechanism is a gas-surface reaction which involves both gas-phase and surface adsorbed reactants. However, the two reactants within the CI mechanism do not chemically react with each other. The energy from the collision of the gas-phase reactant induces desorption of adsorbed atoms/molecules from the surface, and hence these reactions usually involve high-speed particles (super-/hyperthermal velocities) [373, 382, 383, 135]. The incident particle may or may not adsorb onto the surface. Representative reaction for both the above possibilities are listed below.

$$O(g) + N(s) \longrightarrow N(g) + O(s) \qquad O_2(g) + N(s) \longrightarrow O_2(g) + N(g) + (s) \quad \text{(A.2)}$$

A.3 Eley-Rideal (ER) mechanism

An ER reaction is a direct impact mechanism, in which gas-phase particle reacts upon impact with an adsorbed species on the surface to form products. where a gas-phase atom/molecule directly interacts with a reactant present on the surface to form gaseous products. The gas-phsae particle does not adsorb onto the surface before the reaction. A representative ER reaction is shown below:

$$O(g) + O(s) \longrightarrow O_2(g) + (s). \quad \text{(A.3)}$$

Appendix B

Additional Gas-Surface (GS) reactions

B.1 Adsorption-mediated GS reactions

B.1.1 Dissociative Adsorption

The dissociative adsorption reaction is slightly more complicated as it can involve multiple adsorbing species and also multiple gas-phase products. A general dissociative adsorption reaction can be represented by:

$$A(g) + \alpha(s) = \underbrace{B1(s) + B2(s)...}_{\alpha \text{ adsorbing products}} \quad + \quad \underbrace{C1(g) + C2(g)...}_{\beta \text{ gas-phase products}}$$

The probability of the adsorption for this case is given by:

$$P_{DA} = P_{ad} * k_{DA} \tag{B.1}$$

k_{DA} is the rate constant for the dissociative adsorption reaction. The gas-phase products might become thermally accommodated to the surface temperature or still maintain the characteristics of the incoming energy. Hence the Cercignani-Lampi-Lord (CLL) model [301, 302] can used to obtain the outgoing velocities of the gas-phase products. Hence for dissociative adsorption, in addition to the rate constant, the scattering model parameters for the scattered gas-phase species must also be specified (k_{DA} + β scattering model parameters). In the case where β is zero, it represents a case where there is no gas-phase species and all the dissociated species adsorb on the surface.

B.1.2 Condensation

The condensation reaction is very similar to the LH type 3 mechanism, except that the products are bulk-phase, instead of surface species. The calculation of the probability is also very similar.

$$M(g) + (s) \longrightarrow M(b) + (s) \tag{B.2}$$

$$P_{cond} = P_{ad}(M) * k_{cond} \tag{B.3}$$

Unlike the LH mechanisms, the adsorption of species is not listed as a separate reaction. Hence, in addition to the rate of the reaction, the equilibrium constant (of the intermediates) from the Kisliuk's model should also be specified.

B.1.3 Adsorption-Mediated Dissociation

In the adsorption-mediated pathway, the molecule first adsorbs on the surface, undergoes dissociation into adsorbed products, which finally desorb into the gas-phase. All the sub-processes in this reaction occurs quickly and the gas-phase products are formed immediately after the reactant molecule strikes the surface. A representative dissociation reactions with and without bulk-phase products are shown below.

$$A_2(g)+(s) \longrightarrow 2A(g)+(s) \qquad MA_2(g)+(s) \longrightarrow 2A(g)+(s)+M(b) \tag{B.4}$$

The probability of the dissociation is computed by the following equation.

$$P_{AMD} = P_{ad}(A_2/MA_2) * k_{AMD} \tag{B.5}$$

P_{ad} is the adsorption probability of the reactant molecule and k_{AMD} is the rate constant for the dissociation reaction.

Within the adsorption-mediated dissociation reaction, the final products are formed on the surface although they desorb quickly into the gas-phase. Thus, the products are in thermal equilibrium with the surface and exit based on a MB distribution and cosine angular distribution. However the presence of a desorption energy barrier or local hot-spots might change the final distribution of the products. The thermal scattering model (Section 2.6.2) can be used to describe the final distribution of the products.

B.2 Direct impact GS reactions

B.2.1 Impact Dissociation

The overall reaction for the impact dissociation mechanism is similar to the adsorption-mediated mechanism. However, in the case of impact dissociation, the reactant does not adsorb on the surface and undergoes dissociation upon impact on the surface. A representative impact dissociation reaction with and without the bulk atoms is shown below.

$$A_2(g)+(s) \longrightarrow 2A(g)+(s) \qquad MA_2(g)+(s) \longrightarrow 2A(g)+(s)+M(b) \quad \text{(B.6)}$$

Note that it is not necessary for the reactant molecule to strike an empty surface site. This reaction could occur even when the surface site is occupied. The probability of the dissociation is simply equal to the rate constant k_{ID}.

$$P_{ID} = k_{ID} \quad \text{(B.7)}$$

The products formed through impact dissociation reactions might not be in thermal equilibrium with the surface and can be adequately represented using the CLL scattering model (Section 2.6.1).

B.2.2 Collision-Induced (CI) Mechanism

A CI mechanism involves both gas-phase and surface adsorbed reactants, where the energy from the collision of the gas-phase reactant induces desorption of adsorbed atoms/molecules from the surface. Representative reaction for different types of CI reactions are listed below.

$$A(g) + B(s) \longrightarrow B(g) + A(s) \qquad A(g) + B(s) \longrightarrow A(g) + B(g) + (s) \quad \text{(B.8)}$$

The probability of this reaction will depend on the interaction potential between the two particles and also on the bond energy between the adsorbed species and the surface [373, 384, 383, 385]. This dependence can vary widely based on the exact reaction pathway. The "Dynamic Displacement" mechanism proposed by Rettner and co-workers [384] is shown to depend only on the bond energy of the adsorbed species and energy of the incoming particles and does not depend upon its type or the interaction between the particles. However, the collision-induced desorption mechanism reported by Beckerle *et al.,* [383, 382] suggests a dependence on the energy, type and angle of the incoming gas-phase species. In order to account for all these dependencies, a generalized expression is proposed below.

$$P_{CI} = k_{CI} * (E_{in})^m \, cos^n(\theta) \frac{N_{B(s)} F_N}{S_p} \quad \text{(B.9)}$$

k_{CI} is the rate constant of the reaction, having a functional form similar to an Arrhenius expression, thus capturing the dependence on the surface temperature and the bond energy of the adsorbed species. m is the exponent of the incoming energy term. This ensures that the dependence is not limited to a linear relationship and can take any value, which accounts for the interaction between the particles. n is the exponent of the cosine angular expression. Different values for n are proposed in the literature; $n = 0$, essentially signifying no dependence on

the angle [383]; $n = 1$, the amount of energy directed along the surface normal [459]; $n = 2$, the so-called "normal" energy, obtained from velocity expressions [460]. In addition, a variation of the n values as energy changes is also reported in literature [385, 382].

Thus, for computing the probability, k_{CI}, m and n needs to be specified. The desorbing species will be thermally accommodated to the surface, but the local surface hot-spots could lead to greater energies. The thermal desorption scattering model (Section 2.6.2) can be used to adequately model the distributions of the desrbing CI product. Finally, if the incoming gas-phase atom does not adsorb, additional parameters must also be given as input for describing the scattering of the gas-phase reactant. The CLL model (Section 2.6.1) can be used to capture the scattering details of the gas-phase reactant.

B.2.3 Eley-Rideal (ER) Mechanism

An ER reaction is an impulsive surface mechanism, where a gas-phase atom/-molecule directly interacts with a reactant present on the surface to form gaseous products. The reaction kinetics of this mechanism are dependent upon both the surface and gas-phase reactant:

$$A(g) + B(s) \longrightarrow AB(g) + (s). \tag{B.10}$$

Similar to the CI mechanism, the probability of an ER reaction can also be a function of the incoming gas-particle energy and angle as well as the reaction rate constant (function of surface temperature):

$$P_{ER} = k_{ER} \left(E_{in}\right)^m cos^n(\theta) \frac{N_{B(s)} F_N}{S_p}. \tag{B.11}$$

The scattering of the ER products can be described using a non-thermal scattering model (Section 2.6.4).

Appendix C

Additional Pure-Surface (PS) reactions

C.1 LH type 4

Modeling of LH type 4 mechanism is easier since the products are adsorbed species. Representative reactions for LH type 4 mechanism are shown below.

$$A(s) + B(s) \longrightarrow AB(s) + (s) \tag{C.1a}$$

$$A(s) + A(s) \longrightarrow A_2(s) + (s) \tag{C.1b}$$

$$A(s) + M(b) \longrightarrow AM(s) \tag{C.1c}$$

The characteristic frequencies and times are calculated similar to LH type 2 mechanism. Only the rate constant for the reaction k_{LH4} needs to be specified.

C.2 Sublimation

The sublimation reaction is very similar to LH type 2 reaction, except that the reactants are bulk-phase species, instead of adsorbed species.

$$(s) + M(b) \longrightarrow M(g) + (s) \tag{C.2}$$

The formula for computing the characteristic times and frequencies remain the same, however, they will now be based on the available empty sites, rather than filled sites. Since this reaction involves a gas-phase product, the desorption barrier

of the particular species should be specified in addition to the rate constant k_{sub}.

Appendix D

Combining scattering models

In many instances, a combination of scattering models may be required for representing the scattering of the same species over a range of conditions. For example, the physics of scattering at hyperthermal energies may be completely different from the scattering at thermal energies. Hence some provisions are required for using a combination of the available models to accurately capture the scattering over a wide range of conditions.

D.1 Energy threshold transition

Based on the energy of the incoming gas-phase atom/molecule the effective interaction experienced and the physics of scattering is completely different. They can be broadly classified into two regimes: (i) Thermal and (ii) Structural regime. When the energy of the molecule is relatively low compared to the thermal energy of the surface such that the effective interaction surface is relatively flat, then the interaction belongs to the thermal scattering regime. On the other hand, the structure regime corresponds to the case when the incident energy of the incoming particle are much higher compared to the surface thermal energies such that the surface vibrations are negligible. The effective interaction surface is rough on the atomic scale and the gaseous atom/molecule experiences the atomic structure of the surface atoms.

Thus, within the thermal regime scattering models such as the CLL, non-thermal and thermal models can be used to adequately represent the interaction of the gaseous species with the surface. The impulsive scattering model can be used to describe the gas-surface interaction in the structure regime. A continuous

variation of the various scattering parameters as a function of energy is expected. However, in the absence such detailed information simple transition between the different models can be used based on specified energy threshold.

Some reasonable threshold transition options are listed below.

i. One threshold: A single energy threshold value is specified along with two scattering models. Incident gas atoms/molecules with energy greater than the specified value is scattered based on the first model, while the second model is used to scatter the particles with lower energies. This is the most basic model which abruptly transitions from model to another.

ii. Two threshold - two models: Two energy threshold values are specified along with two scattering models. Particles with energy greater than the first threshold is scattered using the first scattering model, while particles with energy lesser than the second threshold is scattered using the second model. For particle energies in between the two energy thresholds a linear interpolation of the two models based on the incident energy is applied to get the final scattered properties. This creates a smoother transition between the different scattering models in comparison with the one threshold model.

iii. Two threshold - three models: Two energy threshold values along with three scattering models are specified. Particles with energies greater than the first threshold, in between the two values and lesser than the second threshold are scattered using the first, second and the third model respectively. This is illustrative of a case where the physics of the transition from the structure to the thermal regime is much different from either of the two regimes.

D.2 Fraction based splitting

Another instance where a combination of gas-surface interaction models are required is when a fraction of species formed by a reaction mechanism scatter differently. For example, thermal mechanisms occurring when high energy particles

are incident on the surface tends to have a small component that is non-thermal (super-thermal). This is termed as fraction based splitting of the particles under different scattering models. A generic way to implement this fraction based splitting is to specify any number of probability values (they must sum to 1), followed by an equal number of scattering models.

Appendix E

Bias introduced when total probability exceeds 1

This appendix outlines the importance of normalization when the total probability of a sequence of events becomes greater than 1. Without normalization, a bias will be introduced towards the initial events (reactions), even when the probability of each reaction is less than 1. Consider the following case with 5 events A, B, C, D, E, with the given probabilities (column 2 of Table E1).

Table E1: Un-normalized and normalized reaction probabilities of events

Events	Un-normalized probability (from rate constants)	Un-normalized probability cumulative	Un-normalized probability SPARTA output	Normalized probability
A	0.40	0.40	0.40	0.20
B	0.30	0.70	0.30	0.15
C	0.20	0.90	0.20	0.10
D	0.60	1.50	0.10	0.30
E	0.50	2.00	0.00	0.25
Sum	2.00	-	1.00	1.00

Reactions in SPARTA are performed using the standard Monte Carlo technique for a sequence of events:

- A random number is drawn for the reaction probability.
- The reaction probability is compared against a cumulative probability $\sum_{i=1}^{i=n} Prob(E_i)$, where n increases from 1 to the total number of events.
- When the value of the reaction probability is less than $\sum_{i=1}^{i=n} Prob(E_i)$, then the n^{th} reaction is performed.

Using this methodology, and the un-normalized probability values, the actual occurrence of the five events are shown in column 4 of Table E1. Notice, that the probability of events A, B, and C remains unaltered; the probability of D gets reduced to 0.1 and event E does not occur at all. Until the cumulative probability (column 3 of Table E1) stays less than 1, the probability of the events remain

unaltered. When the cumulative probability exceeds 1, the probability of that particular event is cutoff (such that the cumulative probability is equal to 1). The probability of the remaining events are zero. As you can clearly observe, a bias is introduced towards the initial events (reactions).

When the probability of each event is normalized by the sum of the un-normalized probability, the values given in column 5 of Table E1 is obtained. These values retain the relative ratio of the original un-normalized provabilities, while having a cumulative probability of 1. This ensures that the relative probabilities of all the events remain unchanged and no bias is present towards the initial reactions.

Appendix F

Obtaining prescribed distributions

Although DSMC is very intuitive, sometimes sampling specific distributions for the different properties of the system, especially scattering properties from the surface, might not be straightforward. This section presents methods to sample prescribed distributions for the VDF and the angular distributions. These can be used to obtain the distributions described previously or any other user specified distributions.

F.1 VDF

In order to obtain the prescribed distribution for the velocity or energy of the particles scattered from the surface, it is first important to recognize the form of the prescribed distribution. In many instances instead of the VDF, the speed distribution function (SDF) or the distribution corresponding to the flux is specified. For example, the Maxwell-Boltzmann distribution has the following different forms when expressed as VDF, SDF or flux PDF.

$$VDF \propto exp\left(-\frac{mv^2}{k_bT}\right) \qquad SDF \propto v^2 exp\left(-\frac{mv^2}{k_bT}\right) \qquad flux\ PDF \propto v^3 exp\left(-\frac{mv^2}{k_bT}\right) \tag{F.1}$$

In this section, VDF is used as a generic term to describe any distribution relating to the velocity or energy of the particles. In order to obtain the correct distribution, the velocities of the scattering particles from the surface must be chosen based on the flux PDF [461]. The scattering of particles from the surface

is similar to the effusive movement of gases through a plane. Hence, first the prescribed distribution must be properly converted into the flux PDF form before applying any of the standard Monte Carlo techniques to obtain the specified distribution. Based on the exact form of the distribution, corresponding techniques such as the inversion of the CDF or the acceptance rejection method can be used to obtain the final components of the velocities. These standard techniques for sampling the prescribed distribution can be found in many texts including Bird [53], Shen [461], Frenkel and Smit [462] and Lesar [463]. While applying the acceptance rejection scheme for the VDF, it might be more efficient to use importance sampling [462] since most of the distributions involve a exponential function. The sharpness of the exponential function makes the random sampling very time consuming.

The process of converting the distribution into the flux form is straightforward in many cases, however care must be taken when the distribution is dependent on the angle of scattering. Also in some cases, the normal and the tangential distributions are available separately. In such a case, the tangential velocity can be employed directly while the normal component must be converted to the flux form [461]. If the inversion of the normal and tangential distributions are not straightforward, then it is recommended to convert them into a single combined distribution and apply the standard techniques to choose the total speed. Later the final angles can be used to obtain the separate components of the velocities.

F.2 Angular distribution

The most important feature to remember while sampling angular distribution is the presence of the sine of the polar angle in the expression for the solid angle.

$$d\Omega = sin(\theta) d\theta d\phi \tag{F.2}$$

θ is the polar angle while ϕ is the azimuth angle. Excluding this $sin(\theta)$ while sampling the distribution has been the source of confusion and error in the past [464].

If the polar and azimuth distribution are not independent, the expression of the solid angle must be used directly within the sampling techniques. In the case where the two distributions are independent of each other, the azimuth sampling can be done without any additional factors. The polar sampling on the other hand must include the $sin(\theta)$ component.

$$f(\theta) = g(\theta) * sin(\theta) \tag{F.3}$$

where $g(\theta)$ is the required distribution in the polar direction, while $f(\theta)$ must be used within the sampling algorithms.

F.2.1 Additional options

There are two optional arguments available for obtaining more complicated angular distributions. These are the *step* and *double* options.

F.2.1.1 *Step* option

In many cases, it is observed that the decay rate of the product flux on either side of the θ_{peak} is different [5, 255, 273, 10]. Goodman [10] proposed a physical reasoning for the observed faster decay rate in the angular distribution of the product fluxes on the surface side away from the peak (approaching 90).

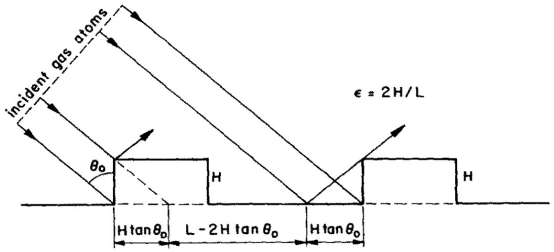

Figure F1: Surface step model [10]. The surface is assumed to consist of steps of average height H and average periodicity L.

The surface is assumed to consist of periodic steps of average height H and average periodicity L. The particles that strike the side of the step or very close to the step within $H * tan(\theta_0)$ will not be scattered on the reflection side of the normal. This would result in reduction of the product flux closer to the surface (approaching 90). Hence a simple correction was proposed based on the parameter $\epsilon = 2H/L$:

$$f_{corr} = \begin{cases} 1 - \epsilon\, tan(\theta_0), & \text{if} \tan(\theta_0) < \epsilon^{-1} \\ 0, & \text{otherwise} \end{cases} \tag{F.4}$$

The term ϵ is a free parameter that must be specified. A representative angular distribution using the *step* option is shown in Fig. F2 (a).

F.2.1.2 *Double* option

Another option to specify the angular distribution of the products is the *double* option. In this option, the angular distribution on either sides of the peak are represented by a different cosine power decay: n_1, n_2. Although such a distribution is not derived from physical reasoning, it provides a lot of flexibility to directly match the observed experimental distribution [107, 106]. Fig. F2 (b) shows a representative angular distribution using the *double* option.

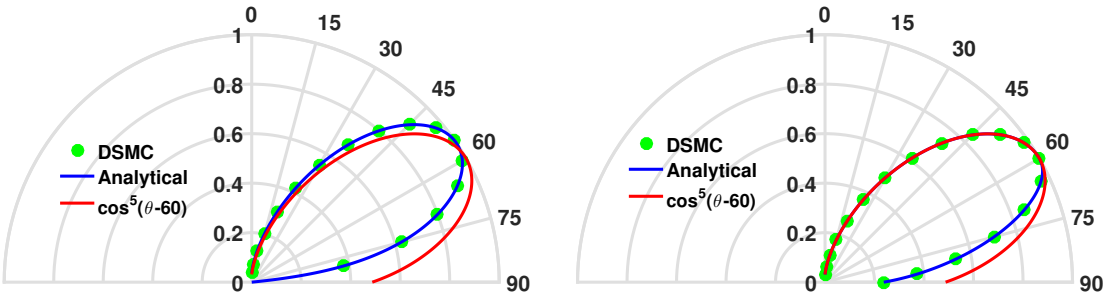

Figure F2: Representative in-plane angular distributions of products formed via impulsive scattering (IS) of a hyperthermal beam from a smooth surface: lobular distribution of polar angle θ with $\theta_{peak} = 60$ and $n = 5$. (a) Distribution using the step option with $\epsilon = 0.1$. (b) Distribution using the double option with $n_2 = 10$.

Appendix G

Hysteresis

Here the consistency between the observed hysteresis in the CO flux and the inferred reaction mechanisms is examined along with the assumptions regarding the surface coverage. At low temperatures, there is higher probability of forming CO{b}, which occupies the surface leading to a high coverage. As the temperature increases, there is lower probability of forming of CO{b} and the steady state surface coverage decreases. However, since the desorption of CO{b} is extremely slow, it takes a very long time to reach steady state. It is noted that for the temperature survey, the times between the change in the sample temperature and the measurements were much shorter. Thus, data collected in a temperature survey for which surface temperatures are increased corresponds to a surface coverage which is higher than the steady state value. This leads to greater CO product fluxes, since the LH1 reaction of CO is catalyzed by adsorbed atoms. Such an effect is not observed in the decreasing temperature cycle since less CO{b} is present on the surface at higher temperatures, and the surface coverage increases with decreasing temperature. Hence, the slow desorption of CO{b} no longer creates a lag in the surface coverage time-to-steady-state which is the mechanism responsible for the observed hysteresis during the temperature survey with increasing temperature. Thus, the decreasing temperature cycle is expected to be consistent with the steady state values and is therefore used in the present study to construct the reaction probabilities. In addition, reduced hysteresis was observed in the experiments for a more gradual temperature change. This is consistent with the above explanation since the surface coverage would be much closer to its steady state value when the rate of temperature change is lower. At very high

temperatures, both the increase in the CO{b} desorption rate, and the decrease in the probability of CO{b} formation reduces the time to attain steady state. Thus, the hysteresis disappears at very high temperatures and both the decreasing and increasing temperature cycle gives the same CO product fluxes (Fig. 4 (c) of Murray *et al.* [5]).

Appendix H

Evidence of adsorbed O atoms to promote LH1 CO formation reaction

As discussed, a hysteresis was observed in the CO product flux (Fig. 4 (c) of Murray *et al.* [5]), whose magnitude was dependent on the rate of change of surface temperature. An additional set of experiments measured the product fluxes after rapidly increasing the temperature of the vitreous carbon sample. The vitreous carbon sample was initially heated to T=800 K and exposed to the pulsed oxygen beam to reach a steady state of oxidation. The temperature of the sample was then rapidly increased to T=1875 K within a matter of seconds, and the time variation of the product fluxes was measured (Fig. H1) with continued exposure of the sample to the pulsed beam.

The purpose of this experiment was to characterize the amount of time required for the surface oxidation product fluxes to reach a steady state. Only O, O_2 and CO products were observed at this high temperature. As seen in Fig. H1 (a,b), the O and O_2 products reach a steady state quickly, while the flux of CO shows a gradual decrease over time (Fig. H1(c)), consistent with the hysteresis observed in the CO product flux [5]. These results suggest that products which reside on the surface at 800 K and which desorb as O, desorb immediately after the surface temperature is increased to 1875 K. It is noted that this is consistent with the observation that the long distribution tail of O atoms is not observed above 1700 K. In other words, the slow O desorption rate increases and becomes "fast" at this high temperature. The constant O/O_2 product fluxes observed in Fig. H1 (a,b) at long times are merely sustained from the incident pulsed beam.

The TOF distribution of the CO products at various times during this experiment is shown in Fig. H1 (d). It is evident from the profiles at t=8 min, 45 min

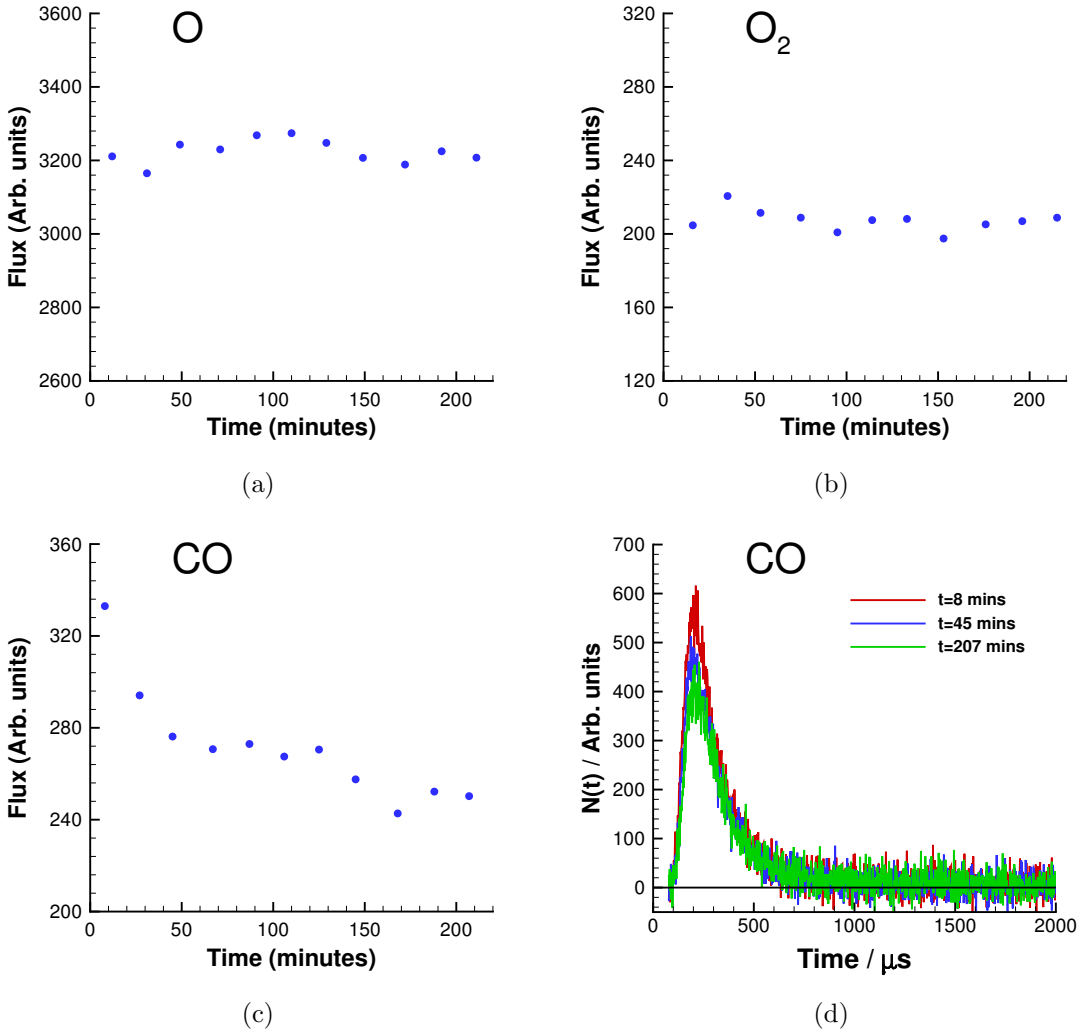

Figure H1: Variation of experimentally measured product flux with time for (a) O, (b) O_2, (c) CO, and (d) TOF distribution of CO after sudden increase in substrate temperature from 800 K to 1875 K during bombardment with O/O_2 beam at $\theta_i = 45$ on a vitreous carbon surface, from Murray *et al.* [5].

and 207 min, that the difference in the measured CO product fluxes arises from a prompt mechanism that follows a MB distribution at time t=0 ms. There are two possible pathways that could explain the observed flux variation of prompt CO with time: (i) tightly bound CO (that has a slow spontaneous desorption rate) that is released as a result of a collision-induced mechanism immediately after the beam strikes the surface; or (ii) the prompt CO formation requires adsorbed O atoms to promote the reaction.

Experimental studies in the literature regarding the collision-induced desorption process suggest that these reaction products are significant only when the energies of the incident particles are much higher than 10 eV [465]. Hence, it is unlikely that the observed difference in the CO product fluxes are a result of a collision-induced desorption process. The slow transient behavior observed in the CO TOF distribution peak however, directly coincides with the decrease in oxygen surface coverage due to slow CO desorption products that are not detected in the TOF data.

References

[1] S. J. Poovathingal, M. Qian, V. J. Murray, and T. K. Minton, "Reactive and scattering dynamics of hyperthermal o and o2 from a carbon fiber network," *The Journal of Physical Chemistry C*, 2018, https://scholarworks.montana.edu/xmlui/handle/1/14696.

[2] E. C. Stern, "Microscale modeling of porous thermal protection system materials," Ph.D. dissertation, University of Minnesota, 2015.

[3] J. Marschall and M. MacLean, "Finite-rate surface chemistry model, i: Formulation and reaction system examples," in *42nd AIAA Thermophysics Conference*, 2011, p. 3783.

[4] P. Kisliuk, "The sticking probabilities of gases chemisorbed on the surfaces of solids," *Journal of Physics and Chemistry of Solids*, vol. 3, no. 1-2, pp. 95–101, 1957.

[5] V. J. Murray, B. C. Marshall, P. J. Woodburn, and T. K. Minton, "Inelastic and Reactive Scattering Dynamics of Hyperthermal O and O2 on Hot Vitreous Carbon Surfaces," *Journal of Physical Chemistry C*, vol. 119, no. 26, pp. 14 780–14 796, 2015.

[6] K. Swaminathan-Gopalan, A. Borner, V. J. Murray, S. J. Poovathingal, T. K. Minton, N. N. Mansour, and K. A. Stephani, "Development and validation of a carbon surface oxidation model from molecular beam experiments," *Under Review*, pp. –, 2018.

[7] V. J. Murray, E. J. Smoll Jr, and T. K. Minton, "Dynamics of graphite oxidation at high temperature," *The Journal of Physical Chemistry C*, vol. 122, no. 12, pp. 6602–6617, 2018.

[8] B. Bendow and S.-C. Ying, "Phonon-induced desorption of adatoms from crystal surfaces. i. formal theory," *Physical Review B*, vol. 7, no. 2, p. 622, 1973.

[9] G. Ertl, *Reactions at solid surfaces*. John Wiley & Sons, 2010, vol. 14.

[10] F. O. Goodman, "Determination of characteristic surface vibration temperatures by molecular beam scattering: Application to specular scattering in the h-lif (001) system," *Surface Science*, vol. 46, no. 1, pp. 118–128, 1974.

[11] R. N. Gupta, J. M. Yos, R. A. Thompson, and K.-P. Lee, "A review of reaction rates and thermodynamic and transport properties for an 11-species air model for chemical and thermal nonequilibrium calculations to 30000 k," 1990.

[12] C. Park, "Review of chemical-kinetic problems of future nasa missions. i-earth entries," *Journal of Thermophysics and Heat transfer*, vol. 7, no. 3, pp. 385–398, 1993.

[13] C. Park, J. T. Howe, R. L. Jaffe, and G. V. Candler, "Review of chemical-kinetic problems of future nasa missions. ii-mars entries," *Journal of Thermophysics and Heat transfer*, vol. 8, no. 1, pp. 9–23, 1994.

[14] D. Bose and G. V. Candler, "Thermal rate constants of the n2+ o no+ n reaction using ab initio 3 a and 3 a potential energy surfaces," *The Journal of chemical physics*, vol. 104, no. 8, pp. 2825–2833, 1996.

[15] D. Bose and G. V. Candler, "Thermal rate constants of the o 2+ n no+ o reaction based on the a 2 and a 4 potential-energy surfaces," *The Journal of chemical physics*, vol. 107, no. 16, pp. 6136–6145, 1997.

[16] K. Suzuki, H. Kubota, K. Fujita, and T. Abe, "Chemical nonequilibrium stagnation ablation analysis of muses-c superorbital re-entry capsule," *Journal of spacecraft and rockets*, vol. 35, no. 3, pp. 407–409, 1998.

[17] D. Olynick, Y.-K. Chen, and M. E. Tauber, "Aerothermodynamics of the stardust sample return capsule," *Journal of Spacecraft and Rockets*, vol. 36, no. 3, pp. 442–462, 1999.

[18] C. Park, R. L. Jaffe, and H. Partridge, "Chemical-kinetic parameters of hyperbolic earth entry," *Journal of Thermophysics and Heat transfer*, vol. 15, no. 1, pp. 76–90, 2001.

[19] I. D. Boyd, "Modeling backward chemical rate processes in the direct simulation monte carlo method," *Physics of Fluids*, vol. 19, no. 12, p. 126103, 2007.

[20] A. Martin, I. Cozmuta, M. J. Wright, and I. D. Boyd, "Kinetic rates for gas-phase chemistry of phenolic-based carbon ablator in atmospheric air," *Journal of Thermophysics and Heat Transfer*, vol. 29, no. 2, pp. 222–240, 2015.

[21] J. D. Bender, P. Valentini, I. Nompelis, Y. Paukku, Z. Varga, D. G. Truhlar, T. Schwartzentruber, and G. V. Candler, "An improved potential energy surface and multi-temperature quasiclassical trajectory calculations of n2+ n2 dissociation reactions," *The Journal of chemical physics*, vol. 143, no. 5, p. 054304, 2015.

[22] P. Valentini, T. E. Schwartzentruber, J. D. Bender, I. Nompelis, and G. V. Candler, "Direct molecular simulation of nitrogen dissociation based on an ab initio potential energy surface," *Physics of Fluids*, vol. 27, no. 8, p. 086102, 2015.

[23] A. Sahai, B. Lopez, C. Johnston, and M. Panesi, "Adaptive coarse graining method for energy transfer and dissociation kinetics of polyatomic species," *The Journal of chemical physics*, vol. 147, no. 5, p. 054107, 2017.

[24] T. E. Magin, M. Panesi, A. Bourdon, R. L. Jaffe, and D. W. Schwenke, "Coarse-grain model for internal energy excitation and dissociation of molecular nitrogen," *Chemical Physics*, vol. 398, pp. 90–95, 2012.

[25] A. Munafo, M. Panesi, and T. Magin, "Boltzmann rovibrational collisional coarse-grained model for internal energy excitation and dissociation in hypersonic flows," *Physical Review E*, vol. 89, no. 2, p. 023001, 2014.

[26] A. Munafo, Y. Liu, and M. Panesi, "Modeling of dissociation and energy transfer in shock-heated nitrogen flows," *Physics of Fluids*, vol. 27, no. 12, p. 127101, 2015.

[27] M. Panesi, R. L. Jaffe, D. W. Schwenke, and T. E. Magin, "Rovibrational internal energy transfer and dissociation of n 2 (1 σ g+)- n (4 s u) system in hypersonic flows," *The Journal of chemical physics*, vol. 138, no. 4, p. 044312, 2013.

[28] R. Macdonald, A. Munafò, C. Johnston, and M. Panesi, "Nonequilibrium radiation and dissociation of co molecules in shock-heated flows," *Physical Review Fluids*, vol. 1, no. 4, p. 043401, 2016.

[29] R. L. Jaffe, M. Grover, S. Venturi, D. W. Schwenke, P. Valentini, T. E. Schwartzentruber, and M. Panesi, "Comparison of potential energy surface and computed rate coefficients for n 2 dissociation," *Journal of thermophysics and heat transfer*, vol. 32, no. 4, pp. 869–881, 2018.

[30] P. Valentini, T. E. Schwartzentruber, J. D. Bender, and G. V. Candler, "Dynamics of nitrogen dissociation from direct molecular simulation," *Physical Review Fluids*, vol. 1, no. 4, p. 043402, 2016.

[31] N. Singh and T. Schwartzentruber, "Nonequilibrium internal energy distributions during dissociation," *Proceedings of the National Academy of Sciences*, vol. 115, no. 1, pp. 47–52, 2018.

[32] M. S. Grover, T. E. Schwartzentruber, Z. Varga, and D. G. Truhlar, "Vibrational energy transfer and collision-induced dissociation in o+ o 2 collisions," *Journal of Thermophysics and Heat Transfer*, pp. 1–11, 2019.

[33] S. Poovathingal, T. E. Schwartzentruber, V. J. Murray, T. K. Minton, and G. V. Candler, "Finite-rate oxidation model for carbon surfaces from molecular beam experiments," *AIAA Journal*, vol. 55, no. 5, pp. 1644–1658, 2017.

[34] S. Poovathingal, T. E. Schwartzentruber, V. J. Murray, and T. K. Minton, "Molecular simulation of carbon ablation using beam experiments and resolved microstructure," *AIAA Journal*, vol. 54, no. 1, pp. 1–12, 2016.

[35] C. R. Alba, "A Nonequilibrium Finite-Rate Carbon Ablation Model for Radiating Earth Re-entry Flows," Ph.D. dissertation, Air Force Institute of Technology, Wright-Patterson Air Force Base, Ohio, 2015.

[36] S. V. Zhluktov and T. Abe, "Viscous Shock-Layer Simulation of Airflow past Ablating Blunt Body with Carbon Surface," *Journal of Thermophysics and Heat Transfer*, vol. 13, no. 1, pp. 50–59, 1999.

[37] C. Park, "Effects of atomic oxygen on graphite ablation," *AIAA Journal*, vol. 14, no. 11, pp. 1640–1642, nov 1976.

[38] Y.-K. Chen and F. S. Milos, "Navier-stokes solutions with finite rate ablation for planetary mission earth reentries," *Journal of Spacecraft and Rockets*, vol. 42, no. 6, pp. 961–970, 2005.

[39] N. Afonina, V. Gromov, and V. Kovalev, "Catalysis modeling for thermal protection systems of vehicles entering into martian atmosphere," *35th AIAA Thermophysics Conference, AIAA Paper 2011-2832*, 2001.

[40] C. Sorensen, P. Valentini, and T. E. Schwartzentruber, "Uncertainty analysis of reaction rates in a finite-rate surface-catalysis model," *Journal of Thermophysics and Heat Transfer*, vol. 26, no. 3, pp. 407–416, 2012.

[41] M. MacLean, T. Wadhams, M. Holden, and B. Hollis, "Investigation of blunt bodies with co2 test gas including catalytic effects," *38th AIAA Thermophysics Conference, AIAA Paper 2005-4693*, 2005.

[42] A. Nawaz, D. M. Driver, I. Terrazas-Salinas, and S. Sepka, "Surface catalysis and oxidation on stagnation point heat flux measurements in high enthalpy arc jets," in *44th AIAA Thermophysics Conference*, 2013, p. 3138.

[43] O. Deutschmann, U. Riedel, and J. Warnatz, "Modelling of surface reactions in hypersonic re-entry flow fields," in *Aerothermodynamics for space vehicles*, vol. 367, 1995, p. 305.

[44] R. Cattolica and R. Schefer, "The effect of surface chemistry on the development of the [oh] in a combustion boundary layer," in *Symposium (International) on combustion*, vol. 19. Elsevier, 1982, pp. 311–318.

[45] D. Bradley, G. Dixon-Lewis, S. E.-D. Habik, and E. Mushi, "The oxidation of graphite powder in flame reaction zones," in *Symposium (International) on Combustion*, vol. 20. Elsevier, 1985, pp. 931–940.

[46] J. Graham, A. Brown, A. Hall, and W. Watt, "The rates of reaction of carbon and graphite materials with combustion gases at high temperatures," in *Proceedings of the 1st Conference on Industrial Carbon and Graphite*, 1957, p. 309.

[47] J. González, M. C. Del Ruiz, A. Bohé, and D. Pasquevich, "Oxidation of carbons in the presence of chlorine," *Carbon*, vol. 37, no. 12, pp. 1979–1988, jan 1999.

[48] H. D. Allendorf and D. E. Rosner, "Comparative studies of the attack of pyrolytic and isotropic graphite by atomic and molecular oxygen at high temperatures." *AIAA Journal*, vol. 6, no. 4, pp. 650–654, apr 1968.

[49] R. H. Hurt and B. S. Haynes, "On the origin of power-law kinetics in carbon oxidation," *Proceedings of the Combustion Institute*, vol. 30, no. 2, pp. 2161–2168, jan 2005.

[50] J. Walls and R. Strickland-Constable, "Oxidation of carbon between 10002400C," *Carbon*, vol. 1, no. 3, pp. 333–338, apr 1964.

[51] K. G. Neoh, J. B. Howard, and A. F. Sarofim, "Soot Oxidation in Flames," in *Particulate Carbon*. Boston, MA: Springer US, 1981, pp. 261–282.

[52] P. A. Libby and T. R. Blake, "Burning carbon particles in the presence of water vapor," *Combustion and Flame*, vol. 41, pp. 123–147, 1981.

[53] G. Bird, *Molecular Gas Dynamics and the Direct Simulation of Gas Flows*. Oxford: Oxford University Press, 1994.

[54] X. Guo, D. Singh, J. Murthy, and A. A. Alexeenko, "Numerical simulation of gas-phonon coupling in thermal transpiration flows," *Physical Review E - Statistical, Nonlinear, and Soft Matter Physics*, vol. 80, no. 4, pp. 1–10, 2009.

[55] D. Singh, X. Guo, A. Alexeenko, J. Y. Murthy, and T. S. Fisher, "Modeling of subcontinuum thermal transport across semiconductor-gas interfaces," *Journal of Applied Physics*, vol. 106, no. 2, 2009.

[56] J.-P. M. Peraud, C. D. Landon, and N. G. Hadjiconstantinou, "Monte Carlo Methods for Solving the Boltzmann Transport Equation," *Annual Review of Heat Transfer*, vol. 17, no. N/A, pp. 205–265, 2014. [Online]. Available: http://www.dl.begellhouse.com/references/5756967540dd1b03, 7deb9f2f1087a9e3,1d883b612ccfafde.html

[57] K. A. Stephani, D. B. Goldstein, and P. L. Varghese, "A non-equilibrium surface reservoir approach for hybrid DSMC/Navier-Stokes particle generation," *Journal of Computational Physics*, vol. 232, no. 1, pp. 468–481, 2013.

[58] T. R. Deschenes, T. D. Holman, and I. D. Boyd, "Effects of rotational energy relaxation in a modular particle-continuum method," *Journal of Thermophysics and Heat Transfer*, vol. 25, no. 2, pp. 218–227, 2011.

[59] K. Swaminathan-Gopalan, S. Subramaniam, and K. A. Stephani, "Generalized chapman-enskog continuum breakdown parameters for chemically reacting flows," *Physical Review Fluids*, vol. 1, no. 8, p. 083402, 2016.

[60] S. Subramaniam, K. Swaminathan Gopalan, and K. A. Stephani, "Assessment of continuum breakdown for high-speed chemically reacting wake flows," in *46th AIAA Thermophysics Conference*, 2016, p. 4434.

[61] S. Subramaniam and K. A. Stephani, "Influence of surface chemistry on continuum breakdown in high-speed chemically reacting flows," in *47th AIAA Thermophysics Conference*, 2017, p. 4343.

[62] S. Subramaniam and K. A. Stephani, "Assessment of continuum breakdown for chemically reacting wake flows," *Physical Review Fluids*, vol. 3, no. 12, p. 123401, 2018.

[63] R. Jambunathan and D. A. Levin, "Chaos: An octree-based pic-dsmc code for modeling of electron kinetic properties in a plasma plume using mpi-cuda parallelization," *Journal of Computational Physics*, vol. 373, pp. 571–604, 2018.

[64] R. Jambunathan and D. A. Levin, "A hybrid cpu-gpu parallel octree direct simulation monte carlo approach," in *22nd AIAA Computational Fluid Dynamics Conference*, 2015, p. 3057.

[65] S. S. Sawant, O. Tumuklu, R. Jambunathan, and D. A. Levin, "Application of adaptively refined unstructured grids in dsmc to shock wave simulations," *Computers & Fluids*, vol. 170, pp. 197–212, 2018.

[66] Q. Sun and I. D. Boyd, "A direct simulation method for subsonic, microscale gas flows," *Journal of Computational Physics*, vol. 179, no. 2, pp. 400–425, 2002.

[67] J. I. Paredes, A. Martínez-Alonso, and J. M. D. Tascón, "Multiscale imaging and tip-scratch studies reveal insight into the plasma oxidation of graphite," *Langmuir*, vol. 23, no. 17, pp. 8932–8943, 2007.

[68] J. I. Paredes, A. Martínez-Alonso, and J. M. D. Tascón, "Early Stages of Plasma Oxidation of Graphite:Nanoscale Physicochemical Changes As Detected by Scanning Probe Microscopies," *Langmuir*, vol. 18, no. 11, pp. 4314–4323, 2002.

[69] P. Pattabiraman, N. Rodriguez, B. Jang, and R. Baker, "A study of the interaction of atomic oxygen with various carbonaceous materials," *Carbon*, vol. 28, no. 6, pp. 867 – 878, 1990.

[70] C. Wong, R. T. Yang, and B. L. Halpern, "The mode of attack of oxygen atoms on the basal plane of graphite," *The Journal of Chemical Physics*, vol. 78, no. 6, pp. 3325–3328, 1983.

[71] D. Rosner and H. Allendorf, "High temperature oxidation of carbon by atomic oxygen," *Carbon*, vol. 3, no. 2, pp. 153 – 156, 1965.

[72] H. Marsh, E. O'Hair, R. Reed, and W. F. K. Wynne-Jones, "Reaction of atomic oxygen with carbon," *Nature*, vol. 198, p. 1195, 1963.

[73] H. Marsh, T. E. O'Hair, and W. F. K. Wynne-Jones, "Oxidation of carbons and graphites by atomic oxygen kinetic studies," *Trans. Faraday Soc.*, vol. 61, pp. 274–284, 1965.

[74] R. Larciprete, P. Lacovig, S. Gardonio, A. Baraldi, and S. Lizzit, "Atomic oxygen on graphite: Chemical characterization and thermal reduction," *The Journal of Physical Chemistry C*, vol. 116, no. 18, pp. 9900–9908, 2012.

[75] J. Thomas, "Reactivity of carbon: Some current problems and trends," *Carbon*, vol. 8, no. 4, pp. 413 – 421, 1970.

[76] M. Barber, E. Evans, and J. Thomas, "Oxygen chemisorption on the basal faces of graphite: an xps study," *Chemical Physics Letters*, vol. 18, no. 3, pp. 423 – 425, 1973.

[77] R. Larciprete, S. Fabris, T. Sun, P. Lacovig, A. Baraldi, and S. Lizzit, "Dual path mechanism in the thermal reduction of graphene oxide," *Journal of the American Chemical Society*, vol. 133, no. 43, pp. 17 315–17 321, 2011, pMID: 21846143.

[78] J. Hahn, "Kinetic study of graphite oxidation along two lattice directions," *Carbon*, vol. 43, no. 7, pp. 1506 – 1511, 2005.

[79] D. Lamoen and B. N. J. Persson, "Adsorption of potassium and oxygen on graphite: A theoretical study," *The Journal of Chemical Physics*, vol. 108, no. 8, pp. 3332–3341, 1998.

[80] T. Sun, S. Fabris, and S. Baroni, "Surface precursors and reaction mechanisms for the thermal reduction of graphene basal surfaces oxidized by atomic oxygen," *The Journal of Physical Chemistry C*, vol. 115, no. 11, pp. 4730–4737, 2011.

[81] H. Marsh, T. O'Hair, and L. Wynne-Jones, "The carbon-atomic oxygen reaction: surface-oxide formation on paracrystalline carbon and graphite," *Carbon*, vol. 7, no. 5, pp. 555IN1559–558IN2566, 1969.

[82] D. C. Sorescu, K. D. Jordan, and P. Avouris, "Theoretical study of oxygen adsorption on graphite and the (8,0) single-walled carbon nanotube," *The Journal of Physical Chemistry B*, vol. 105, no. 45, pp. 11 227–11 232, 2001.

[83] R. T. Yang and C. Wong, "Mechanism of Single-Layer Graphite Oxidation: Evaluation by Electron Microscopy," *Science*, vol. 214, no. 4519, pp. 437–438, 1981.

[84] B. McCarroll and D. McKee, "The reactivity of graphite surfaces with atoms and molecules of hydrogen, oxygen and nitrogen," *Carbon*, vol. 9, no. 3, pp. 301 – 311, 1971.

[85] S. Poovathingal, T. E. Schwartzentruber, V. Murray, T. K. Minton, and G. V. Candler, "Finite-rate oxidation model for carbon surfaces from molecular beam experiments," in *46th AIAA Thermophysics Conference*, 2016, p. 3842.

[86] R. T. Yang and C. Wong, "Kinetics and mechanism of oxidation of basal plane on graphite," *The Journal of Chemical Physics*, vol. 75, no. 9, pp. 4471–4476, 1981.

[87] S. M. Lee, Y. H. Lee, Y. G. Hwang, J. R. Hahn, and H. Kang, "Defect-induced oxidation of graphite," *Phys. Rev. Lett.*, vol. 82, pp. 217–220, Jan 1999.

[88] K. T. Nicholson, T. K. Minton, and S. J. Sibener, "Spatially anisotropic etching of graphite by hyperthermal atomic oxygen," *The Journal of Physical Chemistry B*, vol. 109, no. 17, pp. 8476–8480, 2005.

[89] D. Chen, A. Holmen, Z. Sui, and X. Zhou, "Carbon mediated catalysis: A review on oxidative dehydrogenation," *Chinese Journal of Catalysis*, vol. 35, no. 6, pp. 824–841, 2014.

[90] J. H. Zhou, Z. J. Sui, J. Zhu, P. Li, D. Chen, Y. C. Dai, and W. K. Yuan, "Characterization of surface oxygen complexes on carbon nanofibers by TPD, XPS and FT-IR," *Carbon*, vol. 45, no. 4, pp. 785–796, apr 2007.

[91] F. Rodríguez-Reinoso, "The role of carbon materials in heterogeneous catalysis," *Carbon*, vol. 36, no. 3, pp. 159–175, jan 1998.

[92] J. H. Zhou, Z. J. Sui, P. Li, D. Chen, Y. C. Dai, and W. K. Yuan, "Structural characterization of carbon nanofibers formed from different carbon-containing gases," *Carbon*, vol. 44, no. 15, pp. 3255–3262, dec 2006.

[93] J. L. Figueiredo, M. F. Pereira, M. M. Freitas, and J. J. Órfão, "Modification of the surface chemistry of activated carbons," *Carbon*, vol. 37, no. 9, pp. 1379–1389, jan 1999.

[94] T. J. Zhao, W. Z. Sun, X. Y. Gu, M. Rønning, D. Chen, Y. C. Dai, W. K. Yuan, and A. Holmen, "Rational design of the carbon nanofiber catalysts for oxidative dehydrogenation of ethylbenzene," *Applied Catalysis A: General*, vol. 323, pp. 135–146, apr 2007.

[95] M. F. R. Pereira, J. L. Figueiredo, J. J. Órfao, P. Serp, P. Kalck, and Y. Kihn, "Catalytic activity of carbon nanotubes in the oxidative dehydrogenation of ethylbenzene," *Carbon*, vol. 42, no. 14, pp. 2807–2813, jan 2004.

[96] H. Muckenhuber and H. Grothe, "The heterogeneous reaction between soot and NO2 at elevated temperature," *Carbon*, vol. 44, no. 3, pp. 546–559, mar 2006.

[97] Y. Otake and R. G. Jenkins, "Characterization of oxygen-containing surface complexes created on a microporous carbon by air and nitric acid treatment," *Carbon*, vol. 31, no. 1, pp. 109–121, jan 1993.

[98] A. Dandekar, R. T. Baker, and M. A. Vannice, "Characterization of activated carbon, graphitized carbon fibers and synthetic diamond powder using TPD and DRIFTS," *Carbon*, vol. 36, no. 12, pp. 1821–1831, jan 1998.

[99] H. Muckenhuber and H. Grothe, "The Reaction Between Soot and NO2 – Investigation on Functional Groups Using TPD-MS," *Topics in Catalysis*, vol. 30/31, no. 1-4, pp. 287–291, jul 2004.

[100] G. Barco, A. Maranzana, G. Ghigo, M. Causà, and G. Tonachini, "The oxidized soot surface: Theoretical study of desorption mechanisms involving oxygenated functionalities and comparison with temperature programed desorption experiments," *Journal of Chemical Physics*, vol. 125, no. 19, 2006.

[101] A. Montoya, T.-T. T. Truong, F. Mondragón, and T. N. Truong, "CO Desorption from Oxygen Species on Carbonaceous Surface: 1. Effects of the Local Structure of the Active Site and the Surface Coverage," *The Journal of Physical Chemistry A*, vol. 105, no. 27, pp. 6757–6764, 2001.

[102] H. P. Boehm, "Surface oxides on carbon and their analysis: A critical assessment," *Carbon*, vol. 40, no. 2, pp. 145–149, 2002.

[103] F. Vallejos-Burgos, N. Díaz-Pérez, Á. Silva-Villalobos, R. Jiménez, X. García, and L. R. Radovic, "On the structural and reactivity differences between biomass- and coal-derived chars," *Carbon*, vol. 109, pp. 253–263, 2016.

[104] J. C. Ferguson, F. Panerai, J. Lachaud, A. Martin, S. C. Bailey, and N. N. Mansour, "Modeling the oxidation of low-density carbon fiber material based on micro-tomography," *Carbon*, vol. 96, pp. 57–65, 2016.

[105] J. C. Ferguson, F. Panerai, J. Lachaud, and N. N. Mansour, "Theoretical study on the micro-scale oxidation of resin-infused carbon ablators," *Carbon*, vol. 121, pp. 552–562, 2017.

[106] A. Borner, K. Swaminathan-Gopalan, K. A. Stephani, V. J. Murray, S. Poovathingal, T. K. Minton, F. Panerai, and N. N. Mansour, "Dsmc analysis of molecular beam experiments on light-weight carbon preform ablators," in *47th AIAA Thermophysics Conference*, 2017, p. 3687.

[107] K. Swaminathan Gopalan, A. Borner, K. A. Stephani, V. Murray, S. Poovathingal, T. Minton, and N. N. Mansour, "Dsmc analysis of molecular beam experiments for oxidation of carbon based ablators," in *55th AIAA Aerospace Sciences Meeting*, 2017, p. 1845.

[108] E. C. Stern, S. Poovathingal, I. Nompelis, T. E. Schwartzentruber, and G. V. Candler, "Nonequilibrium flow through porous thermal protection materials, part i: Numerical methods," *Journal of Computational Physics*, 2017.

[109] J. F. Orrego, F. Zapata, T. N. Truong, and F. Mondragón, "Heterogeneous CO2 evolution from oxidation of aromatic carbon-based materials," *Journal of Physical Chemistry A*, vol. 113, no. 29, pp. 8415–8420, 2009.

[110] A. Montoya, F. Mondragón, and T. N. Truong, "CO2 adsorption on carbonaceous surfaces: a combined experimental and theoretical study," *Carbon*, vol. 41, no. 1, pp. 29–39, 2003.

[111] A. Montoya, F. Mondragón, and T. N. Truong, "Formation of CO precursors during char gasification with O2, CO2 and H2O," *Fuel Processing Technology*, vol. 77-78, pp. 125–130, jun 2002.

[112] J. F. Espinal, A. Montoya, F. Mondragon, and T. N. Truong, "A DFT Study of Interaction of Carbon Monoxide with Carbonaceous Materials," *J. Phys. Chem. B*, vol. 108, no. Copyright (C) 2012 American Chemical Society (ACS). All Rights Reserved., pp. 1003–1008, 2004.

[113] A. Montoya, F. Mondragón, and T. N. Truong, "First-principles kinetics of CO desorption from oxygen species on carbonaceous surface," *Journal of Physical Chemistry A*, vol. 106, no. 16, pp. 4236–4239, 2002.

[114] K. Sendt and B. S. Haynes, "Density functional study of the chemisorption of O2 on the zig-zag surface of graphite," *Combustion and Flame*, vol. 143, no. 4, pp. 629–643, 2005.

[115] K. Sendt and B. S. Haynes, "Density functional study of the reaction of carbon surface oxides: the behavior of ketones." *The journal of physical chemistry. A*, vol. 109, no. 15, pp. 3438–3447, 2005.

[116] K. Sendt and B. S. Haynes, "Density functional study of the chemisorption of O2 across two rings of the armchair surface of graphite," *Journal of Physical Chemistry C*, vol. 111, no. 14, pp. 5465–5473, 2007.

[117] K. Sendt and B. S. Haynes, "Density functional study of the reaction of O2 with a single site on the zigzag edge of graphene," *Proceedings of the Combustion Institute*, vol. 33, no. 2, pp. 1851–1858, 2011.

[118] K. Sendt and B. S. Haynes, "Density functional study of the chemisorption of O<inf>2</inf> on the armchair surface of graphite," *Proceedings of the Combustion Institute*, vol. 30 II, no. 2, pp. 2141–2149, 2005.

[119] L. R. Radovic, A. F. Silva-Villalobos, A. B. Silva-Tapia, and F. Vallejos-Burgos, "On the mechanism of nascent site deactivation in graphene," *Carbon*, vol. 49, no. 11, pp. 3471–3487, 2011.

[120] L. R. Radovic, A. B. Silva-Tapia, and F. Vallejos-Burgos, "Oxygen migration on the graphene surface. 1. Origin of epoxide groups," *Carbon*, vol. 49, no. 11, pp. 3471–3487, 2011.

[121] A. M. Oyarzún, L. R. Radovic, and T. Kyotani, "An update on the mechanism of the graphene-NO reaction," *Carbon*, vol. 86, pp. 58–68, 2015.

[122] A. M. Oyarzún, A. J. Salgado-Casanova, X. A. Garciá-Carmona, and L. R. Radovic, "Kinetics of oxygen transfer reactions on the graphene surface: Part I. NO vs. O2," *Carbon*, vol. 99, pp. 472–484, 2016.

[123] L. R. Radovic, "Active Sites in Graphene and the Mechanism of CO2 Formation in Carbon Oxidation," *Journal of the American Chemical Society*, vol. 131, no. 9, pp. 17 166–17 175, dec 2009.

[124] T. J. Frankcombe and S. C. Smith, "On the microscopic mechanism of carbon gasification: A theoretical study," *Carbon*, vol. 42, no. 14, pp. 2921–2928, 2004.

[125] A. Sánchez and F. Mondragón, "Role of the epoxy group in the heterogeneous CO2 evolution in carbon oxidation reactions," *Journal of Physical Chemistry C*, vol. 111, no. 2, pp. 612–617, 2007.

[126] J. J. Kane, C. Karthik, R. Ubic, W. E. Windes, and D. P. Butt, "An oxygen transfer model for high purity graphite oxidation," *Carbon*, vol. 59, pp. 49–64, 2013.

[127] J. J. Kane, C. I. Contescu, R. E. Smith, G. Strydom, and W. E. Windes, "Understanding the reaction of nuclear graphite with molecular oxygen: Kinetics, transport, and structural evolution," *Journal of Nuclear Materials*, vol. 493, pp. 343–367, 2017.

[128] C. R. Alba, R. B. Greendyke, and J. Marschall, "Development of a nonequilibrium finite-rate ablation model for radiating earth reentry flows," *Journal of Spacecraft and Rockets*, vol. 53, no. 1, pp. 98–120, 2015.

[129] G. Candler, "Nonequilibrium processes in hypervelocity flows: an analysis of carbon ablation models," in *50th AIAA Aerospace Sciences Meeting including the New Horizons Forum and Aerospace Exposition*, 2012, p. 724.

[130] G. V. Candler, C. R. Alba, and R. B. Greendyke, "Characterization of carbon ablation models including effects of gas-phase chemical kinetics," *Journal of Thermophysics and Heat Transfer*, vol. 31, no. 3, pp. 512–526, 2017/12/19 2017.

[131] F. Zaera, "Use of molecular beams for kinetic measurements of chemical reactions on solid surfaces," *Surface Science Reports*, vol. 72, no. 2, pp. 59–104, may 2017.

[132] F. Zaera, "Infrared and molecular beam studies of chemical reactions on solid surfaces," *International Reviews in Physical Chemistry*, vol. 21, no. 3, pp. 433–471, jul 2002.

[133] G. O. Sitz, "Gas surface interactions studied with state-prepared molecules," *Reports on Progress in Physics*, vol. 65, no. 8, pp. 1165–1193, aug 2002.

[134] L. Juurlink, D. Killelea, and A. Utz, "State-resolved probes of methane dissociation dynamics," *Progress in Surface Science*, vol. 84, no. 3-4, pp. 69–134, apr 2009.

[135] A. W. Kleyn, "Molecular beams and chemical dynamics at surfaces," *Chemical Society Reviews*, vol. 32, no. 2, pp. 87–95, feb 2003.

[136] C. T. Rettner, D. J. Auerbach, J. C. Tully, and A. W. Kleyn, "Chemical dynamics at the gas-surface interface," *Journal of Physical Chemistry*, vol. 100, no. 31, pp. 13 021–13 033, 1996.

[137] J. C. Tully, "Chemical dynamics at metal surfaces," *Annual Review of Physical Chemistry*, vol. 51, no. 1, pp. 153–178, oct 2000.

[138] M. J. Cardillo, "Molecular beam scattering from solid surfaces: He diffraction, hyperthermal scattering, and surface dynamics," *Surface Science*, vol. 299-300, pp. 277–283, jan 1994.

[139] K. Rendulic and A. Winkler, "Adsorption and desorption dynamics as seen through molecular beam techniques," *Surface Science*, vol. 299-300, pp. 261–276, jan 1994.

[140] C. R. Arumainayagam and R. J. Madix, "Molecular beam studies of gas-surface collision dynamics," *Progress in Surface Science*, vol. 38, no. 1, pp. 1–102, jan 1991.

[141] J. Barker and D. Auerbach, "Gassurface interactions and dynamics; Thermal energy atomic and molecular beam studies," *Surface Science Reports*, vol. 4, no. 1-2, pp. 1–99, jan 1984.

[142] S. Bernasek and G. Somorjai, "Molecular beam scattering from solid surfaces," *Progress in Surface Science*, vol. 5, pp. 377–439, jan 1975.

[143] P. Casavecchia, "Chemical reaction dynamics with molecular beams," *Reports on Progress in Physics*, vol. 63, no. 3, pp. 355–414, mar 2000.

[144] D. Olander, W. Siekhaus, R. Jones, and J. Schwarz, "Reactions of modulated molecular beams with pyrolytic graphite. i. oxidation of the basal plane," *The Journal of Chemical Physics*, vol. 57, no. 1, pp. 408–420, 1972.

[145] R. Jones, D. Olander, W. Siekhaus, and J. Schwarz, "Investigation of gas–solid reactions by modulated molecular beam mass spectrometry," *Journal of Vacuum Science and Technology*, vol. 9, no. 6, pp. 1429–1441, 1972.

[146] T. Engel and H. Kuipers, "A molecular-beam investigation of the reaction h2+ 12o2 h2o on pd (111)," *Surface Science*, vol. 90, no. 1, pp. 181–196, 1979.

[147] C. T. Rettner, "Reaction of an H-atom beam with Cl/Au(111): Dynamics of concurrent EleyRideal and LangmuirHinshelwood mechanisms," *The Journal of Chemical Physics*, vol. 101, no. 2, p. 1529, 1994.

[148] M. Braunstein, A. L. Brunsvold, D. J. Garton, and T. K. Minton, "Measurements and simulations of high energy $O(^3P)$+$Ar(^1S)$ angular scattering: Single and multi-collision regimes," *The Journal of Chemical Physics*, vol. 120, no. 5, p. 2238, 2004.

[149] A. S. Galhena, S. Dagan, C. M. Jones, R. L. Beardsley, and V. H. Wysocki, "Surface-induced dissociation of peptides and protein complexes in a quadrupole/time-of-flight mass spectrometer," *Analytical Chemistry*, vol. 80, no. 5, pp. 1425–1436, 2008.

[150] M. Asscher and G. Somorjai, "Energy redistribution in diatomic molecules on surfaces," in *Dynamics on Surfaces*. Springer, 1984, pp. 117–134.

[151] A. Benninghoven, "Chemical Analysis of Inorganic and Organic Surfaces and Thin Films by Static Time-of-Flight Secondary Ion Mass Spectrometry (TOF-SIMS)," *Angewandte Chemie International Edition in English*, vol. 33, no. 10, pp. 1023–1043, jun 1994.

[152] C. Combellas, F. Kanoufi, J. Pinson, and F. I. Podvorica, "Time-of-flight secondary ion mass spectroscopy characterization of the covalent bonding between a carbon surface and aryl groups," *Langmuir*, vol. 21, no. 1, pp. 280–286, 2005.

[153] R. E. Peterson and B. J. Tyler, "Analysis of organic and inorganic species on the surface of atmospheric aerosol using time-of-flight secondary ion mass spectrometry (TOF-SIMS)," *Atmospheric Environment*, vol. 36, no. 39-40, pp. 6041–6049, dec 2002.

[154] M. Wagner and D. G. Castner, "Characterization of adsorbed protein films by time-of-flight secondary ion mass spectrometry with principal component analysis," *Langmuir*, vol. 17, no. 15, pp. 4649–4660, 2001.

[155] H. B. Lu, C. T. Campbell, D. J. Graham, and B. D. Ratner, "Surface characterization of hydroxyapatite and related calcium phosphates by XPS and TOF-SIMS," *Analytical Chemistry*, vol. 72, no. 13, pp. 2886–2894, 2000.

[156] D. C. Gray, I. Tepermeister, and H. H. Sawin, "Phenomenological modeling of ion-enhanced surface kinetics in fluorine-based plasma etching," *Journal of Vacuum Science & Technology B: Microelectronics and Nanometer Structures*, vol. 11, no. 4, p. 1243, jul 1993.

[157] R. A. Rossen and H. H. Sawin, "Ion-enhanced gas-surface kinetics: The Si-Cl_2-Ar^+ system," *Applied Physics Letters*, vol. 45, no. 8, pp. 860–862, oct 1984.

[158] R. A. Rossen and H. H. Sawin, "Time-of-flight and surface residence time measurements for ion-enhanced Si-Cl_2 reaction products," *Journal of Vacuum Science & Technology A: Vacuum, Surfaces, and Films*, vol. 5, no. 4, pp. 1595–1599, jul 1987.

[159] H. H. Sawin and R. P. Merrill, "Fourier analysis of linear surface kinetics in reactive molecular beam scattering," *Journal of Vacuum Science and Technology*, vol. 19, no. 1, pp. 40–46, may 1981.

[160] S. K. Kulkarni, S. M. Gates, C. M. Greenlief, and H. H. Sawin, "Kinetics and mechanics of Si_2H_6 surface decomposition on Si," *Journal of Vacuum Science & Technology A: Vacuum, Surfaces, and Films*, vol. 8, no. 3, pp. 2956–2959, may 1990.

[161] S. Kulkarni, S. Gates, B. Scott, and H. Sawin, "Modulated molecular beam scattering of disilane on silicon," *Surface Science*, vol. 239, no. 1-2, pp. 13–25, dec 1990.

[162] F. H. M. Sanders, A. W. Kolfschoten, J. Dieleman, R. A. Haring, A. Haring, and A. E. de Vries, "Ionassisted etching of silicon by molecular chlorine," *Journal of Vacuum Science & Technology A: Vacuum, Surfaces, and Films*, vol. 2, no. 2, pp. 487–491, apr 1984.

[163] P. Doppelt, G. Hallais, J. Pinson, F. Podvorica, and S. Verneyre, "Surface modification of conducting substrates. Existence of azo bonds in the structure of organic layers obtained from diazonium salts," *Chemistry of Materials*, vol. 19, no. 18, pp. 4570–4575, 2007.

[164] P. van Velzen, J. Ponjeé, and A. Benninghoven, "The kinetics of a surface-chemical reaction: A time-of-flight secondary ion mass spectrometry study," *Applied Surface Science*, vol. 37, no. 2, pp. 147–159, jan 1989.

[165] J. Sunner, E. Dratz, and Y.-C. Chen, "Graphite Surface-Assisted Laser Desorption/ Ionization Time-of-Flight Mass Spectrometry of Peptides and Proteins from Liquid Solutions," *Anal. Chem*, vol. 67, pp. 4335–4342, 1995.

[166] J. Libuda, I. Meusel, J. Hartmann, and H.-J. Freund, "A molecular beam/-surface spectroscopy apparatus for the study of reactions on complex model catalysts," *Review of Scientific Instruments*, vol. 71, no. 12, p. 4395, nov 2000.

[167] R. W. Linton, M. P. Mawn, A. M. Belu, J. M. DeSimone, M. O. Hunt, Y. Z. Menceloglu, H. G. Cramer, and A. Benninghoven, "Time-of-flight secondary ion mass spectrometric analysis of polymer surfaces and additives," *Surface and Interface Analysis*, vol. 20, no. 12, pp. 991–999, nov 1993.

[168] W. L. Guthrie, T. Lin, S. T. Ceyer, and G. A. Somorjai, "The angular and velocity distributions of NO scattered from the Pt(111) crystal surface," *The Journal of Chemical Physics*, vol. 76, no. 12, pp. 6398–6407, jun 1982.

[169] E. Niehuis, T. Heller, H. Feld, and A. Benninghoven, "Design and performance of a reflectron based timeofflight secondary ion mass spectrometer with electrodynamic primary ion mass separation," *Journal of Vacuum Science & Technology A: Vacuum, Surfaces, and Films*, vol. 5, no. 4, pp. 1243–1246, jul 1987.

[170] E. Niehuis, T. Heller, U. Jürgens, and A. Benninghoven, "Surface and trace analysis by highresolution timeofflight secondary ion mass spectrometry," *Journal of Vacuum Science & Technology A: Vacuum, Surfaces, and Films*, vol. 7, no. 3, pp. 1823–1828, may 1989.

[171] G. S. Hwang, C. M. Anderson, M. J. Gordon, T. A. Moore, T. K. Minton, and K. P. Giapis, "Gas-Surface Dynamics and Profile Evolution during Etching of Silicon," *Physical Review Letters*, vol. 77, no. 14, pp. 3049–3052, sep 1996.

[172] H. Wang, D. G. Castner, B. D. Ratner, and S. Jiang, "Probing the orientation of surface-immobilized immunoglobulin G by time-of-flight secondary ion mass spectrometry," *Langmuir*, vol. 20, no. 5, pp. 1877–1887, 2004.

[173] B. Willerding, H. Steininger, K. Snowdon, and W. Heiland, "Time-of-flight measurements of light molecular ions scattered at grazing incidence from a Ni(111) surface," *Nuclear Instruments and Methods in Physics Research Section B: Beam Interactions with Materials and Atoms*, vol. 2, no. 1-3, pp. 453–456, mar 1984.

[174] D. J. Garton, T. K. Minton, D. Troya, R. Pascual, and G. C. Schatz, "Hyperthermal reactions of o (3p) with alkanes: Observations of novel reaction pathways in crossed-beams and theoretical studies," *The Journal of Physical Chemistry A*, vol. 107, no. 23, pp. 4583–4587, 2003.

[175] M. E. King, K. M. Fiehrer, G. M. Nathanson, and T. K. Minton, "Effects of thermal roughening on the angular distributions of trapping and scattering in gas-liquid collisions," *Journal of Physical Chemistry A*, vol. 101, no. 36, pp. 6556–6561, 1997.

[176] I. Rahinov, R. Cooper, C. Yuan, X. Yang, D. J. Auerbach, and A. M. Wodtke, "Efficient vibrational and translational excitations of a solid metal surface: State-to-state time-of-flight measurements of HCl(v=2,J=1) scattering from Au(111)," *The Journal of Chemical Physics*, vol. 129, no. 21, p. 214708, dec 2008.

[177] T. K. Minton, K. P. Giapis, and T. Moore, "Inelastic scattering dynamics of hyperthermal fluorine atoms on a fluorinated silicon surface," *Journal of Physical Chemistry A*, vol. 101, no. 36, pp. 6549–6555, 1997.

[178] D. J. Garton, T. K. Minton, M. Alagia, N. Balucani, P. Casavecchia, and G. G. Volpi, "Comparative dynamics of Cl(^{2}P) and O(^{3}P) interactions with a hydrocarbon surface," *The Journal of Chemical Physics*, vol. 112, no. 13, p. 5975, mar 2000.

[179] D. J. Garton, T. K. Minton, B. Maiti, D. Troya, and G. C. Schatz, "A crossed molecular beams study of the O(^{3}P)+H_2 reaction: Comparison of excitation function with accurate quantum reactive scattering calculations," *The Journal of Chemical Physics*, vol. 118, no. 4, pp. 1585–1588, jan 2003.

[180] M. E. King, G. M. Nathanson, M. Hanning-Lee, and T. K. Minton, "Probing the microscopic corrugation of liquid surfaces with gas-liquid collisions," *Physical Review Letters*, vol. 70, no. 7, pp. 1026–1029, feb 1993.

[181] J. Zhang, D. J. Garton, and T. K. Minton, "Reactive and inelastic scattering dynamics of hyperthermal oxygen atoms on a saturated hydrocarbon surface," *The Journal of Chemical Physics*, vol. 117, no. 13, pp. 6239–6251, oct 2002.

[182] S. T. Ceyer, W. J. Siekhaus, and G. A. Somorjai, "Design of a molecular beam surface scattering apparatus for velocity and angular distribution measurements," *Journal of Vacuum Science and Technology*, vol. 19, no. 3, pp. 726–732, sep 1981.

[183] S. T. Ceyer, W. L. Guthrie, T. Lin, and G. A. Somorjai, "D_2O product angular and translational energy distributions from the oxidation of deuterium on Pt(111)," *The Journal of Chemical Physics*, vol. 78, no. 11, pp. 6982–6991, jun 1983.

[184] M. G. Tenner, E. W. Kuipers, W. Y. Langhout, A. W. Kleyn, G. Nicolasen, and S. Stolte, "Molecular beam apparatus to study interactions of oriented NO and surfaces," *Surface Science*, vol. 236, no. 1-2, pp. 151–168, oct 1990.

[185] D. R. Olander, W. Siekhaus, R. Jones, and J. A. Schwarz, "Reactions of Modulated Molecular Beams with Pyrolytic Graphite. I. Oxidation of the Basal Plane," *The Journal of Chemical Physics*, vol. 57, no. 1, pp. 408–420, 1972.

[186] A. Borner, K. Swaminathan-Gopalan, K. A. Stephani, and N. N. Mansour, "Detailed DSMC surface chemistry modeling of the oxidation of carbon-based ablators," in *30th International Symposium on Rarefied Gas Dynamics 2016*. AIP Publishing, 2016.

[187] K. Swaminathan-Gopalan and K. A. Stephani, "Construction of Finite Rate Surface Chemistry Models from Molecular Beam Experimental Data," *47th AIAA Thermophysics Conference, AIAA Paper 2017-4347*, pp. 1–17, 2017.

[188] K. Swaminathan Gopalan, A. Borner, and K. A. Stephani, "Development of a detailed surface chemistry framework in dsmc," *56th AIAA Aerospace Sciences Meeting, AIAA Paper 2018-0494*, pp. 1–32, 2018.

[189] A. Borner, K. Swaminathan-Gopalan, K. Stephani, S. Poovathingal, V. Murray, T. Minton, F. Panerai, and N. Mansour, "Investigation of the high-energy oxidation of fiberform from dsmc analysis of molecular beam experiments," 2017.

[190] K. Swaminathan-Gopalan and K. A. Stephani, "Construction of finite rate surface chemistry models from pulsed hyperthermal beam experimental data," *AIP Advances*, vol. 9, no. 3, p. 035246, 2019.

[191] Y.-K. Chen and F. S. Milos, "Ablation and thermal response program for spacecraft heatshield analysis," *Journal of Spacecraft and Rockets*, vol. 36, no. 3, pp. 475–483, 1999.

[192] A. J. Amar, B. F. Blackwell, and J. R. Edwards, "One-dimensional ablation using a full newton's method and finite control volume procedure," *Journal of Thermophysics and Heat Transfer*, vol. 22, no. 1, pp. 71–82, 2008.

[193] Y.-K. Chen, T. Gökçen, and K. T. Edquist, "Two-dimensional ablation and thermal response analyses for mars science laboratory heat shield," *Journal of Spacecraft and Rockets*, vol. 52, no. 1, pp. 134–143, 2014.

[194] H. Weng and A. Martin, "Multidimensional modeling of pyrolysis gas transport inside charring ablative materials," *Journal of Thermophysics and Heat Transfer*, vol. 28, no. 4, pp. 583–597, 2014.

[195] H. Weng, S. C. Bailey, and A. Martin, "Numerical study of iso-q sample geometric effects on charring ablative materials," *International Journal of Heat and Mass Transfer*, vol. 80, pp. 570–596, 2015.

[196] H. Weng and A. Martin, "Numerical investigation of thermal response using orthotropic charring ablative material," *Journal of Thermophysics and Heat Transfer*, vol. 29, no. 3, pp. 429–438, 2015.

[197] M. Wang and Z. Li, "Simulations for gas flows in microgeometries using the direct simulation monte carlo method," *International Journal of Heat and Fluid Flow*, vol. 25, no. 6, pp. 975–985, 2004.

[198] A. J. Amar, B. Oliver, B. Kirk, G. Salazar, and J. Droba, "Overview of the charring ablator response (char) code," in *46th AIAA Thermophysics Conference*, 2016, p. 3385.

[199] J. Lachaud, N. Mansour, A. Ceballos, D. Pejakovic, L. Zhang, and J. Marschall, "Validation of a volume-averaged fiber-scale model for the oxidation of a carbon-fiber preform," in *42nd AIAA Thermophysics Conference*, 2011, p. 3640.

[200] P. Schrooyen, K. Hillewaert, T. E. Magin, and P. Chatelain, "Fully implicit discontinuous galerkin solver to study surface and volume ablation competition in atmospheric entry flows," *International Journal of Heat and Mass Transfer*, vol. 103, pp. 108–124, 2016.

[201] S. Whitaker, "Theory and applications of transport in porous media: The method of volume averaging, vol. 13," 1998.

[202] J. Lachaud, I. Cozmuta, and N. N. Mansour, "Multiscale approach to ablation modeling of phenolic impregnated carbon ablators," *Journal of Spacecraft and Rockets*, vol. 47, no. 6, pp. 910–921, 2010.

[203] K. Stephani, D. Goldstein, and P. Varghese, "Generation of a hybrid dsmc/cfd solution for gas mixtures with internal degrees of freedom," in *50th AIAA Aerospace Sciences Meeting including the New Horizons Forum and Aerospace Exposition*, 2012, p. 648.

[204] G. Groskopf, M. Kloker, and K. Stephani, "Temperature/rarefaction effects in hypersonic boundary-layer flow with an oblique roughness element," in *41st AIAA Fluid Dynamics Conference and Exhibit*, 2011, p. 3251.

[205] K. Stephani, D. Goldstein, and P. Varghese, "Effects of rarefaction on hypersonic boundary layer flow over discrete surface roughness," in *48th AIAA Aerospace Sciences Meeting Including the New Horizons Forum and Aerospace Exposition*, 2010, p. 456.

[206] K. Swaminathan Gopalan and K. A. Stephani, "Calibration of dsmc parameters for transport processes in ionized air mixtures," in *45th AIAA Thermophysics Conference*, 2015, p. 3373.

[207] D. Chandel, I. Nompelis, and G. V. Candler, "Numerical simulation of propagation of strong shock waves," in *55th AIAA Aerospace Sciences Meeting*, 2017, p. 0744.

[208] K. Swaminathan-Gopalan, "Consistent treatment of transport properties of weakly-ionized gas mixtures in dsmc," Ph.D. dissertation, 2015.

[209] D. Chandel, I. Nompelis, G. V. Candler, and A. M. Brandis, "Cfd predictions of high enthalpy shocks in nitrogen," in *AIAA Aviation 2019 Forum*, 2019, p. 3078.

[210] I. D. Boyd and T. E. Schwartzentruber, *Nonequilibrium Gas Dynamics and Molecular Simulation*. Cambridge University Press, 2017.

[211] S. S. Sawant, R. Jambunathan, O. Tumuklu, B. Korkut, and D. A. Levin, "Study of shock-shock interactions using an unstructured amr octree dsmc code," in *54th AIAA Aerospace Sciences Meeting*, 2016, p. 0501.

[212] G. Groskopf, M. Kloker, K. Stephani, O. Marxen, and G. Iaccarino, "Hypersonic flows with discrete oblique surface roughness and their stability properties," *Proceedings of the 2010 Summer Program*, pp. 405–422, 2010.

[213] K. Stephani, D. Goldstein, and P. Varghese, "Development of a hybrid dsmc/navier-stokes solver with application to the sts-119 boundary layer transition flight experiments," in *49th AIAA Aerospace Sciences Meeting including the New Horizons Forum and Aerospace Exposition*, 2011, p. 534.

[214] K. Stephani, D. Goldstein, and P. Varghese, "Parametric study of hypersonic boundary layer flow over discrete surface roughness using a hybrid dsmc/navier-stokes solver," in *41st AIAA Fluid Dynamics Conference and Exhibit*, 2011, p. 3250.

[215] K. Stephani, D. B. Goldstein, and P. L. Varghese, "Consistent treatment of transport properties for five-species air direct simulation monte carlo/navier-stokes applications," *Physics of fluids*, vol. 24, no. 7, p. 077101, 2012.

[216] K. A. Stephani, "Development of a hybrid dsmc/cfd method for hypersonic boundary layer flow over discrete surface roughness," Ph.D. dissertation, 2012.

[217] K. Swaminathan-Gopalan and K. A. Stephani, "Recommended direct simulation monte carlo collision model parameters for modeling ionized air transport processes," *Physics of Fluids*, vol. 28, no. 2, p. 027101, 2016.

[218] D. Chandel, I. Nompelis, and G. V. Candler, "Computations of high enthalpy shock-waves in electric arc shock-tube (east) at nasa ames," in *2018 AIAA Aerospace Sciences Meeting*, 2018, p. 1722.

[219] E. C. Stern, I. Nompelis, T. E. Schwartzentruber, and G. V. Candler, "Microscale Simulations of Porous TPS Materials: Application to Permeability," *11th AIAA/ASME Joint Thermophysics and Heat Transfer Conference, AIAA Paper 2014-2247*, pp. 1–15, 2014.

[220] E. C. Stern, I. Nompelis, T. E. Schwartzentruber, and G. V. Candler, "Microscale Simulations of Porous TPS materials: Ablating Microstructures and Micro-tomography," *53rd AIAA Aerospace Sciences Meeting, AIAA Paper 2015-1450*, pp. 1–14, 2015.

[221] C. White, T. J. Scanlon, and R. E. Brown, "Permeability of ablative materials under rarefied gas conditions," *Journal of Spacecraft and Rockets*, 2015.

[222] A. Borner, F. Panerai, and N. N. Mansour, "High temperature permeability of fibrous materials using direct simulation monte carlo," *International Journal of Heat and Mass Transfer*, vol. 106, pp. 1318–1326, 2017.

[223] R. Jambunathan, D. A. Levin, A. Borner, J. C. Ferguson, and F. Panerai, "Prediction of gas transport properties through fibrous carbon preform microstructures using direct simulation monte carlo," *International Journal of Heat and Mass Transfer*, vol. 130, pp. 923–937, 2019.

[224] C. White, T. J. Scanlon, and R. E. Brown, "Permeability of ablative materials under rarefied gas conditions," *Journal of Spacecraft and Rockets*, vol. 53, no. 1, pp. 134–142, 2015.

[225] R. Jambunathan and D. A. Levin, "Advanced parallelization strategies using hybrid mpi-cuda octree dsmc method for modeling flow through porous media," *Computers & Fluids*, vol. 149, pp. 70–87, 2017.

[226] R. Jambunathan and D. A. Levin, "Gridless direct simulation monte carlo approach for analysis of fractal-like spore aggregates," in *11th AIAA/ASME Joint Thermophysics and Heat Transfer Conference*, 2014, p. 2131.

[227] R. Jambunathan, "Advanced parallelization strategies using hybrid mpi-cuda dsmc method for modeling flow through porous media," in *46th AIAA Thermophysics Conference, 2016*. American Institute of Aeronautics and Astronautics Inc, AIAA, 2016.

[228] R. Jambunathan and D. A. Levin, "Forest of octree dsmc simulations of flow through porous media," in *AIP Conference Proceedings*, vol. 1786, no. 1. AIP Publishing, 2016, p. 050009.

[229] R. Jambunathan and D. A. Levin, "Grid-free octree approach for modeling heat transfer to complex geometries," *Journal of Thermophysics and Heat Transfer*, no. null, pp. 379–393, 2016.

[230] P. Agrawal, J. F. Chavez-Garcia, and J. Pham, "Fracture in phenolic impregnated carbon ablator," *Journal of Spacecraft and Rockets*, vol. 50, no. 4, pp. 735–741, 2013.

[231] R. Jambunathan, A. Borner, J. Ferguson, F. Panerai, and D. A. Levin, "Prediction of thermal protection system material permeability and tortuosity factor using direct simulation monte carlo," in *2018 AIAA Aerospace Sciences Meeting*, 2018, p. 0497.

[232] J. Lachaud and G. L. Vignoles, "A brownian motion technique to simulate gasification and its application to c/c composite ablation," *Computational materials science*, vol. 44, no. 4, pp. 1034–1041, 2009.

[233] G. L. Vignoles, "Image segmentation for phase-contrast hard x-ray cmt of c/c composites," *Carbon*, vol. 39, no. 2, pp. 167–173, 2001.

[234] N. N. Mansour, F. Panerai, A. Martin, D. Y. Parkinson, A. MacDowell, T. Fast, G. Vignoles, and J. Lachaud, "A new approach to light-weight ablators analysis: from micro-tomography measurements to statistical analysis and modeling," in *44th AIAA Thermophysics Conference*, 2013, p. 2768.

[235] R. Gosse, "Pyrolysis gas modeling of tps materials using finite-volume method and issues with validation," in *42nd AIAA Thermophysics Conference*, 2011, p. 3641.

[236] S. S. Sawant, P. Rao, A. Harpale, H. B. Chew, and D. A. Levin, "Micro-scale thermal response modeling of avcoat-like tps," in *2018 AIAA Aerospace Sciences Meeting*, 2018, p. 0495.

[237] J. Lachaud and N. N. Mansour, "Porous-material analysis toolbox based on openfoam and applications," *Journal of Thermophysics and Heat Transfer*, vol. 28, no. 2, pp. 191–202, 2014.

[238] R. M. Kendall, E. P. Bartlett, R. A. Rindall, and C. B. Moyer, *An analysis of the coupled chemically reacting boundary layer and charring ablator*. National Aeronautics and Space Administration, 1968.

[239] Y.-K. Chen and F. Milos, "Three-dimensional ablation and thermal response simulation system," in *38th AIAA Thermophysics Conference*, 2005, p. 5064.

[240] Y.-K. Chen, F. Milos, and T. Gokcen, "Validation of a three-dimensional ablation and thermal response simulation code," in *10th AIAA/ASME Joint Thermophysics and Heat Transfer Conference*, 2010, p. 4645.

[241] F. S. Milos and Y.-K. Chen, "Two-dimensional ablation, thermal response, and sizing program for pyrolyzing ablators," *Journal of Spacecraft and Rockets*, vol. 46, no. 6, pp. 1089–1099, 2009.

[242] A. J. Amar, B. F. Blackwell, and J. Edwards, "Development and verification of a one-dimensional ablation code including pyrolysis gas flow," *Journal of Thermophysics and Heat Transfer*, vol. 23, no. 1, pp. 59–71, 2009.

[243] A. Martin and I. D. Boyd, "Non-darcian behavior of pyrolysis gas in a thermal protection system," *Journal of Thermophysics and Heat Transfer*, vol. 24, no. 1, pp. 60–68, 2010.

[244] A. Martin and I. Boyd, "Mesh tailoring for strongly coupled computation of ablative material in nonequilibrium hypersonic flow," in *10th AIAA/ASME Joint Thermophysics and Heat Transfer Conference*, 2010, p. 5062.

[245] A. Martin and I. D. Boyd, "Strongly coupled computation of material response and nonequilibrium flow for hypersonic ablation," *Journal of Spacecraft and Rockets*, vol. 52, no. 1, pp. 89–104, 2014.

[246] J. Hepburn, F. Northrup, G. Ogram, J. Polanyi, and J. Willamson, "Rotationally inelastic scattering from surfaces co (g)+ lif (oo1)," *Chemical Physics Letters*, vol. 85, no. 2, pp. 127–130, 1982.

[247] G. Kubiak, J. Hurst Jr, H. Rennagel, G. McClelland, and R. Zare, "Direct inelastic scattering of nitric oxide from clean ag (111): Rotational and fine structure distributions," *The Journal of chemical physics*, vol. 79, no. 10, pp. 5163–5178, 1983.

[248] A. Mödl, H. Robota, J. Segner, W. Vielhaber, M. Lin, and G. Ertl, "Rotational state distributions of no molecules after interaction with germanium surfaces," *The Journal of chemical physics*, vol. 83, no. 9, pp. 4800–4807, 1985.

[249] G. O. Sitz, A. C. Kummel, and R. N. Zare, "Direct inelastic scattering of n2 from ag (111). i. rotational populations and alignment," *The Journal of chemical physics*, vol. 89, no. 4, pp. 2558–2571, 1988.

[250] J. L. Siders and G. O. Sitz, "Molecular beam study of n2 scattering from si (100)," in *Laser Techniques for Surface Science II*, vol. 2547. International Society for Optics and Photonics, 1995, pp. 206–217.

[251] D. Jacobs, K. Kolasinski, S. Shane, and R. Zare, "Rotational population and alignment distributions for inelastic scattering and trapping/desorption of no on pt (111)," *The Journal of Chemical Physics*, vol. 91, no. 5, pp. 3182–3195, 1989.

[252] K. R. Lykke and B. D. Kay, "Rotationally inelastic gas–surface scattering: Hcl from au (111)," *The Journal of chemical physics*, vol. 92, no. 4, pp. 2614–2623, 1990.

[253] M. A. Hines and R. N. Zare, "The interaction of co with ni (111): Rainbows and rotational trapping," *The Journal of chemical physics*, vol. 98, no. 11, pp. 9134–9147, 1993.

[254] J. Häger, D. Glatzer, H. Kuze, M. Fink, and H. Walther, "Rotationally excited no molecules incident on a graphite surface: molecular rotation and translation after scattering," *Surface science*, vol. 374, no. 1-3, pp. 181–190, 1997.

[255] D. Glatzer, J. Häger, M. Fink, and H. Walther, "Rotationally excited NO molecules incident on a graphite surface: in- and out-of-plane angular distributions," *Surface Science*, vol. 374, no. 1, pp. 169–180, 1997.

[256] T. Engel, "A molecular beam investigation of he, co, and o2 scattering from pd (111)," *The Journal of Chemical Physics*, vol. 69, no. 1, pp. 373–385, 1978.

[257] M. Cardillo, C. Ching, E. Greene, and G. Becker, "Molecular-beam apparatus for the study of gas–surface interactions," *Journal of Vacuum Science and Technology*, vol. 15, no. 2, pp. 423–428, 1978.

[258] M. J. Cardillo, "Gas-surface interactions studied with molecular beam techniques," *Annual Review of Physical Chemistry*, vol. 32, no. 1, pp. 331–357, 1981.

[259] M. Spruit, E. Kuipers, M. Tenner, J. Kimman, and A. Kleyn, "Molecular-beam scattering of o2 and ar from ag (111)," *Journal of Vacuum Science & Technology A: Vacuum, Surfaces, and Films*, vol. 5, no. 4, pp. 496–500, 1987.

[260] L. Brown and S. Sibener, "A molecular beam scattering investigation of the oxidation of co on rh (111). i. kinetics and mechanism," *The Journal of chemical physics*, vol. 89, no. 2, pp. 1163–1169, 1988.

[261] L. Brown and S. Sibener, "A molecular beam scattering investigation of the oxidation of co on rh (111). ii. angular and velocity distributions of the co2 product," *The Journal of Chemical Physics*, vol. 90, no. 5, pp. 2807–2815, 1989.

[262] M. G. Tenner, E. W. Kuipers, W. Y. Langhout, A. W. Kleyn, G. Nicolasen, and S. Stolte, "Molecular beam apparatus to study interactions of oriented no and surfaces," *Surface Science*, vol. 236, no. 1-2, pp. 151–168, 1990.

[263] C. R. Arumainayagam and R. J. Madix, "Molecular beam studies of gas-surface collision dynamics," *Progress in Surface science*, vol. 38, no. 1, pp. 1–102, 1991.

[264] J. Libuda and H.-J. Freund, "Molecular beam experiments on model catalysts," *Surface Science Reports*, vol. 57, no. 7-8, pp. 157–298, 2005.

[265] V. Ramesh and D. Marsden, "Rotational and translational accommodation coefficients of nitrogen on nickel, silver and gold," *Vacuum*, vol. 24, no. 7, pp. 291–294, 1974.

[266] F. Frenkel, J. Häger, W. Krieger, H. Walther, C. Campbell, G. Ertl, H. Kuipers, and J. Segner, "Rotationally inelastic gas-surface scattering investigated by laser-induced fluorescence," *Physical Review Letters*, vol. 46, no. 2, p. 152, 1981.

[267] A. Kleyn, A. Luntz, and D. Auerbach, "Rotational energy transfer in direct inelastic surface scattering: No on ag (111)," *Physical Review Letters*, vol. 47, no. 16, p. 1169, 1981.

[268] Y. Watanabe, H. Yamaguchi, M. Hashinokuchi, K. Sawabe, S. Maruyama, Y. Matsumoto, and K. Shobatake, "Trampoline motions in xe–graphite (0 0 0 1) surface scattering," *Chemical physics letters*, vol. 413, no. 4-6, pp. 331–334, 2005.

[269] Y. Watanabe, H. Yamaguchi, M. Hashinokuchi, K. Sawabe, S. Maruyama, Y. Matsumoto, and K. Shobatake, "Energy transfer in hyperthermal xe-graphite surface scattering," *The European Physical Journal D-Atomic, Molecular, Optical and Plasma Physics*, vol. 38, no. 1, pp. 103–109, 2006.

[270] J. Oh, T. Kondo, K. Arakawa, Y. Saito, J. Nakamura, W. Hayes, and J. Manson, "Scattering of co and n2 molecules by a graphite surface," *Journal of Physics: Condensed Matter*, vol. 24, no. 35, p. 354001, 2012.

[271] N. A. Mehta, V. J. Murray, C. Xu, D. A. Levin, and T. K. Minton, "Non-reactive scattering of n2 from layered graphene using molecular beam experiments and molecular dynamics," *The Journal of Physical Chemistry C*, vol. 122, no. 18, pp. 9859–9874, 2018.

[272] W. W. Hayes, J. Oh, T. Kondo, K. Arakawa, Y. Saito, J. Nakamura, and J. R. Manson, "Scattering of O2 from a graphite surface," *Journal of Physics: Condensed Matter*, vol. 24, no. 10, p. 104010, mar 2012. [Online]. Available: http://stacks.iop.org/0953-8984/24/i=10/a=104010?key=crossref.3ca410ac79899ccddde09c00fdad970c

[273] F. O. Goodman, *Dynamics of gas-surface scattering*. Elsevier, 1976.

[274] F. O. Goodman, "Three-dimensional hard spheres theory of scattering of gas atoms from a solid surface i. limit of large incident speed," *Surface Science*, vol. 7, no. 3, pp. 391–421, 1967.

[275] R. Brako and D. Newns, "Differential cross section for atoms inelastically scattered from surfaces," *Physical Review Letters*, vol. 48, no. 26, p. 1859, 1982.

[276] R. Brako and D. Newns, "Energy and angular distribution of atoms scattered from surfaces," *Surface Science*, vol. 117, no. 1-3, pp. 42–52, 1982.

[277] H.-D. Meyer and R. Levine, "Multiphonon energy transfer in atom-surface scattering," *Chemical physics*, vol. 85, no. 2, pp. 189–200, 1984.

[278] V. Bortolani and A. Levi, "Atom-surface scattering theory," *La Rivista del Nuovo Cimento (1978-1999)*, vol. 9, no. 11, pp. 1–77, 1986.

[279] C. T. Rettner and M. N. R. Ashfold, *Dynamics of gas-surface interactions*. Royal Society of Chemistry London, 1991, vol. 3.

[280] J. R. Manson, "Inelastic scattering from surfaces," *Physical Review B*, vol. 43, no. 9, pp. 6924–6937, mar 1991. [Online]. Available: https://link.aps.org/doi/10.1103/PhysRevB.43.6924

[281] J. Manson, V. Celli, and D. Himes, "Multiphonon scattering from surfaces," *Physical Review B*, vol. 49, no. 4, p. 2782, 1994.

[282] J. Manson, "Atom-surface scattering in the classical limit: Temperature and energy dependence," *Physical Review B*, vol. 58, no. 4, p. 2253, 1998.

[283] I. Iftimia and J. R. Manson, "Theory of Molecule-Surface Scattering at Thermal and Hyperthermal Energies," *Physical Review Letters*, vol. 87, no. 9, p. 093201, aug 2001. [Online]. Available: https://link.aps.org/doi/10.1103/PhysRevLett.87.093201

[284] I. Iftimia and J. R. Manson, "Theory of mixed classical-quantum scattering of molecules from surfaces," *Physical Review B*, vol. 65, no. 12, p. 125401, feb 2002. [Online]. Available: https://link.aps.org/doi/10.1103/PhysRevB.65.125401

[285] A. Rana, R. Ravichandran, J. Park, and R. Myong, "Microscopic molecular dynamics characterization of the second-order non-navier-fourier constitutive laws in the poiseuille gas flow," *Physics of Fluids*, vol. 28, no. 8, p. 082003, 2016.

[286] M. Ayub, A. Zander, D. Huang, C. Howard, and B. Cazzolato, "Molecular dynamics simulations of acoustic absorption by a carbon nanotube," *Physics of Fluids*, vol. 30, no. 6, p. 066101, 2018.

[287] J. Blömer and A. Beylich, "Molecular dynamics simulation of energy accommodation of internal and translational degrees of freedom at gas–surface interfaces," *Surface science*, vol. 423, no. 1, pp. 127–133, 1999.

[288] K. Yamamoto, H. Takeuchi, and T. Hyakutake, "Characteristics of reflected gas molecules at a solid surface," *Physics of Fluids*, vol. 18, no. 4, p. 046103, 2006.

[289] K. Yamamoto, H. Takeuchi, and T. Hyakutake, "Scattering properties and scattering kernel based on the molecular dynamics analysis of gas-wall interaction," *Physics of Fluids*, vol. 19, no. 8, p. 087102, 2007.

[290] N. Yamanishi, Y. Matsumoto, and K. Shobatake, "Multistage gas–surface interaction model for the direct simulation monte carlo method," *Physics of Fluids*, vol. 11, no. 11, pp. 3540–3552, 1999.

[291] N. A. Mehta, D. A. Levin, V. J. Murray, and T. K. Minton, "Study of non-reactive scattering from graphene using molecular beam experiments and molecular dynamics," *AIP Conference Proceedings*, vol. 1786, no. 1, pp. 100 003(1–8), 2016.

[292] N. Andric and P. Jenny, "Molecular dynamics investigation of energy transfer during gas-surface collisions," *Physics of Fluids*, vol. 30, no. 7, p. 077104, 2018.

[293] M. Majumder, H. N. Bhandari, S. Pratihar, and W. L. Hase, "Chemical dynamics simulation of low energy n2 collisions with graphite," *The Journal of Physical Chemistry C*, vol. 122, no. 1, pp. 612–623, 2017.

[294] M. Majumder, K. Gibson, S. Sibener, and W. L. Hase, "Chemical dynamics simulations and scattering experiments for o2 collisions with graphite," *The Journal of Physical Chemistry C*, vol. 122, no. 28, pp. 16 048–16 059, 2018.

[295] N. A. Mehta, D. A. Levin, and A. van Duin, "Molecular dynamics studies of thermal accommodation on carbon surfaces," in *11th AIAA/ASME Joint Thermophysics and Heat Transfer Conference*, 2014, p. 2681.

[296] N. A. Mehta and D. A. Levin, "Molecular dynamics studies of nitrogen collision on graphene and quartz surfaces," in *54th AIAA Aerospace Sciences Meeting*, 2016, p. 0502.

[297] N. A. Mehta and D. A. Levin, "Molecular-dynamics-derived gas–surface models for use in direct-simulation monte carlo," *Journal of Thermophysics and Heat Transfer*, vol. 31, no. 4, pp. 757–771, 2017.

[298] J. C. Maxwell, "Vii. on stresses in rarified gases arising from inequalities of temperature," *Philosophical Transactions of the royal society of London*, no. 170, pp. 231–256, 1879.

[299] M. Knudsen and J. Partington, "The kinetic. theoryof gases. some modern aspects," *The Journal of Physical Chemistry*, vol. 39, no. 2, pp. 307–307, 1935.

[300] C. Cercignani and M. Lampis, "Kinetic models for gas-surface interactions," *transport theory and statistical physics*, vol. 1, no. 2, pp. 101–114, 1971.

[301] R. Lord, "Some extensions to the cercignani–lampis gas–surface scattering kernel," *Physics of Fluids A: Fluid Dynamics*, vol. 3, no. 4, pp. 706–710, 1991.

[302] R. Lord, "Some further extensions of the cercignani–lampis gas–surface interaction model," *Physics of Fluids*, vol. 7, no. 5, pp. 1159–1161, 1995.

[303] W. L. Nichols and J. H. Weare, "Homonuclear diatomic scattering from solid surfaces: A hard cube model," *The Journal of Chemical Physics*, vol. 62, no. 9, pp. 3754–3762, 1975.

[304] W. L. Nichols and J. H. Weare, "Heteronuclear diatomic scattering from solid surfaces: A hard-cube model," *The Journal of Chemical Physics*, vol. 63, no. 1, pp. 379–383, 1975.

[305] W. L. Nichols and J. H. Weare, "Rotational energy distributions for homonuclear diatomic beams scattered from solid surfaces: A hard-cube model," *The Journal of Chemical Physics*, vol. 66, no. 3, pp. 1075–1078, 1977.

[306] R. M. Logan and R. Stickney, "Simple classical model for the scattering of gas atoms from a solid surface," *The Journal of Chemical Physics*, vol. 44, no. 1, pp. 195–201, 1966.

[307] R. Logan, "Calculation of the energy accommodation coefficient using the soft-cube model," *Surface Science*, vol. 15, no. 3, pp. 387–402, 1969.

[308] J. C. Tully, "Washboard model of gas–surface scattering," *The Journal of chemical physics*, vol. 92, no. 1, pp. 680–686, 1990.

[309] W. Weinberg and R. Merrill, "A simple classical model for trapping in gas–surface interactions," *Journal of Vacuum Science and Technology*, vol. 8, no. 6, pp. 718–724, 1971.

[310] T. Yan, W. L. Hase, and J. C. Tully, "A washboard with moment of inertia model of gas-surface scattering," *The Journal of chemical physics*, vol. 120, no. 2, pp. 1031–1043, 2004.

[311] C. Rettner, J. Barker, and D. Bethune, "Angular and velocity distributions characteristic of the transition between the thermal and structure regimes of gas-surface scattering," *Physical review letters*, vol. 67, no. 16, p. 2183, 1991.

[312] W. A. Alexander, J. Zhang, V. J. Murray, G. M. Nathanson, and T. K. Minton, "Kinematics and dynamics of atomic-beam scattering on liquid and self-assembled monolayer surfaces," *Faraday Discussions*, vol. 157, pp. 355–374, 2012.

[313] S. Subramaniam and K. A. Stephani, "Characterization of state-resolved transport for o+ o2 collisions," in *2018 AIAA Aerospace Sciences Meeting*, 2018, p. 1484.

[314] S. Subramaniam and K. A. Stephani, "Computation of state to state transport coefficients using ab initio potential energy surfaces for the o+ o2 system," in *AIAA Scitech 2019 Forum*, 2019, p. 1050.

[315] C. Kondur, S. Subramaniam, T.-J. Pan, and K. A. Stephani, "Computation of orbiting cross-sections from ab initio potential energy surfaces for recombination of atomic oxygen," in *AIAA Scitech 2019 Forum*, 2019, p. 2282.

[316] T.-J. Pan, C. Kondur, S. Subramaniam, and K. A. Stephani, "A state-resolved recombination model using orbiting cross-sections from the potential energy surface for atomic oxygen in dsmc," in *AIAA Scitech 2019 Forum*, 2019, p. 0797.

[317] T.-J. Pan, T. J. Wilson, and K. A. Stephani, "Vibrational state-specific model for dissociation and recombination of the o 2 (3 σ g-)+ o (3 p) system in dsmc," *The Journal of chemical physics*, vol. 150, no. 7, p. 074305, 2019.

[318] T. Wilson and K. A. Stephani, "State-to-state vibrational energy modeling in dsmc using quasiclassical trajectory calculations for o+ o2," in *46th AIAA Thermophysics Conference*, 2016, p. 3839.

[319] J. Jackson and N. F. Mott, "Energy exchange between inert gas atoms and a solid surface," *Proceedings of the Royal Society of London. Series A, Containing Papers of a Mathematical and Physical Character*, vol. 137, no. 833, pp. 703–717, 1932.

[320] J. Jackson, "A quantum mechanical theory of energy exchanges between inert gas atoms and a solid surface," in *Mathematical Proceedings of the Cambridge Philosophical Society*, vol. 28, no. 1. Cambridge University Press, 1932, pp. 136–164.

[321] J. Lennard-Jones and A. Devonshire, "Diffraction and selective adsorption of atoms at crystal surfaces," *Nature*, vol. 137, no. 3478, p. 1069, 1936.

[322] A. Devonshire, "The interaction of atoms and molecules with solid surfaces vthe diffraction and reflexion of molecular rays," *Proceedings of the Royal Society of London. Series A-Mathematical and Physical Sciences*, vol. 156, no. 887, pp. 37–44, 1936.

[323] J. E. Lennard-Jones and A. Devonshire, "The interaction of atoms and molecules with solid surfaces viithe diffraction of atoms by a surface," *Proceedings of the Royal Society of London. Series A-Mathematical and Physical Sciences*, vol. 158, no. 894, pp. 253–268, 1937.

[324] J. E. Lennard-Jones, "The interaction of atoms and molecules with solid surfaces-xithe dispersal of energy from an activated link," *Proceedings of the Royal Society of London. Series A-Mathematical and Physical Sciences*, vol. 163, no. 912, pp. 127–131, 1937.

[325] J. E. Lennard-Jones and A. Devonshire, "The interaction of atoms and molecules with solid surfaces vithe behaviour of adsorbed helium at low temperatures," *Proceedings of the Royal Society of London. Series A-Mathematical and Physical Sciences*, vol. 158, no. 894, pp. 242–252, 1937.

[326] C. Strachan, "The interaction of atoms and molecules with solid surfaces ixthe emission and absorption of energy by a solid," *Proceedings of the Royal Society of London. Series A-Mathematical and Physical Sciences*, vol. 158, no. 895, pp. 591–605, 1937.

[327] J. Beeby, "The scattering of atoms from surfaces: the one-phonon contribution," *Journal of Physics C: Solid State Physics*, vol. 5, no. 24, p. 3438, 1972.

[328] J. Beeby, "The scattering of atoms from surfaces. ii. the two-phonon terms," *Journal of Physics C: Solid State Physics*, vol. 5, no. 24, p. 3457, 1972.

[329] M. Lagos, "Scattering of atomic beams by surface and bulk phonons," *Surface Science*, vol. 65, no. 1, pp. 124–140, 1977.

[330] M. Lagos, "Scattering of low-energy atoms by metallic surfaces," *Surface Science*, vol. 71, no. 2, pp. 414–432, 1978.

[331] A. Levi, "Quantum theory of atom-surface scattering: Inelastic scattering," *Il Nuovo Cimento B (1971-1996)*, vol. 54, no. 2, p. 357, 1979.

[332] A. Levi and H. Suhl, "Quantum theory of atom-surface scattering: Debye-waller factor," *Surface Science*, vol. 88, no. 1, pp. 221–254, 1979.

[333] W. Brenig, "Theory of inelastic atom-surface scattering: Average energy loss and energy distribution," *Zeitschrift für Physik B Condensed Matter*, vol. 36, no. 1, pp. 81–87, 1979.

[334] D. Kumamoto and R. Silbey, "A self-consistent semiclassical approach to the inelastic scattering of atoms from solid surfaces," *The Journal of Chemical Physics*, vol. 75, no. 10, pp. 5164–5171, 1981.

[335] D. A. Micha, "Interaction of atoms with solid surfaces: Energy transfer in hyperthermal collisions of li+ with w (110)," *The Journal of Chemical Physics*, vol. 74, no. 3, pp. 2054–2058, 1981.

[336] J. Böheim, W. Brenig, T. Engel, and U. Leuthäusser, "Kinetics of nitrogen adsorption on iron," *Surface science*, vol. 131, no. 2-3, pp. 258–272, 1983.

[337] B. Choi and R. Poe, "Theory of phonon inelastic atom–surface scattering. i. quantum mechanical treatment of collision dynamics," *The Journal of chemical physics*, vol. 83, no. 3, pp. 1330–1343, 1985.

[338] M. Jezercak, P. Agrawal, C. B. Smith, and L. M. Raff, "Wave packet studies of gas–surface inelastic scattering and desorption rates," *The Journal of chemical physics*, vol. 88, no. 2, pp. 1264–1271, 1988.

[339] B. Jackson, "Time dependent quantum mechanical theory of gas–surface energy transfer," *The Journal of chemical physics*, vol. 88, no. 2, pp. 1383–1393, 1988.

[340] R. Kosloff and C. Cerjan, "Inelastic he scattering from a xenon overlayer: Dynamical diffraction effects," *The Journal of Chemical Physics*, vol. 90, no. 12, pp. 7556–7563, 1989.

[341] B. Jackson, "A semiclassical study of gas–solid energy transfer: He, ne, and ar on metal surfaces," *The Journal of chemical physics*, vol. 92, no. 2, pp. 1458–1467, 1990.

[342] B. Gumhalter, "Single-and multiphonon atom–surface scattering in the quantum regime," *Physics Reports*, vol. 351, no. 1-2, pp. 1–159, 2001.

[343] J. Jensen, L. Chang, and W. Kohn, "Semiclassical theory for inelastic scattering," *Physical Review A*, vol. 40, no. 3, p. 1198, 1989.

[344] J. Skofronick, G. Bishop, W. Brug, G. Chern, J. Duan, S. Safron, and J. Manson, "Temperature dependence of he atom scattering from nacl (001)," *Superlattices and Microstructures*, vol. 7, no. 3, pp. 239–245, 1990.

[345] K. Burke and W. Kohn, "Finite debye-waller factor for classicalatom-surface scattering," *Physical Review B*, vol. 43, no. 4, p. 2477, 1991.

[346] K. Burke, B. Gumhalter, and D. C. Langreth, "Nearly elastic scattering and the trajectory approximation," *Physical Review B*, vol. 47, no. 19, p. 12852, 1993.

[347] S.-C. Ying and B. Bendow, "Phonon-induced desorption of adatoms from crystal surfaces. ii. numerical computations for a model system," *Physical Review B*, vol. 7, no. 2, p. 637, 1973.

[348] E. Goldys, Z. Gortel, and H. Kreuzer, "Desorption kinetics mediated by surface phonon modes," *Surface Science*, vol. 116, no. 1, pp. 33–65, 1982.

[349] S. Efrima, C. Jedrzejek, K. F. Freed, E. Hood, and H. Metiu, "A one-dimensional model for phonon-induced desorption," *The Journal of chemical physics*, vol. 79, no. 5, pp. 2436–2453, 1983.

[350] E. Hood, C. Jedrzejek, K. F. Freed, and H. Metiu, "A one-dimensional model for phonon-induced desorption. ii. numerical analysis of the desorption of noble gas atoms (argon, krypton, and xenon) from tungsten and carbon monoxide from copper," *The Journal of chemical physics*, vol. 81, no. 7, pp. 3277–3293, 1984.

[351] B. Gumhalter and T. Matsushima, "Energy dissipation during desorption of reaction products: the role of substrate phonons," *Surface science*, vol. 561, no. 2-3, pp. 183–192, 2004.

[352] B. Kelly, "The effect of defects on the basal plane thermal conductivity of a graphite crystal," *Carbon*, vol. 5, no. 3, pp. 247–260, 1967.

[353] R. Taylor, B. Kelly, and K. Gilchrist, "The thermal conductivity of fast neutron irradiated graphite," *Journal of Physics and Chemistry of Solids*, vol. 30, no. 9, pp. 2251–2267, 1969.

[354] K. Nakamura and M. Kitajima, "Ion-irradiation effects on the phonon correlation length of graphite studied by raman spectroscopy," *Physical Review B*, vol. 45, no. 1, p. 78, 1992.

[355] K. Ishioka, M. Hase, M. Kitajima, and K. Ushida, "Ultrafast carrier and phonon dynamics in ion-irradiated graphite," *Applied Physics Letters*, vol. 78, no. 25, pp. 3965–3967, 2001.

[356] A. C. Ferrari, "Raman spectroscopy of graphene and graphite: disorder, electron–phonon coupling, doping and nonadiabatic effects," *Solid state communications*, vol. 143, no. 1-2, pp. 47–57, 2007.

[357] M. A. Gallis, J. R. Torczynski, S. J. Plimpton, D. J. Rader, and T. Koehler, "Direct simulation monte carlo: The quest for speed," in *AIP Conference Proceedings*, vol. 1628, no. 1. AIP, 2014, pp. 27–36.

[358] G. LeBeau, "A parallel implementation of the direct simulation monte carlo method," *Computer Methods in Applied Mechanics and Engineering*, vol. 174, no. 3-4, pp. 319–337, 1999.

[359] G. LeBeau and F. Lumpkin Iii, "Application highlights of the dsmc analysis code (dac) software for simulating rarefied flows," *Computer Methods in Applied Mechanics and Engineering*, vol. 191, no. 6, pp. 595–609, 2001.

[360] D. S. Liechty, "Object-oriented/data-oriented design of a direct simulation monte carlo algorithm," *Journal of Spacecraft and Rockets*, 2015.

[361] M. MacLean, J. Marschall, and D. Driver, "Finite-rate surface chemistry model, ii: Coupling to viscous navier-stokes code," in *42nd AIAA Thermophysics Conference*, 2011, p. 3784.

[362] W. Huffman, "The importance of active surface area in the heterogeneous reactions of carbon," *Carbon*, vol. 29, no. 6, pp. 769–776, 1991.

[363] A. A. Lizzio, H. Jiang, and L. R. Radovic, "On the kinetics of carbon (char) gasification: reconciling models with experiments," *Carbon*, vol. 28, no. 1, pp. 7–19, 1990.

[364] I. Chorkendorff and J. W. Niemantsverdriet, *Concepts of modern catalysis and kinetics*. John Wiley & Sons, 2006.

[365] P. Kisliuk, "The sticking probabilities of gases chemisorbed on the surfaces of solidsii," *J. Phys. Chem. Solids*, vol. 5, pp. 78–84, 1958.

[366] G. A. Somorjai, *Introduction to surface chemistry and catalysis*. John Wiley & Sons, 1994.

[367] G. A. Somorjai and Y. Li, *Introduction to surface chemistry and catalysis*. John Wiley & Sons, 2010.

[368] R. I. Masel, *Principles of adsorption and reaction on solid surfaces*. John Wiley & Sons, 1996, vol. 3.

[369] W. Weinberg, "Precursor intermediates and precursor-mediated surface reactions: General concepts, direct observations and indirect manifestations," in *Kinetics of Interface Reactions*. Springer, 1987, pp. 94–124.

[370] I. G. Pitt, R. G. Gilbert, and K. R. Ryan, "Application of transition-state theory to gas-surface reactions: Barrierless adsorption on clean surfaces," *The Journal of Physical Chemistry*, vol. 98, no. 49, pp. 13 001–13 010, 1994.

[371] B. I. Bentley, *Scattering, Adsorption, and Langmuir-Hinshelwood Desorption Models for Physisorptive and Chemisorptive Gas-Surface Systems*. Air Force Institute of Technology, 2013.

[372] S. J. Lombardo and A. T. Bell, "A monte carlo model for the simulation of temperature-programmed desorption spectra," *Surface Science*, vol. 206, no. 1-2, pp. 101–123, 1988.

[373] P. Junell, M. Hirsimäki, and M. Valden, "Displacement of chemisorbed 12 co from pd {110} by adsorbing hot precursor 13 co molecules," *Physical Review B*, vol. 69, no. 15, p. 155410, 2004.

[374] A. N. Molchanova (Shumakova), A. V. Kashkovsky, and Y. A. Bondar, "A detailed DSMC surface chemistry model," *AIP Conference Proceedings*, vol. 1628, no. 131, pp. 131–138, 2014.

[375] D. T. Gillespie, "A general method for numerically simulating the stochastic time evolution of coupled chemical reactions," *Journal of computational physics*, vol. 22, no. 4, pp. 403–434, 1976.

[376] F. O. Goodman, "Simple model for the velocity distribution of molecules desorbed from surfaces following recombination of atoms," *Surface Science*, vol. 30, no. 3, pp. 525–535, 1972.

[377] A. Hodgson, "State resolved desorption measurements as a probe of surface reactions," *Progress in Surface Science*, vol. 63, no. 1-2, pp. 1–61, jan 2000.

[378] J. Zhang, D. J. Garton, and T. K. Minton, "Reactive and inelastic scattering dynamics of hyperthermal oxygen atoms on a saturated hydrocarbon surface," *The Journal of chemical physics*, vol. 117, no. 13, pp. 6239–6251, 2002.

[379] C. T. Rettner and D. J. Auerbach, "Dynamics of the Eley-Rideal Reaction of D Atoms with H Atoms Adsorbed on Cu(111): Vibrational and Rotational State Distributions of the HD Product," *Physical Review Letters*, vol. 74, no. 22, pp. 4551–4554, may 1995.

[380] E. Quintas-Sánchez, P. Larrégaray, C. Crespos, L. Martin-Gondre, J. Rubayo-Soneira, and J. C. Rayez, "Dynamical reaction pathways in Eley-Rideal recombination of nitrogen from W(100)," *Journal of Chemical Physics*, vol. 137, no. 6, pp. 24 706–121 103, 2012.

[381] T. Zaharia, A. W. Kleyn, and M. A. Gleeson, "Eley-Rideal reactions with N atoms at Ru(0001): Formation of NO and N2," *Physical Review Letters*, vol. 113, no. 5, p. 053201, jul 2014.

[382] J. Beckerle, A. Johnson, and S. Ceyer, "Observation and mechanism of collision-induced desorption: C h 4 on ni (111)," *Physical review letters*, vol. 62, no. 6, p. 685, 1989.

[383] J. Beckerle, A. Johnson, and S. Ceyer, "Collision-induced desorption of physisorbed ch4 from ni (111): Experiments and simulations," *The Journal of Chemical Physics*, vol. 93, no. 6, pp. 4047–4065, 1990.

[384] C. Rettner and J. Lee, "Dynamic displacement of o2 from pt (111): A new desorption mechanism," *The Journal of chemical physics*, vol. 101, no. 11, pp. 10 185–10 188, 1994.

[385] M. Wheeler, D. Seets, and C. Mullins, "Angular dependence of the dynamic displacement of o 2 from pt (111) by atomic oxygen," *The Journal of chemical physics*, vol. 107, no. 5, pp. 1672–1675, 1997.

[386] G. Comsa and R. David, "Dynamical parameters of desorbing molecules," *Surface Science Reports*, vol. 5, no. 4, pp. 145–198, dec 1985.

[387] T. K. Minton and D. J. Garton, "Dynamics of atomic-oxygen-induced polymer degradation in low earth orbit," *Chemical Dynamics in Extreme Environments*, vol. 11, pp. 420–489, 2001.

[388] G. O. Brink, "Electron bombardment molecular beam detector," *Review of Scientific Instruments*, vol. 37, no. 7, pp. 857–860, jul 1966.

[389] M. Ohashi, M. Ozeki, and J. Cui, "New apparatus with double supersonic molecular beams for epitaxial growth and surface reaction studies," *Review of Scientific Instruments*, vol. 70, no. 10, pp. 4037–4043, 1999.

[390] K. P. Giapis, T. A. Moore, and T. K. Minton, "Hyperthermal neutral beam etching," *Journal of Vacuum Science & Technology A: Vacuum, Surfaces, and Films*, vol. 13, no. 3, pp. 959–965, may 1995.

[391] M. Balooch and D. Olander, "Reactions of modulated molecular beams with pyrolytic graphite. iii. hydrogen," *The Journal of Chemical Physics*, vol. 63, no. 11, pp. 4772–4786, 1975.

[392] D. Olander, T. Acharya, and A. Ullman, "Reactions of modulated molecular beams with pyrolytic graphite iv. water vapor," *The Journal of Chemical Physics*, vol. 67, no. 8, pp. 3549–3562, 1977.

[393] J. Kennedy and R. Eberhart, "Particle swarm optimization," *Neural Networks, 1995. Proceedings., IEEE International Conference on*, vol. 4, pp. 1942–1948 vol.4, 1995.

[394] J. Kennedy, "Particle Swarm Optimization," in *Encyclopedia of Machine Learning*. Boston, MA: Springer US, 2011, pp. 760–766.

[395] G. Venter and J. Sobieszczanski-Sobieski, "Particle Swarm Optimization," *AIAA Journal*, vol. 41, no. 8, pp. 1583–1589, aug 2003.

[396] D. C. Sorescu, K. D. Jordan, and P. Avouris, "Theoretical study of oxygen adsorption on graphite and the (8, 0) single-walled carbon nanotube," *The Journal of Physical Chemistry B*, vol. 105, no. 45, pp. 11 227–11 232, 2001.

[397] V. Morón, P. Gamallo, and R. Sayós, "DFT and kinetics study of O/O2 mixtures reacting over a graphite (0001) basal surface," *Theoretical Chemistry Accounts*, vol. 128, no. 4-6, pp. 683–694, 2011.

[398] D. Lamoen and B. Persson, "Adsorption of Potassium and Oxygen on Graphite: A Theoretical Study," *The Journal of Chemical Physics*, vol. 108, no. 8, pp. 3332–3341, 1998.

[399] A. Incze, A. Pasturel, and C. Chatillon, "Oxidation of Graphite by Atomic Oxygen: A First-principles Approach," *Surface Science*, vol. 537, no. 1, pp. 55–63, 2003.

[400] J. T. Paci, H. P. Upadhyaya, J. Zhang, G. C. Schatz, and T. K. Minton, "Theoretical and Experimental Studies of the Reactions between Hyperthermal O(^{3}P) and Graphite: Graphene-Based Direct Dynamics and Beam-Surface Scattering Approaches," *The Journal of Physical Chemistry A*, vol. 113, no. 16, pp. 4677–4685, 2009.

[401] B. Marchon, W. Tysoe, J. Carrazza, H. Heinemann, and G. Somorjai, "Reactive and Kinetic Properties of Carbon Monoxide and Carbon Dioxide on a Graphite Surface," *The Journal of Physical Chemistry*, vol. 92, no. 20, pp. 5744–5749, 1988.

[402] M. Rubeš, J. Kysilka, P. Nachtigall, and O. Bludskỳ, "DFT/CC investigation of physical adsorption on a graphite (0001) surface," *Physical Chemistry Chemical Physics*, vol. 12, no. 24, pp. 6438–6444, 2010.

[403] B. Marchon, J. Carrazza, H. Heinemann, and G. Somorjai, "TPD and XPS studies of O2, CO2, and H2O adsorption on clean polycrystalline graphite," *Carbon*, vol. 26, no. 4, pp. 507–514, 1988.

[404] B. C. Marshall, E. J. Smoll, S. M. Purcell, M. L. Costen, K. G. McKendrick, and T. K. Minton, "Scattering dynamics of oxygen atoms on imidazolium tetrafluoroborate ionic liquid surfaces: Dependence on alkyl chain length," *The Journal of Physical Chemistry C*, vol. 120, no. 23, pp. 12 472–12 483, 2016.

[405] I. G. Pitt, R. G. Gilbert, and K. R. Ryan, "Application of Transition-State Theory to Gas-Surface Reactions: Barrierless Adsorption on Clean Surfaces," *The Journal of Physical Chemistry*, vol. 98, no. 49, pp. 13 001–13 010, dec 1994.

[406] G. Blyholder and H. Eyring, "Kinetics of graphite oxidation," *Journal of Physical Chemistry (U.S.)*, vol. Vol: 61, May 1957.

[407] D. E. Rosner and H. D. Allendorf, "Comparative Studies of the Attack of Pyrolytic and Isotropic Graphite by Atomic and Molecular Oxygen at High Temperatures," *AIAA Journal*, vol. 6, no. 4, pp. 650–654, 1968.

[408] G. N.-K. Liu, "High temperature oxidation of graphite by a dissociated oxygen beam," Ph.D. dissertation, Massachusetts Institute of Technology, Cambridge, Massachusetts, 1973.

[409] R. Zacharia, "Desorption of gases from graphitic and porous carbon surfaces," Ph.D. dissertation, Freie Universität Berlin, 2004.

[410] C. Stegelmann, A. Andreasen, and C. T. Campbell, "Degree of rate control: How much the energies of intermediates and transition states control rates," *Journal of the American Chemical Society*, vol. 131, no. 23, pp. 8077–8082, 2009.

[411] J. C. Ferguson, F. Panerai, A. Borner, and N. N. Mansour, "Puma: the porous microstructure analysis software," *SoftwareX*, vol. 7, pp. 81–87, 2018.

[412] J. C. Ferguson, F. Panerai, F. Semeraro, A. Borner, J. Thornton, R. King, P. Diaz-Hyland, K. Swaminathan-Gopalan, and N. N. Mansour, "Recent developments to the porous microstructure analysis (puma) software," 2018.

[413] K. Swaminathan-Gopalan, A. Borner, and K. Stephani, "Development of a detailed surface chemistry framework in sparta," 2017.

[414] F. Panerai, J. C. Ferguson, J. Lachaud, A. Martin, M. J. Gasch, and N. N. Mansour, "Micro-tomography based analysis of thermal conductivity, diffusivity and oxidation behavior of rigid and flexible fibrous insulators," *International Journal of Heat and Mass Transfer*, vol. 108, pp. 801–811, 2017.

[415] F. O. Goodman, "Simple model for the velocity distribution of molecules desorbed from surfaces following recombination of atoms," *Surface Science*, vol. 30, no. 3, pp. 525–535, 1972.

[416] K. Swaminathan Gopalan and K. A. Stephani, "Effective oxidation model for light-weight carbon preform ablators," in *AIAA Scitech 2019 Forum*, 2019, p. 0245.

[417] H. Deng, T. Ozawa, and D. Levin, "Analysis of chemistry models for dsmc simulations of the atmosphere of io," *Journal of thermophysics and heat transfer*, vol. 26, no. 1, pp. 36–46, 2012.

[418] N. Parsons, D. A. Levin, A. C. Walker, C. H. Moore, D. B. Goldstein, P. L. Varghese, and L. Trafton, "Influence of ab initio chemistry models on simulations of the ionian atmosphere," *Icarus*, vol. 239, pp. 32–38, 2014.

[419] C. H. Moore, H. Deng, D. B. Goldstein, D. Levin, P. L. Varghese, L. M. Trafton, B. D. Stewart, and A. C. Walker, "Simulation of plasma interaction with ios atmosphere," in *AIP Conference Proceedings*, vol. 1333, no. 1. AIP, 2011, pp. 1163–1168.

[420] C. Moore, A. Walker, D. Goldstein, P. Varghese, L. Trafton, N. Parsons, and D. Levin, "Dsmc simulations of the plasma bombardment on io's sublimated and sputtered atmosphere," in *50th AIAA Aerospace Sciences Meeting including the New Horizons Forum and Aerospace Exposition*, 2012, p. 560.

[421] T. Ozawa, D. Levin, and I. Wysong, "Chemical reaction modeling for hypervelocity collisions between o and hcl," *Physics of Fluids*, vol. 19, no. 5, p. 056102, 2007.

[422] H. Deng, C. Moore, D. Levin, D. Goldstein, and P. Varghese, "Analysis of so 2+ o chemistry models for simulations of the atmosphere of io," in *AIP Conference Proceedings*, vol. 1333, no. 1. AIP, 2011, pp. 1139–1144.

[423] N. Parsons, D. A. Levin, A. C. van Duin, and T. Zhu, "Modeling of molecular nitrogen collisions and dissociation processes for direct simulation monte carlo," *The Journal of chemical physics*, vol. 141, no. 23, p. 234307, 2014.

[424] N. S. Parsons and D. A. Levin, "Dsmc implementation of md/qct generated energy distributions for so2+ o collisions," in *44th AIAA Thermophysics Conference*, 2013, p. 2785.

[425] N. S. Parsons, T. Zhu, D. A. Levin, and A. C. van Duin, "Development of dsmc chemistry models for nitrogen collisions using accurate theoretical calculations," in *52nd Aerospace Sciences Meeting*, 2014, p. 1213.

[426] K. Swaminathan-Gopalan and K. A. Stephani, "Study of inelastic scattering of o2 on carbon: Comparison of molecular dynamics simulation and molecule-surface scattering theory," in *31st International Symposium on Rarefied Gas Dynamics*. AIP Publishing, 2018.

[427] S. Plimpton, "Fast parallel algorithms for short-range molecular dynamics," *Journal of computational physics*, vol. 117, no. 1, pp. 1–19, 1995.

[428] A. C. Van Duin, S. Dasgupta, F. Lorant, and W. A. Goddard, "Reaxff: a reactive force field for hydrocarbons," *The Journal of Physical Chemistry A*, vol. 105, no. 41, pp. 9396–9409, 2001.

[429] Y. K. Shin, L. Gai, S. Raman, and A. C. Van Duin, "Development of a reaxff reactive force field for the pt–ni alloy catalyst," *The Journal of Physical Chemistry A*, vol. 120, no. 41, pp. 8044–8055, 2016.

[430] S. G. Srinivasan, A. C. Van Duin, and P. Ganesh, "Development of a reaxff potential for carbon condensed phases and its application to the thermal fragmentation of a large fullerene," *The Journal of Physical Chemistry A*, vol. 119, no. 4, pp. 571–580, 2015.

[431] C. de Tomas, I. Suarez-Martinez, and N. A. Marks, "Graphitization of amorphous carbons: A comparative study of interatomic potentials," *Carbon*, vol. 109, pp. 681–693, 2016.

[432] S. Poovathingal, T. E. Schwartzentruber, S. G. Srinivasan, and A. C. Van Duin, "Large scale computational chemistry modeling of the oxidation of highly oriented pyrolytic graphite," *The Journal of Physical Chemistry A*, vol. 117, no. 13, pp. 2692–2703, 2013.

[433] L. Bytautas and K. Ruedenberg, "Accurate ab initio potential energy curve of o 2. i. nonrelativistic full configuration interaction valence correlation by the correlation energy extrapolation by intrinsic scaling method," *The Journal of chemical physics*, vol. 132, no. 7, p. 074109, 2010.

[434] L. Bytautas, N. Matsunaga, and K. Ruedenberg, "Accurate ab initio potential energy curve of o 2. ii. core-valence correlations, relativistic contributions, and vibration-rotation spectrum," *The Journal of chemical physics*, vol. 132, no. 7, p. 074307, 2010.

[435] H. J. Berendsen, J. v. Postma, W. F. van Gunsteren, A. DiNola, and J. Haak, "Molecular dynamics with coupling to an external bath," *The Journal of chemical physics*, vol. 81, no. 8, pp. 3684–3690, 1984.

[436] E. Josyula, *Hypersonic Nonequilibrium Flows: Fundamentals and Recent Advances*. American Institute of Aeronautics and Astronautics, Inc., 2015.

[437] W. W. Hayes and J. R. Manson, "Scattering of Xe from Graphite," *The Journal of Physical Chemistry A*, vol. 115, no. 25, pp. 6838–6842, jun 2011. [Online]. Available: http://pubs.acs.org/doi/abs/10.1021/jp111153q

[438] A. Muis and J. Manson, "Rare gas scattering from molten metals examined with classical scattering theory," *The Journal of chemical physics*, vol. 107, no. 5, pp. 1655–1663, 1997.

[439] A. Muis and J. Manson, "Calculations of the energy accommodation coefficient using classical scattering theory," *Surface science*, vol. 486, no. 1, pp. 82–94, 2001.

[440] E. Pollak and J. Manson, "Temperature dependence in atom–surface scattering," *Journal of Physics: Condensed Matter*, vol. 24, no. 10, p. 104001, 2012.

[441] J. Oh, T. Kondo, K. Arakawa, Y. Saito, W. W. Hayes, J. R. Manson, and J. Nakamura, "Angular Intensity Distribution of a Molecular Oxygen Beam Scattered from a Graphite Surface," *The Journal of Physical Chemistry A*, vol. 115, no. 25, pp. 7089–7095, jun 2011. [Online]. Available: http://pubs.acs.org/doi/abs/10.1021/jp112394m

[442] J. Oh, T. Kondo, K. Arakawa, Y. Saito, J. Nakamura, W. W. Hayes, and J. R. Manson, "Scattering of CO and N2 molecules by a graphite surface," *Journal of Physics: Condensed Matter*, vol. 24, no. 35, p. 354001, sep 2012. [Online]. Available: http://stacks.iop.org/0953-8984/24/i=35/a=354001?key=crossref.b6bd9aa399b8389ba21b1d63543d1fe4

[443] K. Swaminathan-Gopalan, T. Zhu, E. Ertekin, and K. A. Stephani, "Structural and thermal effects of ion-irradiation induced defect configurations in silicon," *Physical Review B*, vol. 95, no. 18, p. 184109, 2017.

[444] J. Hahn, "Kinetic study of graphite oxidation along two lattice directions," *Carbon*, vol. 43, no. 7, pp. 1506–1511, 2005.

[445] K. T. Nicholson, T. K. Minton, and S. Sibener, "Spatially anisotropic etching of graphite by hyperthermal atomic oxygen," *The Journal of Physical Chemistry B*, vol. 109, no. 17, pp. 8476–8480, 2005.

[446] R. Edel, T. Grabnic, B. Wiggins, and S. Sibener, "Atomically-resolved oxidative erosion and ablation of basal plane hopg graphite using supersonic beams of o2 with scanning tunneling microscopy visualization," *The Journal of Physical Chemistry C*, 2018.

[447] H. Allendorf and D. Rosner, "Comparative studies of the attack of pyrolytic and isotropic graphite by atomic and molecular oxygen at high temperatures." *AIAA journal*, vol. 6, no. 4, pp. 650–654, 1968.

[448] H. D. Allendorf and D. E. Rosner, "Primary products in the attack of graphite by atomic oxygen and diatomic oxygen above 1100 k," *Carbon*, vol. 7, no. 4, pp. 515–518, 1969.

[449] D. Rosner and H. Allendorf, "High temperature oxidation of carbon by atomic oxygen," *Carbon*, vol. 3, no. 2, pp. 153–156, 1965.

[450] J. Walls and R. Strickland-Constable, "Oxidation of carbon between 1000–2400 c," *Carbon*, vol. 1, no. 3, pp. 333IN23 335–334 338, 1964.

[451] F. Panerai, A. Martin, N. N. Mansour, S. A. Sepka, and J. Lachaud, "Flow-tube oxidation experiments on the carbon preform of a phenolic-impregnated carbon ablator," *Journal of Thermophysics and Heat Transfer*, vol. 28, no. 2, pp. 181–190, 2014.

[452] P. Klemens and D. Pedraza, "Thermal conductivity of graphite in the basal plane," *Carbon*, vol. 32, no. 4, pp. 735–741, 1994.

[453] D. Nika, S. Ghosh, E. Pokatilov, and A. Balandin, "Lattice thermal conductivity of graphene flakes: Comparison with bulk graphite," *Applied Physics Letters*, vol. 94, no. 20, p. 203103, 2009.

[454] A. Alofi and G. Srivastava, "Thermal conductivity of graphene and graphite," *Physical Review B*, vol. 87, no. 11, p. 115421, 2013.

[455] T. Zhu, K. Swaminathan-Gopalan, K. J. Cruse, K. Stephani, and E. Ertekin, "Vibrational energy transport in hybrid ordered/disordered nanocomposites: Hybridization and avoided crossings of localized and delocalized modes," *Advanced Functional Materials*, vol. 28, no. 17, p. 1706268, 2018.

[456] T. Zhu, K. Swaminathan-Gopalan, K. Stephani, and E. Ertekin, "Thermoelectric phonon-glass electron-crystal via ion beam patterning of silicon," *Physical Review B*, vol. 97, no. 17, p. 174201, 2018.

[457] T. Katayama, D. Sekiba, K. Mukai, Y. Yamashita, F. Komori, and J. Yoshinobu, "Adsorption states and dissociation processes of oxygen molecules on cu (100) at low temperature," *The Journal of Physical Chemistry C*, vol. 111, no. 41, pp. 15 059–15 063, 2007.

[458] W. Wang and Y. Zhao, "The direct and precursor mediated dissociation rates of h 2 on a ni (111) surface," *Physical Chemistry Chemical Physics*, vol. 17, no. 8, pp. 5901–5912, 2015.

[459] C. Rettner, E. Schweizer, and C. Mullins, "Desorption and trapping of argon at a 2h–w (100) surface and a test of the applicability of detailed balance to a nonequilibrium system," *The Journal of Chemical Physics*, vol. 90, no. 7, pp. 3800–3813, 1989.

[460] A. Raukema and A. W. Kleyn, "Transient trapping desorption of molecules at surfaces," *Physical review letters*, vol. 74, no. 21, p. 4333, 1995.

[461] C. Shen, *Rarefied gas dynamics: fundamentals, simulations and micro flows*. Springer Science & Business Media, 2006.

[462] D. Frenkel and B. Smit, *Understanding molecular simulation: from algorithms to applications*. Academic press, 2001, vol. 1.

[463] R. LeSar, *Introduction to computational materials science: fundamentals to applications*. Cambridge University Press, 2013.

[464] J. Greenwood, "The correct and incorrect generation of a cosine distribution of scattered particles for monte-carlo modelling of vacuum systems," *Vacuum*, vol. 67, no. 2, pp. 217–222, 2002.

[465] T. K. Minton, J. Zhang, D. J. Garton, and J. W. Seale, "Collision-assisted erosion of hydrocarbon polymers in atomic-oxygen environments," *High Performance Polymers*, vol. 12, no. 1, pp. 27–42, 2000.